

**WAVE-CURRENT INTERACTION IN
STRONGLY SHEARED MEAN FLOWS**

BY

ZHIFEI DONG, JAMES T. KIRBY AND FENGYAN SHI

RESEARCH REPORT NO. CACR-16-03
NOVEMBER 2016

SUPPORTED BY THE NATIONAL SCIENCE FOUNDATION,
PHYSICAL OCEANOGRAPHY PROGRAM.
GRANT NOS. OCE-0926974 AND OCE-1334325



CENTER FOR APPLIED COASTAL RESEARCH

Ocean Engineering Laboratory
University of Delaware
Newark, Delaware 19716

TABLE OF CONTENTS

LIST OF FIGURES	ix
LIST OF VARIABLES	xxvii
ABSTRACT	xxxii
 Chapter	
1 INTRODUCTION	1
1.1 Current Effects on Waves	3
1.2 Wave Effects on Current	5
1.3 Outline of the Thesis	13
2 MULTIPLE-SCALE EXPANSION OF GOVERNING EQUATIONS	14
2.1 Governing Equations	15
2.2 Wave-averaged Forces	16
2.3 Linear Wave Problem in Two Horizontal Dimensions	17
2.4 Multiple-scale Approach	18
2.4.1 Multiple scale expansion of momentum equation and boundary conditions	21
2.4.2 Multiple scale expansion of vorticity equations	26
3 WAVE DYNAMICS	30
3.1 First-order Wave Motions	30
3.1.1 Linear wave vorticity	31
3.1.2 Wave vorticity for constant shear current	32

3.1.3	Numerical solution to wave Rayleigh equation	36
3.1.3.1	Verification of numerical solution	39
3.1.4	Perturbation solution to wave Rayleigh equation	42
3.1.5	Numerical and $O(\epsilon)$ perturbation solution comparison	44
3.1.6	Depth-weighted current	57
3.2	Second-order Wave Motions	57
3.2.1	Compatibility condition and wave action equation	60
3.2.2	Wave action equation for depth-uniform current	61
3.2.3	Wave action equation for constant shear current	62
3.2.4	Wave action equation for weak shear current	62
3.2.5	Numerical study of wave action equation	64
3.2.5.1	Group velocity from wave action equation and dispersion relation	64
3.2.5.2	Wave action and action flux comparison	68
3.2.5.3	Absolute group velocity comparison	71
3.2.6	Second order wave vorticity	76
3.2.7	Perturbation solution to the second order wave Rayleigh equation	76
4	MEAN FLOW DYNAMICS	79
4.1	Mean Flow Momentum	79
4.2	Mean Flow Vorticity	83
4.3	Wave-averaged Forces	85
4.4	Vortex Force for Strong Depth Uniform Current	86
4.5	Vortex Force for Weak Current: Comparison with MRL04	87
4.6	Vortex Force for Constantly Sheared Current	89
4.7	Wave-averaged Forces with Full Perturbation Solutions	91
4.8	Depth-integrated Equations for Wave-averaged Flow	102
5	THE COUPLED NHWAVE/SWAN MODEL ($NH\overline{WAVE}$)	105
5.1	Introduction to NHWAVE Model	107
5.1.1	Governing equations	108
5.1.2	Boundary Conditions	110

5.1.3	Turbulence Model	111
5.2	Introduction to SWAN Wave Model	111
5.2.1	Wave Action Balance Equation	112
5.3	Coupling Scheme of NHWAVE and SWAN	113
5.4	Numerical Application of Vortex Forces by Uchiyama <i>et al.</i> (2010) . .	114
5.4.1	Governing equations	114
5.4.2	Application in model	119
5.4.2.1	Stokes drift velocity	119
5.4.2.2	Vortex force	120
5.4.2.3	Wave dissipation	120
5.4.2.4	Continuity equation	121
5.4.2.5	Boundary condition	121
5.4.2.6	Momentum equation	122
5.5	Numerical Application of the Present Formulation	123
5.5.1	Governing equations	123
5.6	Application to Longshore Current Simulation	126
5.6.1	Model setup	126
5.6.2	Results from Uchiyama <i>et al.</i> (2010) vortex force	129
5.6.3	Results from the present vortex force	139
5.7	Application to Columbia River	144
5.7.1	Model Setup	144
6	APPLICATION OF WAVE VORTEX FORCE TO LANGMUIR CIRCULATION USING $NH\overline{WAVE}$	165
6.1	Model Setup	166
6.1.1	Governing Equations	166

6.1.2	Model Setup	168
6.2	Results	170
6.2.1	Comparison with Tejada-Martinez and Grosch (2007)	170
6.2.2	Flow structure	174
7	CONCLUSIONS	183
7.1	Theory	183
7.2	Numerical Application	185
	REFERENCES	187
	Appendix	
A	WAVE SOLUTIONS FOR SPECIAL CURRENT PROFILES	194
A.1	Waves in a stationary domain with slowly varying depth	194
A.2	Depth uniform current	196
A.3	Constant shear current	196
B	DERIVATION OF GENERAL FORM OF WAVE-AVERAGED FORCES	198
B.1	Bernoulli head: κ	198
B.2	Horizontal vortex force \mathbf{J}	199
B.3	Vertical vortex force K	199
C	DERIVATION OF WAVE-AVERAGED FORCES FOR WEAK CURRENT	200

LIST OF FIGURES

1.1	GLM results (Groeneweg and Klopman, 1998) and experimental results (Klopman, 1994) for the first order Eulerian-mean horizontal velocity amplitude profile. Both the model results and experimental results indicate that the following current decreases the vertical gradient of velocity amplitude, while the opposing current increases the vertical gradient. See Figure 2 in Groeneweg and Klopman (1998)	6
3.1	Waves propagating over a constantly sheared current. Suppose the flow $\mathbf{q}_{0,0}$ and shear $\mathbf{\Omega}^s$ is in x -direction on a flat bed. The angle between wave direction and flow direction is θ . Results from Section 3.1.2 indicate that the amplitude of wave vorticity is affected by the oblique angle θ and current shear. When $\theta = 0$ or $\theta = \pm\pi$, waves are either exactly following the current or opposing the current. Wave vorticity is zero in this case. For a fixed $\theta \neq 0, \pm\pi$ and vertical level z , wave vorticity increases as current shear turns larger and decreases as current shear turns smaller. For a fixed current shear, wave vorticity changes with oblique angle θ in a more complicated way as in Equation (3.33) - (3.35).	33
3.2	Surface wave vorticity changes with oblique wave angle ($kh = 1$). Upper: waves following current. The oblique wave angle varies from $-\pi/2$ to $\pi/2$. Lower: waves opposing current. The oblique wave angle varies from $\pi/2$ to $3\pi/2$. Blue Dash-dot: x -component ($\xi_{1,1}^x$); Blue Star: y -component ($\xi_{1,1}^y$); Blue Solid: z -component ($\chi_{1,1}$); Red Dash: total ($\sqrt{\chi_{1,1}^2 + \xi_{1,1}^2}$). Results are calculated based on Equation (3.33) - (3.35).	36
3.3	Surface wave vorticity changes with oblique wave angle ($kh = 0.2$). Upper: waves following current. The oblique wave angle varies from $-\pi/2$ to $\pi/2$. Lower: waves opposing current. The oblique wave angle varies from $\pi/2$ to $3\pi/2$. Blue Dash-dot: x -component ($\xi_{1,1}^x$); Blue Star: y -component ($\xi_{1,1}^y$); Blue Solid: z -component ($\chi_{1,1}$); Red Dash: total ($\sqrt{\chi_{1,1}^2 + \xi_{1,1}^2}$). Results are calculated based on Equation (3.33) - (3.35).	37

3.4	Verification of numerical solution to Rayleigh equation. (Upper) Measured current velocity profiles at Columbia River mouth (blue solid line) with 6th order polynomial curve fitting (red dashed line) (Kilcher and Nash, 2010). The measured data indicates a strong surface current (up to 2.3 m/s with strong vertical shear during ebb tide. (Lower) Absolute wave phase speed c change over non-dimensional wave number kh obtained from numerical solution.	40
3.5	Verification of numerical solution to Rayleigh Equation. (Upper Left) Depth uniform current velocity profile with 6th order polynomial curve fitting (red dashed line). The current velocity is set as -3.5 m/s. (Upper Right) Comparison of analytical solution (blue '+') and numerical solution (blue solid line). The vertical resolution $dz = 0.1$ m. (Lower Left) Constant shear current velocity profile with 6th order polynomial curve fitting (red dashed line). The current velocity is set as -3.5 m/s at water surface and 0 m/s at the bottom. (Lower Right) Comparison of analytical solution (blue '+') and numerical solution (blue solid line). The vertical resolution $dz = 0.1$ m. The results indicate that numerical solutions converge to these two analytical solutions.	41
3.6	Wave phase speed comparison between perturbation solution up to $O(\epsilon^2)$ and numerical solution with analytical current velocity profiles: Depth uniform current (Upper Panel), Linearly sheared current (Lower Panel). The maximum current speed is set as 3.5 m/s to meet strong current assumption. The left figure of each panel shows original profile and 6th order polynomial fitting curves. The right figure of each panel shows the non dimensional wave phase speed normalized by the numerical solution (c_{dir}). As the figure indicates, shorter waves are more sensitive to the ambient current than longer waves. Additionally, the accuracy of perturbation solution goes higher with increasing orders. The $O(\epsilon)$ perturbation solution is a good approximation to numerical solution.	46

3.7	Wave phase speed comparison between perturbation solution up to $O(\epsilon^2)$ and numerical solution with analytical current velocity profiles: Cosine-shape current (Upper Panel) and Power law shape current (Lower Panel). The maximum current speed is set as 3.5 m/s to meet strong current assumption. The left figure of each panel shows original profile and 6th order polynomial fitting curves. The right figure of each panel shows the non dimensional wave phase speed normalized by the numerical solution (c_{dir}). Figure indicates that shorter waves are more sensitive to the ambient current than longer waves. The $O(\epsilon)$ perturbation solution is a good approximation to numerical solution.	47
3.8	Measured cross-shore current speed profiles seaward from Columbia River mouth during an ebb tide (Kilcher and Nash, 2010). This data was taken from the R/V Pt. Sur, during the July 2004 RISE cruise (http://makani.coas.oregonstate.edu/rise/). The transect is one of the cruise routes by the R/V Pt. Sur. The ship moves seaward from the river mouth during an ebb tide. Therefore the current data have slight time difference. The horizontal axis represents the cross-shore distance seaward from the river mouth ($x = 0$ km). The vertical axis represents the vertical elevation. Blue Solid: ocean bottom elevation along the transect. Black Dash: zero current speed line at each cross-shore location. Blue Dash: measured current speed at each cross-shore location. The length of legend represents 2 m/s current speed. As the figure indicates, the maximum current speed exceeds 2 m/s at the river mouth where water depth is shallower. The current speed decrease seaward with increasing water depth. .	48
3.9	Wave phase speed comparison between perturbation solution up to $O(\epsilon^2)$ and numerical solution with measured current velocity profiles at Columbia river mouth - opposing currents. This data was taken from the R/V Pt. Sur, during the July 2004 RISE cruise (http://makani.coas.oregonstate.edu/rise/). The Upper Panel shows a typical current profile during ebb tide. The Lower Panel shows vertically well-mixed current profile during ebb tide. Both no-current assumption and depth-average current assumption cause wave phase speed to deviate from the exact solution. The deviation depends on both current magnitude and current shear. Strong current with strong shear causes larger deviation.	50

3.10	Wave phase speed comparison between perturbation solution up to $O(\epsilon^2)$ and numerical solution with measured current velocity profiles at Columbia river mouth - following currents. This data was taken from the R/V Pt. Sur, during the July 2004 RISE cruise (http://makani.coas.oregonstate.edu/rise/). The current profiles are exactly reversed from Figure 3.9 to provide waves solution when following current.	51
3.11	Comparison of wave orbital velocity amplitude vertical distribution for short wave ($kh = 2$), intermediate wave ($kh = 1$) and long wave ($kh = 0.4$) on the opposing current: (Upper) horizontal orbital velocity and (Lower) vertical orbital velocity amplitude. The current is assumed to be co-directional with waves. Therefore, only one horizontal direction is considered. The vertical axis represents water depth. The horizontal axis represents velocity. The comparison shows the wave orbital velocity amplitude is increased by the opposing current. K&C $O(\epsilon)$ solution is a fairly good approximation to numerical solution.	53
3.12	Comparison of wave vorticity amplitude vertical distribution for short wave ($kh = 2$), intermediate wave ($kh = 1$) and long wave ($kh = 0.4$) on the opposing current. The current is assumed to be co-directional with waves. Therefore, the wave vorticity is only in horizontal direction. In this case, the vorticity is only determined by the current profile and not related to the wave number. The values of wave vorticity are the same. The vertical axis represents water depth. The horizontal axis represents wave vorticity. The comparison shows that K&C $O(\epsilon)$ solution is a better approximation to numerical solution.	54
3.13	Comparison of wave orbital velocity amplitude vertical distribution for short wave ($kh = 2$), intermediate wave ($kh = 1$) and long wave ($kh = 0.4$) on the following current: (Upper) horizontal orbital velocity and (Lower) vertical orbital velocity amplitude. The current is assumed to be co-directional with waves. Therefore, only one horizontal direction is considered. The vertical axis represents water depth. The horizontal axis represents velocity. The comparison shows the wave orbital velocity amplitude is decreased by the following current. K&C $O(\epsilon)$ solution is a fairly good approximation to numerical solution.	55

- 3.14 Comparison of wave vorticity amplitude vertical distribution for short wave ($kh = 2$), intermediate wave ($kh = 1$) and long wave ($kh = 0.4$) on the following current. The current is assumed to be co-directional with waves. Therefore, the wave vorticity is only in horizontal direction. In this case, the vorticity is only determined by the current profile and not related to the wave number. The values of wave vorticity are the same. The vertical axis represents water depth. The horizontal axis represents wave vorticity. The comparison shows that K&C $O(\epsilon)$ solution is a better approximation to numerical solution. 56
- 3.15 Depth-weighted current velocity for exponential current profile. Consider the current speed is 1.0 m/s at the water surface and decreases exponentially to zero over depth. The depth-averaged current speed for this current profile is less than 0.1 m/s. If depth-averaged current is used in wave solution, the current effect is negligible. However, the depth-weighted current is very different and varies for different wave numbers. The equivalent current speed is larger for larger wave number. 58
- 3.16 (Opposing constant shear current) Convergence of group speed ($\partial\omega/\partial k$) and the group speed ($cg_a N/N$) (3.96) and (3.97) with different wave number steps (dk). Blue '+': Analytical absolute group velocity; Red Solid: Absolute group velocity from wave action equation; Blue Dash: Absolute group velocity from dispersion relation. Upper Panel: $dk = 0.014$, Lower Panel: $dk = 0.005$. The figure indicates that the group velocity ($\partial\omega/\partial k$) converges to the group velocity ($cg_a N/N$) as dk becomes smaller. Both numerical group velocities gradually deviate from analytical solution as kh increases (shorter waves). The difference between numerical group velocities and analytical group velocity is within 7 %. 66
- 3.17 (Following constant shear current) Convergence of group speed ($\partial\omega/\partial k$) and the group speed ($cg_a N/N$) (3.96) and (3.97) with different wave number steps (dk). Blue '+': Analytical absolute group velocity; Red Solid: Absolute group velocity from wave action equation; Blue Dash: Absolute group velocity from dispersion relation. Upper Panel: $dk = 0.014$, Lower Panel: $dk = 0.005$. The figure indicates that the group velocity ($\partial\omega/\partial k$) converges to the group velocity ($cg_a N/N$) as dk becomes smaller. Both numerical group velocities gradually deviate from analytical solution as kh increases (shorter waves). The difference between numerical group velocities and analytical group velocity is within 3 %. 67

3.18	(Opposing constant shear current) Wave action and wave action flux comparison. Blue '+' : Analytical results; Red Solid: Numerical results; Black '*': Results based on depth-averaged current; Green 'o': Results based on depth-weighted current. The dimensional wave action and action flux are calculated using wave amplitude $a = 1$ m. Upper Panel: Wave action on the left and non-dimensional wave action on the right. The wave action comparison suggests that the differences between analytical value and these assumptions are less than 2 %. Lower Panel: Wave action flux on the left and non-dimensional wave action flux on the right.	69
3.19	(Following constant shear current) Wave action and wave action flux comparison. Blue '+' : Analytical results; Red Solid: Numerical results; Black '*': Results based on depth-averaged current; Green 'o': Results based on depth-weighted current. The dimensional wave action and action flux are calculated using wave amplitude $a = 1$ m. Upper Panel: Wave action on the left and non-dimensional wave action on the right. The wave action comparison suggests that the differences between analytical value and these assumptions are less than 2 %. Lower Panel: Wave action flux on the left and non-dimensional wave action flux on the right.	70
3.20	(Opposing constant shear current) Comparison of absolute group velocities. Blue '+' : Analytical results; Red Solid: Numerical results; Black '*': Results based on depth-averaged current; Green 'o': Results based on depth-weighted current. The dimensional group velocity is given at the Left Panel. The non-dimensional group velocity based on analytical solution is given at the Right Panel. The four solutions deviate from analytical solution as kh increases. . . .	72
3.21	(Following constant shear current) Comparison of absolute group velocities. Blue '+' : Analytical results; Red Solid: Numerical results; Black '*': Results based on depth-averaged current; Green 'o': Results based on depth-weighted current. The dimensional group velocity is given at the Left Panel. The non-dimensional group velocity based on analytical solution is given at the Right Panel. . .	73
3.22	(Opposing constant shear current) Comparison of absolute group velocity for depth-weighted current with and without $k\partial\tilde{U}/\partial k$. (Left Panel) Absolute group velocity. (Right Panel) Non-dimensional absolute group velocity based on analytical solutions. Figure indicates that there is bigger errors for by neglecting this term. . .	74

3.23	(Following constant shear current) Comparison of absolute group velocity for depth-weighted current with and without $k\partial\tilde{U}/\partial k$. (Left Panel) Absolute group velocity. (Right Panel) Non-dimensional absolute group velocity based on analytical solutions. Figure indicates that there is bigger errors for by neglecting this term. . .	75
4.1	Opposing constant shear current and deep water ($\alpha = -1, kh = 3$). Blue Solid indicates MRL04 results; Red Dash indicates DK16 results. Upper Left: the surface current velocity is -3.5 m/s and bottom current velocity is zero. Upper Right: DK16 Stokes drift velocity is slightly larger than MRL04 for the opposing current. Lower Left: DK16 x -component vortex force magnitude is slightly larger than MRL04. Lower Right: DK16 y -component vortex force magnitude is smaller than MRL04.	92
4.2	Following constant shear current in deep water ($\alpha = 1, kh = 3$). Blue Solid indicates MRL04 results; Red Dash indicates DK16 results. Upper Left: the surface current velocity is 3.5 m/s and bottom current velocity is zero. Upper Right: DK16 Stokes drift velocity is slightly smaller than MRL04 for the opposing current. Lower Left: DK16 x -component vortex force magnitude is slightly smaller than MRL04. Lower Right: DK16 y -component vortex force magnitude is smaller than MRL04.	93
4.3	Opposing constant shear current in intermediate water ($\alpha = -1, kh = 1$). Blue Solid indicates MRL04 results; Red Dash indicates DK16 results. Upper Left: the surface current velocity is -3.5 m/s and bottom current velocity is zero. Upper Right: DK16 Stokes drift velocity is slightly smaller than MRL04 near the water surface and larger near the bottom. The velocity profile tends to be depth uniform. Lower Left: DK16 x -component vortex force magnitude is slightly larger than MRL04. Lower Right: DK16 y -component vortex force changes sign compared to MRL04 due to the current shear effect.	94

- 4.4 Following constant shear current and deep water ($\alpha = 1, kh = 1$). Blue Solid indicates MRL04 results; Red Dash indicates DK16 results. Upper Left: the surface current velocity is 3.5 m/s and bottom current velocity is zero. Upper Right: DK16 Stokes drift velocity is slightly larger than MRL04 near the water surface and smaller near the water bottom. The velocity profile tends to be depth uniform. Lower Left: DK16 x -component vortex force magnitude is slightly smaller than MRL04. Lower Right: DK16 y -component vortex force changes sign compared to MRL04 due to the current shear effect. 95
- 4.5 Opposing constant shear current in shallow water ($\alpha = -1, kh = 0.2$). Blue Solid indicates MRL04 results; Red Dash indicates DK16 results. Upper Left: the surface current velocity is -3.5 m/s and bottom current velocity is zero. Upper Right: DK16 Stokes drift velocity is slightly smaller than MRL04 near the water surface and larger near the bottom. The velocity profile tends to be depth uniform. Lower Left: DK16 x -component vortex force magnitude is slightly larger than MRL04. Lower Right: DK16 y -component vortex force changes sign compared to MRL04 due to the current shear effect. The MRL04 result is nearly zero. 96
- 4.6 Following constant shear current and deep water ($\alpha = 1, kh = 0.2$). Blue Solid indicates MRL04 results; Red Dash indicates DK16 results. Upper Left: the surface current velocity is 3.5 m/s and bottom current velocity is zero. Upper Right: DK16 Stokes drift velocity is slightly larger than MRL04 near the water surface and smaller near the bottom. The velocity profile tends to be depth uniform. Lower Left: DK16 x -component vortex force magnitude is slightly smaller than MRL04. Lower Right: DK16 y -component vortex force changes sign compared to MRL04 due to the current shear effect. The MRL04 result is nearly zero. 97
- 4.7 Following constant shear current in shallow water ($\alpha = 0.2, kh = 0.2$). Blue Solid indicates MRL04 results; Red Dash indicates DK16 results. Upper Left: the surface current velocity is -3.5 m/s. Upper Right: DK16 Stokes drift velocity converges to MRL04 for smaller current shear. Lower Left: DK16 x -component vortex force converges to MRL04 result. Lower Right: DK16 y -component vortex force converges to MRL04 result for smaller current shear. The MRL04 result is non-zero and proportional to Stokes drift velocity. 98

4.8	Following constant shear current in shallow water ($\alpha = 1, kh = 0.2$). Blue Solid indicates MRL04 results; Red Dash indicates DK16 results. Upper Left: the surface current velocity is -0.5 m/s. Upper Right: DK16 Stokes drift velocity converges to MRL04 for smaller surface current velocity. Lower Left: DK16 x -component vortex force converges to MRL04 result. Lower Right: DK16 y -component vortex force converges to MRL04 result for smaller surface current velocity. The MRL04 result is non-zero.	99
5.1	Domain decomposition of SWAN and NHWAVE. SWAN uses a single direction domain decomposition. The direction is chosen for dimension with more grid cells. NHWAVE uses a more flexible decomposition technique.	114
5.2	(Upper) Cross-shore distribution of water depth and incident significant wave height. Solid line: water depth; Dotted Line: significant wave height. The bathymetry is idealized as a planar beach with slope $1/80$. The incident significant wave height is set as 2 m offshore. As waves approaching nearshore, the wave height increases due to shoaling effect and decreases to zero due to break at the surfzone. (Lower) Cross-shore distribution of wave dissipation (ϵ^b/ρ_0).	128
5.3	(Upper) Cross-shore and vertical distribution of undertow with maximum velocity 0.15 m/s . Black dotted line: zero-velocity at each cross-shore location; Blue solid line: x -direction velocity at each cross-shore location. (Lower) Color map of eddy viscosity in $x - z$ coordinate plane. Results are based on Uchiyama <i>et al.</i> (2010) vortex force formulation and $k - \epsilon$ turbulence model.	129
5.4	(Upper) Cross-shore distribution of depth-averaged x -component Stokes drift velocity u^{st} and undertow u^c . Solid line: undertow; Dotted line: Stokes drift velocity. (Middle) Cross-shore distribution of depth-averaged longshore current. Solid line: model output; Dotted line: analytical solution. (Lower) Cross-shore distribution of mean surface elevation. Solid line: model output; Dotted line: analytical solution. The analytical cross-shore profile of η^c is approximately retrieved by integrating Equation (5.135) from offshore boundary with $\eta^c = \eta^{st}$. Results are based on Uchiyama <i>et al.</i> (2010) vortex force formulation.	131

5.5	Color map of current velocity in cross-shore section ($x - z$ coordinate plane). (Upper) cross-shore (x -component) current velocity u^c . (Middle) longshore (y -component) current velocity v^c . (Lower) vertical (z -component) current velocity w^c . Results are based on Uchiyama <i>et al.</i> (2010) vortex force formulation.	132
5.6	Color map of wave Stokes drift velocity in cross-shore section ($x - z$ coordinate plane). (Upper) cross-shore (x -component) Stokes velocity u^{st} . (Middle) longshore (y -component) Stokes velocity v^{st} . (Lower) vertical (z -component) Stokes velocity w^{st} . Results are based on Uchiyama <i>et al.</i> (2010) vortex force formulation.	133
5.7	Color map of wave breaking dissipation force (\mathbf{B}^b) in cross-shore section ($x - z$ coordinate plane). The wave dissipation force is applied in wave direction and therefore has cross-shore and longshore component. (Upper) cross-shore (x -component) wave dissipation. (Lower) longshore (y -component) wave dissipation. Results are based on Uchiyama <i>et al.</i> (2010) vortex force formulation.	135
5.8	Color map of wave vortex force in $x - z$ coordinate plain. (Upper) x -component vortex force. (Middle) y -component vortex force. (Lower) z -component vortex force. Results are based on Uchiyama <i>et al.</i> (2010) vortex force formulation.	136
5.9	Color map of wave Bernoulli head gradient in $x - z$ coordinate plain. (Upper) x -component Bernoulli head gradient. (Middle) y -component Bernoulli head gradient. (Lower) z -component Bernoulli head gradient. Results are based on Uchiyama <i>et al.</i> (2010) vortex force formulation.	137
5.10	Color map of wave-averaged force (- Bernoulli head gradient + vortex force) in $x - z$ coordinate plain. (Upper) x -component wave-averaged force. (Middle) y -component wave-averaged force. (Lower) z -component wave-averaged force. Results are based on Uchiyama <i>et al.</i> (2010) vortex force formulation.	138
5.11	(Upper) Cross-shore and vertical distribution of DK undertow and MC undertow. Black dotted line: zero-velocity at each cross-shore location; Blue solid line: MC undertow at each cross-shore location. Red dotted line: DK undertow at each cross-shore location. (Lower) Color map of DK eddy viscosity in $x - z$ coordinate plane. Results are based on the present vortex force formulation.	140

5.12	(Upper) Cross-shore distribution of depth-averaged x -component Stokes drift velocity u^{st} and undertow u^c . Blue solid line: MC undertow; Black solid line: DK undertow; Red dotted line: MC Stokes drift velocity. Black dotted line: DK Stokes drift velocity. (Middle) Cross-shore distribution of depth-averaged longshore current. Blue solid line: MC longshore current; Black starred line: DK longshore current; Red dotted line: analytical solution. (Lower) Cross-shore distribution of mean surface elevation. Blue solid line: MC mean surface; Black starred line: DK mean surface; Red dotted line: analytical solution. Results are based on the present vortex force formulation.	141
5.13	Color map of current velocity difference (DK - MC) in $x - z$ coordinate plain. (Upper) x -component current velocity u^c difference. (Middle) y -component current velocity v^c difference. (Lower) z -component current velocity w^c difference. Results are based on present vortex force formulation.	142
5.14	Color map of wave Stokes drift velocity difference (DK - MC) in $x - z$ coordinate plain. (Upper) x -component current velocity u^{st} difference. (Middle) y -component current velocity v^{st} difference. (Lower) z -component current velocity w^{st} difference. Results are based on the present vortex force formulation.	143
5.15	Color map of wave-averaged force difference (- Bernoulli head gradient + vortex force, DK - MC) in $x - z$ coordinate plain. (Upper) x -component wave-averaged force. (Middle) y -component wave-averaged force. (Lower) z -component wave-averaged force. Results are based on the present vortex force formulation.	144
5.16	Aerial view of the mouth of Columbia River. Green solid line: profile of bathymetry used in the model setup. The distance is about 14.3 km Yellow point: USACE Wave Information Studies (WIS) station locations (83014, 83015)	146
5.17	Wave Rose at WIS station 83014. Plots are based on wave hindcast model data from 1980 to 2011. The wave rose suggests that the dominant wave direction is from west to east. The dominant significant wave height is between 1 m - 3 m. Figure provided by USACE WIS website (http : //wis.usace.army.mil/data/pac/wvrs/ST83014.WAVE_allyrs.png)	147

5.18	Wave Rose at WIS station 83015. Plots are based on wave hindcast model data from 1980 to 2011. The wave rose suggests that the dominant wave direction is from west to east. The dominant significant wave height is between 1 m and 3 m. Figure provided by USACE WIS website (http : //wis.usace.army.mil/data/pac/wvrs/ST83015_WAVE_all yrs.png)	148
5.19	NHWAVE only result. Cross-shore bathymetry, water surface level and current profiles at mouth of Columbia River (MCR). The water depth starts with 26.4 m at the river mouth and ends with 91.3 m offshore. The water depth at the sand bar is about 16.5 m. The mean water surface ranges from -0.27 m to -0.02 m. Current profiles are plotted every 1100 m across shore. The maximum current speed is about 1.46 m/s appearing above the sand bar. A reverse flow appears near the plume front between $x = 10$ km and $x = 14$ km due to pressure gradient from salt water to fresh water.	149
5.20	NHWAVE only result. Contour map of current velocity components. Upper: current velocity in x -direction (cross-shore). Equal fluxes are added at both sides of cross-shore domain. Due to the mass conservation, u component reaches its maximum over the sand bar. Lower: current velocity in z -direction (vertical). Its magnitude is much less than u component.	150
5.21	NHWAVE only result. Contour map of water salinity and density. The freshwater flows into the salt water domain from eastern boundary and forms a plume near the surface due to buoyancy. . .	151
5.22	SWAN only result. Upper: Significant wave height; Middle: Peak wave direction; Lower: wave dissipation. The wave height at the western boundary is 3 m. Then wave height increases before the sand bar and decreases after the sand bar. The wave direction is mostly from the west. The wave dissipation is very small since waves are in deep water.	152

5.23	Cross-shore bathymetry, water surface level and comparison of current profiles at Columbia River mouth. Red Dash: NHWAVE only current profile as shown in Figure 5.19; Blue Solid: $NH\overline{WAVE}$ coupled current profile. The mean water surface ranges from -0.37 m to -0.1 m. Current profiles are plotted every 1120 m across shore. The maximum current speed is about 1.58 m/s appearing above the sand bar. Compared with NHWAVE only result, there is an offshore velocity near the bottom between $x = 3$ km and $x = 9$ km in $NH\overline{WAVE}$ coupled result. Meanwhile, there is an onshore velocity in middle layer between $x = 3$ km and $x = 9$ km.	153
5.24	Cross-shore bathymetry, water surface level, salinity contour and current velocity difference profiles at Columbia River mouth. The green dotted line is 27 PSU salinity contour of $NH\overline{WAVE}$ result. The red dotted line is 27 PSU salinity contour of NHWAVE result. The cross-shore velocity difference is obtained by subtracting NHWAVE only result from $NH\overline{WAVE}$ coupled result. The mean water surface ranges from -0.37 m to -0.1 m. Current velocity difference is calculated by subtracting NHWAVE only output from $NH\overline{WAVE}$ coupled output. The profiles are plotted every 1120 m across shore. The maximum current speed difference is about 0.31 m/s appearing near $x = 6$ km. The plots indicate that the opposing-waves create vertical variations in current cross-shore velocity.	154
5.25	Cross-shore bathymetry, water surface level and current shear $\partial u/\partial z$ profiles at the mouth of Columbia River. The plot indicates that most of the current shear appears at the plume front. There is also shear near the bottom.	155
5.26	Contour map of current velocity components generated by $NH\overline{WAVE}$ coupled model. Upper: current velocity in x -direction (cross-shore). Equal fluxes are added at both sides of cross-shore domain. Due to the mass conservation, u component reaches its maximum over the sand bar. The magnitude of u is confined near the surface due to stratification. Lower: current velocity in z -direction (vertical). There is an upwelling seaward of plume front and downwelling beneath the plume front. Its magnitude is much less than u component. There are pluses in w velocity near the plume base over the sand bar.	157

- 5.27 Contour map of current velocity anomaly generated by $NH\overline{WAVE}$ - NHWAVE results. Black Solid: 27 PSU salinity contour of $NH\overline{WAVE}$ results. Pink Solid: 27 PSU salinity contour of NHWAVE results. Upper: current velocity anomaly in x -direction (cross-shore). The u velocity is accelerated by waves between $x = 8$ km and $x = 12$ km. The u velocity at the plume front is slowing down. An offshore velocity is generated near the bottom beneath the plume front. Lower: current velocity anomaly in z -direction (vertical). There is an upward anomaly landward of the plume front and downward anomaly right beneath the plume front. 158
- 5.28 Contour map of current velocity anomaly generated by $NH\overline{WAVE}$ - NHWAVE results with Uchiyama's vortex force formulation. Black Solid: 27 PSU salinity contour of $NH\overline{WAVE}$ results. Pink Solid: 27 PSU salinity contour of NHWAVE results. Upper: current velocity anomaly in x -direction (cross-shore). The u velocity is accelerated by waves between $x = 8$ km and $x = 12$ km. The u velocity at the plume front is slowing down. A offshore velocity is generated near the bottom beneath the plume front. Lower: current velocity anomaly in z -direction (vertical). There is an upward anomaly landward of the plume front and downward anomaly right beneath the plume front. 159
- 5.29 Contour map of water salinity. The water flows into the salt water domain with 0 PSU at eastern boundary. The flow is stratified and forms plume front at the upper layer. The comparison with NHWAVE only salinity (Figure 5.21) indicates that the plume front is thicken and extended offshore by waves. 160
- 5.30 Contour map of wave-induced Stokes drift velocity. Upper: x -direction Stokes drift velocity component. u component reaches its maximum at the sand bar, which is about 0.04 m/s. Middle: y -direction Stokes drift velocity component. v component is negligible since waves mainly propagate in cross-shore direction. Lower: vertical direction Stokes drift velocity component. w component is generated by the bathymetry and mass conservation in Stokes drift velocity (Figure 5.44). 161

5.31	Contour map of vortex force. Upper: x -component. The x component of vortex force is about 10^{-4} m/s ² . There is a positive vortex force at the plume front, where the fresh water is mixing with salt water. The x component vortex force appears along the plume base with negative value up and positive values down. Lower: vertical component of vortex force emerges at the sand bar. The vertical component of vortex force emerges near the plume front with negative values up and positive values down. There are pulses in both x and z component of vortex force, which is caused by the cross-shore variation of current shear.	162
5.32	Contour map of Bernoulli head gradient. Upper: x component of Bernoulli head gradient is positive offshore of the sand bar and negative onshore of the sand bar. It is mainly because of the wave set down near the sand bar. The gradient is larger over shallow water area than deep area. The gradient drives the current offshore at the sand bar area. Both y and vertical components of Bernoulli head gradient are negligible.	163
5.33	Comparison of significant wave height and total wave dissipation between SWAN only and $NHWAVE$ coupled. Upper: significant wave height. Lower: total wave dissipation. Red Dash: results from SWAN model only; Blue Solid: results from $NHWAVE$ coupled model depth-averaged current. Green Dash: results from $NHWAVE$ coupled model depth-weighted current. The wave height at the western boundary is set as 3 m. The wave height gradually increases as approaching to the river mouth due to shoaling effect. In the presence of the opposing current, the significant wave height at the sand bar is slightly larger than SWAN only case (see Figure 5.22). The total wave dissipation at the sand bar is also larger than the SWAN only case due to the increasing wave height. The depth-weighted current generates very similar result as depth-averaged current.	164
6.1	The Langmuir circulation flow pattern. The wind-generated mean flow is developed at the ocean surface with spanwise variations. Meanwhile, a downward flow is formed below the windrows while an upward flow is formed between the windrows. The cell is roughly in square form with size ranging from 2 m to 300 m. The circulation can be represented as a set of vortices of alternating signs in horizontal direction. Figure from Thorpe (2004).	166

6.2	Wind-driven shear flow (x -direction) velocity profile after 50 hour run $U^c(z)$. Maximum velocity is 0.48 m/s at the surface and minimum velocity is 0.23 m/s near the bottom. Wind velocity (10 m above sea surface) is 10 m/s in x -direction only. Drag coefficient is set as 0.0013	169
6.3	Color maps of partially (time, x and y direction) averaged fluctuating velocity components on the $y - z$ plane for flow with LC at $Re=395$ ($La_t = 0.7, L=6H$). Velocity normalized by mean center line velocity in x -direction. (a) Normalized x -direction fluctuating velocity U . (b) Normalized z -direction fluctuating velocity W . (c) Normalized y -direction fluctuating velocity V . Cited from Figure 3 in Tejada-Martinez and Grosch (2007).	170
6.4	Color maps of partially (time, x and y direction) averaged fluctuating velocity components on the $y - z$ plane for flow without LC at $Re=395$ ($La_t = \infty, L=6H$). Velocity normalized by mean center line velocity in x -direction. (a) Normalized x -direction fluctuating velocity U . (b) Normalized z -direction fluctuating velocity V . (c) Normalized y -direction fluctuating velocity W . Cited from Figure 4 in Tejada-Martinez and Grosch (2007).	171
6.5	Color maps of fluctuating velocity components on the $y - z$ plane for flow with LC ($La_t = 0.7, L=2\pi H$). Results are based on the present formulation. Velocity normalized by the total mean velocity in x -direction. (Top) Normalized x -direction fluctuating velocity U . (Middle) Normalized y -direction fluctuating velocity V . (Bottom) Normalized z -direction fluctuating velocity W . Perturbations with magnitude up to 0.025 m/s are added to only U in initial condition.	172
6.6	Color maps of fluctuating velocity components on the $y - z$ plane for flow with LC ($La_t = 0.7, L=2\pi H$). Results are based on the simple version formulation. Velocity normalized by the total mean velocity in x -direction. (Top) Normalized x -direction fluctuating velocity U . (Middle) Normalized y -direction fluctuating velocity V . (Bottom) Normalized z -direction fluctuating velocity W . Perturbations with magnitude up to 0.025 m/s are added to only U in initial condition.	173
6.7	Color maps of vortex force on the $y - z$ plane for flow with LC ($La_t = 0.7, L=2\pi H$). Results are based on the present formulation. (Upper) x component of vortex force. The x component is nonzero. (Middle) y component of vortex force. The y component has alternating signs in spanwise direction. (Lower) z component of vortex force.	175

6.8	Color maps of vortex force on the $y - z$ plane for flow with LC ($La_t = 0.7, L=2\pi H$). Results are based on the simple version formulation. Results are based on the present formulation. (Upper) x component of vortex force. The x component is all zero. (Middle) y component of vortex force. The y component is symmetric in spanwise direction. (Lower) z component of vortex force.	176
6.9	Crosswind distribution of mean velocity components on the $y - z$ plane for flow with LC ($La_t = 0.7, L=2\pi H$). Velocity normalized by the total mean velocity in x -direction. (Top) Normalized x -direction fluctuating velocity. (Middle) Normalized y -direction fluctuating velocity. (Bottom) Normalized z -direction fluctuating velocity. Perturbations with magnitude up to 0.025 m/s are added to U and V in initial condition. Solid line: flow near surface ($z = -1.25$ m); Dash-dot line: flow at middle depth ($z = -7.5$ m); Dotted line: flow near bottom ($z = -13.75$ m).	177
6.10	Color maps of partially averaged fluctuating velocity components on the $y - z$ plane for flow with LC ($La_t = \infty, L=6H$). Velocity normalized by the total mean velocity in x -direction. (Top) Normalized x -direction fluctuating velocity. (Middle) Normalized y -direction fluctuating velocity. (Bottom) Normalized z -direction fluctuating velocity. Perturbations with magnitude up to 0.025 m/s are added to U and V in initial condition. Solid line: flow near surface ($z = -1.25$ m); Dash-dot line: flow at middle depth ($z = -7.5$ m); Dotted line: flow near bottom ($z = -13.75$ m).	178
6.11	Profile of the averaged velocity over horizontal directions (x and y) with LC ($La_t = 0.7, L=2\pi H$). Velocity normalized by the total mean velocity in x -direction. (Top) Normalized x -direction mean velocity U . (Middle) Normalized y -direction mean velocity V . (Bottom) Normalized z -direction mean velocity W . Perturbations with magnitude up to 0.025 m/s are added to U in initial condition. The vertical and crosswind transport is nearly zero.	179
6.12	Profile of the averaged velocity over horizontal directions (x and y) with LC ($La_t = \infty, L=2\pi H$). Velocity normalized by the total mean velocity in x -direction. (Top) Normalized x -direction mean velocity U . (Middle) Normalized y -direction mean velocity V . (Bottom) Normalized z -direction mean velocity W . Perturbations with magnitude up to 0.025 m/s are added to U in initial condition.	180

6.13 Profile of the averaged velocity component U over horizontal directions (x and y) with LC. Velocity normalized by the total mean velocity in x -direction. Solid line: $La_t = 0.7$, $L = 2\pi H$; Dash-dot line: $La_t = 0.4$, $L = 2\pi H$; Dotted line: $La_t = 0.7$, $L = 4/3 H$. Figure indicates smaller Langmuir number La_t and longer wave length L_w tend to homogenize shear flow in vertical direction. 182

LIST OF VARIABLES

- a, A wave amplitude
- α^r fraction of wave energy converted to wave rollers
- A^R wave roller area
- \mathbf{A}_n polynomial coefficient for \mathbf{I}
- B_n polynomial coefficient for L
- $B_{n,m}$ bottom wave forcing
- \mathbf{B}^b wave breaking forcing
- \mathbf{B}^{wd} wave bottom streaming forcing
- c_D drag coefficient
- \mathbf{c} wave phase velocity
- \mathbf{c}_r wave relative phase velocity
- c_r modulus of wave relative phase velocity
- \mathbf{c}_g wave group velocity
- \mathbf{c}_{g_a} wave absolute group velocity
- \mathbf{c}_{g_r} wave relative group velocity
- $C_{1,1}, C_{2,1}$ interior forcing in Rayleigh equation
- $D_{1,1}, D_{2,1}$ surface forcing in Rayleigh equation
- D total water depth in NHWAVE
- $E_{1,1}, E_{2,1}$ bottom forcing in Rayleigh equation
- E total wave energy
- \mathbf{E}^* depth-dependent wave energy

f dimensionless function related to \mathbf{q}^w
 f_0, f_1 dimensionless function in perturbation solution
 f^b wave breaking vertical function
 f^{wd} wave bottom streaming vertical function
 $F_{n,m}$ continuity wave forcing
 F Froude number
 \mathbf{F}^w non-conservative wave forcing
 h still water depth
 H actual water depth
 H_w wave height
 $H_{n,m}$ surface kinetic wave forcing
 \mathbf{I} dimensionless function related to \mathbf{q}
 I_1 integration function used in perturbation
 I_2 integration function used in perturbation
 \mathbf{J} horizontal wave vortex force
 \mathbf{k} wave number vector
 $\hat{\mathbf{k}}$ unit wave number vector
 k modulus of wave number \mathbf{k}
 k_x x component of wave number
 k_y y component of wave number
 K vertical wave vortex force
 K_2 ϵ^2 vertical wave vortex force
 K_3 ϵ^3 vertical wave vortex force
 L dimensionless function related to σ_w
 La_t Langmuir number
 L_w wave length

$\mathbf{M}_{n,m}$ horizontal momentum wave forcing
 N wave action density
 N^r wave roller action density
 $N_{n,m}$ vertical momentum wave forcing
 $\mathbf{O}_{n,m}$ horizontal vorticity wave forcing
 p total pressure
 p_d total dynamic pressure
 p^c mean pressure
 p^w wave pressure
 $P_{n,m}$ vertical vorticity wave forcing
 \mathbf{q} total horizontal velocity
 \mathbf{q}^c current horizontal velocity
 q_s^c modulus of current horizontal velocity
 \mathbf{q}^w wave horizontal velocity
 \mathbf{q}^{st} horizontal stokes drift velocity
 \mathbf{Q}^{st} wave stokes drift (transport)
 \mathbf{Q}^r roller Stokes transport
 Q dimensionless variable related to f
 Q_s fraction of broken waves from SWAN
 $Q_{1,1}^*$ forcing term used in vortex force
 Re Reynolds number
 $S_{n,m}$ surface dynamic wave forcing
 \mathbf{S}_p dynamic pressure forcing
 $\mathbf{S}_w^{(1)}, \mathbf{S}_w^{(2)}, \mathbf{S}_w^{(NC)}$ wave forcing
 \mathbf{S}_τ stress forcing
 t wave-scale time coordinate

t^* time coordinate Cartesian coordinate
 \mathbf{T} slow-scale time coordinate
 \mathbf{u} total 3D velocity
 \mathbf{u}^c current 3D velocity
 \mathbf{u}^w wave 3D velocity
 \mathbf{u}^{st} wave 3D velocity
 u_τ friction velocity
 w total vertical velocity
 w^c current vertical velocity
 w^w wave vertical velocity
 w^{st} vertical stokes drift velocity
 $\mathbf{x} = (x, y)$ wave-scale horizontal coordinates
 x^* x-direction Cartesian coordinate
 $\mathbf{X} = (X, Y)$ slow-scale horizontal coordinates
 y^* y-direction Cartesian coordinate
 η instantaneous surface elevation
 z vertical coordinate
 z^* z-direction Cartesian coordinate
 \hat{z} dimensionless vertical coordinate
 $\mathbf{\Omega}$ total 3D vorticity
 $\mathbf{\Omega}^s$ vertical shear of current horizontal velocity
 ξ total horizontal vorticity
 χ total vertical vorticity
 η^c mean surface elevation
 η^w wave-induced instantaneous surface elevation
 η^{pc} current-induced mean surface elevation

ξ^c mean horizontal vorticity
 χ^c mean vertical vorticity
 η^{st} wave-induced mean surface elevation
 ξ^w wave horizontal vorticity
 χ^w wave vertical vorticity
 $\nabla_h = (\frac{\partial}{\partial x}, \frac{\partial}{\partial y})$ wave-scale horizontal derivative
 $\nabla_H = (\frac{\partial}{\partial X}, \frac{\partial}{\partial Y})$ slow-scale horizontal derivative
 ϵ wave slope parameter
 ϵ^w total wave dissipation
 ϵ^b wave dissipation due to breaking
 ϵ^r wave roller dissipation
 ϵ^{wd} wave dissipation due to bottom friction
 ϵ^{wp} wave dissipation due to whitecapping
 θ wave oblique angle relative to mean flow
 Θ wave phase function
 μ wave depth parameter
 ω_w, ω_0 wave absolute frequency
 ω vertical velocity in σ coordinate
 σ vertical coordinate in NHWAVE
 σ_w wave intrinsic frequency
 σ_s surface wave intrinsic frequency
 κ wave Bernoulli head
 $\kappa_2 \epsilon^2$ wave Bernoulli head
 $\kappa_3 \epsilon^3$ wave Bernoulli head

ABSTRACT

Existing theories of wave-current interaction mostly assume that waves propagate on currents which vary weakly in the vertical direction. In most cases, the assumption is satisfied. However, at the mouth of rivers with very energetic discharge such as the Columbia River, the current becomes strongly sheared due to stratification and tidal effects. The wave-current interaction for waves on strongly sheared current needs to be discussed. In this study, a new theory is first developed to formulate the interaction of small-amplitude surface gravity waves with strongly sheared current in finite-depth water. In contrast to existing formulations, where waves at the leading order respond to a depth-uniform current field, the present formulation allows for an arbitrary degree of vertical current shear, leading to a description of wave vertical structure in terms of solutions to the Rayleigh stability equation. The Rayleigh equation is then solved using both numerical and perturbation methods. The perturbation solutions are recommended in numerical modeling to avoid directly solving Rayleigh equation for each coupling time step (Dong and Kirby, 2012). As a special case, the constantly sheared current profile is used to provide analytical wave solutions and to evaluate the performance of numerical solver and different orders of perturbation solutions. The leading order wave vorticity for constantly sheared current is discussed. The magnitude of wave vorticity is determined by the current vertical shear and the oblique wave angle to current direction. Wave orbital velocity and vorticity are calculated using the current velocity profile measured at the mouth of Columbia River (MCR). The comparison of numerical solutions with perturbation solutions suggests that the second order perturbation solution successfully captures the features of current shear effect on the wave vertical structures. Furthermore, the solvability condition for the second order inhomogeneous Rayleigh equation leads to the wave action conservation equation. The

wave action equation is evaluated using wave solutions for constantly sheared currents. Results show that both the wave action and action flux are modified by the current vertical shear effect. For the mean flow part, the wave-averaged forcing terms for the description of the mean flow dynamics are presented using the Craik-Leibovich vortex force formalism. The present vortex force formulation is compared with the Uchiyama *et al.* (2010) formulation using wave solutions for constantly sheared current. The wave-current interaction theory is then applied to a coupled system of NHWAVE and SWAN, which extends the existing formalism to include the strong shear effect. Three cases have been tested in the numerical application part. Test case (1) is the obliquely incident waves on a planar beach. As waves propagate onshore with an oblique angle, they break near the beach face and generate offshore undertow in the cross-shore direction and strong current in the alongshore direction. This case is used to compare the present vortex force formulation with Uchiyama *et al.* (2010) without activating SWAN. Test case (2) is wave propagation on highly stratified, vertically sheared current at the mouth of Columbia River (MCR). During the ebb tide, the strong fresh water discharge and ebb tidal current creates a strongly sheared offshore current at MCR. The strongly sheared current meets and interacts with the incident waves. This case is designed for the analysis of wave effects on currents and current effects on waves. Both NHWAVE and SWAN are activated and coupled in the simulation. Test case (3) is the formation of Langmuir circulation in the presence of wind-driven current and waves. The water surface wind creates a wind-driven flow, which interacts with surface gravity waves also propagating in downwind direction. The wave-current interaction generates Langmuir cells in cross-wind direction.

Chapter 1

INTRODUCTION

The study of surface gravity wave effects on nearshore hydrodynamics, marine structures and sediment transport has been a main task for coastal engineers and scientists. Given a certain time period in the ocean, waves are the periodic motions while current is the continuous and directed movement. The definition of waves and current depends on the spatial and temporal scales of interest. Diurnal and semidiurnal tides, for example, can be treated as currents during several wind-generated surface gravity wave periods, or as waves over time scale of a few hours. Ocean waves usually consist of various wave periods and wavelengths, and are therefore called spectral waves. The short waves actually ride on the long waves during propagation. In the deep water, the longer waves propagate faster than the shorter waves. The relation between wave number (k) and wave frequency (ω_0) is called dispersion relation, expressed as $\omega_0^2 = gk \tanh kh$, where g is gravity and h is water depth. The short waves oscillate within their own periods. At the same time, the short wave properties such as wave amplitude, wave period and wavelength vary slowly due to the effects of long waves. If the spatial and temporal scales of the long waves are much larger than the short waves, the long wave-induced water particle flow can be treated as current within several short wave periods.

Surface gravity waves usually coexist with currents generated by wind, tide, river discharge and long waves. Thus wave-current interaction plays a very important role in understanding the combined action of waves and current in coastal waters. Waves in complex coastal environments are strongly affected by spatial and temporal variations of current, which can induce wave shoaling, refractive and focussing/defocussing effects in analogy to bathymetry variations. In turn, waves can force and modify the mean

flow dynamics, strengthen ocean mixing processes and alter the wave-averaged boundary layers. In wave models, the effects of current are usually realized through adding a representative current velocity in the dispersion relation and wave action equation, assuming a depth-uniform current structure. Models of wave effects in ocean circulation have also been extensively developed over the past decades, with the parameterized wave-averaged forces extended to three dimensions based on either the radiation stress formalism or the Craik-Leibovich vortex force formalism. The main idea is to include the surface gravity wave effects on the large-scale mean flow circulation without determining phase-resolved wave motions. The coupled model system usually consists of a wave model, with the evolution of wave action density affected by the mean flow, and an ocean circulation model, with the wave-averaged forces driving or modifying the mean flow. In most of the existing wave-current interaction formulations, the current field may be strong (i.e., $|u|/c = O(1)$), but its variations over depth is assumed to be weak or absent. Few existing studies have considered the interaction of waves with strongly sheared current, in which the currents arbitrary vertical shear enters into the leading order wave dynamics. It is true that, in most cases, current velocity magnitude is relatively small compared to wave phase speed in coastal regions. However, strongly sheared currents are often observed in areas with abrupt bathymetry changes or energetic river discharge. For estuaries such as the Columbia River, due to the narrow outlet to the ocean, strong tidal currents and significant freshwater discharge, the currents at the tidal plume often exceed 3 m/s during ebb tides. At the same time, strong vertical current shear is formed due to the highly stratified condition at the tidal plume front (Hickey *et al.*, 2010; Kilcher and Nash, 2010). The current velocity magnitude has been observed to be more than one third of the wave phase speed in the tidal plume, and current shear is comparable to wave frequency (see Section 3.1 below). Therefore, the wave-current interaction theory needs to be extended to include strongly sheared current (Dong and Kirby, 2012).

1.1 Current Effects on Waves

Studies of wave motions in domains with background currents focus on the current effects on waves. The current effects are mostly discussed in wave dispersion relation, wave energy evolution as well as wave vertical structure. The simplest way to include current effects is to consider waves propagating on a depth uniform current ($\bar{\mathbf{U}}$). The Doppler-shifted intrinsic frequency ($\sigma_0 = \omega_0 - \bar{\mathbf{U}} \cdot \mathbf{k}$) is then introduced in dispersion relation $\sigma_0^2 = gk \tanh kh$. Wave energy is also advected by the current in addition to the relative wave group velocity $\mathbf{c}_{ga} = \mathbf{c}_{gr} + \bar{\mathbf{U}}$. \mathbf{c}_{ga} is absolute group velocity and \mathbf{c}_{gr} is relative group velocity. With the assumption of constant wave frequency ω_0 and current-free environment, it is easy to prove that wave energy (E) is conserved during the slow evolution without energy source/sink terms.

$$\frac{\partial E}{\partial T} + \nabla_H \cdot (\mathbf{c}_g E) = 0 \quad (1.1)$$

However, the conclusion becomes invalid in the presence of horizontally varying current. If the current is time dependent and varying in horizontal direction, the intrinsic frequency is no longer constant. The current then does work on the waves through the interaction between strain rate of current and wave radiation stress (Longuet-Higgins and Stewart, 1960; Whitham, 1962). Hence wave energy is not conserved. Instead, wave action, defined as wave energy divided by intrinsic frequency, is conserved during evolution over varying currents (Bretherton and Garrett, 1968). According to

$$\frac{\partial}{\partial T} \left(\frac{E}{\sigma_0} \right) + \nabla_H \cdot \left[(\mathbf{c}_{gr} + \bar{\mathbf{U}}) \frac{E}{\sigma_0} \right] = 0 \quad (1.2)$$

The derivation of a mild slope equation governing linear waves propagating over slowly varying depth and currents also leads to the conservation equation for the wave action without further approximation (Kirby, 1984).

According to the wave energy equation and wave action equation, waves can be "stopped" by the opposing current when the current speed reaches the value of relative wave group speed $\bar{\mathbf{U}} = -\mathbf{c}_{gr}$ (Peregrine and Jonsson, 1983).

In the real world, currents can vary both horizontally and vertically. An easy way to include vertical current shear is to assume constant shear in the current $\mathbf{U} =$

$\mathbf{U}_s + \boldsymbol{\Omega}^s z$, where \mathbf{U}_s is the surface current velocity and $\boldsymbol{\Omega}^s$ is the constant vertical shear. Analytical solutions can be obtained for linear wave theory (Thompson, 1949). Consequently, the current shear appears in the dispersion relation in addition to the intrinsic frequency.

$$\sigma_s^2 = \left(g - \frac{\sigma_s \boldsymbol{\Omega}^s \cdot \mathbf{k}}{k^2}\right) k \tanh kH \quad (1.3)$$

where σ_s is the intrinsic frequency at the water surface. $H = h + \bar{\eta}$ is the actual water depth including flow-induced surface elevation $\bar{\eta}$. The dispersion relation is given for the 2D current velocity. The expression of wave total energy is modified by current shear. In this particular case, wave action conservation is proved for steady and 1D constantly sheared current (Jonsson *et al.*, 1978).

Additionally, a generalized Lagrangian mean (GLM) method has been developed to study the nonlinearity of waves on rotational mean flows. The three-dimensional wave action density is proved to be a conserved wave property on the mean flows (Andrews and McIntyre, 1978a; Andrews and McIntyre, 1978b). However, the depth integration of the equivalent form of wave action equation does not converge to those obtained from former studies (Bretherton and Garrett, 1968; Jonsson *et al.*, 1978). The study of internal and surface gravity wave propagation on an inhomogeneous, slowly varying mean flow leads to the wave action conservation equation (Voronovich, 1976). The resulting equation is valid for arbitrary current profiles.

When considering strong currents with arbitrary vertical shear, the Laplace equation is no longer valid to describe the wave motion. The strong current with strong vertical shear assumption leads to the Rayleigh instability equation. Starting with the Rayleigh equation, perturbation methods are used to examine the vertical current shear effect on the linear wave orbital velocity and dispersion relation. Assuming either a weak current or a strong current with weak shear, the Rayleigh equation may be solved by perturbation method to introduce current effects in wave solutions (Kirby and Chen, 1989; Stewart and Joy, 1974; Skop, 1987). For the weak current case, currents do not

affect the leading order solutions for waves. At first order, the concept of the depth-weighted current ($\tilde{\mathbf{U}}$) is discussed.

$$\tilde{\mathbf{U}} = \frac{2k}{\sinh 2kH} \int_{-H}^0 \mathbf{U}(z) \cosh 2k(H+z) dz \quad (1.4)$$

It is also noted that the depth-weighted current is function of wave number. In consequence, the advection velocity in the wave action equation will have an extra term related to changes in wave number. The second order approximation is shown to improve the first order result significantly for long waves on the linear shear current (see Figure 2 in Kirby and Chen, 1989 and Banihashemi *et al.*, 2016). Shrira (1993) showed how this can be extended to all orders. Additionally, numerical solutions to wave Rayleigh equation based on measured current profile data have been utilized to evaluate the approximation in the perturbation solutions (Dong and Kirby, 2012). The comparison with numerical and analytical results demonstrates that the second order perturbation approximation successfully captures the strongly sheared current effects on wave vertical structures. The second order approximation can be used in wave-current interaction models to avoid numerically solving wave Rayleigh equation, which is time-consuming.

Meanwhile, several lab experiments have been done to measure the vertical structure of wave orbital velocity and current velocity for waves following or opposing the current (Klopman, 1992; Klopman, 1994). The wave orbital velocity profiles are also studied using General Lagrangian Mean method. Results suggest that the vertical gradient of the amplitude of horizontal orbital velocity decreases when interacting with following current and increases with opposing current, which qualitatively agrees with observations (see Figure 1.1 and Groeneweg and Klopman, 1998).

1.2 Wave Effects on Current

The wave effects on current have been explored to explain the nearshore phenomena. As surface gravity waves propagate shoreward from the deep ocean to coastal waters, the wave group velocity is decreased due to decreasing water depth and waves

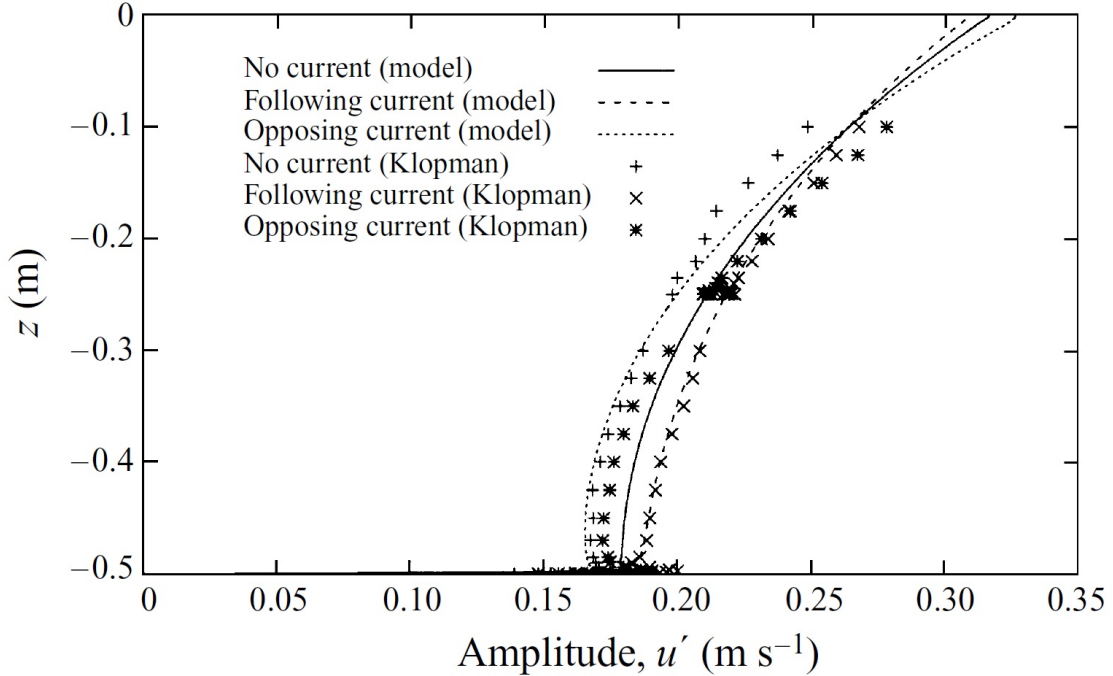


Figure 1.1: GLM results (Groeneweg and Klopman, 1998) and experimental results (Klopman, 1994) for the first order Eulerian-mean horizontal velocity amplitude profile. Both the model results and experimental results indicate that the following current decreases the vertical gradient of velocity amplitude, while the opposing current increases the vertical gradient. See Figure 2 in Groeneweg and Klopman (1998)

begin to break. During wave transformation, several fundamental nearshore processes are generated such as longshore current and undertow.

Wave-average impacts on current are interpreted either in the radiation stress formalism or the vortex force formalism. The difference between the concepts of radiation stress and vortex force lies in the treatment of the advection terms $\mathbf{u} \cdot \nabla \mathbf{u}$ in momentum equation (Lane *et al.*, 2007). The advection term, combined with continuity equation, yields wave-averaged forces in radiation stress formalism according to $\mathbf{u} \cdot \nabla \mathbf{u} + \mathbf{u}(\nabla \cdot \mathbf{u}) = \nabla \cdot (\mathbf{u} \otimes \mathbf{u})$, while another operation on the advection term yields the vortex force formalism according to $\mathbf{u} \cdot \nabla \mathbf{u} = \frac{1}{2} \nabla (\mathbf{u} \cdot \mathbf{u}) - \mathbf{u} \times (\nabla \times \mathbf{u})$. The first term on RHS is the gradient of Bernoulli head, which contributes to the pressure gradient force within the water column. The second term on RHS is called the vortex force.

The flow vorticity is defined as $\boldsymbol{\Omega} = \nabla \times \mathbf{u}$.

Early studies focused on wave-averaging of the depth-integrated momentum equation. The study of the interactions of short waves with long waves (or currents) successfully explains the short wave steepening at long wave crests and flattening at long wave troughs (Longuet-Higgins and Stewart, 1960; Longuet-Higgins and Stewart, 1961). As mentioned earlier, long waves or currents do work on short waves through the interaction of a wave energy flux property called "radiation stress" and the current strain rate, where the radiation stress $S_{\alpha\beta}$ for plane waves is given by

$$S_{\alpha\beta} = \begin{pmatrix} S_{xx} & S_{xy} \\ S_{yx} & S_{yy} \end{pmatrix} \quad (1.5)$$

where

$$\begin{aligned} S_{xx} &= \left[\frac{k_x^2 c_g}{k^2 c} + \left(\frac{c_g}{c} - \frac{1}{2} \right) \right] E \\ S_{xy} &= S_{yx} = \left(\frac{k_x k_y c_g}{k^2 c} \right) E \\ S_{yy} &= \left[\frac{k_y^2 c_g}{k^2 c} + \left(\frac{c_g}{c} - \frac{1}{2} \right) \right] E \end{aligned}$$

Here, c_g is wave group speed and c is wave phase speed. E is the wave energy given earlier in this chapter. The divergence of radiation stress appears in the Lagrangian mean flow momentum equation as a source/sink term, and can be used to predict several important processes such as wave setup/down (Bowen *et al.*, 1968), surf beat (Longuet-Higgins and Stewart, 1962; Longuet-Higgins and Stewart, 1964) and the generation of longshore current (Bowen, 1969; Longuet-Higgins, 1970a; Longuet-Higgins, 1970b). The wave set-down and set-up are changes in mean sea level due to the cross-shore gradient of radiation stress before and after the breaking point. Surf beat is caused by the slow spatial variation in radiation stress of wave groups (long waves). The longshore current is formed from the balance between bottom stress and the cross-shore gradient of the longshore component of radiation stress.

The radiation stress considered by Longuet-Higgins and Stewart (1960, 1961) is based on the wave-averaging of depth-integrated momentum equation, which consists

of both mean flow and the wave field. Hence the divergence of radiation stress implies the changes in the overall flow momentum. It is not clear to describe the interactions between the mean flow and waves (Hasselmann, 1971). The study of wave-induced currents in the surfzone attempts to separate radiation stress into three components in terms of wave energy dissipation, the gradient of a volume force and some extra rotational terms (Dingemans *et al.*, 1987). The extra rotational terms are related to vortex force. The study indicates that the driving force to the mean flow is closely proportional to the wave energy dissipation rate in the surfzone while the extra rotational terms are insignificant. Outside of the surfzone, wave energy dissipation has less effects than the other two terms. In the presence of opposing mean flows, the extra rotational terms are responsible for the widening of jets. The simulated examples show that driving force formulation in terms of wave dissipation gives better results than radiation stress formulation. The resulting formulation by Dingemans *et al.* (1987) is applied to the Delft3D model as wave-averaged driving forces.

Independently, the vortex force formalism has been developed to explain the possible mechanism for the generation of Langmuir circulation (Craik and Leibovich, 1976; Thorpe, 2004). Langmuir circulation was first discovered and characterized by Irving Langmuir in the Sargasso Sea in 1927 (Langmuir, 1938). As wind blows over the surface of lakes or ocean, bands of foam or other floating materials are formed in the downwind direction. These bands are produced by a spanwise flow convergence near the surface. A downward flow is formed below the bands while an upward flow is formed between the bands. The details of Langmuir circulation will be discussed in Chapter 6. It is suggested by Craik and Leibovich (1976) that the generation of Langmuir circulation is due to a vortex force involving the interaction of Stokes drift induced by wind waves and the vertical shear in turbulent fluid. Another attempt is then made to derive the effect of wave-averaged forces on the depth-integrated mean flow momentum equation in terms of Craik-Leibovich vortex force formalism (Smith, 2006). It starts with the wave-averaged, depth-integrated Lagrangian mean flow, removes wave momentum evolution terms based on wave action conservation and introduces

wave dissipation B^b , the gradient of Bernoulli head $\nabla_H \bar{\kappa}$ and the vortex force ($\bar{\mathbf{J}}$). The depth-integrated wave forces (\mathbf{F}^w) are given

$$\mathbf{F}^w = B^b \hat{\mathbf{k}} + \mathbf{Q}^{st} \times (\nabla_H \times \bar{\mathbf{U}}) - \bar{\mathbf{U}}(\nabla_H \cdot \mathbf{Q}^{st}) - H \nabla_H \bar{\kappa} \quad (1.6)$$

$\hat{\mathbf{k}}$ is unit wave number vector. $\mathbf{Q}^{st} = Ek/\sigma_0$ is wave-induced Stokes transport. The second term is the reaction to wave refraction by currents known as vortex force. The third term comes from the surface boundary condition during depth-integration. It represents the effects of wave-induced Stokes drift on the mean flow. The fourth term is the gradient of Bernoulli head.

The original definition of radiation stress is based on the depth-integrated momentum equation. In three dimensional ocean circulation modeling, the depth dependent radiation stress is apparent in the momentum balance. Efforts have been made to study the mass and momentum transfer between short waves and large-scale flows in a three dimensional Eulerian frame of reference (Hasselmann, 1971). It is found that the wave effects on the mean flow can be described by an interaction stress tensor in momentum $T_{ij}^{int} = -(\overline{u'_i u'_j} + \delta_{ij} p^w)$ and a mass transfer at surface $M_\alpha = \int_{\zeta}^{\zeta+\zeta'} u_\alpha dz$. u'_i is wave orbital velocity. Operator $\overline{(\)}$ is the wave average, p^w is the wave contribution to mean pressure field, ζ is the mean surface and ζ' is wave-induced instantaneous surface. The mass transfer M_α is the Stokes transport \mathbf{Q}^{st} over the entire water column. The depth integration of the interaction stress T_{ij}^{int} is related but not equal to radiation stress considered by Longuet-Higgins and Stewart (1960, 1964). The radiation stress enters in the overall momentum balance consisting of both the mean motion and wave field. The interaction stress describes the momentum transfer from wave field to mean flow.

Later in the study by Newberger and Allen (2007a), the Eulerian analysis of the wave-averaged forces on three dimensional mean circulation in the surf zone is discussed and indicates that wave forces on the mean flow consist of a depth-dependent body

force and a surface stress caused by wave breaking. The body force is given by

$$F_x^b = -\frac{1}{2} \frac{\partial}{\partial X} \left(\frac{E}{H} \right) + \frac{Ek_y}{\sigma_0 H} \left(\frac{\partial \bar{V}}{\partial X} - \frac{\partial \bar{U}}{\partial Y} + f_0 \right) \quad (1.7)$$

$$F_y^b = -\frac{1}{2} \frac{\partial}{\partial Y} \left(\frac{E}{H} \right) - \frac{Ek_x}{\sigma_0 H} \left(\frac{\partial \bar{V}}{\partial X} - \frac{\partial \bar{U}}{\partial Y} + f_0 \right) \quad (1.8)$$

where $\partial/\partial X, \partial/\partial Y$ are the spatial gradient and current velocity \bar{U} and \bar{V} are assumed to be depth-independent in shallow water (surf zone). f_0 is Coriolis force. The first term in (1.7) and (1.8) represents the gradient of total wave energy. The second term is related to the vortex force. The surface stress terms are proportional to wave energy dissipation B^b , which is the main driving force to mean flow. The formulation is applied to the extended Princeton Ocean Model (POM) to predict mean circulation in the surf zone using the DUCK94 experiment (Newberger and Allen, 2007b). In addition, a σ coordinate-based theory is introduced by deriving the depth-dependent radiation stress in mean flow momentum equation (Mellor, 2003). The author assumes monochromatic linear wave solutions and takes wave-average of the three dimensional flow momentum equation without depth integration. The resulting equation separates the wave-averaged forces from mean flow. The depth-dependent radiation stress terms ($S_{\alpha\beta}, \overline{\tilde{s}_\alpha \tilde{p}}$) are given by

$$S_{\alpha\beta} = kHE \left[\frac{k_\alpha k_\beta}{k^2} F_{CS} F_{CC} + \delta_{\alpha\beta} (F_{CS} F_{CC} - F_{SS} F_{CS}) \right] \quad (1.9)$$

$$\overline{\tilde{s}_\alpha \tilde{p}} = (F_{CC} - F_{SS}) E^{1/2} \frac{\partial}{\partial x_\alpha} (E^{1/2} F_{SS}) \quad (1.10)$$

where

$$\begin{aligned} \tilde{s}_\alpha &= \frac{\partial \tilde{s}}{\partial x_\alpha} \\ \tilde{s} &= a F_{SS} \cos \phi \\ F_{SS} &= \frac{\sinh kH(1 + \zeta)}{\sinh KH} \\ F_{CS} &= \frac{\cosh kH(1 + \zeta)}{\sinh KH} \\ F_{SC} &= \frac{\sinh kH(1 + \zeta)}{\cosh KH} \\ F_{CC} &= \frac{\cosh kH(1 + \zeta)}{\cosh KH} \end{aligned}$$

a is wave amplitude and ϕ is wave phase function. The term $\overline{s_\alpha \tilde{p}}$ is an additional radiation stress term that vertically integrates to zero. The term $S_{\alpha\beta}$, after depth integration, is identical to the original definition (Longuet-Higgins and Stewart, 1961). The formulation is then applied to the wave-current interaction model, in which the ocean circulation model (USGS/ROMS) provides sea surface elevation, water depth and current velocity to the wave model (SWAN) while the wave model (SWAN) returns bulk wave properties to the ocean circulation model (USGS/ROMS) to calculate depth dependent radiation stress (Warner *et al.*, 2008). Nevertheless, it is pointed out that the formulation is problematic in a simple test case of shoaling waves because of its inappropriate treatment of pressure terms in the radiation stress (Ardhuin *et al.*, 2008a). Instead, a generalized Lagrangian mean (GLM) theory of the current-wave-turbulence combined three dimensional equation is provided by Ardhuin *et al.* (2008b). It applies GLM average to the Reynolds-average Navier-Stokes equations. The mean flow is allowed to have weak curvature in the vertical profile. The depth-weighted current of Kirby and Chen (1989) is used to get linear wave intrinsic frequency. The resulting wave force consists of a depth-uniform, wave-induced kinematic pressure term S^J and a shear-induced pressure term S^{shear} . In response, a revised form of the radiation stress in the Cartesian coordinates is provided by Mellor (2005, 2008). Mellor (2015) combines the derivation of both vertically integrated and vertically dependent radiation stress for consistency of theory. The formulation is adopted in the COAWST model for surf zone and rip-current applications (Kumar *et al.*, 2011). Several test cases including longshore current and rip-current are performed and compared with observations to evaluate the depth dependent radiation stress, which remains to be controversial.

The vortex force formalism has been widely accepted as a dominant mechanism for generating Langmuir circulation. The formalism has more recently been applied to improve the description of wave-current interaction in ocean circulation models. A multi-scale asymptotic theory of wave-current interaction using the vortex force formulation is developed in coastal region (McWilliams *et al.*, 2004). Both infragravity

waves (long waves) and surface gravity waves riding on large scale weak current are considered and separated by using a multi-scale asymptotic expansion. For the surface gravity wave equations, a WKB representation is applied to get linear wave solution. Then, the Fredholm Alternative theorem is used to get the wave action equation. The slow variation of short waves in time and space appears in long wave and mean flow equations as a wave-averaged force. The vortex force (\mathbf{J}, K) are given by

$$\mathbf{J} = -\hat{\mathbf{z}} \times \mathbf{q}^{St}(\chi^c + f) - w^{St} \frac{\partial \mathbf{q}^c}{\partial z} \quad (1.11)$$

$$K = \mathbf{q}^{St} \cdot \frac{\partial \mathbf{q}^c}{\partial z} \quad (1.12)$$

where \mathbf{q}^{St} is horizontal Stokes drift velocity. w^{St} is vertical Stokes drift velocity. \mathbf{q}^c is horizontal mean flow velocity. χ^c is the vertical vorticity of mean flow. The currents considered in the problem are too weak in comparison to wave phase speed to affect the wave action equation at leading order, which means that waves can not feel the current at leading order. Later the vortex force formalism is compared with the depth-dependent radiation stress in coastal waters (Lane *et al.*, 2007). It is suggested that the vortex force formalism gives a clean decomposition of the physics. The Bernoulli head is the pressure adjustment due to wave setup related effects. The vortex force is the combined effects of Stokes drift and current vorticity. In comparison, the radiation stress lacks of meaningful physical decomposition. Meanwhile, Mellor (2016) compares both radiation stress and vortex force formulations and argues in favor of the radiation stress theory. The vortex force formalism is later implemented in surf zone circulation model in computing the effects of waves on currents (Uchiyama *et al.*, 2010; Kumar *et al.*, 2012).

Shi *et al.* (2006) formulate a Craik-Leibovich wave vortex force for a quasi-3D circulation model. In the model, numerical consistency in using two different types of wave forces (radiation stress and vortex force) are discussed. The model is validated in rip currents simulation. Results suggest that the Craik-Leibovich vortex force formulation gives a closer result than the radiation stress formulation. The paper also indicates that a tight model coupling plays a key role in the wave-current interaction.

1.3 Outline of the Thesis

In the dissertation, we first present a new framework to describe the wave-current interaction for arbitrarily sheared current. Following McWilliams *et al.* (2004), we consider motions which consist of superposition of small amplitude surface gravity waves and a spatially and temporally slowly-varying current. In Chapter 2, the multiple scale expansion and wave-averaging method are implemented to separate wave and mean flow effects at different orders. Both momentum equations and vorticity equations are examined in this chapter. In Chapter 3, we focus on the wave dynamics. The wave Rayleigh equation is solved using both numerical solutions and perturbation solutions up to the second order. As a special case, the constantly sheared current is adopted to provide analytical wave solutions and validate the perturbation method and numerical solver. The leading order wave velocity and vorticity are then discussed for constantly sheared current. Measured current profiles at the mouth of the Columbia River (MCR) are used to test the perturbation solutions. Additionally, the wave action equation for the arbitrarily sheared current profile is derived and compared with Voronovich (1976). The wave action equation is then simplified for the case of constant shear and compared with Jonsson *et al.* (1978). The wave action and absolute group velocity are also discussed using both numerical and perturbation solutions. In Chapter 4, equations for mean flow dynamics with wave-averaged forces are presented. The resulting vortex force formulation is compared with McWilliams *et al.* (2004) for constantly sheared current. The wave-averaged forces based on perturbation solutions are provided for later numerical application. In Chapter 5, the vortex force formulations from both Uchiyama *et al.* (2010) and the present theory are implemented in NHWAVE/SWAN coupled model ($\overline{\text{NHWAVE}}$ thereafter). The $\overline{\text{NHWAVE}}$ model is then applied to two test cases: 1) Obliquely incident waves on a sloping beach. 2) wave-current interaction at the mouth of Columbia River (MCR). In Chapter 6, the vortex force formulation is used to simulate the formation of Langmuir circulation in an ideal computational domain. Results are discussed and compared with Tejada-Martinez and Grosch (2007). The conclusions of this study are presented in Chapter 7.

Chapter 2

MULTIPLE-SCALE EXPANSION OF GOVERNING EQUATIONS

In this chapter, we separate wave motions and current using a multiple-scale expansion. We start with the Euler equations and decompose the motion into wave and current components. The current is treated as slowly varying motion with longer scales in time and space compared to waves. Thus mean flow dynamics can be separated from wave dynamics according to different scales. Following Phillips (1966), any variables such as velocity, pressure, surface elevation and vorticity can be separated into waves and current. We take ϕ for example. ϕ can be written as the superposition of currents and waves.

$$\phi = \phi^c + \phi^w \quad (2.1)$$

where ϕ^c represents mean flow variable and ϕ^w represents the wave variable. The mean flow is separated from oscillatory flows by applying wave-average " $\langle \cdot \rangle$ " to the variable in Eulerian framework, which is defined as the average over the wave phase.

$$\langle \cdot \rangle = \frac{k_0}{2\pi} \int_0^{\frac{2\pi}{k_0}} \cdot dx = \frac{\omega_0}{2\pi} \int_0^{\frac{2\pi}{\omega_0}} \cdot dt \quad (2.2)$$

Mean flow variables remain while the oscillatory variables are assumed to be removed after wave-averaging. This is an Eulerian mean method.

$$\langle \phi^c \rangle = \phi^c \quad (2.3)$$

$$\langle \phi^w \rangle = 0 \quad (2.4)$$

The linear wave solution can induce other harmonics of oscillation due to nonlinearity. We apply the WKB representation to the wave motion to include these harmonics. In general, we expand all dependent variables in multiple scales. The Eulerian equations are then sorted into mean flow equations and wave equations.

2.1 Governing Equations

We consider incompressible, inviscid flow governed by the Euler equations. Due to current vertical shear, wave motions are not typically irrotational. A turbulence model and stratification effects can be added to our formulation later, follow McWilliams *et al.* (2004). We separate our problem into horizontal and vertical directions by defining the coordinates $(x, y, z, t) = (\mathbf{x}, z, t)$, velocity $\mathbf{u} = (u, v, w) = \mathbf{q} + w\mathbf{i}_z$ and gradient vector $\nabla = (\partial/\partial x, \partial/\partial y, \partial/\partial z) = (\nabla_h, \partial/\partial z)$. We use p for pressure, h for still water depth and η for instantaneous water surface elevation. The governing equations and boundary conditions are given by

$$\frac{\partial \mathbf{u}}{\partial t} + \mathbf{u} \cdot \nabla \mathbf{u} + \frac{1}{\rho} \nabla p + g\mathbf{i}_z = 0 \quad -h \leq z \leq \eta \quad (2.5)$$

$$\nabla \cdot \mathbf{u} = 0; \quad -h \leq z \leq \eta \quad (2.6)$$

$$w = -\mathbf{q} \cdot \nabla_h h; \quad z = -h \quad (2.7)$$

$$w = \frac{\partial \eta}{\partial t} + \mathbf{q} \cdot \nabla_h \eta; \quad z = \eta \quad (2.8)$$

$$p = 0; \quad z = \eta \quad (2.9)$$

The curl of the momentum equation leads to a vorticity equation, which is used to describe the motion's vorticity dynamics.

$$\frac{\partial \boldsymbol{\Omega}}{\partial t} + (\mathbf{u} \cdot \nabla) \boldsymbol{\Omega} = (\boldsymbol{\Omega} \cdot \nabla) \mathbf{u}; \quad -h \leq z \leq \eta \quad (2.10)$$

where vorticity is defined by $\boldsymbol{\Omega} = \nabla \times \mathbf{u}$, and may be written in terms of horizontal and vertical components as $(\boldsymbol{\xi}, \chi)$. In our problem, the motion consists of strong mean flows with long wave contributions and narrow-banded surface gravity waves. Weakly nonlinear surface gravity waves have small surface slope so that parameter $\epsilon = k_0 a_0 \ll 1$, where k_0 is a representative wave number. And a is a representative wave amplitude. All the scaling in our problem is done based on parameter ϵ . The oscillatory wave motion is described using complex function $e^{i\Theta} = \cos \Theta + i \sin \Theta$, where $\Theta(\mathbf{x}, t)$ is the wave phase function, with wave number and absolute frequency defined by

$$\mathbf{k}(\mathbf{x}, t) = \nabla_h \Theta(\mathbf{x}, t)$$

$$\omega(\mathbf{x}, t) = -\frac{\partial\Theta}{\partial t}(\mathbf{x}, t)$$

\mathbf{k} and ω are assumed to be slowly varying over horizontal and temporal scales. Wave number conservation is given by cross-differentiating Θ to obtain

$$\frac{\partial\mathbf{k}}{\partial t} + \nabla_h\omega = 0 \quad (2.11)$$

2.2 Wave-averaged Forces

To begin with, we make our problem non-dimensional by introducing a set of characteristic scales. We normalize horizontal distance x and y by the characteristic wave length scale k_0^{-1} , vertical distance z and surface elevation η by water depth h_0 , time coordinate t by wave period ω_0^{-1} , horizontal velocity \mathbf{q} by wave phase speed $c_0 = \omega_0/k_0$, vertical velocity w by μc_0 with $\mu = k_0 h_0 \sim O(1)$ for consistency, and pressure p by $\rho g h_0$.

With strong current and strong shear assumption, the current velocity can reach the same magnitude as the wave phase speed, $|\mathbf{u}^c|/c_0 \sim O(1)$. The current vertical shear is comparable to absolute wave frequency, $|\partial\mathbf{u}^c/\partial z|/\omega_0 \sim O(1)$. The wave amplitude is assumed to be far less than wave length, or $a_0 k_0 = \epsilon \ll 1$. The non-dimensional wave variables are of order $O(\epsilon)$.

If we divide the motions into waves and current in the momentum equation and apply wave-averaging, we get the momentum equation for the mean flow alone, given by

$$\frac{\partial\mathbf{u}^c}{\partial t} + \mathbf{u}^c \cdot \nabla \mathbf{u}^c + \frac{1}{\rho} \nabla p^c + g \mathbf{i}_z = -\epsilon^2 \langle \mathbf{u}^w \cdot \nabla \mathbf{u}^w \rangle; \quad -h \leq z \leq \eta \quad (2.12)$$

The RHS term $-\langle \mathbf{u}^w \cdot \nabla \mathbf{u}^w \rangle$ is the wave-averaged force. It can be interpreted either in terms of the radiation stress formalism or the C-L vortex force formalism. In this study, we adopt the vortex force formalism since it gives a clearer physical interpretation of the problem. Considering the relation $\mathbf{u} \cdot \nabla \mathbf{u} = \nabla(\mathbf{u} \cdot \mathbf{u})/2 - \mathbf{u} \times (\nabla \times \mathbf{u})$, we define

$$\kappa = \epsilon^2 \langle \frac{1}{2}(\mathbf{u}^w \cdot \nabla \mathbf{u}^w) \rangle \quad (2.13)$$

$$(\mathbf{J}, K) = \epsilon^2 \langle \mathbf{u}^w \times (\nabla \times \mathbf{u}^w) \rangle \quad (2.14)$$

where κ is Bernoulli head and (\mathbf{J}, K) are vortex forces in horizontal and vertical directions, respectively. Therefore, the RHS term $-\langle \mathbf{u}^w \cdot \nabla \mathbf{u}^w \rangle = -\epsilon^2(\nabla \kappa + \mathbf{J} + K \mathbf{i}_z)$. The body force is the combination of Bernoulli head gradient $\nabla \kappa$ and vortex force (\mathbf{J}, K) . The Bernoulli head gradient represents the wave-induced effects associated with wave set down. The vortex force represents wave refraction caused by the current field.

2.3 Linear Wave Problem in Two Horizontal Dimensions

Due to the retention of arbitrarily large shear in the formulation, the leading order problem for wave motion will not be covered by the usual theory for irrotational waves on a depth-uniform flow. Instead, the wave problem is described by a formulation analogous to the Rayleigh stability equation, extended to allow for possible veering of the horizontal component of the current vector with depth. A preliminary description of the resulting system for the spatially uniform case is provided here. We consider a current field which is constant in time and horizontal coordinates at leading order but arbitrary in vertical direction z . We divide the velocity vector $\mathbf{u} = (\mathbf{q}, w)$ into a steady current component \mathbf{u}^c and wave component \mathbf{u}^w , where $\mathbf{u}^c(z) = (\mathbf{q}^c(z), 0)$ and \mathbf{q}^c is horizontal current velocity, and $\mathbf{u}^w = (\mathbf{q}^w, w^w)$ is wave orbital velocity. By applying wave-averaging and linearizing boundary conditions after expansion about mean water level $\eta^c = 0$, we obtain the equations governing wave motion

$$\frac{\partial \mathbf{q}^w}{\partial t} + \mathbf{q}^c \cdot \nabla_h \mathbf{q}^w + \frac{\partial \mathbf{q}^c}{\partial z} w^w + \frac{1}{\rho} \nabla_h p^w = 0; \quad -h \leq z \leq 0 \quad (2.15)$$

$$\frac{\partial w^w}{\partial t} + \mathbf{q}^c \cdot \nabla_h w^w + \frac{1}{\rho} \frac{\partial p^w}{\partial z} = 0; \quad -h \leq z \leq 0 \quad (2.16)$$

$$\nabla_h \cdot \mathbf{q}^w + \frac{\partial w^w}{\partial z} = 0; \quad -h \leq z \leq 0 \quad (2.17)$$

$$w^w = 0; \quad z = -h \quad (2.18)$$

$$w^w = \frac{\partial \eta^w}{\partial t} + \mathbf{q}^c \cdot \nabla_h \eta^w; \quad z = 0 \quad (2.19)$$

$$p^w = \rho g \eta^w; \quad z = 0 \quad (2.20)$$

We seek solutions in the form of plane periodic waves. Let

$$\mathbf{q}^w = \hat{\mathbf{q}}(z)e^{i\Theta} + c.c.$$

$$w^w = \hat{w}(z)e^{i\Theta} + c.c.$$

$$\eta^w = ae^{i\Theta} + c.c.$$

$$p^w = \hat{p}(z)e^{i\Theta} + c.c.$$

where *c.c.* represents the complex conjugate. Using these definitions in Equation (2.15) - (2.20) and choosing \hat{w} as the dependent variable leads to a Rayleigh equation describing the vertical structure of \hat{w} together with surface and bottom boundary conditions

$$\sigma_w \frac{\partial^2 \hat{w}}{\partial z^2} - (\sigma_w k^2 + \frac{\partial^2 \sigma_w}{\partial z^2}) \hat{w} = 0; \quad -h \leq z \leq 0 \quad (2.21)$$

$$\hat{w} = 0; \quad z = -h \quad (2.22)$$

$$\sigma_s^2 \frac{\partial \hat{w}}{\partial z} - (\sigma_s \frac{\partial \sigma_w}{\partial z} + gk^2) \hat{w} = 0; \quad z = 0 \quad (2.23)$$

$$\sigma_w(z) = \omega - \mathbf{k} \cdot \mathbf{q}^c(z) \quad (2.24)$$

where $\sigma_s = \sigma_w(0)$, the intrinsic frequency at mean water surface level. Equations (2.21) - (2.24) provide the basic linear boundary value problem for waves on a horizontally uniform, vertically sheared mean flow. As is the case for flows in one horizontal dimension, analytic solutions for this problem in simple, closed form are rare; see Peregrine (1975) for a review. Solutions in the case of weak shear may be obtained using a perturbation approach described in Kirby and Chen (1989). For the general case, series solutions have been obtained by He (1988) and Shrira (1993), or numerical solutions may be obtained using a shooting method due to Fenton (1973) and Dong and Kirby (2012). In Chapter 3, we will look for the numerical solutions using Dong and Kirby (2012) method.

2.4 Multiple-scale Approach

In most cases, the spatial and temporal scales of variations of the current and of average properties of the wave field are much larger than the period and wavelength

of individual waves. Thus the scales of wave and current variations may be treated separately. We introduce multiple-scale format in horizontal scale \mathbf{x} and temporal scale t to describe the general modulations of variables,

$$\mathbf{x} = \mathbf{x} + \epsilon \mathbf{x} = \mathbf{x} + \mathbf{X} \quad (2.25)$$

$$t = t + \epsilon t = t + T \quad (2.26)$$

We assume that motions contain both fast scale and slow scale variations. The fast scales denoted by (\mathbf{x}, z, t) are used to describe local wave-like behavior as well as vertical variation, while slow scales are used to illustrate the slowly varying features of the mean flow as well as properties of narrow-banded wave trains in horizontal space and time denoted by (\mathbf{X}, T) . The topography is also assumed to vary slowly in horizontal space as $h = h(\mathbf{X})$. In addition to the general multiple-scale approach, we apply a WKB theory to wave motions to facilitate the isolation of problems at each order (n) for each harmonic frequency (m) as shown below, where n denotes ordering in ϵ and m denotes the harmonic number. We expand the variable ϕ , for instance, as

$$\begin{aligned} \phi &= \sum_{n=0}^{\infty} \epsilon^n \phi_n(\mathbf{x}, z, t, \mathbf{X}, T) \\ &= \sum_{n=0}^{\infty} \epsilon^n \sum_{m=-n}^n \phi_{n,m}(z, \mathbf{X}, T) E^m \end{aligned} \quad (2.27)$$

where $E = e^{i\Theta}$. We require $\phi_{n,-m} = \phi_{n,m}^*$, where ϕ is any physical variable and $*$ denotes complex conjugation (*c.c.* thereafter), in order to obtain real-valued physical quantities. Specifically, the mean flow is represented by terms with $m = 0$, while linear waves are represented by $m = 1$. Quadratic waves appear in terms with $m = 2$ plus slow-scale derivatives of linear wave terms. We note that wave terms with $E^m (m \neq 0)$ are formally removed by wave-averaging. It is thus easy to identify current terms and

waves terms in the expansion. According to

$$\phi^c = \sum_{n=0}^{\infty} \epsilon^n \phi_{n,0} = \phi_{0,0}(\mathbf{X}, z, T) + \epsilon \phi_{1,0}(\mathbf{X}, z, T) + \epsilon^2 \phi_{2,0}(\mathbf{X}, z, T) + \dots \quad (2.28)$$

$$\begin{aligned} \phi^w &= \sum_n \sum_{m \neq 0} \epsilon^n \phi_{n,m} E^m \\ &= \epsilon [\phi_{1,1}(\mathbf{X}, z, T)E + c.c.] + \epsilon^2 [\phi_{2,1}(\mathbf{X}, z, T)E + \phi_{2,2}(\mathbf{X}, z, T)E^2 + c.c.] + \dots \end{aligned} \quad (2.29)$$

Therefore, we expand all variables as follows

$$\begin{pmatrix} \mathbf{q} \\ w \\ \eta \\ p \\ \boldsymbol{\xi} \\ \chi \end{pmatrix} = \sum_{n=0}^{\infty} \epsilon^n \begin{pmatrix} \mathbf{q}_n \\ w_n \\ \eta_n \\ p_n \\ \boldsymbol{\xi}_n \\ \chi_n \end{pmatrix} = \sum_{n=0}^{\infty} \epsilon^n \sum_{m=-n}^n \begin{pmatrix} \mathbf{q}_{nm}(\mathbf{X}, z, T) \\ w_{nm}(\mathbf{X}, z, T) \\ \eta_{nm}(\mathbf{X}, T) \\ p_{nm}(\mathbf{X}, z, T) \\ \boldsymbol{\xi}_{nm}(\mathbf{X}, z, T) \\ \chi_{nm}(\mathbf{X}, z, T) \end{pmatrix} E^m \quad (2.30)$$

We adopt $\epsilon = ka$ as the only scaling parameter in our problem. The instantaneous surface elevation $\eta(\mathbf{x}, t)$ consists of the wave-averaged component $\eta^c(\mathbf{X}, T)$ and the oscillatory component $\eta^w(\mathbf{x}, t, \mathbf{X}, T)$.

$$\eta = \eta^c + \eta^w \quad (2.31)$$

The total mean water depth seen by waves is $h + \eta^c$, hence we expand the surface boundary conditions in Taylor series about the slowly varying water surface level $z = \eta^c$, which is consistent with subsequent use of the theory in numerical models.

$$(\cdot)_{z=\eta} = (\cdot)_{z=\eta^c} + \eta^w \frac{\partial}{\partial z} (\cdot)_{z=\eta^c} + \frac{\eta^{w2}}{2} \frac{\partial^2}{\partial z^2} (\cdot)_{z=\eta^c} + O(\epsilon^3) \quad (2.32)$$

In addition, both fast and slow scale variations are involved in our problem. To simplify it, we use the relation between fast and slow scale coordinates $\mathbf{x} = \mathbf{X}/\epsilon, t = T/\epsilon$ and substitute for fast scale coordinates using slow scale coordinates. The horizontal slow scale gradient is defined as ∇_H . The local slow scale derivative is defined as

$\partial/\partial T$. The phase function then becomes $\Theta(\mathbf{x}, t) = \Theta(\mathbf{X}, T)/\epsilon$, and wave number and frequency are defined as

$$\mathbf{k} = \nabla_h \Theta(\mathbf{x}, t) = \epsilon \nabla_H \left[\frac{1}{\epsilon} \Theta(\mathbf{X}, T) \right] = O(1)$$

$$\omega = \frac{\partial}{\partial t} \Theta(\mathbf{x}, t) = \epsilon \frac{\partial}{\partial T} \left[\frac{1}{\epsilon} \Theta(\mathbf{X}, T) \right] = O(1)$$

The governing equations are given with surface boundary conditions expanded at $z = \eta^c$

$$\epsilon \frac{\partial \mathbf{q}}{\partial T} + \epsilon(\mathbf{q} \cdot \nabla_H) \mathbf{q} + w \frac{\partial \mathbf{q}}{\partial z} + \frac{\epsilon}{\rho} \nabla_H p = 0; \quad -h \leq z \leq \eta^c \quad (2.33)$$

$$\epsilon \frac{\partial w}{\partial T} + \epsilon(\mathbf{q} \cdot \nabla_H) w + w \frac{\partial w}{\partial z} + \frac{1}{\rho} \frac{\partial p}{\partial z} + g = 0; \quad -h \leq z \leq \eta^c \quad (2.34)$$

$$\epsilon \nabla_H \cdot \mathbf{q} + \frac{\partial w}{\partial z} = 0; \quad -h \leq z \leq \eta^c \quad (2.35)$$

$$w = -\epsilon \mathbf{q} \cdot \nabla_H h; \quad z = -h \quad (2.36)$$

$$p + \epsilon \eta^w \frac{\partial p}{\partial z} + \frac{\epsilon^2 \eta^{w^2}}{2} \frac{\partial^2 p}{\partial z^2} + \frac{\epsilon^3 \eta^{w^3}}{6} \frac{\partial^3 p}{\partial z^3} = O(\epsilon^4); \quad z = \eta^c \quad (2.37)$$

$$\begin{aligned} w + \epsilon \eta^w \frac{\partial w}{\partial z} + \frac{\epsilon^2 \eta^{w^2}}{2} \frac{\partial^2 w}{\partial z^2} + \frac{\epsilon^3 \eta^{w^3}}{6} \frac{\partial^3 w}{\partial z^3} &= \epsilon \frac{\partial \eta}{\partial T} + \epsilon(\mathbf{q} + \epsilon \eta^w \frac{\partial \mathbf{q}}{\partial z} + \frac{\epsilon^2 \eta^{w^2}}{2} \frac{\partial^2 \mathbf{q}}{\partial z^2}) \cdot \nabla_H \eta \\ &+ O(\epsilon^4); \quad z = \eta^c \end{aligned} \quad (2.38)$$

2.4.1 Multiple scale expansion of momentum equation and boundary conditions

So far we have the full boundary value problem. Equation (2.13) and (2.14) indicate that the major part of wave-averaged forces are up to $O(\epsilon^3)$. Thus, we are going to expand the governing equations and boundary conditions in multiple scales up to $O(\epsilon^3)$. We only give wave equations up to $O(\epsilon^2)$, since higher order wave solutions are not necessary to get the vortex force formulation in our problem. The expanded equations without further simplification follow:

Horizontal momentum equation:

$$\frac{\partial \mathbf{q}_{0,0}}{\partial z} w_{n,m} - im\sigma_w \mathbf{q}_{n,m} + \frac{im\mathbf{k}}{\rho} p_{n,m} = M_{n,m}; \quad -h \leq z \leq \eta^c \quad (2.39)$$

where,

$$\begin{aligned} M_{0,0} &= 0 \\ M_{1,0} &= -\left[\frac{\partial \mathbf{q}_{0,0}}{\partial T} + \mathbf{q}_{0,0} \cdot \nabla_H \mathbf{q}_{0,0} + \frac{1}{\rho} \nabla_{HP0,0}\right] \\ M_{2,0} &= -\left[\frac{\partial \mathbf{q}_{1,0}}{\partial T} + \mathbf{q}_{0,0} \cdot \nabla_H \mathbf{q}_{1,0} + \frac{1}{\rho} \nabla_{HP1,0} + \mathbf{q}_{1,0} \cdot \nabla_H \mathbf{q}_{0,0} + w_{1,0} \frac{\partial \mathbf{q}_{1,0}}{\partial z}\right. \\ &\quad \left.+ w_{1,1} \frac{\partial \mathbf{q}_{1,-1}}{\partial z} + w_{1,-1} \frac{\partial \mathbf{q}_{1,1}}{\partial z} + i(\mathbf{q}_{1,-1} \cdot \mathbf{k}) \mathbf{q}_{1,1} - i(\mathbf{q}_{1,1} \cdot \mathbf{k}) \mathbf{q}_{1,-1}\right] \\ M_{3,0} &= -\left\{\frac{\partial \mathbf{q}_{2,0}}{\partial T} + \mathbf{q}_{0,0} \cdot \nabla_H \mathbf{q}_{2,0} + \mathbf{q}_{1,0} \cdot \nabla_H \mathbf{q}_{1,0} + \mathbf{q}_{2,0} \cdot \nabla_H \mathbf{q}_{0,0}\right. \\ &\quad \left.+ w_{1,0} \frac{\partial \mathbf{q}_{2,0}}{\partial z} + w_{2,0} \frac{\partial \mathbf{q}_{1,0}}{\partial z} + \frac{1}{\rho} \nabla_{HP2,0} + (\mathbf{q}_{1,1} \cdot \nabla_H \mathbf{q}_{1,-1} + \mathbf{q}_{1,-1} \cdot \nabla_H \mathbf{q}_{1,1})\right. \\ &\quad \left.+ [-i(\mathbf{k} \cdot \mathbf{q}_{1,1}) \mathbf{q}_{2,-1} + i(\mathbf{k} \cdot \mathbf{q}_{1,-1}) \mathbf{q}_{2,1} - i(\mathbf{k} \cdot \mathbf{q}_{2,1}) \mathbf{q}_{1,-1} + i(\mathbf{k} \cdot \mathbf{q}_{2,-1}) \mathbf{q}_{1,1}]\right. \\ &\quad \left.+ w_{1,1} \frac{\partial \mathbf{q}_{2,-1}}{\partial z} + w_{1,-1} \frac{\partial \mathbf{q}_{2,1}}{\partial z} + w_{2,1} \frac{\partial \mathbf{q}_{1,-1}}{\partial z} + w_{2,-1} \frac{\partial \mathbf{q}_{1,1}}{\partial z}\right\} \\ M_{1,1} &= 0 \\ M_{2,1} &= -\left[\frac{\partial \mathbf{q}_{1,1}}{\partial T} + \mathbf{q}_{0,0} \cdot \nabla_H \mathbf{q}_{1,1} + \frac{1}{\rho} \nabla_{HP1,1} + i(\mathbf{k} \cdot \mathbf{q}_{1,0}) \mathbf{q}_{1,1} + \mathbf{q}_{1,1} \cdot \nabla_H \mathbf{q}_{0,0}\right. \\ &\quad \left.+ w_{1,0} \frac{\partial \mathbf{q}_{1,1}}{\partial z} + w_{1,1} \frac{\partial \mathbf{q}_{1,0}}{\partial z}\right] \\ M_{2,2} &= -\left[i(\mathbf{k} \cdot \mathbf{q}_{1,1}) \mathbf{q}_{1,1} + w_{1,1} \frac{\partial \mathbf{q}_{1,1}}{\partial z}\right] \end{aligned}$$

Vertical momentum equation:

$$-im\sigma_w w_{n,m} + \frac{1}{\rho} \frac{\partial p_{n,m}}{\partial z} = N_{n,m}; \quad -h \leq z \leq \eta^c \quad (2.40)$$

where,

$$\begin{aligned} N_{0,0} &= -g \\ N_{1,0} &= 0 \\ N_{2,0} &= -\left[\frac{\partial w_{1,0}}{\partial T} + \mathbf{q}_{0,0} \cdot \nabla_H w_{1,0} + w_{1,0} \frac{\partial w_{1,0}}{\partial z} + \frac{\partial w_{1,1} w_{1,-1}}{\partial z} \right. \\ &\quad \left. - i(\mathbf{q}_{1,1} \cdot \mathbf{k}) w_{1,-1} + i(\mathbf{q}_{1,-1} \cdot \mathbf{k}) w_{1,1} \right] \\ N_{3,0} &= -\left[\frac{\partial w_{2,0}}{\partial T} + \mathbf{q}_{0,0} \cdot \nabla_H w_{2,0} + \frac{\partial w_{1,0} w_{2,0}}{\partial z} + \mathbf{q}_{1,0} \cdot \nabla_H w_{1,0} \right. \\ &\quad \left. + (\mathbf{q}_{1,1} \cdot \nabla_H w_{1,-1} + \mathbf{q}_{1,-1} \cdot \nabla_H w_{1,1}) + i\mathbf{k} \cdot (-\mathbf{q}_{1,1} w_{2,-1} + \mathbf{q}_{1,-1} w_{2,1}) \right. \\ &\quad \left. + i\mathbf{k} \cdot (-\mathbf{q}_{2,1} w_{1,-1} + \mathbf{q}_{2,-1} w_{1,1}) + \frac{\partial w_{1,1} w_{2,-1}}{\partial z} + \frac{\partial w_{1,-1} w_{2,1}}{\partial z} \right] \\ N_{1,1} &= 0 \\ N_{2,1} &= -\left[\frac{\partial w_{1,1}}{\partial T} + \mathbf{q}_{0,0} \cdot \nabla_H w_{1,1} + i(\mathbf{k} \cdot \mathbf{q}_{1,0}) w_{1,1} + \frac{\partial w_{1,0} w_{1,1}}{\partial z} \right] \\ N_{2,2} &= -\left[i(\mathbf{k} \cdot \mathbf{q}_{1,1}) w_{1,1} + w_{1,1} \frac{\partial w_{1,1}}{\partial z} \right] \end{aligned}$$

Continuity equation:

$$\frac{\partial w_{n,m}}{\partial z} + im\mathbf{k}\cdot\mathbf{q}_{n,m} = F_{n,m}; \quad -h \leq z \leq \eta^c \quad (2.41)$$

where,

$$\begin{aligned} F_{0,0} &= 0 \\ F_{1,0} &= -\nabla_H \cdot \mathbf{q}_{0,0} \\ F_{2,0} &= -\nabla_H \cdot \mathbf{q}_{1,0} \\ F_{3,0} &= -\nabla_H \cdot \mathbf{q}_{2,0} \\ F_{1,1} &= 0 \\ F_{2,1} &= -\nabla_H \cdot \mathbf{q}_{1,1} \\ F_{2,2} &= 0 \end{aligned}$$

Bottom boundary condition:

$$w_{n,m} = B_{n,m}; \quad z = -h \quad (2.42)$$

where,

$$\begin{aligned} B_{0,0} &= 0 \\ B_{1,0} &= -\mathbf{q}_{0,0} \cdot \nabla_H h \\ B_{2,0} &= -\mathbf{q}_{1,0} \cdot \nabla_H h \\ B_{3,0} &= -\mathbf{q}_{2,0} \cdot \nabla_H h \\ B_{1,1} &= 0 \\ B_{2,1} &= -\mathbf{q}_{1,1} \cdot \nabla_H h \\ B_{2,2} &= 0 \end{aligned}$$

Kinematic surface boundary condition:

$$w_{n,m} + im\sigma_w\eta_{n,m} = H_{n,m}; \quad z = \eta^c \quad (2.43)$$

where,

$$\begin{aligned}
H_{0,0} &= 0 \\
H_{1,0} &= \frac{\partial\eta_{0,0}}{\partial T} + \mathbf{q}_{0,0} \cdot \nabla_H \eta_{0,0} \\
H_{2,0} &= \frac{\partial\eta_{1,0}}{\partial T} + \mathbf{q}_{0,0} \cdot \nabla_H \eta_{1,0} + \mathbf{q}_{1,0} \cdot \nabla_H \eta_{0,0} \\
&\quad + i(\mathbf{k} \cdot \mathbf{q}_{1,-1})\eta_{1,1} - i(\mathbf{k} \cdot \mathbf{q}_{1,1})\eta_{1,-1} - \eta_{1,1} \frac{\partial w_{1,-1}}{\partial z} - \eta_{1,-1} \frac{\partial w_{1,1}}{\partial z} \\
H_{3,0} &= \frac{\partial\eta_{2,0}}{\partial T} + \mathbf{q}_{0,0} \cdot \nabla_H \eta_{2,0} + \mathbf{q}_{2,0} \cdot \nabla_H \eta_{0,0} + \mathbf{q}_{1,0} \cdot \nabla_H \eta_{1,0} \\
&\quad + \mathbf{q}_{1,1} \cdot \nabla_H \eta_{1,-1} + \mathbf{q}_{1,-1} \cdot \nabla_H \eta_{1,1} \\
&\quad + (\eta_{1,1} \frac{\partial \mathbf{q}_{1,-1}}{\partial z} + \eta_{1,-1} \frac{\partial \mathbf{q}_{1,1}}{\partial z}) \cdot \nabla_H \eta_{0,0} \\
&\quad + \frac{\partial \mathbf{q}_{0,0}}{\partial z} \cdot (\eta_{1,1} \nabla_H \eta_{1,-1} + \eta_{1,-1} \nabla_H \eta_{1,1}) \\
&\quad - \eta_{1,1} \eta_{1,-1} \left(\frac{\partial^2 w_{1,0}}{\partial z^2} - \frac{\partial^2 \mathbf{q}_{0,0}}{\partial z^2} \cdot \nabla_H \eta_{0,0} \right) \\
&\quad + i\mathbf{k} \cdot (-\mathbf{q}_{1,1} \eta_{2,-1} + \mathbf{q}_{1,-1} \eta_{2,1}) + i\mathbf{k} \cdot (-\mathbf{q}_{2,1} \eta_{1,-1} + \mathbf{q}_{2,-1} \eta_{1,1}) \\
&\quad - (\eta_{1,1} \frac{\partial w_{2,-1}}{\partial z} + \eta_{1,-1} \frac{\partial w_{2,1}}{\partial z} + \eta_{2,1} \frac{\partial w_{1,-1}}{\partial z} + \eta_{2,-1} \frac{\partial w_{1,1}}{\partial z}) \\
H_{1,1} &= 0 \\
H_{2,1} &= \frac{\partial\eta_{1,1}}{\partial T} + \mathbf{q}_{0,0} \cdot \nabla_H \eta_{1,1} + \mathbf{q}_{1,1} \cdot \nabla_H \eta_{0,0} + \eta_{1,1} \frac{\partial \mathbf{q}_{0,0}}{\partial z} \cdot \nabla_H \eta_{0,0} \\
&\quad + i(\mathbf{k} \cdot \mathbf{q}_{1,0})\eta_{1,1} - \eta_{1,1} \frac{\partial w_{1,0}}{\partial z} \\
H_{2,2} &= i(\mathbf{k} \cdot \mathbf{q}_{1,1})\eta_{1,1} - \eta_{1,1} \frac{\partial w_{1,1}}{\partial z}
\end{aligned}$$

Dynamic surface boundary condition:

$$p_{n,m} = S_{n,m}; \quad z = \eta^c \quad (2.44)$$

where,

$$\begin{aligned} S_{0,0} &= 0 \\ S_{1,0} &= 0 \\ S_{2,0} &= -(\eta_{1,1} \frac{\partial p_{1,-1}}{\partial z} + \eta_{1,-1} \frac{\partial p_{1,1}}{\partial z}) \\ S_{3,0} &= (\eta_{1,1} \frac{\partial p_{2,-1}}{\partial z} + \eta_{1,-1} \frac{\partial p_{2,1}}{\partial z} + \eta_{2,1} \frac{\partial p_{1,-1}}{\partial z} + \eta_{2,-1} \frac{\partial p_{1,1}}{\partial z}) \\ S_{1,1} &= -\eta_{1,1} \frac{\partial p_{0,0}}{\partial z} \\ S_{2,1} &= -(\eta_{2,1} \frac{\partial p_{0,0}}{\partial z} + \eta_{1,1} \frac{\partial p_{1,0}}{\partial z}) \\ S_{2,2} &= -(\eta_{2,2} \frac{\partial p_{0,0}}{\partial z} + \eta_{1,1} \frac{\partial p_{1,1}}{\partial z}) \end{aligned}$$

2.4.2 Multiple scale expansion of vorticity equations

The vorticity equation is also expanded in multiple scales. First, we rewrite Equation (2.10)

$$\frac{\partial \Omega}{\partial t} + (\mathbf{u} \cdot \nabla) \Omega = (\Omega \cdot \nabla) \mathbf{u}; \quad -h \leq z \leq \eta \quad (2.45)$$

Letting $\Omega = \boldsymbol{\xi} + \chi \mathbf{i}_z$ and considering slow scales, the vorticity equation can be rewritten in horizontal and vertical directions respectively as

$$\epsilon \frac{\partial \boldsymbol{\xi}}{\partial T} = -\epsilon(\mathbf{q} \cdot \nabla_H) \boldsymbol{\xi} + \epsilon(\boldsymbol{\xi} \cdot \nabla_H) \mathbf{q} - w \frac{\partial \boldsymbol{\xi}}{\partial z} + \chi \frac{\partial \mathbf{q}}{\partial z} \quad (2.46)$$

$$\epsilon \frac{\partial \chi}{\partial T} = -\epsilon(\mathbf{q} \cdot \nabla_H) \chi + \epsilon(\boldsymbol{\xi} \cdot \nabla_H) w - w \frac{\partial \chi}{\partial z} + \chi \frac{\partial w}{\partial z} \quad (2.47)$$

The expanded vorticity equations are given as follows.

Horizontal vorticity equation:

$$\frac{\partial \mathbf{q}_{0,0}}{\partial z} \chi_{n,m} - w_{n,m} \frac{\partial \boldsymbol{\xi}_{0,0}}{\partial z} + im[\sigma_w \boldsymbol{\xi}_{n,m} + (\mathbf{k} \cdot \boldsymbol{\xi}_{0,0}) \mathbf{q}_{n,m}] = \mathbf{O}_{n,m}; \quad -h \leq z \leq \eta^c \quad (2.48)$$

where,

$$\begin{aligned} \mathbf{O}_{0,0} &= 0 \\ \mathbf{O}_{1,0} &= \frac{\partial \boldsymbol{\xi}_{0,0}}{\partial T} + \mathbf{q}_{0,0} \cdot \nabla_H \boldsymbol{\xi}_{0,0} - \boldsymbol{\xi}_{0,0} \cdot \nabla_H \mathbf{q}_{0,0} \\ \mathbf{O}_{2,0} &= \frac{\partial \boldsymbol{\xi}_{1,0}}{\partial T} + \mathbf{q}_{0,0} \cdot \nabla_H \boldsymbol{\xi}_{1,0} + \mathbf{q}_{1,0} \cdot \nabla_H \boldsymbol{\xi}_{0,0} \\ &\quad - \boldsymbol{\xi}_{0,0} \cdot \nabla_H \mathbf{q}_{1,0} - \boldsymbol{\xi}_{1,0} \cdot \nabla_H \mathbf{q}_{0,0} + w_{1,0} \frac{\partial \boldsymbol{\xi}_{1,0}}{\partial z} - \chi_{10} \frac{\partial \mathbf{q}_{1,0}}{\partial z} \\ &\quad + i(\mathbf{k} \cdot \mathbf{q}_{1,-1}) \boldsymbol{\xi}_{1,1} - i(\mathbf{k} \cdot \mathbf{q}_{1,1}) \boldsymbol{\xi}_{1,-1} + i(\mathbf{k} \cdot \boldsymbol{\xi}_{1,1}) \mathbf{q}_{1,-1} - i(\mathbf{k} \cdot \boldsymbol{\xi}_{1,-1}) \mathbf{q}_{1,1} \\ &\quad + w_{1,1} \frac{\partial \boldsymbol{\xi}_{1,-1}}{\partial z} + w_{1,-1} \frac{\partial \boldsymbol{\xi}_{1,1}}{\partial z} - \chi_{1,1} \frac{\partial \mathbf{q}_{1,-1}}{\partial z} - \chi_{1,-1} \frac{\partial \mathbf{q}_{1,1}}{\partial z} \\ \mathbf{O}_{3,0} &= \frac{\partial \boldsymbol{\xi}_{2,0}}{\partial T} + \mathbf{q}_{0,0} \cdot \nabla_H \boldsymbol{\xi}_{2,0} + w_{1,0} \frac{\partial \boldsymbol{\xi}_{2,0}}{\partial z} - \boldsymbol{\xi}_{2,0} \cdot \nabla_H \mathbf{q}_{0,0} \\ &\quad + (\mathbf{q}_{1,0} \cdot \nabla_H \boldsymbol{\xi}_{1,0} - \boldsymbol{\xi}_{1,0} \cdot \nabla_H \mathbf{q}_{1,0}) + (\mathbf{q}_{2,0} \cdot \nabla_H \boldsymbol{\xi}_{0,0} - \boldsymbol{\xi}_{0,0} \cdot \nabla_H \mathbf{q}_{2,0}) \\ &\quad + (w_{2,0} \frac{\partial \boldsymbol{\xi}_{1,0}}{\partial z} - \chi_{1,0} \frac{\partial \mathbf{q}_{2,0}}{\partial z} - \chi_{2,0} \frac{\partial \mathbf{q}_{1,0}}{\partial z}) \\ &\quad + (\mathbf{q}_{1,1} \cdot \nabla_H \boldsymbol{\xi}_{1,-1} + \mathbf{q}_{1,-1} \cdot \nabla_H \boldsymbol{\xi}_{1,1} - \boldsymbol{\xi}_{1,1} \cdot \nabla_H \mathbf{q}_{1,-1} - \boldsymbol{\xi}_{1,-1} \cdot \nabla_H \mathbf{q}_{1,1}) \\ &\quad + [-i(\mathbf{k} \cdot \mathbf{q}_{2,1}) \boldsymbol{\xi}_{1,-1} + i(\mathbf{k} \cdot \mathbf{q}_{2,-1}) \boldsymbol{\xi}_{1,1} - i(\mathbf{k} \cdot \mathbf{q}_{1,1}) \boldsymbol{\xi}_{2,-1} + i(\mathbf{k} \cdot \mathbf{q}_{1,-1}) \boldsymbol{\xi}_{2,1}] \\ &\quad - [-i(\mathbf{k} \cdot \boldsymbol{\xi}_{11}) \mathbf{q}_{2,-1} + i(\mathbf{k} \cdot \boldsymbol{\xi}_{1,-1}) \mathbf{q}_{2,1} - i(\mathbf{k} \cdot \boldsymbol{\xi}_{2,1}) \mathbf{q}_{1,-1} + i(\mathbf{k} \cdot \boldsymbol{\xi}_{2,-1}) \mathbf{q}_{1,1}] \\ &\quad + (w_{1,1} \frac{\partial \boldsymbol{\xi}_{2,-1}}{\partial z} + w_{1,-1} \frac{\partial \boldsymbol{\xi}_{2,1}}{\partial z} + w_{2,1} \frac{\partial \boldsymbol{\xi}_{1,-1}}{\partial z} + w_{2,-1} \frac{\partial \boldsymbol{\xi}_{1,1}}{\partial z}) \\ &\quad - (\chi_{1,1} \frac{\partial \mathbf{q}_{2,-1}}{\partial z} + \chi_{1,-1} \frac{\partial \mathbf{q}_{2,1}}{\partial z} + \chi_{2,1} \frac{\partial \mathbf{q}_{1,-1}}{\partial z} + \chi_{2,-1} \frac{\partial \mathbf{q}_{1,1}}{\partial z}) \\ \mathbf{O}_{1,1} &= 0 \\ \mathbf{O}_{2,1} &= \frac{\partial \boldsymbol{\xi}_{1,1}}{\partial T} + \mathbf{q}_{0,0} \cdot \nabla_H \boldsymbol{\xi}_{1,1} + i(\mathbf{k} \cdot \mathbf{q}_{1,0}) \boldsymbol{\xi}_{1,1} + \mathbf{q}_{1,1} \cdot \nabla_H \boldsymbol{\xi}_{0,0} \\ &\quad - \boldsymbol{\xi}_{0,0} \cdot \nabla_H \mathbf{q}_{1,1} - i(\boldsymbol{\xi}_{1,0} \cdot \mathbf{k}) \mathbf{q}_{1,1} - \boldsymbol{\xi}_{1,1} \cdot \nabla_H \mathbf{q}_{0,0} + w_{11} \frac{\partial \boldsymbol{\xi}_{1,0}}{\partial z} \\ &\quad - \chi_{1,0} \frac{\partial \mathbf{q}_{1,1}}{\partial z} + w_{1,0} \frac{\partial \boldsymbol{\xi}_{1,1}}{\partial z} - \chi_{1,1} \frac{\partial \mathbf{q}_{1,0}}{\partial z} \\ \mathbf{O}_{2,2} &= i(\mathbf{q}_{1,1} \cdot \mathbf{k}) \boldsymbol{\xi}_{1,1} - i(\boldsymbol{\xi}_{1,1} \cdot \mathbf{k}) \mathbf{q}_{1,1} + w_{1,1} \frac{\partial \boldsymbol{\xi}_{1,-1}}{\partial z} - \chi_{1,1} \frac{\partial \mathbf{q}_{1,-1}}{\partial z} \end{aligned}$$

Vertical vorticity equation:

$$im[\sigma_w \chi_{n,m} + (\boldsymbol{\xi}_{0,0} \cdot \mathbf{k}) w_{n,m}] = P_{n,m}; \quad -h \leq z \leq \eta^c \quad (2.49)$$

where,

$$\begin{aligned}
P_{0,0} &= 0 \\
P_{1,0} &= 0 \\
P_{2,0} &= \frac{\partial \chi_{1,0}}{\partial T} + \mathbf{q}_{0,0} \cdot \nabla_H \chi_{1,0} - \boldsymbol{\xi}_{0,0} \cdot \nabla_H w_{1,0} + w_{1,0} \frac{\partial \chi_{1,0}}{\partial z} - \chi_{1,0} \frac{\partial w_{1,0}}{\partial z} \\
&\quad + i(\mathbf{k} \cdot \mathbf{q}_{1,-1}) \chi_{1,1} - i(\mathbf{k} \cdot \mathbf{q}_{1,1}) \chi_{1,-1} + i(\mathbf{k} \cdot \boldsymbol{\xi}_{1,1}) w_{1,-1} - i(\mathbf{k} \cdot \boldsymbol{\xi}_{1,-1}) w_{1,1} \\
&\quad + w_{1,-1} \frac{\partial \chi_{1,1}}{\partial z} + w_{1,1} \frac{\partial \chi_{1,-1}}{\partial z} - \chi_{1,1} \frac{\partial w_{1,-1}}{\partial z} - \chi_{1,-1} \frac{\partial w_{1,1}}{\partial z} \\
P_{3,0} &= \frac{\partial \chi_{2,0}}{\partial T} + \mathbf{q}_{0,0} \cdot \nabla_H \chi_{2,0} + w_{1,0} \frac{\partial \chi_{2,0}}{\partial z} \\
&\quad + (\mathbf{q}_{1,0} \cdot \nabla_H \chi_{1,0} - \boldsymbol{\xi}_{1,0} \cdot \nabla_H w_{1,0}) - \boldsymbol{\xi}_{00} \cdot \nabla_H w_{2,0} \\
&\quad + (w_{2,0} \frac{\partial \chi_{1,0}}{\partial z} - \chi_{1,0} \frac{\partial w_{2,0}}{\partial z} - \chi_{2,0} \frac{\partial w_{1,0}}{\partial z}) \\
&\quad + (\mathbf{q}_{1,1} \cdot \nabla_H \chi_{1,-1} + \mathbf{q}_{1,-1} \cdot \nabla_H \chi_{1,1} - \boldsymbol{\xi}_{1,1} \cdot \nabla_H w_{1,-1} - \boldsymbol{\xi}_{1,-1} \cdot \nabla_H w_{1,1}) \\
&\quad + [-i(\mathbf{k} \cdot \mathbf{q}_{2,1}) \chi_{1,-1} + i(\mathbf{k} \cdot \mathbf{q}_{2,-1}) \chi_{1,1} - i(\mathbf{k} \cdot \mathbf{q}_{1,1}) \chi_{2,-1} + i(\mathbf{k} \cdot \mathbf{q}_{1,-1}) \chi_{2,1}] \\
&\quad - [-i(\mathbf{k} \cdot \boldsymbol{\xi}_{1,1}) w_{2,-1} + i(\mathbf{k} \cdot \boldsymbol{\xi}_{1,-1}) w_{2,1} - i(\mathbf{k} \cdot \boldsymbol{\xi}_{2,1}) w_{1,-1} + i(\mathbf{k} \cdot \boldsymbol{\xi}_{2,-1}) w_{1,1}] \\
&\quad + (w_{1,1} \frac{\partial \chi_{2,-1}}{\partial z} + w_{1,-1} \frac{\partial \chi_{2,1}}{\partial z} + w_{2,1} \frac{\partial \chi_{1,-1}}{\partial z} + w_{2,-1} \frac{\partial \chi_{1,1}}{\partial z}) \\
&\quad - (\chi_{1,1} \frac{\partial w_{2,-1}}{\partial z} + \chi_{1,-1} \frac{\partial w_{2,1}}{\partial z} + \chi_{2,1} \frac{\partial w_{1,-1}}{\partial z} + \chi_{2,-1} \frac{\partial w_{1,1}}{\partial z}) \\
P_{1,1} &= 0 \\
P_{2,1} &= \frac{\partial \chi_{1,1}}{\partial T} + \mathbf{q}_{0,0} \cdot \nabla_H \chi_{1,1} + i \mathbf{q}_{1,0} \cdot \mathbf{k} \chi_{1,1} - \boldsymbol{\xi}_{0,0} \cdot \nabla_H w_{1,1} - i(\boldsymbol{\xi}_{1,0} \cdot \mathbf{k}) w_{1,1} \\
&\quad + w_{1,1} \frac{\partial \chi_{1,0}}{\partial z} + w_{1,0} \frac{\partial \chi_{1,1}}{\partial z} - \chi_{1,0} \frac{\partial w_{1,1}}{\partial z} - \chi_{1,1} \frac{\partial w_{1,0}}{\partial z} \\
P_{2,2} &= i(\mathbf{q}_{1,1} \cdot \mathbf{k}) \chi_{1,1} - i(\boldsymbol{\xi}_{1,1} \cdot \mathbf{k}) w_{1,1} + w_{1,1} \frac{\partial \chi_{1,1}}{\partial z} - \chi_{1,1} \frac{\partial w_{1,1}}{\partial z}
\end{aligned}$$

The expressions for current vorticity components ($m = 0$) in terms of velocities are given as

O(1) :

$$\xi_{0,0} = \mathbf{i}_z \times \frac{\partial \mathbf{q}_{0,0}}{\partial z} \quad (2.50)$$

$$\chi_{0,0} = 0 \quad (2.51)$$

O(ϵ) :

$$\xi_{1,0} = \mathbf{i}_z \times \frac{\partial \mathbf{q}_{1,0}}{\partial z} \quad (2.52)$$

$$\chi_{1,0} = \mathbf{i}_z \cdot (\nabla_H \times \mathbf{q}_{0,0}) \quad (2.53)$$

O(ϵ^2) :

$$\xi_{2,0} = \mathbf{i}_z \times \frac{\partial \mathbf{q}_{2,0}}{\partial z} + \nabla_H w_{1,0} \times \mathbf{i}_z \quad (2.54)$$

$$\chi_{2,0} = \mathbf{i}_z \cdot (\nabla_H \times \mathbf{q}_{1,0}) \quad (2.55)$$

The expressions of wave vorticity components for ($m \neq 0$) in terms of velocities are given by

O(ϵ) :

$$\chi_{1,1} = -\frac{(\xi_{0,0} \cdot \mathbf{k}) w_{1,1}}{\sigma_w} \quad (2.56)$$

$$\xi_{1,1} = -i \left[\frac{\partial \mathbf{q}_{0,0}}{\partial z} \frac{w_{1,1} (\xi_{0,0} \cdot \mathbf{k})}{\sigma_w^2} + \frac{\partial \xi_{0,0}}{\partial z} \frac{w_{1,1}}{\sigma_w} \right] - \frac{(\xi_{0,0} \cdot \mathbf{k}) \mathbf{q}_{1,1}}{\sigma_w} \quad (2.57)$$

O(ϵ^2) :

$$\chi_{2,1} = -i \frac{P_{2,1}}{\sigma_w} - \frac{(\xi_{0,0} \cdot \mathbf{k}) w_{2,1}}{\sigma_w} \quad (2.58)$$

$$\begin{aligned} \xi_{2,1} = & -i \left[\frac{\mathbf{O}_{2,1}}{\sigma_w} + i \frac{\partial \mathbf{q}_{0,0}}{\partial z} \frac{P_{2,1}}{\sigma_w^2} + \frac{\partial \mathbf{q}_{0,0}}{\partial z} \frac{w_{2,1} (\xi_{0,0} \cdot \mathbf{k})}{\sigma_w^2} + \frac{\partial \xi_{0,0}}{\partial z} \frac{w_{2,1}}{\sigma_w} \right] \\ & - \frac{(\xi_{0,0} \cdot \mathbf{k}) \mathbf{q}_{2,1}}{\sigma_w} \end{aligned} \quad (2.59)$$

So far, we have expanded equations in multiple scales. All terms that contain products $\phi_{1,1} \phi_{1,-1}$, $\phi_{2,1} \phi_{1,-1}$, $\phi_{1,1} \phi_{2,-1}$ etc., represent contributions of wave terms to the wave-averaged equations such as radiation stresses, dynamic set-up or set-down, etc.. In the next two chapters, we will examine wave dynamics and mean flow dynamics.

Chapter 3

WAVE DYNAMICS

In this chapter, we present wave equations and wave solutions up to $O(\epsilon^2)$. With the strongly sheared mean flow assumption, terms related to the current vertical shear appear in wave equations. Waves are described by the Rayleigh stability equation after manipulation. For arbitrary current shear, series solutions have been obtained by He (1998) and Shrira (1993). Meanwhile, the perturbation solutions based on weak current assumption are provided by Stewart and Joy (1974) and Kirby and Chen (1989). Numerical and perturbation wave solutions are compared for specific current profiles. The constant shear current is adopted to provide analytical wave solutions for validation of numerical and perturbation solutions. Current velocity profiles measured at the mouth of Columbia River (MCR) are also used to compare numerical and perturbation solutions. Wave vorticity is described. The wave orbital velocity and wave vorticity are required to calculate wave-averaged forces. Additionally, the solvability condition at $O(\epsilon^2)$ for the wave problem leads to the wave action conservation equation, which provides the governing equation for wave models including strong current shear effects.

3.1 First-order Wave Motions

The leading order wave equations are given by ($n = 1, m = \pm 1$) terms in the expansion. As we can see, current vertical shear appears in wave momentum equation,

which generates wave vorticity.

$$\frac{\partial \mathbf{q}_{0,0}}{\partial z} w_{1,1} - i\sigma_w \mathbf{q}_{1,1} + \frac{i\mathbf{k}}{\rho} p_{1,1} = 0; \quad -h \leq z \leq \eta^c \quad (3.1)$$

$$-i\sigma_w w_{1,1} + \frac{1}{\rho} \frac{\partial p_{1,1}}{\partial z} = 0; \quad -h \leq z \leq \eta^c \quad (3.2)$$

$$\frac{\partial w_{1,1}}{\partial z} + i\mathbf{k} \cdot \mathbf{q}_{1,1} = 0; \quad -h \leq z \leq \eta^c \quad (3.3)$$

$$w_{1,1} = 0; \quad z = -h \quad (3.4)$$

$$w_{1,1} = -i\sigma_s \eta_{1,1}; \quad z = \eta^c \quad (3.5)$$

$$p_{1,1} = -\eta_{1,1} \frac{\partial p_{0,0}}{\partial z}; \quad z = \eta^c \quad (3.6)$$

To get the Rayleigh (or inviscid Orr-Sommerfeld) stability equation, we multiply Equation (3.1) by \mathbf{k} and take its vertical derivative $\partial/\partial z$. After combining (3.2) - (3.6), we have the Rayleigh equation for the vertical component of wave velocity $w_{1,1}$, given by

$$\sigma_w \frac{\partial^2 w_{1,1}}{\partial z^2} - \left(\frac{\partial^2 \sigma_w}{\partial z^2} + k^2 \sigma_w \right) w_{1,1} = C_{1,1} = 0; \quad -h \leq z \leq \eta^c \quad (3.7)$$

with combined surface boundary condition

$$\sigma_s^2 \frac{\partial w_{1,1}}{\partial z} - \left(\sigma_s \frac{\partial \sigma_w}{\partial z} + gk^2 \right) w_{1,1} = D_{1,1} = 0; \quad z = \eta^c \quad (3.8)$$

and bottom boundary condition (3.4). σ_s is the wave intrinsic frequency at mean surface. The horizontal orbital velocity amplitude $\mathbf{q}_{1,1}$ and pressure field amplitude $p_{1,1}$ are given in terms of $w_{1,1}$ by

$$\mathbf{q}_{1,1}(z) = -\frac{i}{\sigma_w} \left[w_{1,1} \frac{\partial \mathbf{q}_{0,0}}{\partial z} - \frac{\sigma_w^2 \mathbf{k}}{k^2} \frac{\partial}{\partial z} \left(\frac{w_{1,1}}{\sigma_w} \right) \right] \quad (3.9)$$

$$p_{1,1}(z) = \frac{i\rho\sigma_w^2}{k^2} \frac{\partial}{\partial z} \left(\frac{w_{1,1}}{\sigma_w} \right) \quad (3.10)$$

3.1.1 Linear wave vorticity

The leading order wave vorticity amplitude is obtained from wave vorticity equation expansion ($n = 1, m = 1$) in Equation (2.56) and (2.57).

$$\chi_{1,1} = -\frac{(\mathbf{k} \cdot \boldsymbol{\xi}_{0,0}) w_{1,1}}{\sigma_w} \quad (3.11)$$

$$\boldsymbol{\xi}_{1,1} = -i \left[\frac{\partial \mathbf{q}_{0,0}}{\partial z} \frac{w_{1,1}}{\sigma_w^2} (\mathbf{k} \cdot \boldsymbol{\xi}_{0,0}) + \frac{\partial \boldsymbol{\xi}_{0,0}}{\partial z} \frac{w_{1,1}}{\sigma_w} \right] - \frac{(\mathbf{k} \cdot \boldsymbol{\xi}_{0,0}) \mathbf{q}_{1,1}}{\sigma_w} \quad (3.12)$$

where $\chi_{1,1}$ is wave vertical vorticity amplitude and $\boldsymbol{\xi}_{1,1}$ is horizontal vorticity amplitude. It is clear that wave vorticity is induced by current horizontal vorticity $\boldsymbol{\xi}_{0,0}$. The non-divergence of wave vorticity $\nabla \cdot \boldsymbol{\Omega} = 0$ at $(n = 1, m = 1)$ yields

$$i\mathbf{k} \cdot \boldsymbol{\xi}_{1,1} + \frac{\partial \chi_{1,1}}{\partial z} = 0 \quad (3.13)$$

which is used in mean flow dynamics in Chapter 4.

3.1.2 Wave vorticity for constant shear current

The constant shear current is usually adopted to illustrate current effects on linear wave solutions. The linear wave solutions for constant shear current are given in Appendix A.3. Constantin (2011) considers a constant shear flow beneath a irrotational wave train and above a flat bed and suggests that the flow only allows exactly following waves or opposing waves to exist. The flow vorticity has to be orthogonal to the wave direction. In other words, irrotational oblique waves are prohibited in the flow field. Now let's consider a constant shear current

$$\mathbf{q}_{0,0} = \mathbf{q}_{0,0}^s + \boldsymbol{\Omega}^s z \quad (3.14)$$

where $\mathbf{q}_{0,0}^s$ is surface current velocity and $\boldsymbol{\Omega}^s = \partial \mathbf{q}_{0,0} / \partial z$ is constant shear as seen in Figure 3.1. If $\mathbf{q}_{0,0}^s$ and $\boldsymbol{\Omega}^s$ are not co-directional, the current velocity rotates over depth. The Ekman spiral is a good example of current velocity rotating with depth. In Chapter 2, we have obtained the flow vorticity

$$\boldsymbol{\xi}_{0,0} = \mathbf{i}_z \times \frac{\partial \mathbf{q}_{0,0}}{\partial z} \quad (3.15)$$

For the constantly sheared flow, the vorticity then becomes

$$\boldsymbol{\xi}_{0,0} = \mathbf{i}_z \times \boldsymbol{\Omega}^s \quad (3.16)$$

When the waves are exactly following or opposing the two-dimensional constantly sheared flow, the wave number vector is orthogonal to the flow vorticity

$$\mathbf{k} \cdot \boldsymbol{\xi}_{0,0} = 0 \quad (3.17)$$

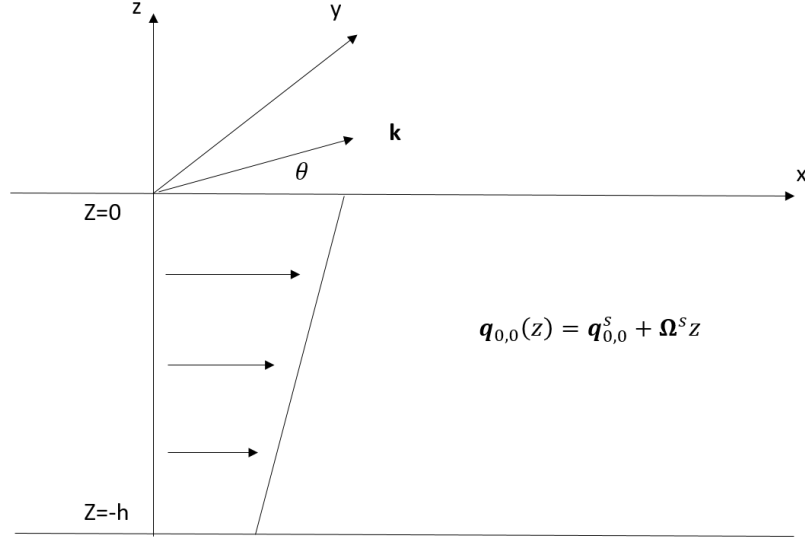


Figure 3.1: Waves propagating over a constantly sheared current. Suppose the flow $\mathbf{q}_{0,0}$ and shear Ω^s is in x -direction on a flat bed. The angle between wave direction and flow direction is θ . Results from Section 3.1.2 indicate that the amplitude of wave vorticity is affected by the oblique angle θ and current shear. When $\theta = 0$ or $\theta = \pm\pi$, waves are either exactly following the current or opposing the current. Wave vorticity is zero in this case. For a fixed $\theta \neq 0, \pm\pi$ and vertical level z , wave vorticity increases as current shear turns larger and decreases as current shear turns smaller. For a fixed current shear, wave vorticity changes with oblique angle θ in a more complicated way as in Equation (3.33) - (3.35).

And the wave vorticity reduces to zero. The wave is still irrotational in Constantin (2011)'s case.

$$\chi_{1,1} = 0 \quad (3.18)$$

$$\xi_{1,1} = 0 \quad (3.19)$$

Thus, Constantin (2011)'s theorem is only applicable to irrotational waves. Ellingsen (2016) suggests that waves that propagate in all directions over a constantly sheared flow may become rotational. When the wave direction has an angle with the flow, it is associated with an undulating perturbation of the vorticity field. The so-called undulating perturbation in the vorticity field is the wave vorticity discussed here. Now,

let's discuss the effect of oblique wave angle on wave vorticity. The linear wave solutions on constant shear currents is given by

$$w_{1,1}(z) = -i\sigma_s\eta_{1,1}F_{ss} \quad (3.20)$$

$$\mathbf{q}_{1,1}(z) = -\frac{\sigma_s\eta_{1,1}\boldsymbol{\Omega}^s}{\sigma}F_{ss} + \frac{\sigma_s\eta_{1,1}\mathbf{k}}{k^2}(kF_{cs} + \frac{\mathbf{k}\cdot\boldsymbol{\Omega}^s}{\sigma}F_{ss}) \quad (3.21)$$

$$\sigma_s = \omega - \mathbf{k}\cdot\mathbf{q}_{0,0}^s \quad (3.22)$$

$$\sigma_w = \sigma_s - \mathbf{k}\cdot\boldsymbol{\Omega}^s z \quad (3.23)$$

$$F_{ss} = \frac{\sinh k(h+z)}{\sinh kh} \quad (3.24)$$

$$F_{cs} = \frac{\cosh k(h+z)}{\sinh kh} \quad (3.25)$$

The wave vorticity is re-written in terms of wave amplitude $\eta_{1,1}$ as

$$\chi_{1,1} = i\frac{(\mathbf{k}\cdot\boldsymbol{\xi}_{0,0})\sigma_s\eta_{1,1}F_{ss}}{\sigma_w} \quad (3.26)$$

$$\boldsymbol{\xi}_{1,1} = -\frac{(\mathbf{k}\cdot\boldsymbol{\xi}_{0,0})}{\sigma_w}\left[\frac{\sigma_s\eta_{1,1}\mathbf{k}}{k^2}(kF_{cs} + \frac{\mathbf{k}\cdot\boldsymbol{\Omega}^s}{\sigma_w}F_{ss})\right] \quad (3.27)$$

The horizontal component of wave vorticity ($\boldsymbol{\xi}_{1,1}$) follows the wave direction. As shown in Figure 3.1, the flow is considered in x -direction. The current shear and flow vorticity are given as

$$\boldsymbol{\Omega}^s = \Omega^s\mathbf{i}_x \quad (3.28)$$

$$\boldsymbol{\xi}_{0,0} = \Omega^s\mathbf{i}_y \quad (3.29)$$

The waves propagate over the flow at an angle θ , so that

$$\mathbf{k} = k\cos\theta\mathbf{i}_x + k\sin\theta\mathbf{i}_y \quad (3.30)$$

$$\mathbf{k}\cdot\boldsymbol{\xi}_{0,0} = k\Omega^s\sin\theta \quad (3.31)$$

$$\mathbf{k}\cdot\boldsymbol{\Omega}^s = k\Omega^s\cos\theta \quad (3.32)$$

The wave vorticity now becomes

$$\chi_{1,1} = i \frac{k\Omega^s \sigma_s \eta_{1,1}}{\sigma_s - (k\Omega^s \cos \theta)z} F_{ss} \sin \theta \quad (3.33)$$

$$\xi_{1,1}^x = -\frac{k\Omega^s \sigma_s \eta_{1,1}}{\sigma_s - (k\Omega^s \cos \theta)z} \left[F_{cs} \sin \theta \cos \theta + \frac{\Omega^s}{\sigma_s - (k\Omega^s \cos \theta)z} F_{ss} \sin \theta \cos^2 \theta \right] \quad (3.34)$$

$$\xi_{1,1}^y = -\frac{k\Omega^s \sigma_s \eta_{1,1}}{\sigma_s - (k\Omega^s \cos \theta)z} \left[F_{cs} \sin^2 \theta + \frac{\Omega^s}{\sigma_s - (k\Omega^s \cos \theta)z} F_{ss} \sin^2 \theta \cos \theta \right] \quad (3.35)$$

The wave vorticity decreases from water surface to bottom. For a fixed oblique angle $\theta \neq 0$ or $\pm \pi$ and vertical level z , wave vorticity increases as current shear becomes larger and decreases as current shear becomes smaller. However, the relation between wave vorticity and the oblique angle is more complicated. For following waves, the wave angle varies within $-\pi/2 \leq \theta \leq \pi/2$; for opposing waves, the wave angle varies within $\pi/2 \leq \theta \leq 3\pi/2$. To illustrate the effects of oblique angle on wave vorticity, we consider waves with amplitude 2 m propagate on a constantly sheared flow with surface velocity $q_{0,0}^s = 3.5$ m/s. The water depth is set as $H = 25$ m. Assuming that current velocity drops to zero at the bottom, the current vertical shear is calculated as $\Omega^s = q_{0,0}^s/H = 0.14$ s⁻¹. We vary the oblique wave angle for both following and opposing currents. The effects of wave length are also including by considering intermediate water waves ($kh = 1$) and shallow water waves ($kh = 0.2$). The results of surface wave vorticity are shown in Figures 3.2 and 3.3. In general, the wave vorticity of intermediate water waves ($kh = 1$) is larger than the that of shallow water waves ($kh = 0.2$). The results also indicate that wave vorticity is zero when waves and current are co-directional. Otherwise, wave vorticity is nonzero. The magnitude of wave vorticity increases with the oblique angle and reaches to its maximum when waves are perpendicular to current (see red dashed line). The x -component of wave vorticity reaches to its maximum when the angle between waves and current is $\pi/4$ (see blue dash-dotted line). The y -component of wave vorticity doesn't alter signs for this case (see blue starred line). Both y -component and z -component of wave vorticity reach the maximum (or minimum) unless when the angle between waves and current

is $\frac{\pi}{2}$.

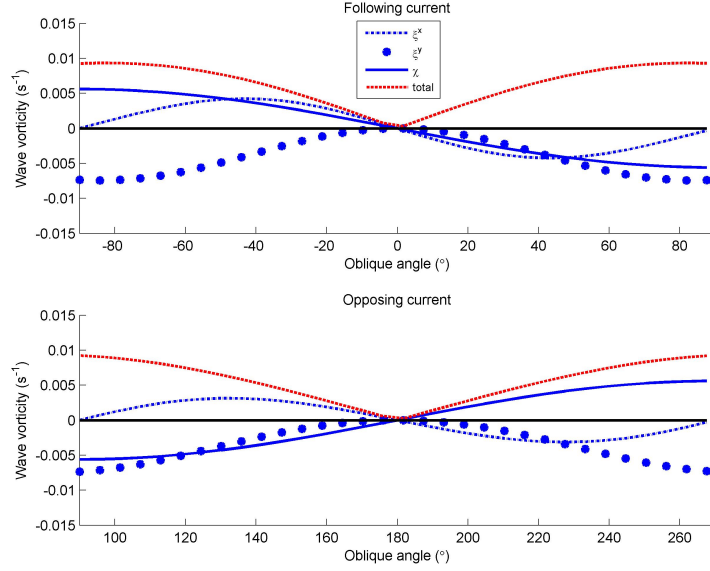


Figure 3.2: Surface wave vorticity changes with oblique wave angle ($kh = 1$). Upper: waves following current. The oblique wave angle varies from $-\pi/2$ to $\pi/2$. Lower: waves opposing current. The oblique wave angle varies from $\pi/2$ to $3\pi/2$. Blue Dash-dot: x -component ($\xi_{1,1}^x$); Blue Star: y -component ($\xi_{1,1}^y$); Blue Solid: z -component ($\chi_{1,1}$); Red Dash: total ($\sqrt{\chi_{1,1}^2 + \xi_{1,1}^2}$). Results are calculated based on Equation (3.33) - (3.35).

3.1.3 Numerical solution to wave Rayleigh equation

In the theory for depth uniform current and constant shear current, the wave vertical orbital velocity can be written in terms of the hyperbolic sine function (see Appendix A). However, in the presence of arbitrarily sheared mean flow, the vertical structure of wave orbital velocity are no longer in this form. For the Rayleigh equation, we non-dimensionalize $w_{1,1}(z)$ with wave amplitude $\eta_{1,1}$ and surface intrinsic frequency σ_s ,

$$w_{1,1}(z) = -i\sigma_s\eta_{1,1}f(z) \quad (3.36)$$

where $f(\eta^\epsilon) = 1$. The non-dimensional depth-dependent function $f(z)$ can be obtained numerically using a shooting method. σ_s is surface intrinsic frequency at the mean

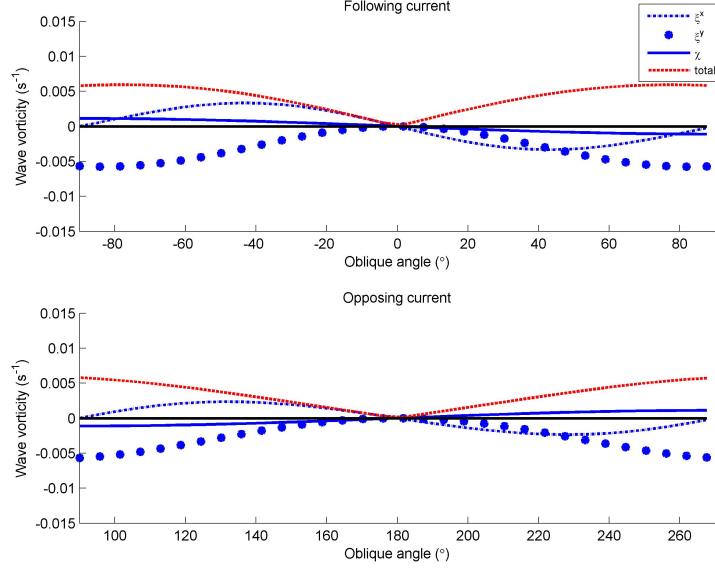


Figure 3.3: Surface wave vorticity changes with oblique wave angle ($kh = 0.2$). Upper: waves following current. The oblique wave angle varies from $-\pi/2$ to $\pi/2$. Lower: waves opposing current. The oblique wave angle varies from $\pi/2$ to $3\pi/2$. Blue Dash-dot: x -component ($\xi_{1,1}^x$); Blue Star: y -component ($\xi_{1,1}^y$); Blue Solid: z -component ($\chi_{1,1}$); Red Dash: total ($\sqrt{\chi_{1,1}^2 + \xi_{1,1}^2}$). Results are calculated based on Equation (3.33) - (3.35).

surface, which is defined in Equation (2.24). We also introduce the vertical structure function for the intrinsic frequency,

$$\sigma_w(z) = \sigma_s L(z) \quad (3.37)$$

The Rayleigh equation can be rewritten as following

$$f'' - \left(k^2 + \frac{L''}{L}\right)f = 0; \quad -h \leq z \leq \eta^c \quad (3.38)$$

$$f(-h) = 0; \quad (3.39)$$

$$f' = \left(L' + \frac{gk^2}{\sigma_s}\right)f; \quad z = \eta^c \quad (3.40)$$

where

$$f' = \frac{df}{dz} \quad (3.41)$$

For a strong current with arbitrary shear, the Rayleigh equation has no analytical solutions. Following Kirby and Chen (1989), two methods are used to solve Rayleigh equation in this paper: direct numerical solution and perturbation approximation. A numerical solution to Rayleigh equation can be obtained by transforming the boundary value problem into an initial value problem and solving it using a shooting method. First, we introduce the mean water depth $H = h + \eta^c$. The still water depth h and mean water surface η^c vary slowly in time and space. Thus, the actual water depth H can be treated as a constant for local waves. We introduce a new variable $Q(z) = f/(Hf')$ and a non-dimensionalized vertical coordinate $\hat{z} = z/H$. We have $\hat{z} = -1$ at the bottom and $\hat{z} = 0$ at the water surface. After substituting them into Rayleigh equation, we have

$$\frac{dQ}{d\hat{z}} = 1 - \gamma^2 Q^2; \quad -1 \leq \hat{z} \leq 0 \quad (3.42)$$

$$\gamma^2(\hat{z}) = (kH)^2 + \frac{L''}{L} \quad (3.43)$$

$$Q = \frac{\sigma_s^2}{gk^2H + \sigma_s^2L'}; \quad \hat{z} = 0 \quad (3.44)$$

$$Q = 0; \quad \hat{z} = -1 \quad (3.45)$$

Now look at the relation between $L(\hat{z})$ and current profile. We also assume that current horizontal velocity $\mathbf{q}^c(\hat{z}) = q_s^c \mathbf{I}(\hat{z})$, where q_s^c is the surface current velocity magnitude and the non-dimensional vector function $\mathbf{I}(\hat{z})$ represents current direction and vertical profile. It is noteworthy that the current direction may rotate over depth. The intrinsic frequency is expressed using current as

$$\sigma_w(\hat{z}) = \omega - q_s^c \mathbf{k} \cdot \mathbf{I}(\hat{z}) = \sigma_s L(\hat{z}) \quad (3.46)$$

So that

$$L(\hat{z}) = \frac{\omega}{\sigma_s} - \frac{q_s^c \mathbf{k} \cdot \mathbf{I}(\hat{z})}{\sigma_s} \quad (3.47)$$

Solving the problem requires that current velocity $\mathbf{q}^c(z)$ distribution to be known. The current velocity is approximated using a polynomial expansion as below.

$$\mathbf{I}(\hat{z}) = \frac{\mathbf{q}^c}{q_s^c} + \mathbf{A}_1 \hat{z} + \mathbf{A}_2 \hat{z}^2 + \mathbf{A}_3 \hat{z}^3 + \dots \quad (3.48)$$

$$L(\hat{z}) = 1 + B_1 \hat{z} + B_2 \hat{z}^2 + B_3 \hat{z}^3 + \dots \quad (3.49)$$

$$B_n = -\frac{q_s^c \mathbf{k} \cdot \mathbf{A}_n}{\sigma_s} \quad (n = 1, 2, 3\dots) \quad (3.50)$$

Then, we obtain numerical solutions for both $Q(\hat{z})$ and phase speed c using a shooting method. Specifically, we first give a starting value for c , then march the solution from bottom $\hat{z} = -1$ to the surface $\hat{z} = 0$ to get $Q(0)$. We can use phase speed calculated without current effects as the starting value. At the same time, we can get the value of $Q(0)$ directly through surface boundary condition. If the difference between these two $Q(0)$ value is within a tolerable limit 10^{-4} , we find the solution for $Q(z)$ and c . Otherwise, we use the new c from the surface boundary condition and march the solution again until we are satisfied with the magnitude of error.

3.1.3.1 Verification of numerical solution

We verify the numerical solution based on the shooting method to Rayleigh equation by changing the vertical resolution dz . The current velocity profile measured at the mouth of Columbia River (MCR) is used in the verification (see Figure 3.4). This data set was taken from the R/V Pt. Sur, during the July 2004 RISE cruise (<http://makani.coas.oregonstate.edu/rise/>). The shooting method can use any dz , including an adaptive value. The convergence of the shooting method depends on the size of dz . Figure 3.4 illustrates that numerical solutions converge as the resolution dz gets smaller. When $dz < 1$ m, the numerical solution becomes stable.

The Rayleigh equation has analytical solutions for both depth uniform current and constant shear current. Hence we compare the analytical solution and numerical solution for these two cases as shown in Figure 3.5. Apparently, neither depth uniform current nor constant shear current needs 6th order polynomial fitting. However, 6th order polynomial fitting will later be used for measured current profiles. Here we use

it for consistency. The plots indicate that numerical solutions converge to these two analytical solutions.

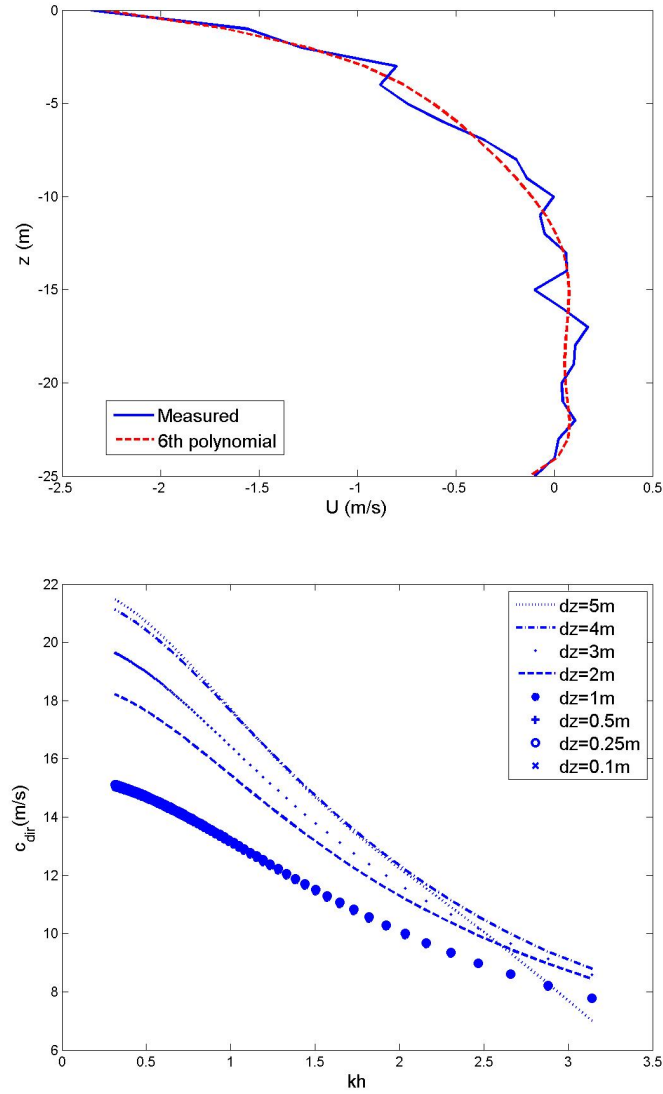


Figure 3.4: Verification of numerical solution to Rayleigh equation. (Upper) Measured current velocity profiles at Columbia River mouth (blue solid line) with 6th order polynomial curve fitting (red dashed line) (Kilcher and Nash, 2010). The measured data indicates a strong surface current (up to 2.3 m/s) with strong vertical shear during ebb tide. (Lower) Absolute wave phase speed c change over non-dimensional wave number kh obtained from numerical solution.

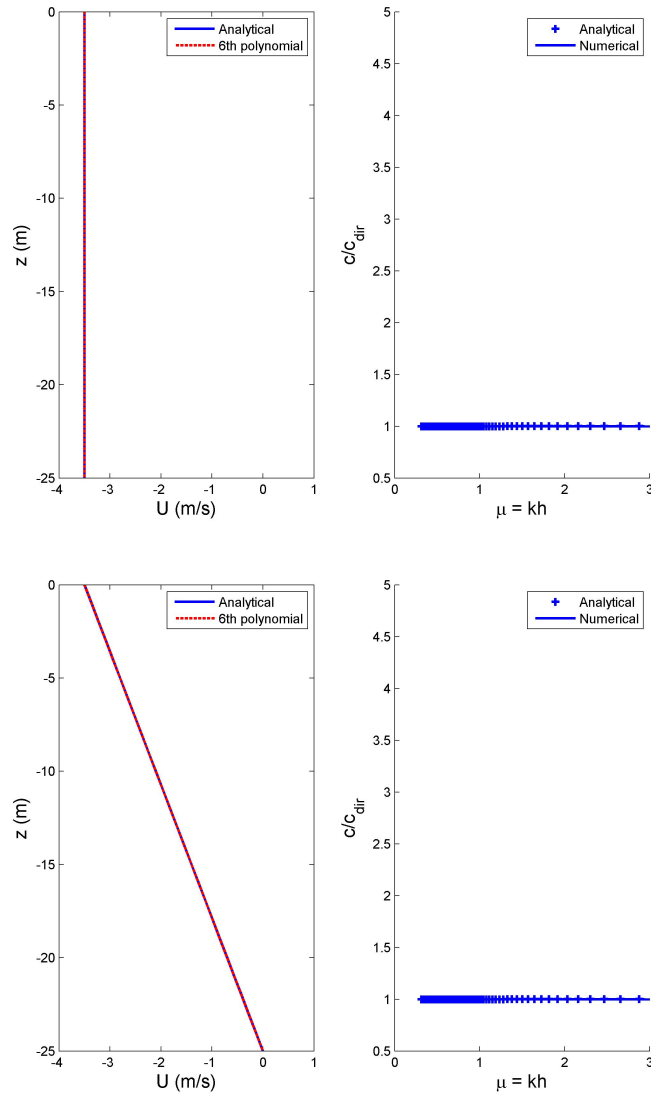


Figure 3.5: Verification of numerical solution to Rayleigh Equation. (Upper Left) Depth uniform current velocity profile with 6th order polynomial curve fitting (red dashed line). The current velocity is set as -3.5 m/s. (Upper Right) Comparison of analytical solution (blue '+') and numerical solution (blue solid line). The vertical resolution $dz = 0.1$ m. (Lower Left) Constant shear current velocity profile with 6th order polynomial curve fitting (red dashed line). The current velocity is set as -3.5 m/s at water surface and 0 m/s at the bottom. (Lower Right) Comparison of analytical solution (blue '+') and numerical solution (blue solid line). The vertical resolution $dz = 0.1$ m. The results indicate that numerical solutions converge to these two analytical solutions.

3.1.4 Perturbation solution to wave Rayleigh equation

In the coupled system of ocean circulation model and wave model, getting the exact wave solutions from Rayleigh equation requires that we use the shooting method at each time step and horizontal grid location unless the solution varies slowly enough, which is computationally expensive. On the one hand, we want to include current vertical shear effects on wave orbital velocity and vorticity to calculate wave forces. On the other hand, we would like to avoid expensive computation cost by directly solving the Rayleigh equation. Thus an alternative wave solution is needed.

By assuming strong current, we have the Froude number $F = q_{0,0s}/\sqrt{gH} \sim 1$, where $q_{0,0s}$ is surface current horizontal speed and \sqrt{gH} is the wave phase speed in shallow water. The representative mean water depth at the river mouth is $h = 15$ m. According to the observations at Columbia River mouth, the maximum surface current speed can reach to 3.5 m/s, which means $F = 0.28$ (Hickey *et al.*, 2010). This Froude number is pretty large for most places. Hence it is possible that higher order perturbation solution is a good alternative. Now we are going to examine it. The approximate solution can be approached using perturbation method (Kirby and Chen, 1989) by assuming the current speed to be small relative to the wave phase speed in the Rayleigh equation. Here we assume relatively weak current $\mathbf{q}_{0,0} \sim \epsilon \mathbf{q}_{0,0}(z)$, and retain solutions in order of $O(\epsilon^n)$.

$$c = \frac{\omega}{k} = c_0 + \epsilon c_1 + \epsilon^2 c_2 + \dots + \epsilon^n c_n \quad (3.51)$$

$$\begin{aligned} w_{1,1} &= w_{1,1}^{(0)} + \epsilon w_{1,1}^{(1)} + \epsilon^2 w_{1,1}^{(2)} + \dots + \epsilon^n w_{1,1}^{(n)} \\ &= -i\sigma_s \eta_{1,1} \frac{f_0(z) + \epsilon f_1(z) + \epsilon^2 f_2(z) + \dots + \epsilon^n f_n(z)}{f_0(\eta^c)} \end{aligned} \quad (3.52)$$

where c is the absolute wave phase speed. We set $f_n(\eta^c) = 0$ for $n > 0$. $w_{1,1}$ is the vertical component of wave orbital velocity amplitude and has to converge to kinetic surface boundary condition at the mean water surface. Applying the perturbation expansion to the Rayleigh equation, at order $O(\epsilon^0)$, we obtain linear wave solutions for the current-free case. We obtain a hyperbolic wave vertical structure and the classic

dispersion relations.

$$f_0(z) = \sinh k(h+z) \quad (3.53)$$

$$c_0^2 = \frac{g}{k} \tanh kH \quad (3.54)$$

Since the current velocity is weak, at leading order, waves feel no current. We move on to $O(\epsilon)$ solutions. The vertical structure of wave orbital velocity is modified by current profile shown in $f_1(z)$.

$$f_1(z) = -\left[\frac{\hat{\mathbf{k}} \cdot \mathbf{q}_{0,0}(z) + \hat{\mathbf{k}} \cdot \mathbf{q}_{0,0}(-h)}{c_0} + \frac{2kI_1(z)}{c_0}\right]f_0(z) + \frac{2I_2(z)}{c_0} \frac{\partial f_0}{\partial z} \quad (3.55)$$

$$I_1(z) = \int_{-h}^z \hat{\mathbf{k}} \cdot \mathbf{q}_{0,0}(\zeta) \sinh 2k(h+\zeta) d\zeta \quad (3.56)$$

$$I_2(z) = \int_{-h}^z \hat{\mathbf{k}} \cdot \mathbf{q}_{0,0}(\zeta) \cosh 2k(h+\zeta) d\zeta \quad (3.57)$$

$$c_1 = \frac{2k}{\sinh 2kH} \int_{-h}^{\eta^c} \hat{\mathbf{k}} \cdot \mathbf{q}_{0,0}(z) \cosh 2k(h+z) dz \quad (3.58)$$

$$\begin{aligned} c_2 &= \frac{c_1}{2c_0} [4kI_1(\eta^c) - (1 + 2 \cosh 2kH)c_1] \\ &+ \frac{c_0 k^2}{2g f_0^2(\eta^c)} \int_{-h}^{\eta^c} [\hat{\mathbf{k}} \cdot \mathbf{q}_{00}(z)]^2 [1 + 2 \cosh^2 k(h+z)] dz \\ &+ \frac{2c_0 k^3}{g f_0^2(\eta^c)} \int_{-h}^{\eta^c} [I_2(z) \frac{\partial I_1}{\partial z} - I_1(z) \frac{\partial I_2}{\partial z}] dz \end{aligned} \quad (3.59)$$

where $\hat{\mathbf{k}} = \mathbf{k}/k$ is the unit wave number vector. c_1 is the $O(\epsilon)$ correction to wave phase speed and also known as the depth-weighted current in Kirby and Chen (1989). c_2 is the $O(\epsilon^2)$ correction to wave phase speed. The current speed we use in Rayleigh equation is the current velocity projection in wave direction $\hat{\mathbf{k}} \cdot \mathbf{q}_{0,0}(z)$. If we keep perturbation solutions up to $O(\epsilon)$, we have the linear wave solutions in the form below.

$$w_{1,1}^{(0)} = -i\sigma_s \eta_{1,1} \frac{f_0(z)}{f_0(\eta^c)} \quad (3.60)$$

$$w_{1,1}^{(1)} = -i\sigma_s \eta_{1,1} \frac{f_1(z)}{f_0(\eta^c)} \quad (3.61)$$

$$\sigma_w(z) = k(c_0 + c_1) - \mathbf{k} \cdot \mathbf{q}_{00}(z) \quad (3.62)$$

We use perturbation solution as an approximation to Rayleigh equation. The horizontal orbital velocity amplitude and wave pressure amplitude can be expressed using $w_{1,1}$.

$$\mathbf{q}_{1,1}^{(0)} = -\frac{i}{\sigma_w} \left[w_{1,1}^{(0)} \frac{\partial \mathbf{q}_{0,0}}{\partial z} - \frac{\mathbf{k}}{k^2} \left(\sigma_w \frac{\partial w_{1,1}^{(0)}}{\partial z} - w_{1,1}^{(0)} \frac{\partial \sigma_w}{\partial z} \right) \right] \quad (3.63)$$

$$\mathbf{q}_{1,1}^{(1)} = -\frac{i}{\sigma_w} \left[w_{1,1}^{(1)} \frac{\partial \mathbf{q}_{0,0}}{\partial z} - \frac{\mathbf{k}}{k^2} \left(\sigma_w \frac{\partial w_{1,1}^{(1)}}{\partial z} - w_{1,1}^{(1)} \frac{\partial \sigma_w}{\partial z} \right) \right] \quad (3.64)$$

$$p_{1,1}^{(0)} = \frac{i\rho}{k^2} \left(\sigma_w \frac{\partial w_{1,1}^{(0)}}{\partial z} - w_{1,1}^{(0)} \frac{\partial \sigma_w}{\partial z} \right) \quad (3.65)$$

$$p_{1,1}^{(1)} = \frac{i\rho}{k^2} \left(\sigma_w \frac{\partial w_{1,1}^{(1)}}{\partial z} - w_{1,1}^{(1)} \frac{\partial \sigma_w}{\partial z} \right) \quad (3.66)$$

The $O(\epsilon)$ wave vorticity obtained in Chapter 2 can be re-written in terms of perturbation solution.

$$\chi_{1,1}^{(0)} = -\frac{(\boldsymbol{\xi}_{0,0} \cdot \mathbf{k}) w_{1,1}^{(0)}}{\sigma_w} \quad (3.67)$$

$$\chi_{1,1}^{(1)} = -\frac{(\boldsymbol{\xi}_{0,0} \cdot \mathbf{k}) w_{1,1}^{(1)}}{\sigma_w} \quad (3.68)$$

$$\boldsymbol{\xi}_{1,1}^{(0)} = -i \left[\frac{\partial \mathbf{q}_{0,0}}{\partial z} \frac{(\boldsymbol{\xi}_{0,0} \cdot \mathbf{k}) w_{1,1}^{(0)}}{\sigma_w^2} + \frac{\partial \boldsymbol{\xi}_{0,0}}{\partial z} \frac{w_{1,1}^{(0)}}{\sigma_w} \right] - \frac{(\boldsymbol{\xi}_{0,0} \cdot \mathbf{k}) \mathbf{q}_{1,1}^{(0)}}{\sigma_w} \quad (3.69)$$

$$\boldsymbol{\xi}_{1,1}^{(1)} = -i \left[\frac{\partial \mathbf{q}_{0,0}}{\partial z} \frac{(\boldsymbol{\xi}_{0,0} \cdot \mathbf{k}) w_{1,1}^{(1)}}{\sigma_w^2} + \frac{\partial \boldsymbol{\xi}_{0,0}}{\partial z} \frac{w_{1,1}^{(1)}}{\sigma_w} \right] - \frac{(\boldsymbol{\xi}_{0,0} \cdot \mathbf{k}) \mathbf{q}_{1,1}^{(1)}}{\sigma_w} \quad (3.70)$$

So far, we have the numerical solution and perturbation solution up to $O(\epsilon)$ for wave Rayleigh equation. In the next section, we will compare the wave phase speed between numerical solution and perturbation solutions up to $O(\epsilon^2)$. The $O(\epsilon^2)$ wave solutions are not necessary for our problem. Results indicate that perturbation approximation up to $O(\epsilon)$ is a fairly good approximation.

3.1.5 Numerical and $O(\epsilon)$ perturbation solution comparison

In last section, both numerical method and perturbation method are used to solve Rayleigh equation. As discussed in Kirby and Chen (1989), stronger surface current velocity $q_{0,0s}$, stronger current shear $\partial \mathbf{q}_{0,0} / \partial z$ and longer wave period $2\pi/\omega$ result in less accuracy of the $O(\epsilon)$ perturbation solution. In this section, we evaluate the performance of perturbation solutions using numerical results.

Three example profiles with known velocity distribution are given in Kirby and Chen (1989). They are linear shear current (3.71), cosine profile (3.72) and power law profile (3.73).

$$U(z) = U_s \left(1 + \alpha \frac{z}{h}\right) \quad (3.71)$$

$$U(z) = U_s \cos \alpha \frac{z}{h} \quad (3.72)$$

$$U(z) = U_s \left(1 + \frac{z}{h}\right)^{1/7} \quad (3.73)$$

where α is a non-dimensional shear parameter. We use the three profiles along with the depth uniform current to investigate the accuracy of perturbation solutions. The water depth is set as 5 m for all the current profiles. The maximum velocity is set as -3.5 m/s so that the Froude number $F = 0.5$. Larger Froude number indicates stronger current effect. Hence, we use $F = 0.5$ to illustrate the upper limit of current effect. We consider waves propagating against current. The wave number varies from $\mu = kh \sim 0.3$ to $\mu = kh \sim 3$, which covers both short waves and long waves. The numerical solution is first validated with decreasing the vertical resolution from $dz = 5$ m to $dz = 0.1$ m as shown in Figure 3.4. We give the perturbation solutions up to $O(\epsilon^2)$, numerical solution as well as solution using depth-averaged current. We use the ratio c/c_{dir} to illustrate the difference between numerical solution and other solutions, where c_{dir} is numerical solution of wave phase speed. The comparison results are shown in Figure 3.6 and 3.7. In general, all the current assumptions gives better approximation for long waves ($kh \ll 1$) than short waves ($kh \gg 1$). $O(\epsilon)$ perturbation solution is a better approximation than the depth-average current (see Lower Right in Figure 3.6 and 3.7).

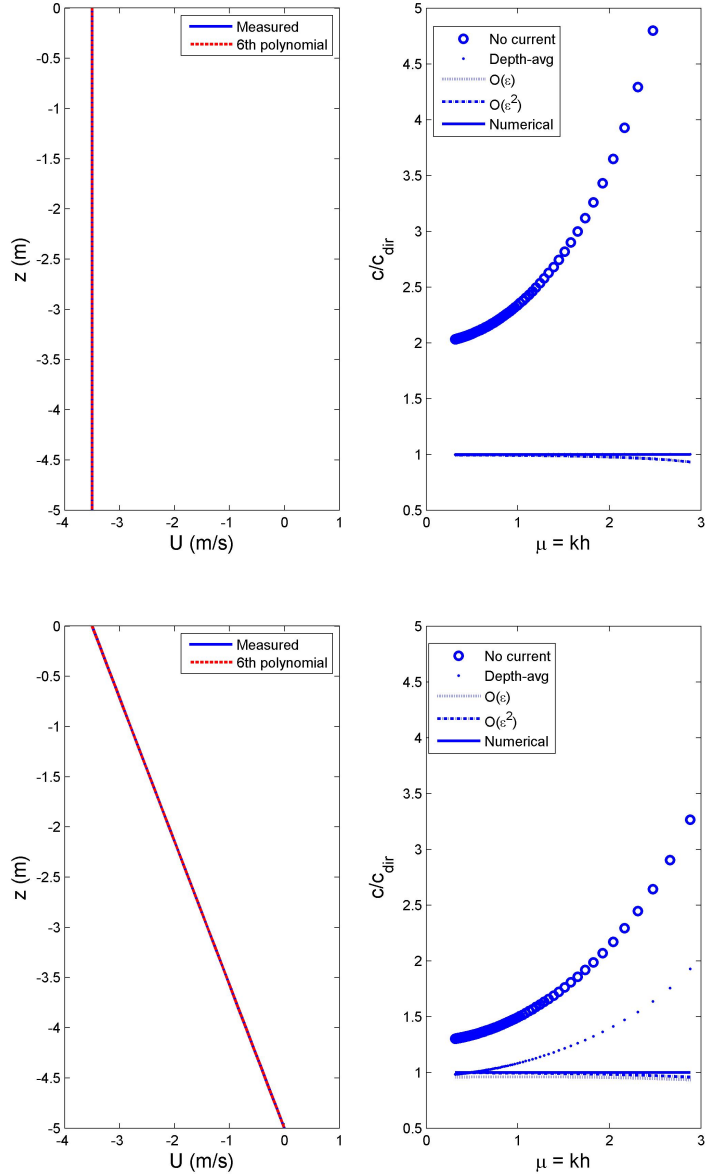


Figure 3.6: Wave phase speed comparison between perturbation solution up to $O(\epsilon^2)$ and numerical solution with analytical current velocity profiles: Depth uniform current (Upper Panel), Linearly sheared current (Lower Panel). The maximum current speed is set as 3.5 m/s to meet strong current assumption. The left figure of each panel shows original profile and 6th order polynomial fitting curves. The right figure of each panel shows the non dimensional wave phase speed normalized by the numerical solution (c_{dir}). As the figure indicates, shorter waves are more sensitive to the ambient current than longer waves. Additionally, the accuracy of perturbation solution goes higher with increasing orders. The $O(\epsilon)$ perturbation solution is a good approximation to numerical solution.

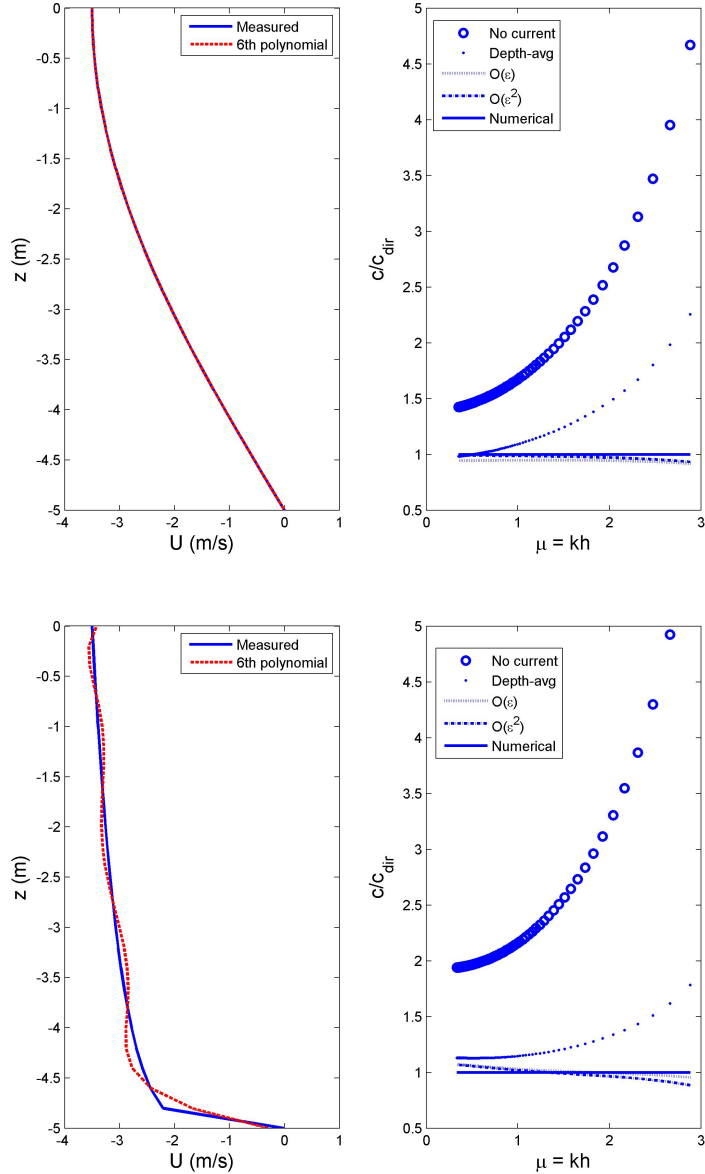


Figure 3.7: Wave phase speed comparison between perturbation solution up to $O(\epsilon^2)$ and numerical solution with analytical current velocity profiles: Cosine-shape current (Upper Panel) and Power law shape current (Lower Panel). The maximum current speed is set as 3.5 m/s to meet strong current assumption. The left figure of each panel shows original profile and 6th order polynomial fitting curves. The right figure of each panel shows the non dimensional wave phase speed normalized by the numerical solution (c_{dir}). Figure indicates that shorter waves are more sensitive to the ambient current than longer waves. The $O(\epsilon)$ perturbation solution is a good approximation to numerical solution.

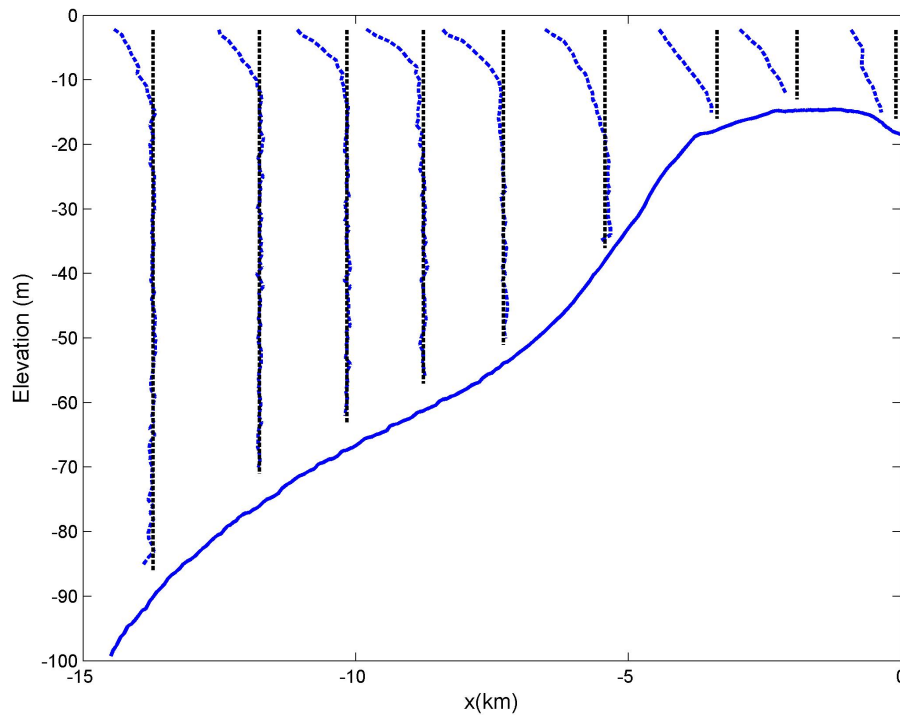


Figure 3.8: Measured cross-shore current speed profiles seaward from Columbia River mouth during an ebb tide (Kilcher and Nash, 2010). This data was taken from the R/V Pt. Sur, during the July 2004 RISE cruise (<http://makani.coas.oregonstate.edu/rise/>). The transect is one of the cruise routes by the R/V Pt. Sur. The ship moves seaward from the river mouth during an ebb tide. Therefore the current data have slight time difference. The horizontal axis represents the cross-shore distance seaward from the river mouth ($x = 0$ km). The vertical axis represents the vertical elevation. Blue Solid: ocean bottom elevation along the transect. Black Dash: zero current speed line at each cross-shore location. Blue Dash: measured current speed at each cross-shore location. The length of legend represents 2 m/s current speed. As the figure indicates, the maximum current speed exceeds 2 m/s at the river mouth where water depth is shallower. The current speed decrease seaward with increasing water depth.

To give a general idea of how strong the current is in the real world, we use the current velocity data measured at the mouth of Columbia River (MCR). The

Columbia River is on the U.S. west coast and well known for its huge freshwater discharge. Due to narrow outlet to the ocean, highly stratified density field and strong tidal currents in addition to river flow, the surface current in the tidal plume can exceed 3 m/s during strong ebb tides as shown in Figure 3.8 (Hickey *et al.*, 2010). It is an ideal estuary to study the current shear effects on wave dynamics. The current data used in the paper is from RISE (River Influences on Shelf Ecosystems) project measured by Ocean Mixing Group, Oregon State University (Kilcher and Nash, 2010). This data was taken from the R/V Pt. Sur, during the July 2004 RISE cruise (<http://makani.coas.oregonstate.edu/rise/>). The data set contains velocity with two direction components based on 30 second-average, water depth and location of sampling. Consider a group of waves with amplitude $a = 1$ m propagating shoreward on the opposing current at MCR. The wave number varies from $\mu = kh \sim 0.3$ to $\mu = kh \sim 3$, which covers both short waves and long waves. We take several current velocity profiles at the river mouth and fit 6th order polynomial curves to the data points.

The comparison results of measured current profiles are shown in Figure 3.9 (opposing current) and 3.10 (following current). The measured current velocity profiles have many zigzags, which require higher order polynomial fitting method to catch. However, higher order polynomial fitting makes the numerical solver unstable for some cases. The opposing Both opposing current and following current results suggest that the $O(\epsilon)$ perturbation solution is a significant improvement compared to depth-average current approximation, while the $O(\epsilon^2)$ perturbation solution does not contribute more than 5 % correction. Therefore, the $O(\epsilon)$ perturbation solution is a good approximation to Rayleigh equation in our problem. It is noteworthy that $F_{max} \sim 0.2$ for this case. We use the current profile in Figure 3.9 (Upper) to solve Rayleigh equation. The reason is that this shape of current velocity profile is very typical during strong ebb tides at river plume, where maximum current speed and strong vertical shear appearing near the surface.

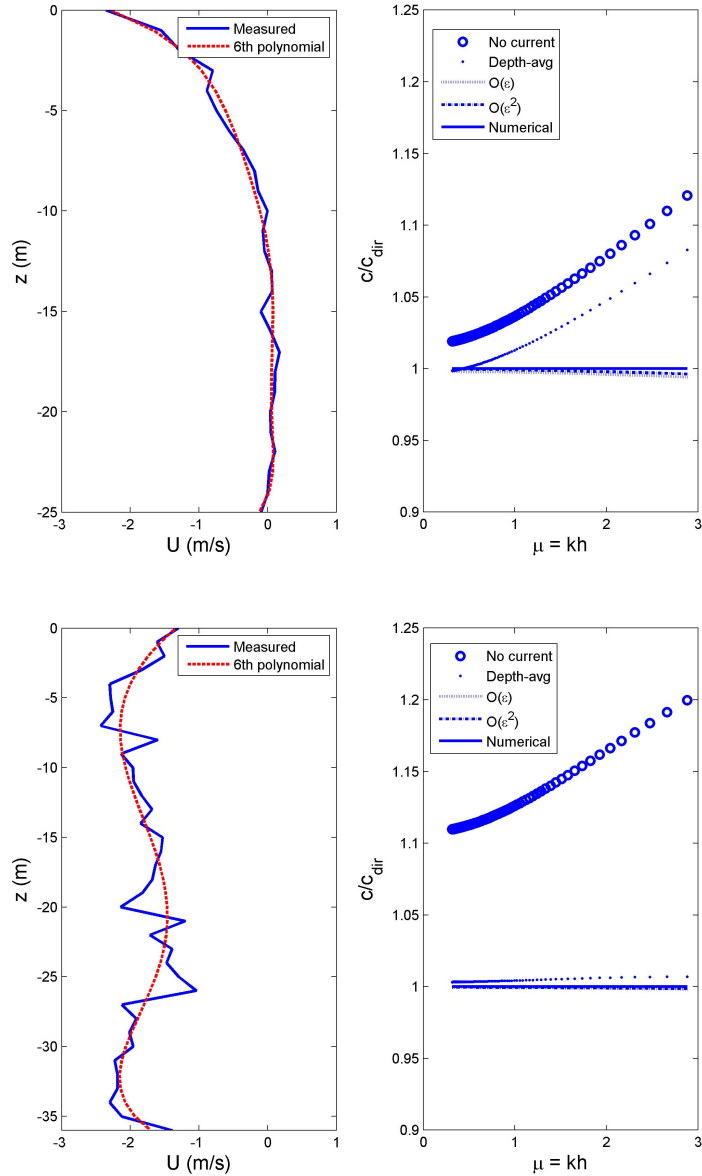


Figure 3.9: Wave phase speed comparison between perturbation solution up to $O(\epsilon^2)$ and numerical solution with measured current velocity profiles at Columbia river mouth - opposing currents. This data was taken from the R/V Pt. Sur, during the July 2004 RISE cruise (<http://makani.coas.oregonstate.edu/rise/>). The Upper Panel shows a typical current profile during ebb tide. The Lower Panel shows vertically well-mixed current profile during ebb tide. Both no-current assumption and depth-average current assumption cause wave phase speed to deviate from the exact solution. The deviation depends on both current magnitude and current shear. Strong current with strong shear causes larger deviation.

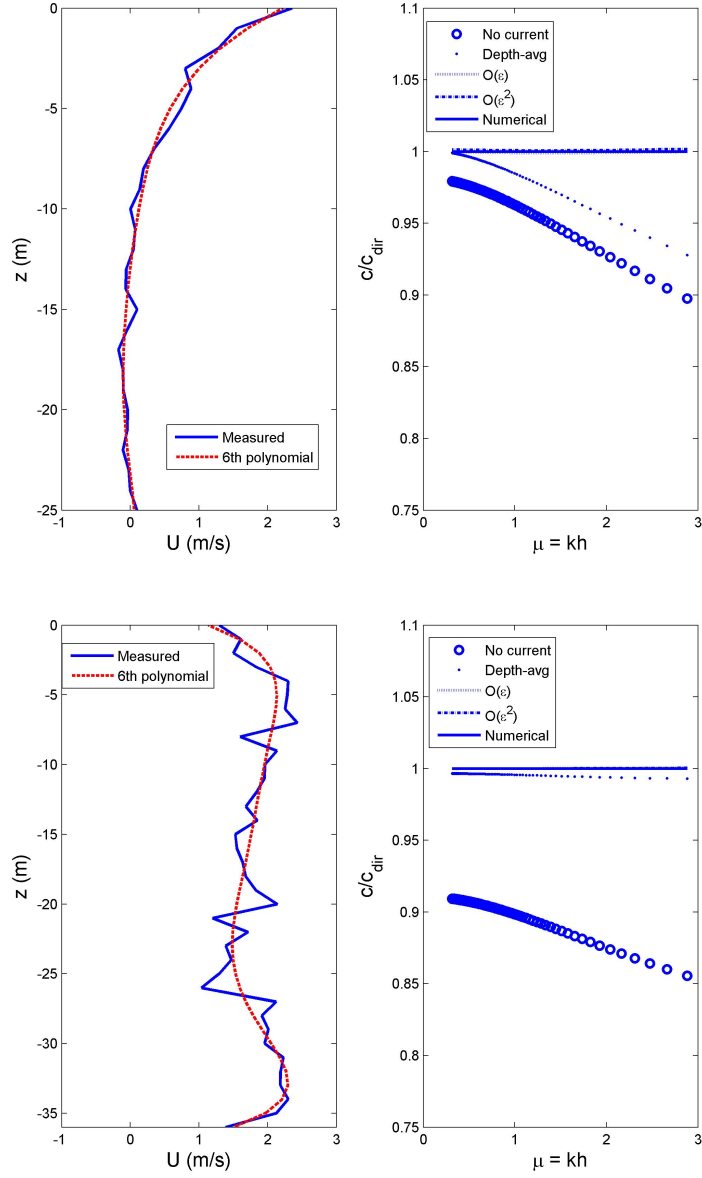


Figure 3.10: Wave phase speed comparison between perturbation solution up to $O(\epsilon^2)$ and numerical solution with measured current velocity profiles at Columbia river mouth - following currents. This data was taken from the R/V Pt. Sur, during the July 2004 RISE cruise (<http://makani.coas.oregonstate.edu/rise/>). The current profiles are exactly reversed from Figure 3.9 to provide waves solution when following current.

The current profiles from the upper left of Figure 3.9 and 3.10 are used to examine the current effect on wave vertical structures. The shape of current profile is very typical during the ebb tide or flood tide at the MCR. The current is assumed to be co-directional with waves. Thus, only one component of horizontal velocity is considered.

Figure 3.11 and 3.12 illustrates the vertical structure of wave orbital velocity and vorticity for the opposing current. Figure 3.13 and 3.14 illustrates the vertical structure of wave orbital velocity and vorticity for the following current. Results of short wave ($kh = 2$), intermediate wave ($kh = 1$) and long wave ($kh = 0.4$) are compared in the plots. The comparison suggests that short waves have larger vertical gradient in orbital velocities than long waves. In the presence of current shear, wave vertical structure is significantly modified. The current shear effect is confined in the upper layer for this case. The $O(\epsilon)$ perturbation solution successfully captures current shear effect on wave orbital velocity and vorticity compared to the numerical solution.

The wave orbital velocity amplitude is increased by the opposing current (see Figure 3.11) and decreased by the following current (see Figure 3.13). The comparison of wave vorticity (Figure 3.12 and 3.14) also indicates that when current is co-directional with waves, the wave vorticity is determined by current shear and not related to wave number.

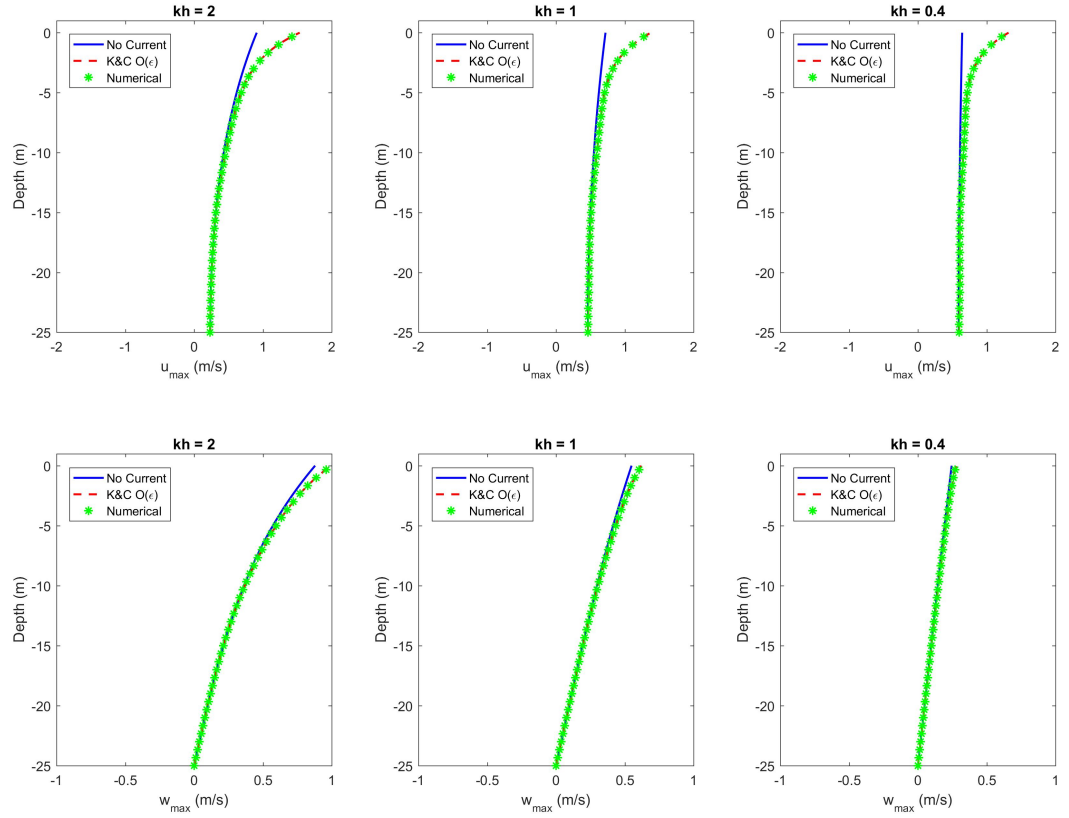


Figure 3.11: Comparison of wave orbital velocity amplitude vertical distribution for short wave ($kh = 2$), intermediate wave ($kh = 1$) and long wave ($kh = 0.4$) on the opposing current: (Upper) horizontal orbital velocity and (Lower) vertical orbital velocity amplitude. The current is assumed to be co-directional with waves. Therefore, only one horizontal direction is considered. The vertical axis represents water depth. The horizontal axis represents velocity. The comparison shows the wave orbital velocity amplitude is increased by the opposing current. K&C $O(\epsilon)$ solution is a fairly good approximation to numerical solution.

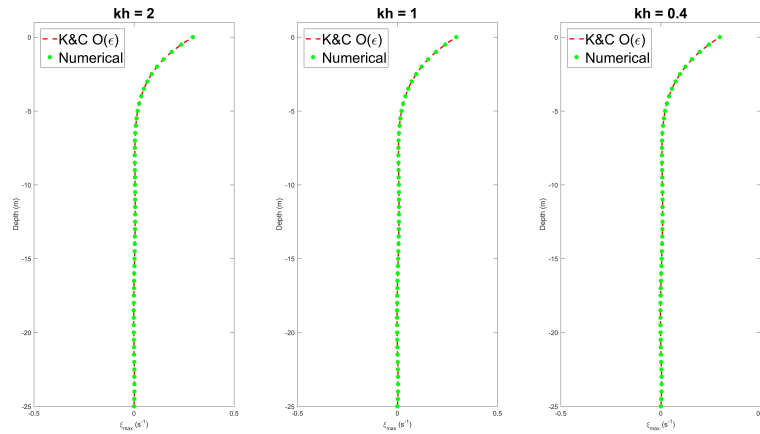


Figure 3.12: Comparison of wave vorticity amplitude vertical distribution for short wave ($kh = 2$), intermediate wave ($kh = 1$) and long wave ($kh = 0.4$) on the opposing current. The current is assumed to be co-directional with waves. Therefore, the wave vorticity is only in horizontal direction. In this case, the vorticity is only determined by the current profile and not related to the wave number. The values of wave vorticity are the same. The vertical axis represents water depth. The horizontal axis represents wave vorticity. The comparison shows that K&C $O(\epsilon)$ solution is a better approximation to numerical solution.

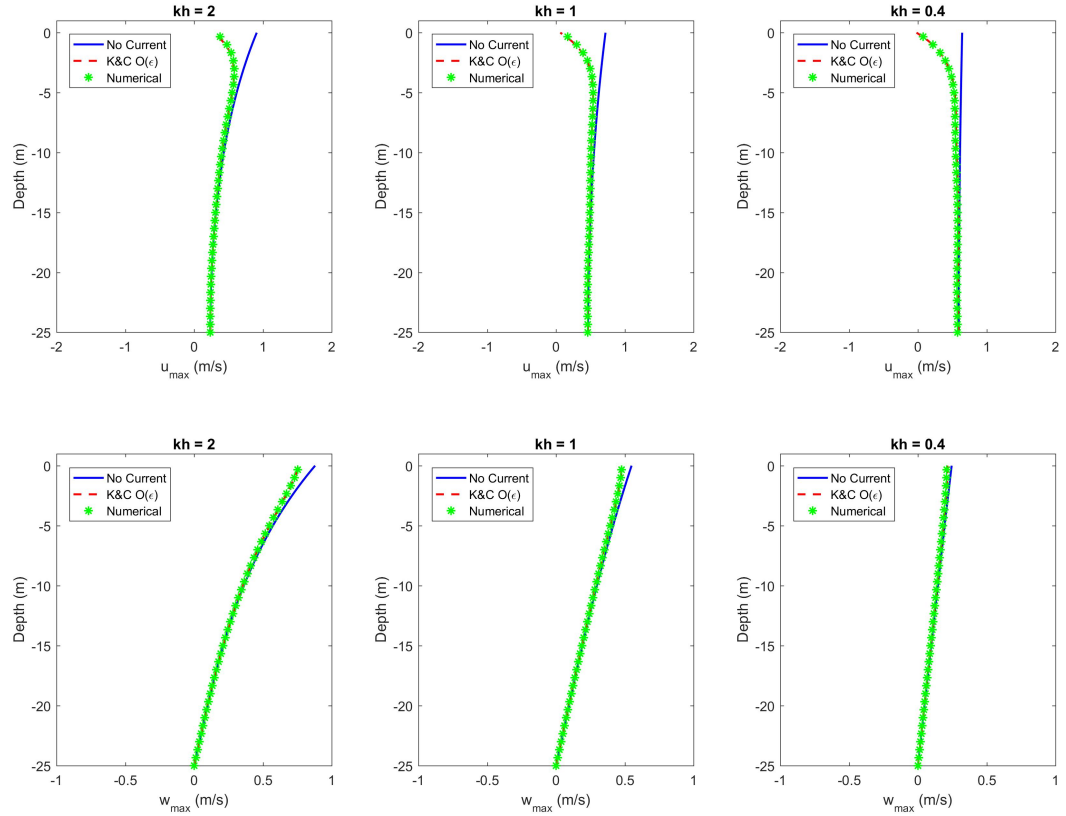


Figure 3.13: Comparison of wave orbital velocity amplitude vertical distribution for short wave ($kh = 2$), intermediate wave ($kh = 1$) and long wave ($kh = 0.4$) on the following current: (Upper) horizontal orbital velocity and (Lower) vertical orbital velocity amplitude. The current is assumed to be co-directional with waves. Therefore, only one horizontal direction is considered. The vertical axis represents water depth. The horizontal axis represents velocity. The comparison shows the wave orbital velocity amplitude is decreased by the following current. K&C $O(\epsilon)$ solution is a fairly good approximation to numerical solution.

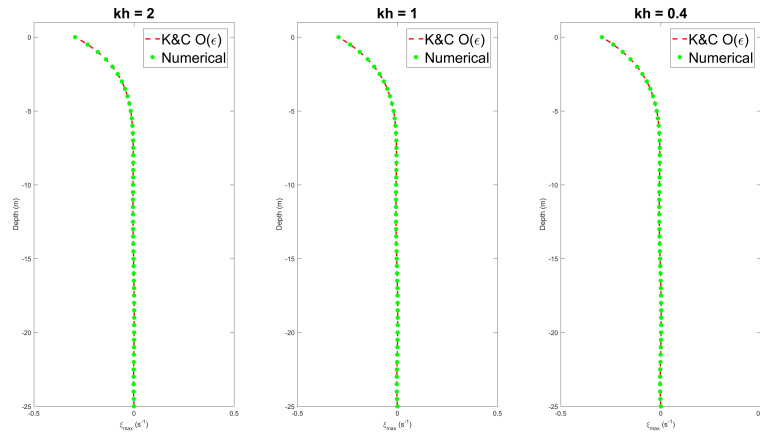


Figure 3.14: Comparison of wave vorticity amplitude vertical distribution for short wave ($kh = 2$), intermediate wave ($kh = 1$) and long wave ($kh = 0.4$) on the following current. The current is assumed to be co-directional with waves. Therefore, the wave vorticity is only in horizontal direction. In this case, the vorticity is only determined by the current profile and not related to the wave number. The values of wave vorticity are the same. The vertical axis represents water depth. The horizontal axis represents wave vorticity. The comparison shows that K&C $O(\epsilon)$ solution is a better approximation to numerical solution.

3.1.6 Depth-weighted current

The current in KC89 $O(\epsilon)$ perturbation solution is also known as depth-weighted current, which has been proved above as a good approximation to numerical solution in the last section. The advantage of using depth-weighted current velocity in wave equations is that it considers the wave vertical structure as well as the wave length. According to the classic wave theory, wave motions are confined near the water surface and decay exponentially with depth. Thus current profiles with velocity confined to the water surface have larger effects on waves than profiles with velocity confined to the bottom such as undertow, where nearly no wave motions exist. Additionally, the ratio of current velocity to wave phase speed U/c indicates current effect on waves. Larger ratio suggests stronger current effect. Long waves have larger wave phase speed than short waves. Thus, long waves get less current effect than short waves.

In this part, we consider analytical current profile with an exponential shape $U(z) = e^{-z}$ as shown in Figure 3.15. The current velocity starts with 1 m/s at the surface and decays exponentially to 0 m/s at the bottom. The depth-average value of the current profile is rather small because of the rapid decrease of velocity over depth. However, the depth-weighted current is very different. For long waves, wave phase speed is relatively large. Depth-weighted current is closer to the depth-averaged current. As waves become shorter, the current effect is increasing and depth-weighted current is closer to the maximum velocity at the surface. Different current profile shapes result in different depth-weighted current value. By using the depth-weighted current, we can evaluate the effect of different current profiles on waves.

3.2 Second-order Wave Motions

To get wave-averaged forces, we need wave solutions up to $O(\epsilon^2)$. Therefore the second order wave equations are necessary in our problem, which are given by terms in the $(n = 2, m = 1)$

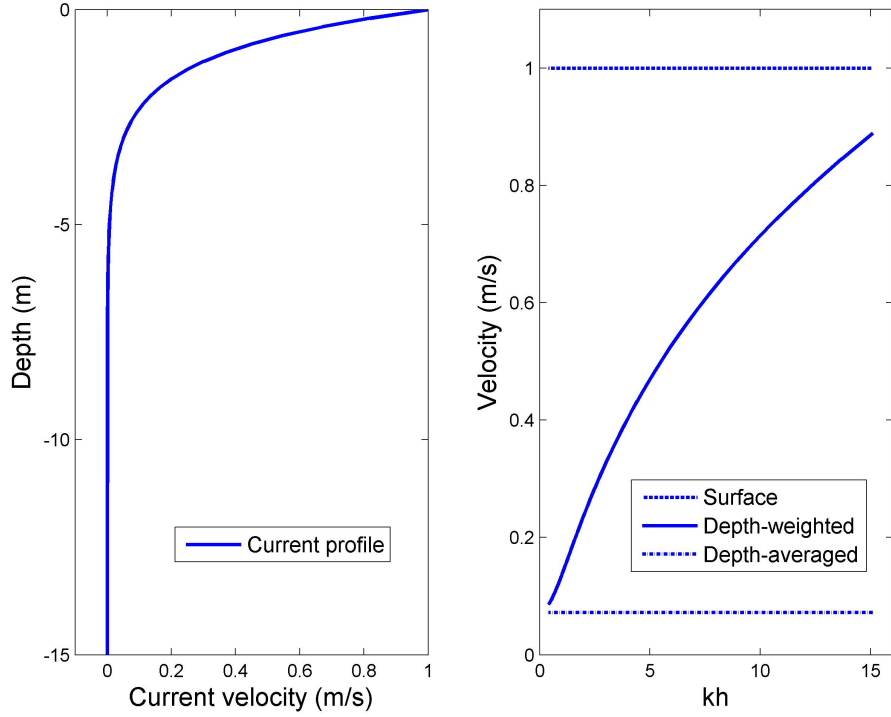


Figure 3.15: Depth-weighted current velocity for exponential current profile. Consider the current speed is 1.0 m/s at the water surface and decreases exponentially to zero over depth. The depth-averaged current speed for this current profile is less than 0.1 m/s. If depth-averaged current is used in wave solution, the current effect is negligible. However, the depth-weighted current is very different and varies for different wave numbers. The equivalent current speed is larger for larger wave number.

$$\begin{aligned}
\frac{\partial \mathbf{q}_{0,0}}{\partial z} w_{2,1} - i\sigma_w \mathbf{q}_{2,1} + \frac{i\mathbf{k}}{\rho} p_{2,1} = & -\left[\frac{\partial \mathbf{q}_{1,1}}{\partial T} + \mathbf{q}_{0,0} \cdot \nabla_H \mathbf{q}_{1,1} + \frac{1}{\rho} \nabla_H p_{1,1} + i(\mathbf{q}_{1,0} \cdot \mathbf{k}) \mathbf{q}_{1,1} \right. \\
& \left. + \mathbf{q}_{1,1} \cdot \nabla_H \mathbf{q}_{0,0} + w_{1,0} \frac{\partial \mathbf{q}_{1,1}}{\partial z} + w_{1,1} \frac{\partial \mathbf{q}_{1,0}}{\partial z} \right]; \quad -h \leq z \leq \eta^c
\end{aligned} \tag{3.74}$$

$$\begin{aligned}
-i\sigma_w w_{2,1} + \frac{1}{\rho} \frac{\partial p_{2,1}}{\partial z} = & -\left[\frac{\partial w_{1,1}}{\partial T} + \mathbf{q}_{0,0} \cdot \nabla_H w_{1,1} + i(\mathbf{q}_{1,0} \cdot \mathbf{k}) w_{1,1} + \frac{\partial(w_{1,0} w_{1,1})}{\partial z} \right]; \\
& -h \leq z \leq \eta^c
\end{aligned} \tag{3.75}$$

$$\frac{\partial w_{2,1}}{\partial z} + i\mathbf{k} \cdot \mathbf{q}_{2,1} = -\nabla_H \cdot \mathbf{q}_{1,1}; \quad -h \leq z \leq \eta^c \tag{3.76}$$

$$w_{2,1} = -\mathbf{q}_{1,1} \cdot \nabla_H h; \quad z = -h \quad (3.77)$$

$$w_{2,1} = \frac{\partial \eta_{1,1}}{\partial T} + \mathbf{q}_{0,0} \cdot \nabla_H \eta_{1,1} - i\sigma_s \eta_{2,1} + \mathbf{q}_{1,0} \cdot (i\mathbf{k}) \eta_{1,1} \\ - \eta_{1,1} \frac{\partial w_{1,0}}{\partial z} + (\mathbf{q}_{1,1} + \eta_{1,1} \frac{\partial \mathbf{q}_{0,0}}{\partial z}) \cdot \nabla_H \eta_{0,0}; \quad z = \eta^c \quad (3.78)$$

$$p_{2,1} = -(\eta_{2,1} \frac{\partial p_{0,0}}{\partial z} + \eta_{1,1} \frac{\partial p_{1,0}}{\partial z}); \quad z = \eta^c \quad (3.79)$$

The variations of leading order mean surface elevation $\eta_{0,0}$ no longer appear in wave surface boundary condition (3.78) after switching reference level. In the next chapter, ($n = 2, m = 0$) mean flow dynamics indicate that $\mathbf{q}_{1,0}$ and $p_{1,0}$ only yield trivial solutions based on strong current assumption. The related terms are deleted in the equations. We rearrange the wave equations in the same way as $O(\epsilon)$ wave equations to get $O(\epsilon^2)$ Rayleigh equation for $O(\epsilon^2)$ wave vertical orbital velocity amplitude $w_{2,1}$ with boundary conditions.

$$\sigma_w \frac{\partial^2 w_{2,1}}{\partial z^2} - (\frac{\partial^2 \sigma_w}{\partial z^2} + k^2 \sigma_w) w_{2,1} = C_{2,1}; \quad -h \leq z \leq \eta^c \quad (3.80)$$

$$\sigma_s^2 \frac{\partial w_{2,1}}{\partial z} - (\sigma_s \frac{\partial \sigma_w}{\partial z} + gk^2) w_{2,1} = D_{2,1}; \quad z = \eta^c \quad (3.81)$$

$$w_{2,1} = E_{2,1}; \quad z = -h \quad (3.82)$$

where

$$C_{2,1} = -\left\{ \frac{\partial^2 \mathbf{q}_{1,1}}{\partial T \partial z} \cdot \mathbf{k} + \frac{\partial}{\partial z} (\mathbf{q}_{0,0} \cdot \nabla_H \mathbf{q}_{1,1}) \cdot \mathbf{k} + \frac{\partial}{\partial z} (\sigma_w \nabla_H \cdot \mathbf{q}_{1,1}) \right. \\ \left. + \frac{\partial}{\partial z} (\mathbf{q}_{1,1} \cdot \nabla_H \mathbf{q}_{0,0}) \cdot \mathbf{k} + \frac{\partial}{\partial z} (w_{1,0} \frac{\partial \mathbf{q}_{1,1}}{\partial z}) \cdot \mathbf{k} + \frac{1}{\rho} \mathbf{k} \cdot \nabla_H \frac{\partial p_{1,1}}{\partial z} \right. \\ \left. - ik^2 \left[\frac{\partial w_{1,1}}{\partial T} + \mathbf{q}_{0,0} \cdot \nabla_H w_{1,1} + \frac{\partial}{\partial z} (w_{1,0} w_{1,1}) \right] \right\} \quad (3.83)$$

$$D_{2,1} = -\left\{ gk^2 \left[\frac{\partial \eta_{1,1}}{\partial T} + \mathbf{q}_{0,0} \cdot \nabla_H \eta_{1,1} - \eta_{1,1} \frac{\partial w_{1,0}}{\partial z} + (\mathbf{q}_{1,1} + \eta_{1,1} \frac{\partial \mathbf{q}_{0,0}}{\partial z}) \cdot \nabla_H \eta_{0,0} \right] \right. \\ \left. + \sigma_s \left[\frac{\partial \mathbf{q}_{1,1}}{\partial T} \cdot \mathbf{k} + (\mathbf{q}_{0,0} \cdot \nabla_H \mathbf{q}_{1,1}) \cdot \mathbf{k} + \sigma_w \nabla_H \cdot \mathbf{q}_{1,1} + (\mathbf{q}_{1,1} \cdot \nabla_H \mathbf{q}_{0,0}) \cdot \mathbf{k} \right. \right. \\ \left. \left. + w_{1,0} \frac{\partial \mathbf{q}_{1,1}}{\partial z} \cdot \mathbf{k} + \frac{1}{\rho} \mathbf{k} \cdot \nabla_H p_{1,1} \right] \right\} \quad (3.84)$$

$$E_{2,1} = -\mathbf{q}_{1,1} \cdot \nabla_H h \quad (3.85)$$

The equations are identical to the results in Voronovich (1976). The remaining variables $p_{2,1}$, $\mathbf{q}_{2,1}$ and $\eta_{2,1}$ are written in terms of $w_{2,1}$ and slow scale derivatives of $\mathbf{q}_{1,1}$, $w_{1,1}$, $p_{1,1}$ and $\eta_{1,1}$. These variables can be calculated once we get the solution for $w_{2,1}$.

$$p_{2,1} = \frac{i\rho}{k^2} \left[\mathbf{k} \cdot \left(\frac{\partial \mathbf{q}_{1,1}}{\partial T} + \mathbf{q}_{0,0} \cdot \nabla_H \mathbf{q}_{1,1} + \frac{1}{\rho} \nabla_H p_{1,1} + \mathbf{q}_{1,1} \cdot \nabla_H \mathbf{q}_{0,0} + w_{1,0} \frac{\partial \mathbf{q}_{11}}{\partial z} \right) + \sigma_w \left(\frac{\partial w_{2,1}}{\partial z} + \nabla_H \cdot \mathbf{q}_{1,1} \right) - \frac{\partial \sigma_w}{\partial z} w_{2,1} \right] \quad (3.86)$$

$$\mathbf{q}_{2,1} = -\frac{i}{\sigma_w} \left[\frac{\partial \mathbf{q}_{0,0}}{\partial z} w_{2,1} + \frac{i\mathbf{k}}{\rho} p_{2,1} + \left(\frac{\partial \mathbf{q}_{1,1}}{\partial T} + \mathbf{q}_{0,0} \cdot \nabla_H \mathbf{q}_{1,1} + \frac{1}{\rho} \nabla_H p_{1,1} + \mathbf{q}_{1,1} \cdot \nabla_H \mathbf{q}_{0,0} + w_{1,0} \frac{\partial \mathbf{q}_{1,1}}{\partial z} \right) \right] \quad (3.87)$$

$$\eta_{2,1} = \frac{i}{\sigma_s} \left[w_{2,1} - \left(\frac{\partial \eta_{1,1}}{\partial T} + \mathbf{q}_{0,0} \cdot \nabla_H \eta_{1,1} - \eta_{1,1} \frac{\partial w_{1,0}}{\partial z} + (\mathbf{q}_{1,1} + \eta_{1,1} \frac{\partial \mathbf{q}_{0,0}}{\partial z}) \cdot \nabla_H \eta_{0,0} \right) \right] \quad (3.88)$$

3.2.1 Compatibility condition and wave action equation

For the $O(\epsilon^2)$ wave equations to have non-trivial solutions, the compatibility condition has to be satisfied. This condition then leads to the wave action equation. We introduce variables \hat{f} in the Rayleigh equations.

$$\hat{f}_1 = \frac{w_{1,1}}{\sigma_w} \quad (3.89)$$

$$\hat{f}_2 = \frac{w_{2,1}}{\sigma_w} \quad (3.90)$$

The Rayleigh equation becomes

$$\frac{\partial}{\partial z} \left(\sigma_w^2 \frac{\partial \hat{f}_n}{\partial z} \right) - \sigma_w^2 k^2 \hat{f}_n = C_{n,1}; \quad n = 1, 2 \quad (3.91)$$

$$\sigma_w \left(\sigma_w^2 \frac{\partial \hat{f}_n}{\partial z} - gk^2 \hat{f}_n \right) = D_{n,1} \quad (3.92)$$

$$\sigma_w \hat{f}_n = E_{n,1} \quad (3.93)$$

The compatibility condition from Fredholm Alternative Theorem gives

$$\int_{-h}^{\eta^c} \hat{f}_1 C_{2,1} dz - \frac{\hat{f}_1(\eta^c)}{\sigma_s} D_{2,1} - \sigma_w(-h) \frac{\partial \hat{f}_1}{\partial z}(-h) E_{2,1} = 0 \quad (3.94)$$

It provides the basis for the construction of an action balance equation for slowly varying waves. The unwieldy manipulation of solvability condition yields the conservation of wave action in strongly sheared flow, identical with Voronovich's (1976) results.

$$\frac{\partial N}{\partial T} + \nabla_{H^*} \cdot (\mathbf{c}_{\mathbf{ga}} N) = 0 \quad (3.95)$$

$$N = - \int_{-h}^{\eta^c} \frac{1}{\sigma_w^2 k^2} \frac{\partial^2 \sigma_w}{\partial z^2} |w_{1,1}|^2 dz + \left(\frac{2g}{\sigma_w^3} + \frac{1}{\sigma_w^2 k^2} \frac{\partial \sigma_w}{\partial z} \right) |w_{1,1}|^2 \Big|_{z=\eta^c} \quad (3.96)$$

$$\begin{aligned} \mathbf{c}_{\mathbf{ga}} N &= \int_{-h}^{\eta^c} \left(-\frac{\mathbf{q}_{0,0}}{\sigma_w^2 k^2} \frac{\partial^2 \sigma_w}{\partial z^2} + \frac{1}{\sigma_w k^2} \frac{\partial^2 \mathbf{q}_{0,0}}{\partial z^2} - \frac{2\mathbf{k}}{k^2} \right) |w_{1,1}|^2 dz \\ &+ [\mathbf{q}_{0,0} \left(\frac{2g}{\sigma_w^3} + \frac{1}{\sigma_w^2 k^2} \frac{\partial \sigma_w}{\partial z} \right) - \frac{1}{\sigma_w k^2} \frac{\partial \mathbf{q}_{0,0}}{\partial z} + \frac{2g\mathbf{k}}{\sigma_w^2 k^2}] |w_{1,1}|^2 \Big|_{z=\eta^c} \end{aligned} \quad (3.97)$$

where $w_{1,1}$ is the solution from Rayleigh equation, $|w_{1,1}|^2 = w_{1,1} w_{1,-1}$. N is the wave action. $\mathbf{c}_{\mathbf{ga}} N$ is the wave action flux in the conserved form. The equation is for strong current with arbitrary vertical shape and can be simplified to compare with several special current profiles. The wave action isn't clear in the form of wave energy divided by frequency. However, it can regain this form for some special cases (McWilliams *et al.*, 2004; Jonsson *et al.*, 1978), which are discussed later in this section. The absolute group velocity $\mathbf{c}_{\mathbf{ga}}$ can be obtained from wave action flux divided by wave action $\mathbf{c}_{\mathbf{ga}} N/N$. The absolute group velocity can also be obtained from the dispersion relation by numerical solution. It is shown that the two forms of absolute group velocities converge based on the numerical wave solution (see Figure 3.16 and 3.17).

3.2.2 Wave action equation for depth-uniform current

For depth-uniform strong current, we can get the linear wave solutions. Thus the wave action equations (3.95) - (3.97) can be easily simplified to get the traditional form of the wave action equation as described by Bretherton and Garrett (1968).

$$\frac{\partial}{\partial T} \left(\frac{2|\eta_{1,1}|^2}{\sigma_w} \right) + \nabla_{H^*} \cdot \left[\frac{2(\mathbf{c}_{\mathbf{gr}} + \mathbf{q}_{0,0})|\eta_{1,1}|^2}{\sigma_w} \right] = 0 \quad (3.98)$$

Where $\eta_{1,1}$ and $\eta_{1,-1}$ are wave amplitude complex conjugate and $a^2/4 = |\eta_{1,1}|^2$, so that total wave energy can be expressed as $E = \rho g a^2/2$. The wave action is given as

$$\frac{\partial}{\partial T} \left(\frac{E}{\sigma_w} \right) + \nabla_{H^*} \cdot \left[(\mathbf{c}_{\mathbf{gr}} + \mathbf{q}_{0,0}) \frac{E}{\sigma_w} \right] = 0 \quad (3.99)$$

where the relative group velocity is

$$\mathbf{c}_{\text{gr}} = \frac{\partial \sigma_w}{\partial \mathbf{k}} = \frac{1}{2} \left(1 + \frac{2kH}{\sinh 2kH} \right) \mathbf{c}_r \quad (3.100)$$

$$c_r = \frac{\sigma_w}{k} \quad (3.101)$$

3.2.3 Wave action equation for constant shear current

Jonsson *et al.* (1978) give the wave action conservation for 2D vertical current with constant shear. We use wave solutions for linearly sheared current in Appendix A.3. Note that the real value of wave amplitude $a^2/4 = |\eta_{1,1}|^2$ and considering the complex conjugate relations, Equation (3.96) and (3.97) are reduced to

$$\frac{N}{\rho} = \frac{1}{4} [2g - (\hat{\mathbf{k}} \cdot \boldsymbol{\Omega}^s) c_r] \frac{a^2}{\sigma_s} \quad (3.102)$$

$$\frac{\mathbf{c}_{\text{ga}} N}{\rho} = [\mathbf{c}_{\text{gr}} + \mathbf{q}_{0,0s} + \frac{(\hat{\mathbf{k}} \cdot \boldsymbol{\Omega}^s) c_r c_r - \boldsymbol{\Omega}^s c_r^2}{2g - (\hat{\mathbf{k}} \cdot \boldsymbol{\Omega}^s) c_r}] N \quad (3.103)$$

where $c_r = \sigma_s/k$ and $c_{gr} = \partial \sigma_s / \partial k$. According to Equation (34) and (35) in Jonsson *et al.* (1978), the wave action can be rewritten in the form of wave energy density $E/\bar{\sigma}_w$, where wave energy

$$\frac{E}{\rho} = \frac{[2g - (\hat{\mathbf{k}} \cdot \boldsymbol{\Omega}^s) c_r] a^2 \bar{\sigma}_w}{4 \sigma_s} \quad (3.104)$$

and the relative frequency based on depth-averaged current $\bar{\sigma}_w = \omega - \mathbf{k} \cdot \bar{\mathbf{q}}_{0,0}$. The advection velocity in the wave action equation can be identified as

$$\mathbf{c}_{\text{ga}} = \mathbf{c}_{\text{gr}} + \mathbf{q}_{0,0s} + \frac{\hat{\mathbf{k}}(\hat{\mathbf{k}} \cdot \boldsymbol{\Omega}^s) - \boldsymbol{\Omega}^s}{2g - (\hat{\mathbf{k}} \cdot \boldsymbol{\Omega}^s) c_r} c_r^2 \quad (3.105)$$

The last term accounts for the effect when there is an angle between the wave direction and the current shear. If the current shear and wave are co-directional, this term disappears. For the 2D vertical case, the wave action conservation equation converges to Jonsson *et al.*'s (1978) results.

3.2.4 Wave action equation for weak shear current

To compare with MRL04 wave action equation, we need to assume weak current. Then the linear waves no longer feel current effects at the leading order. The

governing equation is reduced to Laplace's equation. We have the current-free linear wave solutions as (A.1) - (A.3). The second order wave equations are reduced into

$$\frac{\partial^2 w_{2,1}}{\partial z^2} - k^2 w_{2,1} = \frac{C_{2,1}}{\omega}; \quad -h \leq z \leq \eta^c \quad (3.106)$$

$$\frac{\partial w_{2,1}}{\partial z} - \frac{gk^2}{\omega} w_{2,1} = \frac{D_{2,1}}{\omega^2}; \quad z = \eta^c \quad (3.107)$$

$$w_{2,1} = E_{2,1}; \quad z = -h \quad (3.108)$$

with

$$\begin{aligned} C_{2,1} = & -\left\{ \frac{\partial^2 \mathbf{q}_{1,1}}{\partial T \partial z} \cdot \mathbf{k} + \omega \nabla_H \cdot \frac{\partial \mathbf{q}_{1,1}}{\partial z} + \frac{1}{\rho} \mathbf{k} \cdot \nabla_H \frac{\partial p_{1,1}}{\partial z} \right. \\ & + i \frac{\partial}{\partial z} [(\mathbf{q}_{0,0} \cdot \mathbf{k})(\mathbf{q}_{1,1} \cdot \mathbf{k})] + \frac{\partial}{\partial z} (w_{1,1} \frac{\partial \mathbf{q}_{0,0}}{\partial z} \cdot \mathbf{k}) \\ & \left. - ik^2 \left[\frac{\partial w_{1,1}}{\partial T} + i(\mathbf{q}_{0,0} \cdot \mathbf{k}) w_{1,1} + \frac{\partial}{\partial z} (w_{1,0} w_{1,1}) \right] \right\} \end{aligned} \quad (3.109)$$

$$\begin{aligned} D_{21} = & -\left\{ gk^2 \left[\frac{\partial \eta_{1,1}}{\partial T} + i(\mathbf{q}_{0,0} \cdot \mathbf{k}) \eta_{1,1} \right] + \omega \left[\frac{\partial \mathbf{q}_{1,1}}{\partial T} \cdot \mathbf{k} + \omega \nabla_H \cdot \mathbf{q}_{1,1} \right. \right. \\ & \left. \left. + i(\mathbf{q}_{0,0} \cdot \mathbf{k})(\mathbf{q}_{1,1} \cdot \mathbf{k}) + w_{11} \frac{\partial \mathbf{q}_{0,0}}{\partial z} \cdot \mathbf{k} + \frac{1}{\rho} \nabla_H p_{1,1} \cdot \mathbf{k} \right] \right\} \end{aligned} \quad (3.110)$$

$$E_{21} = -\mathbf{q}_{1,1} \cdot \nabla_H h \quad (3.111)$$

Current related terms appear in the second order wave dynamics according to weak current assumption. According to wave ray theory for pure waves, we have

$$\frac{\partial \mathbf{k}}{\partial T} + \mathbf{c}_g \cdot \nabla_H \mathbf{k} + \frac{\omega k}{\sinh 2kH} \nabla_H h = 0 \quad (3.112)$$

$$\frac{\partial \omega}{\partial T} + \mathbf{c}_g \cdot \nabla_H \omega = 0 \quad (3.113)$$

The resulting compatibility condition yields the slow dynamics of complex wave amplitude $\eta_{1,1}$, which is analogous to (5.35) in MRL04.

$$\frac{\partial \eta_{1,1}}{\partial T} + \mathbf{c}_g \cdot \nabla_H \eta_{1,1} + \frac{\eta_{1,1}}{2} \nabla_H \cdot \mathbf{c}_g + i \eta_{1,1} \frac{2k}{\sinh 2kH} \int_{-h}^{\eta^c} \mathbf{k} \cdot \mathbf{q}_{0,0}(\zeta) \cosh 2k(h + \zeta) d\zeta = 0 \quad (3.114)$$

Due to the scaling of our problem, the cubic nonlinear term is left in $O(\epsilon^3)$. The mean water surface contribution does not appear in the equation since we incorporate mean

surface elevation η^c into actual water depth. The equation can be further separated into wave action ($N = E/\omega$) conservation equation and amplitude slow phase dynamics by assuming $\eta_{1,1} = |A|e^{i\Theta}/2$.

$$\frac{\partial N}{\partial T} + \nabla_H \cdot (\mathbf{c}_g N) = 0 \quad (3.115)$$

$$\frac{\partial \Theta}{\partial T} + \mathbf{c}_g \cdot \nabla_H \Theta + \frac{2k}{\sinh 2kH} \int_{-h}^{\eta^c} \mathbf{k} \cdot \mathbf{q}_{0,0}(\zeta) \cosh 2k(h + \zeta) d\zeta = 0 \quad (3.116)$$

In summary, we reproduce MRL04 wave action equation and wave amplitude phase evolution.

3.2.5 Numerical study of wave action equation

Once we have obtained the wave action conservation equation for waves on strongly sheared current, there are several choices for numerical application in wave models in terms of different current assumptions including depth-averaged current, depth-weighted current KC89 $O(\epsilon)$ and $O(\epsilon^2)$ approximation and the Rayleigh numerical solution. Undoubtedly, the numerical Rayleigh solution will yield the exact wave action and flux. It also requires more computational time. We have to decide the best choice to be implemented in wave models. We have compared wave solutions in the previous section. As long as wave solutions are known, it is also easy to compare the wave action equation. In this section, we compare wave action, action flux and absolute group speed in wave action equation based on different wave solutions. We use the constant shear current profile as shown in the lower panel of Figure 3.5. The water depth is assumed to be $h = 25$ m. The surface current velocity is 3.5 m/s. The bottom current velocity is 0 m/s. We consider waves over both opposing current and following current. We also allow the wave number to vary from deep water to shallow water conditions ($0.3 \leq kh \leq 3$).

3.2.5.1 Group velocity from wave action equation and dispersion relation

There are two ways to get the absolute group velocity in the Rayleigh equations. One is obtained by taking the derivative with k of dispersion relation ($\partial\omega/\partial k$). The

other one is obtained by wave action equation ($c_{ga}N/N$). In this case, the absolute group velocity can be easily calculated based on the wave action and wave action flux as shown in Equation (3.95) - (3.97). Now we examine these two absolute group velocities. Both absolute group velocities are based on numerical solutions. Therefore, the group velocity ($c_{ga}N/N$) depends on sizes of vertical resolution (dz). The group velocity ($\partial\omega/\partial k$) depends on sizes of vertical resolution (dz) as well as wave number resolution (dk).

We use the 2D constant shear current to calculate these two group velocity estimates. The current velocity profile is shown in the lower panel of Figure 3.5. We consider both opposing current and following current with the same shape. The analytical wave group velocity is given by

$$c_{ga} = c_{gr} + q_{0,0}^s \quad (3.117)$$

$$c_{gr} = \frac{g(1+G) - \Omega^s G c_r}{2g - \Omega^s c_r} c_r \quad (3.118)$$

The lower panel of Figure 3.4 already shows the convergence of wave phase speed for smaller vertical step (dz). Figure 3.16 and 3.17 show the convergence of these two group velocities with different wave number steps (dk) for opposing current and following current, respectively. The results indicate that

1). As dk becomes smaller, both dispersion relation and wave action group velocities converge to the analytical group velocity.

2). Both numerical group velocities gradually deviate from analytical solution as kh increases.

3). The following current case gives better numerical approximation to analytical solutions.

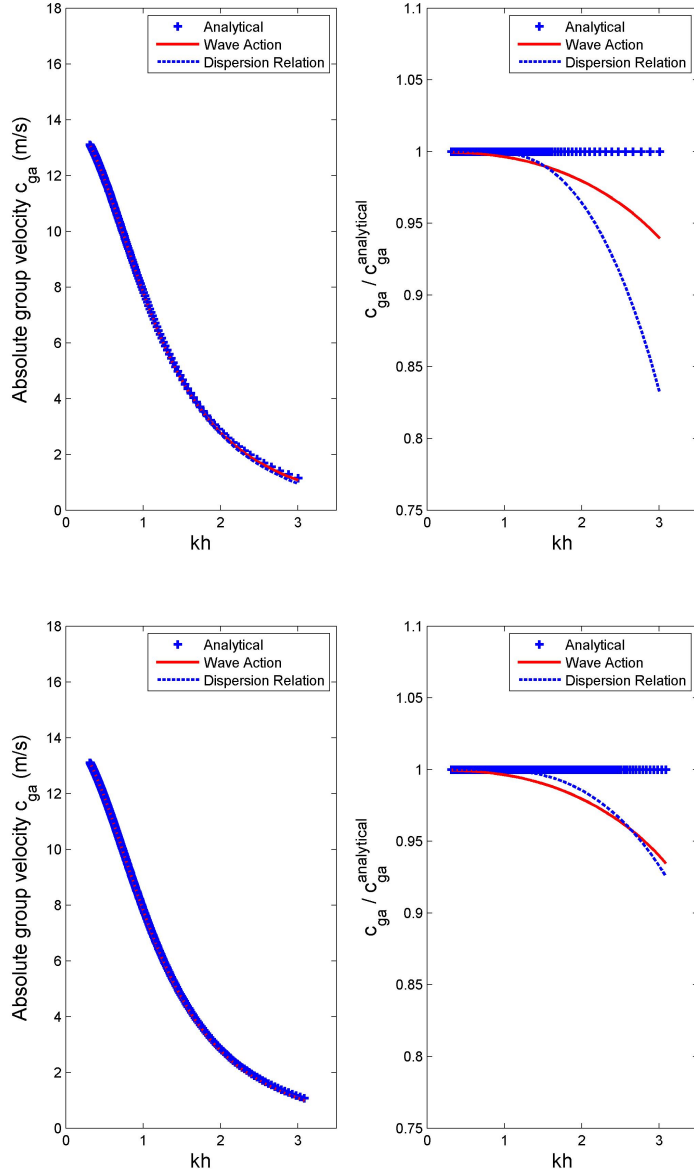


Figure 3.16: (Opposing constant shear current) Convergence of group speed ($\partial\omega/\partial k$) and the group speed ($c_{ga}N/N$) (3.96) and (3.97) with different wave number steps (dk). Blue '+': Analytical absolute group velocity; Red Solid: Absolute group velocity from wave action equation; Blue Dash: Absolute group velocity from dispersion relation. Upper Panel: $dk = 0.014$, Lower Panel: $dk = 0.005$. The figure indicates that the group velocity ($\partial\omega/\partial k$) converges to the group velocity ($c_{ga}N/N$) as dk becomes smaller. Both numerical group velocities gradually deviate from analytical solution as kh increases (shorter waves). The difference between numerical group velocities and analytical group velocity is within 7 %.

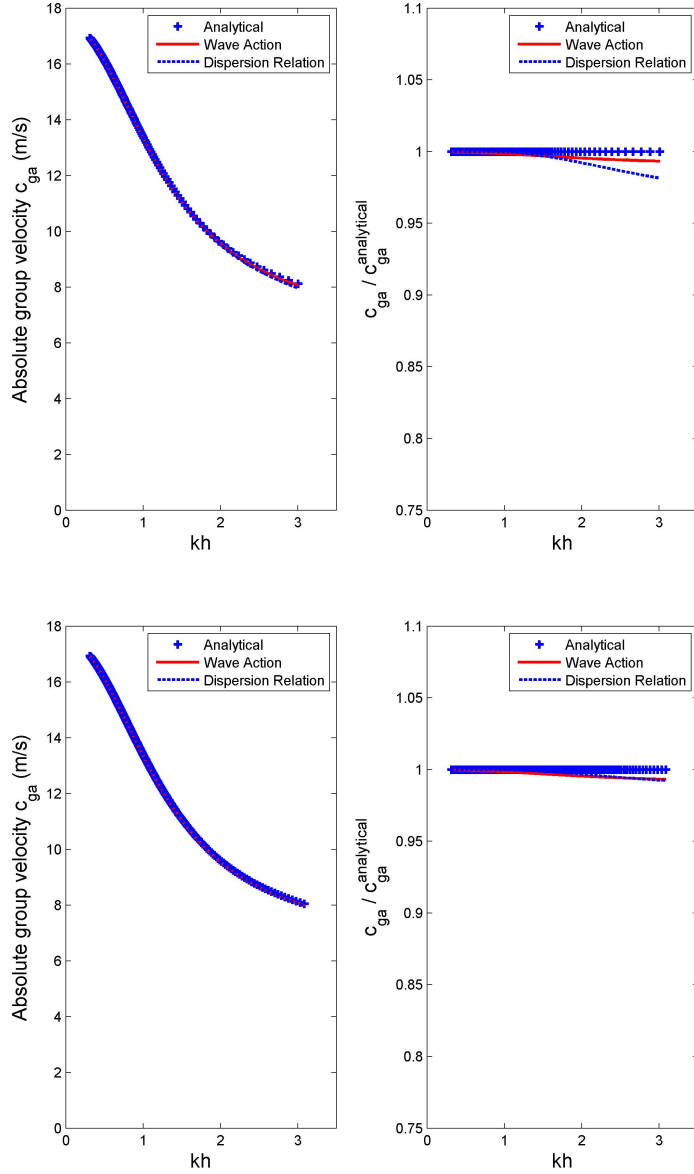


Figure 3.17: (Following constant shear current) Convergence of group speed ($\partial\omega/\partial k$) and the group speed ($c_{ga}N/N$) (3.96) and (3.97) with different wave number steps (dk). Blue '+': Analytical absolute group velocity; Red Solid: Absolute group velocity from wave action equation; Blue Dash: Absolute group velocity from dispersion relation. Upper Panel: $dk = 0.014$, Lower Panel: $dk = 0.005$. The figure indicates that the group velocity ($\partial\omega/\partial k$) converges to the group velocity ($c_{ga}N/N$) as dk becomes smaller. Both numerical group velocities gradually deviate from analytical solution as kh increases (shorter waves). The difference between numerical group velocities and analytical group velocity is within 3 %.

3.2.5.2 Wave action and action flux comparison

The wave action and action flux are also calculated for the 2D constant shear currents. The analytical expressions for wave action and action flux are given in Equation (3.102) and (3.103). We compare the analytical values with four solutions: numerical solution, depth-averaged current, depth-weighted current. In wave models, the depth-averaged current velocity is usually used as an approximation in the wave action flux (Bretherton and Garrett, 1968). Another assumption is the depth-weighted current provided by Kirby and Chen (1989). In contrast to depth-averaged current, the depth-weighted current $\tilde{U}(k)$ is a depth uniform current, which varies with wave number. Thus, the absolute group velocity has an extra term $\partial\tilde{U}/\partial k$ as shown below. This term can be very significant; see, for example, results shown in Banihashemi *et al.* (2016).

$$\omega = \tilde{\sigma} + k\tilde{U} \quad (3.119)$$

$$c_{ga} = \frac{\partial\omega}{\partial k} = \frac{\partial\tilde{\sigma}}{\partial k} + \tilde{U} + k\frac{\partial\tilde{U}}{\partial k} \quad (3.120)$$

The depth-weighted current used in the comparison is actually $\tilde{U} + k\partial\tilde{U}/\partial k$. The comparison results are given in Figure 3.18 and 3.19 for opposing current and following current, respectively.

1). For both directions, the wave action difference between the analytical value and the other solutions are less than 2 %.

2). The wave action flux is decreased by the opposing current and increased by following current.

3). The wave action flux comparison indicates that the four solutions have less accuracy on the opposing current. And the errors grow with non-dimensional wave number kh . The error growth for depth-averaged current is the fastest.

4). Depth-weighted current is a fairly good approximation compared to numerical solution.

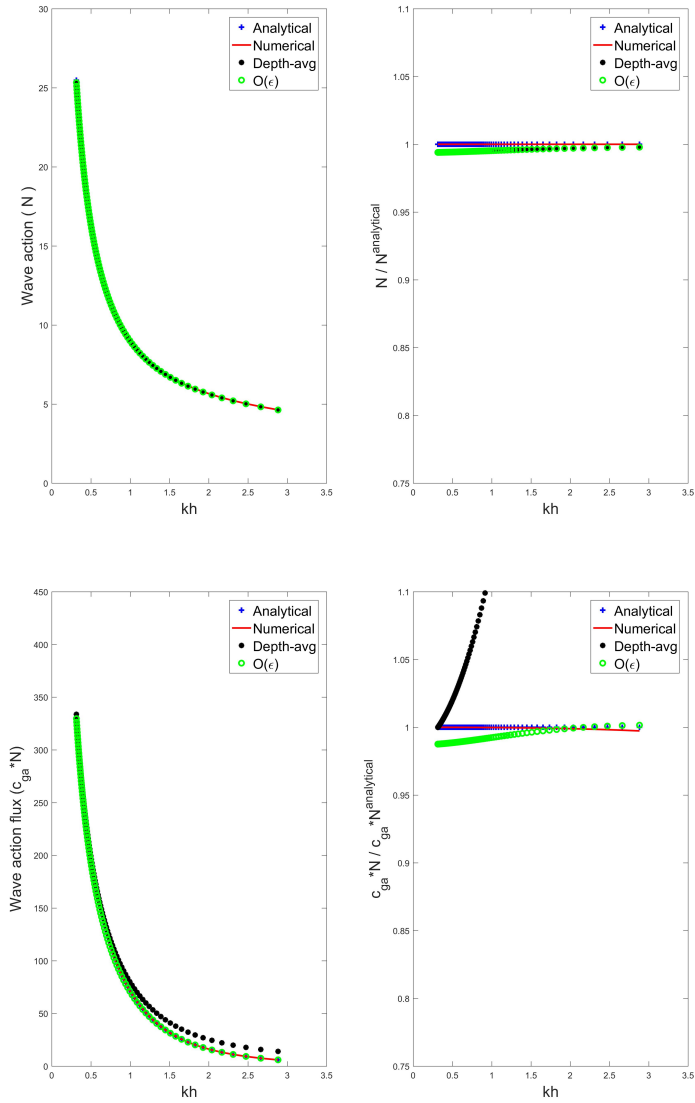


Figure 3.18: (Opposing constant shear current) Wave action and wave action flux comparison. Blue '+': Analytical results; Red Solid: Numerical results; Black '*': Results based on depth-averaged current; Green 'o': Results based on depth-weighted current. The dimensional wave action and action flux are calculated using wave amplitude $a = 1$ m. Upper Panel: Wave action on the left and non-dimensional wave action on the right. The wave action comparison suggests that the differences between analytical value and these assumptions are less than 2 %. Lower Panel: Wave action flux on the left and non-dimensional wave action flux on the right.

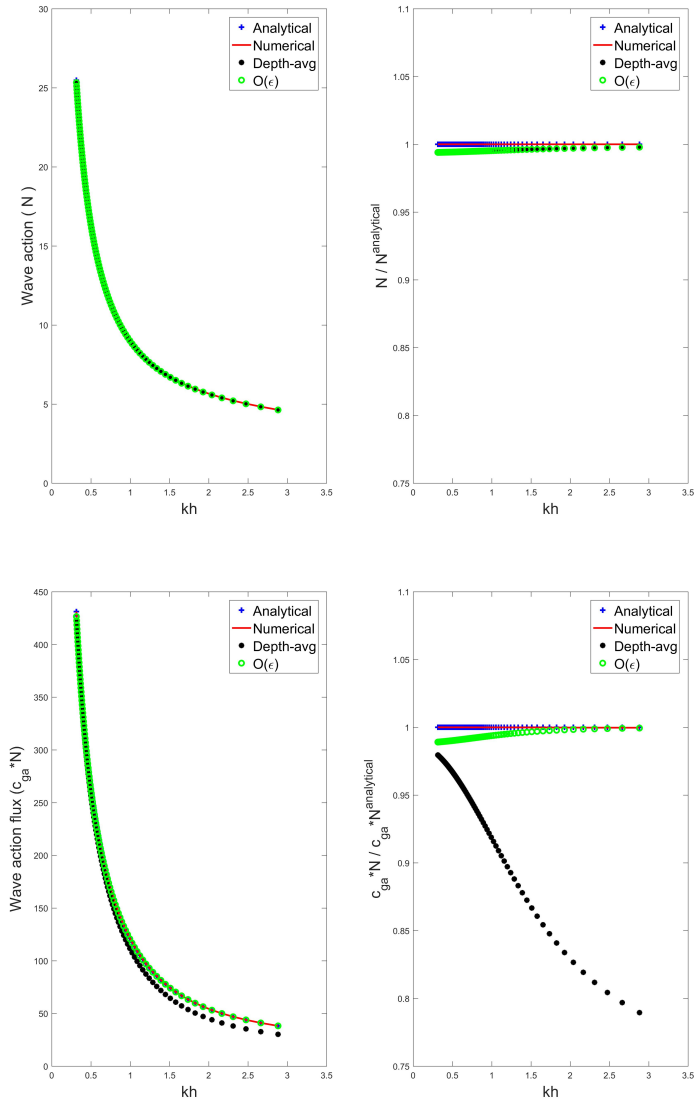


Figure 3.19: (Following constant shear current) Wave action and wave action flux comparison. Blue '+': Analytical results; Red Solid: Numerical results; Black '*': Results based on depth-averaged current; Green 'o': Results based on depth-weighted current. The dimensional wave action and action flux are calculated using wave amplitude $a = 1$ m. Upper Panel: Wave action on the left and non-dimensional wave action on the right. The wave action comparison suggests that the differences between analytical value and these assumptions are less than 2 %. Lower Panel: Wave action flux on the left and non-dimensional wave action flux on the right.

3.2.5.3 Absolute group velocity comparison

Now we compare the absolute group velocity in the wave action equation obtained based on different current assumptions. We also use the 2D constant shear current profiles. We compare numerical solution, depth-averaged current solution and depth-weighted current solution for opposing current and following current, respectively. The comparison results are given in Figure 3.20 and 3.21. The patterns of the group velocity plots are very similar to the wave action flux.

1). The absolute group velocity is decreased by opposing current and increased by following current.

2). The four solutions have less accuracy on the opposing current. And the errors grow with non-dimensional wave number kh . The error growth for depth-averaged current is the fastest.

3). Depth-weighted current is a fairly good approximation compared to numerical solution.

In the COAWST model and Delft3D model, the depth-weighted current \tilde{U} is adopted as an alternative for depth-averaged current (Kumar *et al.*, 2011; Kumar *et al.*, 2012; Van der Westhuysen *et al.*, 2007). However, the depth-weighted current is calculated with a fixed wave number, which usually corresponds to the peak frequency of the wave spectrum. It is also assumed to be the same at all frequencies in SWAN. As discussed above, the depth-weighted current is a function of wave number, $\tilde{U} = \tilde{U}(k)$. Therefore an additional term $k\partial\tilde{U}/\partial k$ will appear in absolute group speed. The dependence on k is neglected in the present implementation of ROMS and Delft3D. Now we evaluate the difference with and without this term. In Figure 3.20 and 3.21, we plot the depth-weighted current including the term $k\partial\tilde{U}/\partial k$. And the approximation of the depth-weighted current to the analytical solution is fairly good. In Figure 3.22 and 3.23, we keep the depth-averaged current as a reference and compare the depth-weighted current with and without the term $k\partial\tilde{U}/\partial k$. Figures for both opposing current and following current indicate that the term $k\partial\tilde{U}/\partial k$ is a significant correction to the absolute group speed.

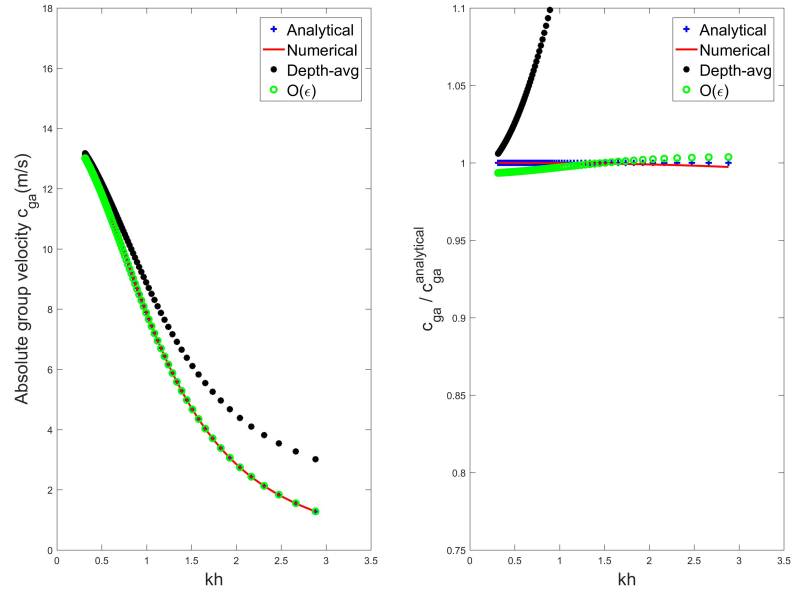


Figure 3.20: (Opposing constant shear current) Comparison of absolute group velocities. Blue '+': Analytical results; Red Solid: Numerical results; Black '*': Results based on depth-averaged current; Green 'o': Results based on depth-weighted current. The dimensional group velocity is given at the Left Panel. The non-dimensional group velocity based on analytical solution is given at the Right Panel. The four solutions deviate from analytical solution as kh increases.

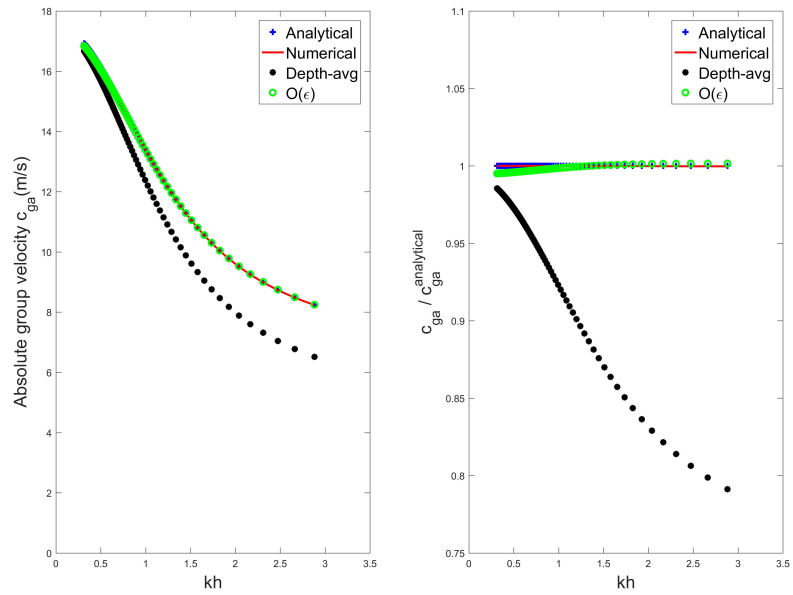


Figure 3.21: (Following constant shear current) Comparison of absolute group velocities. Blue '+': Analytical results; Red Solid: Numerical results; Black '*': Results based on depth-averaged current; Green 'o': Results based on depth-weighted current. The dimensional group velocity is given at the Left Panel. The non-dimensional group velocity based on analytical solution is given at the Right Panel.

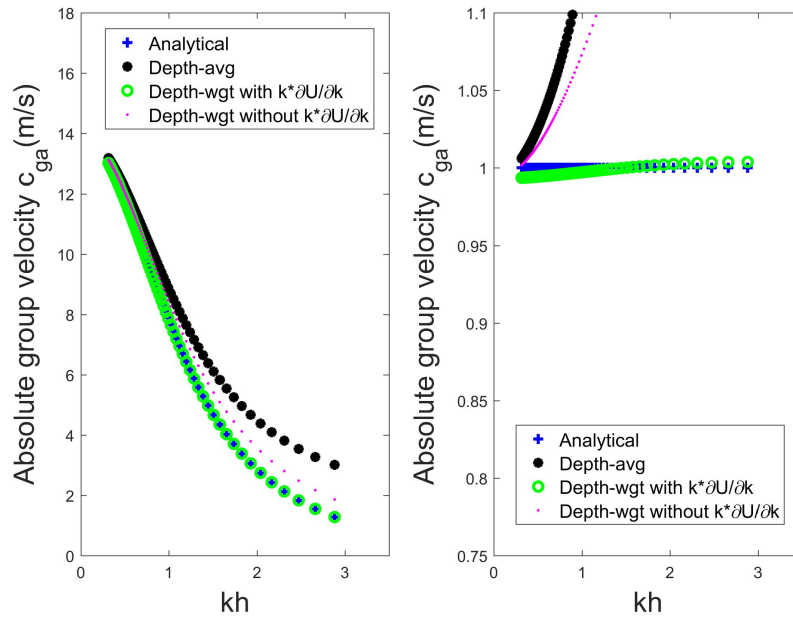


Figure 3.22: (Opposing constant shear current) Comparison of absolute group velocity for depth-weighted current with and without $k \partial \tilde{U} / \partial k$. (Left Panel) Absolute group velocity. (Right Panel) Non-dimensional absolute group velocity based on analytical solutions. Figure indicates that there is bigger errors for by neglecting this term.

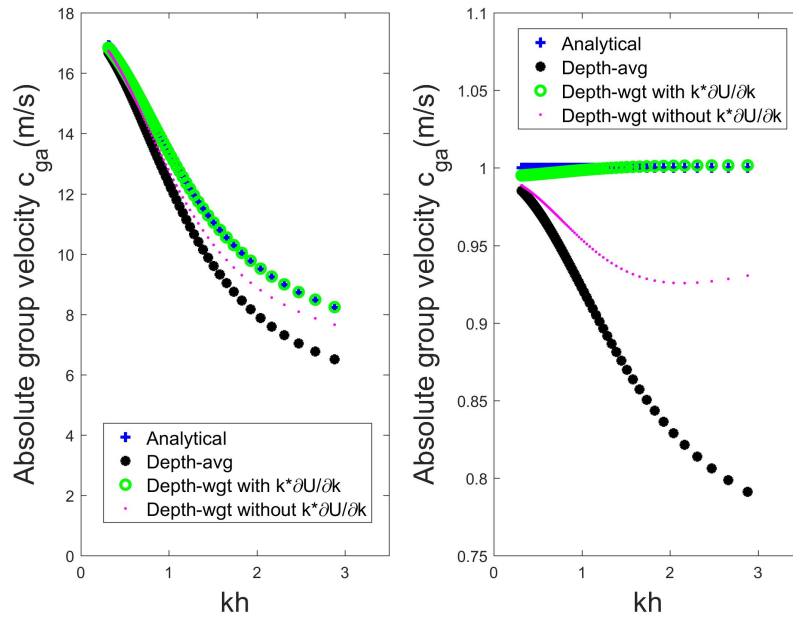


Figure 3.23: (Following constant shear current) Comparison of absolute group velocity for depth-weighted current with and without $k\partial\tilde{U}/\partial k$. (Left Panel) Absolute group velocity. (Right Panel) Non-dimensional absolute group velocity based on analytical solutions. Figure indicates that there is bigger errors for by neglecting this term.

3.2.6 Second order wave vorticity

The second order wave vorticity is given by ($n = 2, m = 1$) vorticity equation expansion. At this order, wave vorticity is induced by the slow scale variations of $O(\epsilon)$ waves and $O(\epsilon^0)$ currents.

$$\chi_{2,1} = -i \frac{P_{2,1}}{\sigma_w} - \frac{(\boldsymbol{\xi}_{0,0} \cdot \mathbf{k}) w_{2,1}}{\sigma_w} \quad (3.121)$$

$$\begin{aligned} \boldsymbol{\xi}_{2,1} = & -i \left[\frac{\mathcal{O}_{2,1}}{\sigma_w} + i \frac{\partial \mathbf{q}_{0,0}}{\partial z} \frac{P_{2,1}}{\sigma_w^2} + \frac{\partial \mathbf{q}_{0,0}}{\partial z} \frac{w_{2,1} (\boldsymbol{\xi}_{0,0} \cdot \mathbf{k})}{\sigma_w^2} + \frac{\partial \boldsymbol{\xi}_{0,0}}{\partial z} \frac{w_{2,1}}{\sigma_w} \right] \\ & - \frac{(\boldsymbol{\xi}_{0,0} \cdot \mathbf{k}) \mathbf{q}_{2,1}}{\sigma_w} \end{aligned} \quad (3.122)$$

$$\begin{aligned} \mathcal{O}_{2,1} = & \frac{\partial \boldsymbol{\xi}_{1,1}}{\partial T} + (\mathbf{q}_{0,0} \cdot \nabla_H) \boldsymbol{\xi}_{1,1} + (\mathbf{q}_{1,1} \cdot \nabla_H) \boldsymbol{\xi}_{0,0} - (\boldsymbol{\xi}_{0,0} \cdot \nabla_H) \mathbf{q}_{1,1} - (\boldsymbol{\xi}_{1,1} \cdot \nabla_H) \mathbf{q}_{0,0} \\ & - \chi_{1,0} \frac{\partial \mathbf{q}_{1,1}}{\partial z} + w_{1,0} \frac{\partial \boldsymbol{\xi}_{1,1}}{\partial z} \end{aligned} \quad (3.123)$$

$$\begin{aligned} P_{2,1} = & \frac{\partial \chi_{1,1}}{\partial T} + (\mathbf{q}_{0,0} \cdot \nabla_H) \chi_{1,1} - (\boldsymbol{\xi}_{0,0} \cdot \nabla_H) w_{1,1} \\ & + w_{1,1} \frac{\partial \chi_{1,0}}{\partial z} + w_{1,0} \frac{\partial \chi_{1,1}}{\partial z} - \chi_{1,0} \frac{\partial w_{1,1}}{\partial z} - \chi_{1,1} \frac{\partial w_{1,0}}{\partial z} \end{aligned} \quad (3.124)$$

The non-divergence of wave vorticity at this order yields

$$\nabla_H \cdot \boldsymbol{\xi}_{1,1} + i \mathbf{k} \cdot \boldsymbol{\xi}_{2,1} + \frac{\partial \chi_{2,1}}{\partial z} = 0 \quad (3.125)$$

which is also used in mean flow equations.

3.2.7 Perturbation solution to the second order wave Rayleigh equation

Now we apply perturbation method to $O(\epsilon^2)$ wave Rayleigh equation. The $O(\epsilon^0)$ perturbation expansion gives:

$$k c_0 \left(\frac{\partial^2 w_{2,1}^{(0)}}{\partial z^2} - k^2 w_{2,1}^{(0)} \right) = C_{2,1}^{(0)}; \quad -h \leq z \leq \eta^c \quad (3.126)$$

$$c_0^2 \frac{\partial w_{2,1}^{(0)}}{\partial z} - g w_{2,1}^{(0)} = D_{2,1}^{(0)}; \quad z = \eta^c \quad (3.127)$$

$$w_{2,1}^{(0)} = E_{2,1}^{(0)}; \quad z = -h \quad (3.128)$$

where

$$C_{2,1}^{(0)} = -\left[\frac{\partial^2 \mathbf{q}_{1,1}^{w(0)}}{\partial T \partial z} \cdot \mathbf{k} + kc_0 \nabla_H \cdot \frac{\partial \mathbf{q}_{1,1}^{w(0)}}{\partial z} + \frac{1}{\rho} \mathbf{k} \cdot \nabla_H \frac{\partial p_{1,1}^{w(0)}}{\partial z} - ik^2 \frac{\partial w_{1,1}^{w(0)}}{\partial T}\right] \quad (3.129)$$

$$D_{2,1}^{(0)} = -\left\{gk^2 \frac{\partial \eta_{1,1}}{\partial T} + kc_0 \left[\frac{\partial \mathbf{q}_{1,1}^{w(0)}}{\partial T} \cdot \mathbf{k} + kc_0 \nabla_H \cdot \mathbf{q}_{1,1}^{w(0)} + \frac{1}{\rho} \nabla_H p_{1,1}^{w(0)} \cdot \mathbf{k}\right]\right\} \quad (3.130)$$

$$E_{2,1}^{(0)} = -\mathbf{q}_{1,1}^{w(0)} \cdot \nabla_H h \quad (3.131)$$

$w_{1,1}^{w(0)}$, $\mathbf{q}_{1,1}^{w(0)}$ and $p_{1,1}^{w(0)}$ are $O(\epsilon^0)$ perturbation solution to the $O(\epsilon)$ wave equations, which exclude current related terms.

$$w_{1,1}^{w(0)}(z) = -ikc_0 \eta_{1,1} F_{ss} \quad (3.132)$$

$$\mathbf{q}_{1,1}^{w(0)}(z) = kc_0 \eta_{1,1} F_{cs} \frac{\mathbf{k}}{k} \quad (3.133)$$

$$p_{1,1}^{w(0)}(z) = \frac{\rho (kc_0)^2 \eta_{1,1}}{k} F_{cs} \quad (3.134)$$

$$F_{ss} = \frac{\sinh k(h+z)}{\sinh kH} \quad (3.135)$$

$$F_{cs} = \frac{\cosh k(h+z)}{\sinh kH} \quad (3.136)$$

The $O(\epsilon^0)$ perturbation solution for $O(\epsilon^2)$ wave Rayleigh equation is given by

$$\begin{aligned} w_{2,1}^{(0)}(z) = & -\frac{g\eta_{1,1}}{kc_0 \cosh kH} (\mathbf{k} \cdot \nabla_H H) \cosh k(h+z) \\ & -\frac{g\eta_{1,1}}{kc_0 \cosh kH} (\mathbf{k} \cdot \nabla_H H) [k(h+z)] \sinh k(h+z) \\ & -g \left[\frac{\eta_{1,1}}{2k^2 c_0 \cosh kH} (\nabla_H \cdot \mathbf{k}) + \frac{\mathbf{k}}{k} \cdot \nabla_H \left(\frac{\eta_{1,1}}{kc_0 \cosh kH} \right) + \frac{\eta_{1,1}}{2k^3 c_0 \cosh kH} (\mathbf{k} \cdot \nabla_H k) \right] \\ & \cdot [k(h+z)] \cosh k(h+z) \\ & -\frac{g\eta_{1,1}}{2k^3 c_0 \cosh kH} (\mathbf{k} \cdot \nabla_H k) [k(h+z)]^2 \sinh k(h+z) \end{aligned} \quad (3.137)$$

Thomas *et al.* (2012) give the second order wave solution for constant shear current. The solutions are very similar to our perturbation results here. The contributions to the second order wave solution $w_{2,1}$ can be divided into three parts. The first part is the spacial variation in bathymetry, or $\nabla_H H$ related terms. It can be removed by assuming flat bottom. The second part is the spacial variation in wave number and frequency, which is $\nabla_H k$, $\nabla_H \sigma_w$ related terms. The third part is the spacial variations

of $O(\epsilon)$ wave amplitude, which is $\nabla_H \eta_{1,1}$ related terms. It is apparent that the second part contribution is far less than the third part.

The other $O(\epsilon^2)$ wave variables can be written in terms of $w_{2,1}^{(0)}$.

$$\begin{aligned}
p_{2,1}^{(0)} &= \frac{i\rho}{k^2} \left[\mathbf{k} \cdot \left(\frac{\partial \mathbf{q}_{1,1}^{(0)}}{\partial T} + \mathbf{q}_{0,0} \cdot \nabla_H \mathbf{q}_{1,1}^{(0)} + \frac{1}{\rho} \nabla_H p_{1,1}^{(0)} + \mathbf{q}_{1,1}^{(0)} \cdot \nabla_H \mathbf{q}_{0,0} + w_{1,0} \frac{\partial \mathbf{q}_{1,1}^{(0)}}{\partial z} \right) \right. \\
&\quad \left. + \sigma_w \left(\frac{\partial w_{2,1}^{(0)}}{\partial z} + \nabla_H \cdot \mathbf{q}_{1,1}^{(0)} \right) - \frac{\partial \sigma_w}{\partial z} w_{2,1}^{(0)} \right] \tag{3.138}
\end{aligned}$$

$$\begin{aligned}
\mathbf{q}_{2,1}^{(0)} &= -\frac{i}{\sigma_w} \left[\frac{\partial \mathbf{q}_{0,0}}{\partial z} w_{2,1}^{(0)} + \frac{i\mathbf{k}}{\rho} p_{2,1}^{(0)} \right. \\
&\quad \left. + \left(\frac{\partial \mathbf{q}_{1,1}^{(0)}}{\partial T} + \mathbf{q}_{0,0} \cdot \nabla_H \mathbf{q}_{1,1}^{(0)} + \frac{1}{\rho} \nabla_H p_{1,1}^{(0)} + \mathbf{q}_{1,1}^{(0)} \cdot \nabla_H \mathbf{q}_{0,0} + w_{1,0} \frac{\partial \mathbf{q}_{1,1}^{(0)}}{\partial z} \right) \right] \tag{3.139}
\end{aligned}$$

$$\begin{aligned}
\eta_{2,1}^{(0)} &= \frac{i}{\sigma_s} \left[w_{2,1}^{(0)} - \left(\frac{\partial \eta_{1,1}}{\partial T} + \mathbf{q}_{0,0} \cdot \nabla_H \eta_{1,1} - \eta_{1,1} \frac{\partial w_{1,0}}{\partial z} \right) \right. \\
&\quad \left. + \left(\mathbf{q}_{1,1}^{(0)} + \eta_{1,1} \frac{\partial \mathbf{q}_{0,0}}{\partial z} \right) \cdot \nabla_H \eta_{0,0} \right] \tag{3.140}
\end{aligned}$$

Wave-averaged forces beyond $O(\epsilon^4)$ does not contribute much to our problem. Therefore we only keep $w_{2,1}^{(0)}$, $\mathbf{q}_{2,1}^{(0)}$, $p_{2,1}^{(0)}$, $\eta_{2,1}^{(0)}$, $\chi_{2,1}^{(0)}$, $\boldsymbol{\xi}_{2,1}^{(0)}$, $\mathcal{O}_{2,1}^{(0)}$, $P_{2,1}^{(0)}$ solutions. Meanwhile, $O(\epsilon^2)$ vorticity perturbation solutions obtained in Chapter 2 are rewritten as below.

$$\chi_{2,1}^{(0)} = -i \frac{P_{2,1}^{(0)}}{\sigma_w} - \frac{(\boldsymbol{\xi}_{0,0} \cdot \mathbf{k}) w_{2,1}^{(0)}}{\sigma_w} \tag{3.141}$$

$$\begin{aligned}
\boldsymbol{\xi}_{2,1}^{(0)} &= -i \left[\frac{\mathcal{O}_{2,1}^{(0)}}{\sigma_w} + i \frac{\partial \mathbf{q}_{0,0}}{\partial z} \frac{P_{2,1}^{(0)}}{\sigma_w^2} + \frac{\partial \mathbf{q}_{0,0}}{\partial z} \frac{w_{2,1}^{(0)} (\boldsymbol{\xi}_{0,0} \cdot \mathbf{k})}{\sigma_w^2} + \frac{\partial \boldsymbol{\xi}_{0,0}}{\partial z} \frac{w_{2,1}^{(0)}}{\sigma_w} \right] \\
&\quad - \frac{(\boldsymbol{\xi}_{0,0} \cdot \mathbf{k}) \mathbf{q}_{2,1}^{(0)}}{\sigma_w} \tag{3.142}
\end{aligned}$$

$$\begin{aligned}
\mathcal{O}_{2,1}^{(0)} &= \frac{\partial \boldsymbol{\xi}_{1,1}^{(0)}}{\partial T} + (\mathbf{q}_{0,0} \cdot \nabla_H) \boldsymbol{\xi}_{1,1}^{(0)} + (\mathbf{q}_{1,1}^{(0)} \cdot \nabla_H) \boldsymbol{\xi}_{0,0} - (\boldsymbol{\xi}_{0,0} \cdot \nabla_H) \mathbf{q}_{1,1}^{(0)} - (\boldsymbol{\xi}_{1,1}^{(0)} \cdot \nabla_H) \mathbf{q}_{0,0} \\
&\quad - \chi_{1,0} \frac{\partial \mathbf{q}_{1,1}^{(0)}}{\partial z} + w_{1,0} \frac{\partial \boldsymbol{\xi}_{1,1}^{(0)}}{\partial z} \tag{3.143}
\end{aligned}$$

$$\begin{aligned}
P_{2,1}^{(0)} &= \frac{\partial \chi_{1,1}^{(0)}}{\partial T} + (\mathbf{q}_{0,0} \cdot \nabla_H) \chi_{1,1}^{(0)} - (\boldsymbol{\xi}_{0,0} \cdot \nabla_H) w_{1,1}^{(0)} \\
&\quad + w_{1,1}^{(0)} \frac{\partial \chi_{1,0}}{\partial z} + w_{1,0} \frac{\partial \chi_{1,1}^{(0)}}{\partial z} - \chi_{1,0} \frac{\partial w_{1,1}^{(0)}}{\partial z} - \chi_{1,1}^{(0)} \frac{\partial w_{1,0}}{\partial z} \tag{3.144}
\end{aligned}$$

Chapter 4

MEAN FLOW DYNAMICS

In this chapter, we present wave-averaged momentum equations, continuity equations, boundary conditions and vorticity equations up to $O(\epsilon^3)$. Wave-averaged forces in the momentum equations are identified in terms of the vortex force formalism including the vortex force and the gradient of the Bernoulli head. Wave-averaged terms also appear in the continuity equation and surface boundary conditions due to Stokes drift. The depth-dependent, wave-averaged forces are discussed using the perturbation solution, and compared with MRL04 formula. Finally, the depth-integrated momentum equations are compared with results from Smith (2006).

4.1 Mean Flow Momentum

First, we look at wave-averaged momentum equations in the multiple scale expansion from Chapter 2. At leading order, the mean flow equations at $(n = 0, m = 0)$ are given by

$$w_{0,0} \frac{\partial \mathbf{q}_{0,0}}{\partial z} = 0; \quad -h \leq z \leq \eta^c \quad (4.1)$$

$$w_{0,0} \frac{\partial w_{0,0}}{\partial z} + \frac{1}{\rho} \frac{\partial p_{0,0}}{\partial z} + g = 0; \quad -h \leq z \leq \eta^c \quad (4.2)$$

$$\frac{\partial w_{0,0}}{\partial z} = 0; \quad -h \leq z \leq \eta^c \quad (4.3)$$

$$w_{0,0} = 0; \quad z = -h \quad (4.4)$$

$$w_{0,0} = 0; \quad z = \eta^c \quad (4.5)$$

$$p_{0,0} = 0; \quad z = \eta^c \quad (4.6)$$

Equation (4.3) - (4.5) generate a trivial solution for $w_{0,0}$. Therefore, the vertical component of leading order current velocity $w_{0,0}$ is always zero and the flow is hydrostatic at this order.

$$w_{0,0}(z, \mathbf{X}, T) = 0; \quad -h \leq z \leq \eta^c \quad (4.7)$$

$$p_{0,0}(z, \mathbf{X}, T) = \rho g(\eta^c - z); \quad -h \leq z \leq \eta^c \quad (4.8)$$

At order ($n = 1, m = 0$), we get

$$\frac{\partial \mathbf{q}_{0,0}}{\partial T} + (\mathbf{q}_{0,0} \cdot \nabla_H) \mathbf{q}_{0,0} + w_{1,0} \frac{\partial \mathbf{q}_{0,0}}{\partial z} + \frac{1}{\rho} \nabla_H p_{0,0} = 0; \quad -h \leq z \leq \eta^c \quad (4.9)$$

$$\frac{1}{\rho} \frac{\partial p_{1,0}}{\partial z} = 0; \quad -h \leq z \leq \eta^c \quad (4.10)$$

$$\frac{\partial w_{1,0}}{\partial z} + \nabla_H \cdot \mathbf{q}_{0,0} = 0; \quad -h \leq z \leq \eta^c \quad (4.11)$$

$$w_{1,0} = -\mathbf{q}_{0,0} \cdot \nabla_H h; \quad z = -h \quad (4.12)$$

$$w_{1,0} = \frac{\partial \eta_{0,0}}{\partial T} + \mathbf{q}_{0,0} \cdot \nabla_H \eta_{0,0}; \quad z = \eta^c \quad (4.13)$$

$$p_{1,0} = 0; \quad z = \eta^c \quad (4.14)$$

In Chapter 2, we divide the instantaneous surface elevation η into a wave-averaged component η^c and an oscillatory component η^w . Consider the multiple scale expansion, the wave-averaged component

$$\eta^c = \sum_{n=0}^{\infty} \epsilon^n \eta_{n,0} = \eta_{0,0} + O(\epsilon) \quad (4.15)$$

$\eta_{0,0}$ is the leading order component of η^c . Based on Equation (4.10) - (4.14), we have

$$w_{1,0}(z, \mathbf{X}, T) = \frac{\partial \eta_{0,0}}{\partial T} + \mathbf{q}_{0,0} \cdot \nabla_H \eta_{0,0} + \int_z^{\eta^c} \nabla_H \cdot \mathbf{q}_{0,0} dz; \quad -h \leq z \leq \eta^c \quad (4.16)$$

$$p_{1,0}(z, \mathbf{X}, T) = 0; \quad -h \leq z \leq \eta^c \quad (4.17)$$

$$\frac{\partial \eta_{0,0}}{\partial T} + \nabla_H \cdot \left(\int_{-h}^{\eta^c} \mathbf{q}_{0,0} dz \right) = 0 \quad (4.18)$$

According to the continuity equation (4.11), $w_{1,0}$ is induced by the slow scale horizontal variations of the leading order current horizontal velocity $\mathbf{q}_{0,0}$. $w_{1,0}$ is needed to get wave action equation in Chapter 3. Equation (4.10) and (4.14) suggest that $p_{1,0}$ is

always zero, indicating that wave-induced mean pressure arises at $O(\epsilon^2)$. Equation (4.18) indicates mean flow mass conservation at leading order.

At order $(n = 2, m = 0)$, quadratic wave terms appear. Based on the linear wave continuity equation (3.3) and the relation between wave complex conjugates (4.19) - (4.21),

$$w_{1,1}\boldsymbol{\xi}_{1,-1} = -w_{1,-1}\boldsymbol{\xi}_{1,1} \quad (4.19)$$

$$\chi_{1,1}\mathbf{q}_{1,-1} = -\chi_{1,-1}\mathbf{q}_{1,1} \quad (4.20)$$

$$(\mathbf{k}\cdot\mathbf{q}_{1,1})\eta_{1,-1} = (\mathbf{k}\cdot\mathbf{q}_{1,-1})\eta_{1,1} \quad (4.21)$$

We rearrange the order $(n = 2, m = 0)$ mean flow equations to get

$$\begin{aligned} \frac{\partial\mathbf{q}_{1,0}}{\partial T} + (\mathbf{q}_{0,0}\cdot\nabla_H)\mathbf{q}_{1,0} + w_{1,0}\frac{\partial\mathbf{q}_{1,0}}{\partial z} + \frac{1}{\rho}\nabla_H p_{1,0} + \mathbf{q}_{1,0}\cdot\nabla_H\mathbf{q}_{0,0} + w_{2,0}\frac{\partial\mathbf{q}_{0,0}}{\partial z} \\ = 0; \quad -h \leq z \leq \eta^c \end{aligned} \quad (4.22)$$

$$\begin{aligned} \frac{\partial w_{1,0}}{\partial T} + \mathbf{q}_{0,0}\cdot\nabla_H w_{1,0} + w_{1,0}\frac{\partial w_{1,0}}{\partial z} + \frac{1}{\rho}\frac{\partial p_{2,0}}{\partial z} = -\frac{\partial}{\partial z}(\mathbf{q}_{1,1}\cdot\mathbf{q}_{1,-1} + w_{1,1}w_{1,-1}) \\ + (\mathbf{q}_{1,1}\times\boldsymbol{\xi}_{1,-1} + \mathbf{q}_{1,-1}\times\boldsymbol{\xi}_{1,1}); \quad -h \leq z \leq \eta^c \end{aligned} \quad (4.23)$$

$$\frac{\partial w_{2,0}}{\partial z} + \nabla_H\cdot\mathbf{q}_{1,0} = 0; \quad -h \leq z \leq \eta^c \quad (4.24)$$

$$w_{2,0} = -\mathbf{q}_{1,0}\cdot\nabla_H h; \quad z = -h \quad (4.25)$$

$$w_{2,0} = \frac{\partial\eta_{1,0}}{\partial T} + \mathbf{q}_{0,0}\cdot\nabla_H\eta_{1,0} + \mathbf{q}_{1,0}\cdot\nabla_H\eta_{0,0}; \quad z = \eta^c \quad (4.26)$$

$$p_{2,0} = -(\eta_{1,1}\frac{\partial p_{1,-1}}{\partial z} + \eta_{1,-1}\frac{\partial p_{1,1}}{\partial z}); \quad z = \eta^c \quad (4.27)$$

The wave-average forces in (4.23) are represented in terms of the Bernoulli head gradient and vortex force by expanding (2.13) and (2.14) at $O(\epsilon)$. It is obvious that only the vertical component (4.23) of momentum equation has the wave-averaged force at this order. The first part on the right hand side is the wave contribution to mean pressure resulting from the vertical variation of Bernoulli head. The second one is part of the wave vortex force. We assume that mean flow velocity is $\mathbf{q}_{0,0}$ and $w_{1,0}$. The wave-induced Stokes velocity is at the order of $O(\epsilon^2)$. The horizontal component of the momentum equation (4.22) is homogenous. Thus, $\mathbf{q}_{1,0}$ along with its corresponding

vertical component $w_{2,0}$ and $\eta_{1,0}$ can be treated as trivial solutions or essentially absorbed in $\mathbf{q}_{0,0}, w_{2,0}, \eta_{0,0}$. We neglect these terms in the wave and mean flow equations thereafter. The dynamic surface boundary condition (4.27) gives the wave-induced pressure $p_{2,0}$.

The order ($n = 3, m = 0$) mean flow equations are given by

$$\begin{aligned} & \frac{\partial \mathbf{q}_{2,0}}{\partial T} + \mathbf{q}_{0,0} \cdot \nabla_H \mathbf{q}_{2,0} + w_{1,0} \frac{\partial \mathbf{q}_{2,0}}{\partial z} + \frac{1}{\rho} \nabla_H p_{2,0} + \mathbf{q}_{2,0} \cdot \nabla_H \mathbf{q}_{0,0} + w_{3,0} \frac{\partial \mathbf{q}_{0,0}}{\partial z} \\ & = [-\nabla_H \cdot (\mathbf{q}_{1,1} \mathbf{q}_{1,-1} + \mathbf{q}_{1,-1} \mathbf{q}_{1,1})] + [\mathbf{i}_z \times (w_{1,1} \boldsymbol{\xi}_{2,-1} + w_{1,-1} \boldsymbol{\xi}_{2,1} + w_{2,1} \boldsymbol{\xi}_{1,-1} + w_{2,-1} \boldsymbol{\xi}_{1,1} \\ & - \mathbf{q}_{1,1} \chi_{2,-1} - \mathbf{q}_{1,-1} \chi_{2,1} - \mathbf{q}_{2,1} \chi_{1,-1} - \mathbf{q}_{2,-1} \chi_{1,1})]; \quad -h \leq z \leq \eta^c \end{aligned} \quad (4.28)$$

$$\begin{aligned} & \frac{1}{\rho} \frac{\partial p_{3,0}}{\partial z} = [-\frac{\partial}{\partial z} (\mathbf{q}_{1,1} \cdot \mathbf{q}_{2,-1} + w_{1,1} w_{2,-1} + \mathbf{q}_{1,-1} \cdot \mathbf{q}_{2,1} + w_{1,-1} w_{2,1})] \\ & + [(\mathbf{q}_{1,1} \times \boldsymbol{\xi}_{2,-1} + \mathbf{q}_{1,-1} \times \boldsymbol{\xi}_{2,1} + \mathbf{q}_{2,1} \times \boldsymbol{\xi}_{1,-1} + \mathbf{q}_{2,-1} \times \boldsymbol{\xi}_{1,1})]; \quad -h \leq z \leq \eta^c \end{aligned} \quad (4.29)$$

$$\frac{\partial w_{3,0}}{\partial z} + \nabla_H \cdot \mathbf{q}_{2,0} = 0; \quad -h \leq z \leq \eta^c \quad (4.30)$$

$$\begin{aligned} & w_{3,0} - \left(\frac{\partial \eta_{2,0}}{\partial T} + \mathbf{q}_{0,0} \cdot \nabla_H \eta_{2,0} + \mathbf{q}_{2,0} \cdot \nabla_H \eta_{0,0} \right) = \\ & \nabla_H \cdot [(\mathbf{q}_{1,1} \eta_{1,-1} + \mathbf{q}_{1,-1} \eta_{1,1}) + \frac{\partial \mathbf{q}_{0,0}}{\partial z} (\eta_{1,1} \eta_{1,-1})] \\ & + (\eta_{1,1} \eta_{1,-1} \frac{\partial^2 \mathbf{q}_{0,0}}{\partial z^2} + \eta_{1,1} \frac{\partial \mathbf{q}_{1,-1}}{\partial z} + \eta_{1,-1} \frac{\partial \mathbf{q}_{1,1}}{\partial z}) \cdot \nabla_H \eta_{0,0}; \quad z = \eta^c \end{aligned} \quad (4.31)$$

$$p_{3,0} = -(\eta_{1,1} \frac{\partial p_{2,-1}}{\partial z} + \eta_{1,-1} \frac{\partial p_{2,1}}{\partial z} + \eta_{2,1} \frac{\partial p_{1,-1}}{\partial z} + \eta_{2,-1} \frac{\partial p_{1,1}}{\partial z}); \quad z = \eta^c \quad (4.32)$$

$$w_{3,0} = -\mathbf{q}_{2,0} \cdot \nabla_H h; \quad z = -h \quad (4.33)$$

The wave-averaged forces in the momentum equations (4.28) and (4.29) are written in terms of vortex force formalism at this order by expanding (2.13) and (2.14). For each momentum equation, the first bracket on the right hand side denotes the gradient of Bernoulli head, and the second bracket denotes vortex force. The kinematic surface boundary condition (4.31) indicates that mean surface variations are affected by horizontal divergence of depth integrated Stokes drift \mathbf{Q}^{St} and horizontal gradient of leading order mean water surface elevation $\eta_{0,0}$. The dynamic surface boundary condition (4.32) gives the higher order wave-induced pressure $p_{3,0}$. The Stokes drift \mathbf{Q}^{st} is identified from (4.31) as

$$\mathbf{Q}^{St} = [\mathbf{q}_{1,1}(\eta^c) \eta_{1,-1} + \mathbf{q}_{1,-1}(\eta^c) \eta_{1,1}] + \frac{\partial \mathbf{q}_{0,0}(\eta^c)}{\partial z} (\eta_{1,1} \eta_{1,-1}) \quad (4.34)$$

It is necessary to interpret the physical meaning of each mean flow variable in the multiple-scale expansion. $\mathbf{q}_{0,0}$ and $w_{1,0}$ stand for leading order current velocity. $w_{1,0}$ is induced by the horizontal variation of $\mathbf{q}_{0,0}$ according to the leading order continuity equation. $\mathbf{q}_{1,1}$ and $w_{1,1}$ give $O(\epsilon)$ linear wave orbital velocities. $\mathbf{q}_{2,1}$ and $w_{2,1}$ are $O(\epsilon^2)$ wave orbital velocities forced by slow variations of $O(\epsilon)$ waves along with current. \mathbf{q}_{10} is $O(\epsilon)$ current horizontal velocity and can be interpreted as weak current. w_{20} is induced by horizontal variation of \mathbf{q}_{10} . These two terms only yield trivial solutions with strong current assumption. Therefore they are neglected in our problem. $\mathbf{q}_{2,0}$ accounts for mean flow velocity related to waves. $w_{3,0}$ is induced by horizontal variation of $\mathbf{q}_{2,0}$. $\eta_{0,0}$ is leading order mean surface elevation related to strong current dynamics. $\eta_{1,0}$ is $O(\epsilon)$ mean surface elevation related to $\mathbf{q}_{1,0}$ and $w_{2,0}$, which are also neglected in our problem. $\eta_{2,0}$ represents wave-induced surface elevation variance known as wave set up/down. $p_{0,0}$ is leading order hydrostatic pressure. $p_{1,0}$ is $O(\epsilon)$ mean pressure and is always zero. $p_{2,0}$ is mean pressure related to wave-averaged quasi-static pressure as well as current dynamic pressure. $p_{3,0}$ is mean pressure related to higher order wave-averaged quasi-static pressure.

4.2 Mean Flow Vorticity

Mean flow quantities only vary over slow scales. Thus we can get mean flow vorticity by taking the curl of mean flow velocity.

$$\xi_{0,0} = \mathbf{i}_z \times \frac{\partial \mathbf{q}_{0,0}}{\partial z} \quad (4.35)$$

$$\xi_{1,0} = \mathbf{i}_z \times \frac{\partial \mathbf{q}_{1,0}}{\partial z} \quad (4.36)$$

$$\xi_{2,0} = \mathbf{i}_z \times \frac{\partial \mathbf{q}_{2,0}}{\partial z} + \nabla_H \times \mathbf{i}_z w_{1,0} \quad (4.37)$$

and

$$\chi_{0,0} = 0 \quad (4.38)$$

$$\chi_{1,0} = \mathbf{i}_z \cdot (\nabla_H \times \mathbf{q}_{0,0}) \quad (4.39)$$

$$\chi_{2,0} = \mathbf{i}_z \cdot (\nabla_H \times \mathbf{q}_{1,0}) \quad (4.40)$$

Mean flow vorticity equations are obtained through expansion of vorticity balance equation (2.48) - (2.49). The vorticity equations below suggest that the slow variations of mean flow vorticity are forced by the curl of wave vortex force.

The leading order vertical vorticity $\chi_{0,0}$ is always zero. $O(\epsilon)$ mean flow vorticity equation only has the horizontal component.

$$\frac{\partial \boldsymbol{\xi}_{0,0}}{\partial T} + (\mathbf{q}_{0,0} \cdot \nabla_H) \boldsymbol{\xi}_{0,0} + w_{1,0} \frac{\partial \boldsymbol{\xi}_{0,0}}{\partial z} = (\boldsymbol{\xi}_{0,0} \cdot \nabla_H) \mathbf{q}_{0,0} + \chi_{1,0} \frac{\partial \mathbf{q}_{0,0}}{\partial z} \quad (4.41)$$

$O(\epsilon^2)$ mean flow vorticity equations are given by

$$\frac{\partial \chi_{1,0}}{\partial T} + (\mathbf{q}_{0,0} \cdot \nabla_H) \chi_{1,0} + w_{1,0} \frac{\partial \chi_{1,0}}{\partial z} = (\boldsymbol{\xi}_{0,0} \cdot \nabla_H) w_{1,0} + \chi_{1,0} \frac{\partial w_{1,0}}{\partial z} \quad (4.42)$$

The $\boldsymbol{\xi}_{1,0}$ and $\chi_{2,0}$ only have trivial solution since $\mathbf{q}_{1,0}$ are trivial solutions. Therefore we neglect the vorticity equations for $\boldsymbol{\xi}_{1,0}$ and $\chi_{2,0}$. We use the relation between linear wave complex conjugate products (4.20) and non-divergence of $O(\epsilon)$ wave vorticity (3.13). The $O(\epsilon^3)$ mean flow vorticity equation is given by

$$\begin{aligned} \frac{\partial \boldsymbol{\xi}_{2,0}}{\partial T} + \mathbf{q}_{0,0} \cdot \nabla_H \boldsymbol{\xi}_{2,0} + w_{1,0} \frac{\partial \boldsymbol{\xi}_{2,0}}{\partial z} &= \frac{\partial \mathbf{q}_{0,0}}{\partial z} \chi_{3,0} - w_{30} \frac{\partial \boldsymbol{\xi}_{0,0}}{\partial z} + \boldsymbol{\xi}_{2,0} \cdot \nabla_H \mathbf{q}_{0,0} \\ &- (\mathbf{q}_{2,0} \cdot \nabla_H \boldsymbol{\xi}_{0,0} - \boldsymbol{\xi}_{0,0} \cdot \nabla_H \mathbf{q}_{2,0}) + \chi_{1,0} \frac{\partial \mathbf{q}_{2,0}}{\partial z} \\ &- \nabla_H \cdot (\mathbf{q}_{1,1} \boldsymbol{\xi}_{1,-1} + \mathbf{q}_{1,-1} \boldsymbol{\xi}_{1,1}) + \nabla_H \cdot (\boldsymbol{\xi}_{1,-1} \mathbf{q}_{1,1} + \boldsymbol{\xi}_{1,1} \mathbf{q}_{1,-1}) \\ &- \frac{\partial}{\partial z} (w_{2,1} \boldsymbol{\xi}_{1,-1} + w_{2,-1} \boldsymbol{\xi}_{1,1} + w_{1,1} \boldsymbol{\xi}_{2,-1} + w_{1,-1} \boldsymbol{\xi}_{2,1}) \\ &- \chi_{1,1} \mathbf{q}_{2,-1} - \chi_{1,-1} \mathbf{q}_{2,1} - \chi_{2,1} \mathbf{q}_{1,-1} - \chi_{2,-1} \mathbf{q}_{1,1} \end{aligned} \quad (4.43)$$

To include $O(\epsilon^3)$ vortex force terms in the vorticity equation, we need to look at the $O(\epsilon^4)$ vertical component of the vorticity equation. The horizontal component is neglected. We also consider the non-divergence of $O(\epsilon^2)$ wave vorticity (3.125) to get

$$\begin{aligned} \frac{\partial \chi_{30}}{\partial T} + \mathbf{q}_{00} \cdot \nabla_H \chi_{30} + w_{10} \frac{\partial \chi_{30}}{\partial z} &= -(\mathbf{q}_{10} \cdot \nabla_H \chi_{20} + \mathbf{q}_{20} \cdot \nabla_H \chi_{10}) \\ &+ (\boldsymbol{\xi}_{00} \cdot \nabla_H w_{30} + \boldsymbol{\xi}_{10} \cdot \nabla_H w_{20} + \boldsymbol{\xi}_{20} \cdot \nabla_H w_{10}) \\ &- (w_{20} \frac{\partial \chi_{20}}{\partial z} + w_{30} \frac{\partial \chi_{10}}{\partial z}) + (\chi_{10} \frac{\partial w_{30}}{\partial z} + \chi_{20} \frac{\partial w_{20}}{\partial z} + \chi_{30} \frac{\partial w_{10}}{\partial z}) \\ &+ \nabla_H \cdot (w_{2,1} \boldsymbol{\xi}_{1,-1} + w_{2,-1} \boldsymbol{\xi}_{1,1} + w_{1,1} \boldsymbol{\xi}_{2,-1} + w_{1,-1} \boldsymbol{\xi}_{2,1}) \\ &- \chi_{1,1} \mathbf{q}_{2,-1} - \chi_{1,-1} \mathbf{q}_{2,1} - \chi_{2,1} \mathbf{q}_{1,-1} - \chi_{2,-1} \mathbf{q}_{1,1} \end{aligned} \quad (4.44)$$

4.3 Wave-averaged Forces

We group the wave forces from the orders of mean flow momentum equations and get the Bernoulli head κ and vortex force (\mathbf{J}, K) as follows.

The Bernoulli head κ and vortex force (\mathbf{J}, K) have the general form below.

$$\begin{aligned} \nabla\kappa &= (\epsilon\nabla_H + \mathbf{i}_z \frac{\partial}{\partial z})[\epsilon^2(\mathbf{q}_{1,1}\cdot\mathbf{q}_{1,-1} + w_{1,1}w_{1,-1}) \\ &+ \epsilon^3(\mathbf{q}_{1,1}\cdot\mathbf{q}_{2,-1} + w_{1,1}w_{2,-1} + \mathbf{q}_{1,-1}\cdot\mathbf{q}_{2,1} + w_{1,-1}w_{2,1})] + O(\epsilon^4) \end{aligned} \quad (4.45)$$

$$\begin{aligned} \mathbf{J} &= \mathbf{i}_z \times [\epsilon^2(w_{1,1}\boldsymbol{\xi}_{1,-1} + w_{1,-1}\boldsymbol{\xi}_{1,1} - \mathbf{q}_{1,1}\chi_{1,-1} - \mathbf{q}_{1,-1}\chi_{1,1}) \\ &+ \epsilon^3(w_{1,1}\boldsymbol{\xi}_{2,-1} + w_{1,-1}\boldsymbol{\xi}_{2,1} + w_{2,1}\boldsymbol{\xi}_{1,-1} + w_{2,-1}\boldsymbol{\xi}_{1,1} \\ &- \mathbf{q}_{1,1}\chi_{2,-1} - \mathbf{q}_{1,-1}\chi_{2,1} - \mathbf{q}_{2,1}\chi_{1,-1} - \mathbf{q}_{2,-1}\chi_{1,1})] + O(\epsilon^4) \end{aligned} \quad (4.46)$$

$$\begin{aligned} K &= \mathbf{i}_z \cdot [\epsilon^2(\mathbf{q}_{1,1} \times \boldsymbol{\xi}_{1,-1} + \mathbf{q}_{1,-1} \times \boldsymbol{\xi}_{1,1}) + \epsilon^3(\mathbf{q}_{1,1} \times \boldsymbol{\xi}_{2,-1} + \mathbf{q}_{1,-1} \times \boldsymbol{\xi}_{2,1} \\ &+ \mathbf{q}_{2,1} \times \boldsymbol{\xi}_{1,-1} + \mathbf{q}_{2,-1} \times \boldsymbol{\xi}_{1,1})] + O(\epsilon^4) \end{aligned} \quad (4.47)$$

The Bernoulli head can be rewritten in terms of $w_{1,1}$, $w_{2,1}$ and their complex conjugates. κ_2, κ_3 can be found in Appendix B, where

$$\kappa = \epsilon^2\kappa_2 + \epsilon^3\kappa_3 + O(\epsilon^4) \quad (4.48)$$

We introduce a depth-dependent, slowly varying variable \mathbf{E}^* , which has the dimension of energy. Detailed derivation of vortex force can be found in Appendix B.

$$\mathbf{E}^*(z, \mathbf{X}, T) = \frac{\sigma_w^2 \mathbf{k}}{k^2} \frac{\partial}{\partial z} \left(\frac{w_{1,1}w_{1,-1}}{\sigma_w^2} \right) \quad (4.49)$$

Then the horizontal vortex force can be expressed in terms of $w_{1,1}$ and its complex conjugates. The vertical vortex force is also rearranged. (See (5.127) and (B.9) in

Appendix B).

$$\begin{aligned}
\mathbf{J}(z, \mathbf{X}, T) &= \mathbf{i}_z \times \left\{ 2 \left[-\frac{D}{DT} \left(\frac{\mathbf{k} \cdot \boldsymbol{\xi}_{0,0}}{\sigma_w^2} \mathbf{E}^* + \frac{\partial \boldsymbol{\xi}_{0,0}}{\partial z} \frac{w_{1,1} w_{1,-1}}{\sigma_w^2} \right) - \frac{\mathbf{E}^*}{\sigma_w^2} \frac{D}{DT} (\mathbf{k} \cdot \boldsymbol{\xi}_{0,0}) \right. \right. \\
&\quad - \frac{w_{1,1} w_{1,-1}}{\sigma_w^2} \frac{D}{DT} \left(\frac{\partial \boldsymbol{\xi}_{0,0}}{\partial z} \right) + \left(-\frac{2w_{1,1} w_{1,-1}}{\sigma_w^2} \frac{\partial \mathbf{q}_{0,0}}{\partial z} + \frac{\mathbf{E}^*}{\sigma_w} \right) \cdot \nabla_H \boldsymbol{\xi}_{0,0} + \frac{\mathbf{E}^*}{\sigma_w} \frac{\partial \chi_{1,0}}{\partial z} \\
&\quad + \left(\frac{2w_{1,1} w_{1,-1}}{\sigma_w^2} \frac{\partial \boldsymbol{\xi}_{0,0}}{\partial z} + \frac{\mathbf{k} \cdot \boldsymbol{\xi}_{0,0}}{\sigma_w^2} \mathbf{E}^* \right) \cdot \nabla_H \mathbf{q}_{0,0} - \frac{\mathbf{k} \cdot \boldsymbol{\xi}_{0,0}}{\sigma_w^2} \mathbf{E}^* \nabla_H \cdot \mathbf{q}_{0,0} \\
&\quad + \boldsymbol{\xi}_{0,0} \cdot \nabla_H \left(\frac{w_{1,1} w_{1,-1}}{\sigma_w^2} \frac{\partial \mathbf{q}_{0,0}}{\partial z} \right) + \frac{w_{1,1} w_{1,-1}}{\sigma_w^2} \boldsymbol{\xi}_{0,0} \cdot \nabla_H \left(\frac{\partial \mathbf{q}_{0,0}}{\partial z} \right) - \frac{\boldsymbol{\xi}_{0,0}}{\sigma_w} \cdot \nabla_H \mathbf{E}^* \left. \right\} \\
&\quad - \chi_{1,0} \mathbf{q}^{st}(z) \} + O(\epsilon^4) \tag{4.50}
\end{aligned}$$

$$K(z, \mathbf{X}, T) = \epsilon^2 K_2 + \epsilon^3 K_3 + O(\epsilon) \tag{4.51}$$

where \mathbf{q}^{st} is depth-dependent Stokes drift velocity. In our problem, we allow strong current with strong vertical shear. Thus, we have extra terms due to the difference in direction between wave vector \mathbf{k} and current velocity $\mathbf{q}_{0,0}$.

$$\begin{aligned}
\mathbf{q}^{st}(z, T, \mathbf{X}) &= \frac{\partial}{\partial z} \left[\frac{\mathbf{k}}{k^2 \sigma_w} \frac{\partial w_{1,1} w_{1,-1}}{\partial z} - \frac{w_{1,1} w_{1,-1}}{\sigma_w^2} \left(\frac{\mathbf{k}}{k^2} \frac{\partial \sigma_w}{\partial z} + \frac{\partial \mathbf{q}_{0,0}}{\partial z} \right) \right] \\
&\quad - \frac{w_{1,1} w_{1,-1}}{\sigma_w^2} \left(\frac{\mathbf{k}}{k^2} \frac{\partial^2 \sigma_w}{\partial z^2} + \frac{\partial^2 \mathbf{q}_{0,0}}{\partial z^2} \right) \tag{4.52}
\end{aligned}$$

In MRL04, the Stokes drift velocity excludes the current shear terms and therefore (4.52) becomes

$$\mathbf{q}^{st}(z, T, \mathbf{X}) = \frac{\partial}{\partial z} \left(\frac{\mathbf{k}}{k^2 \sigma_w} \frac{\partial w_{1,1} w_{1,-1}}{\partial z} \right) \tag{4.53}$$

The MRL04 uses current-free linear wave solutions in the Stokes drift velocity, where

$$w_{1,1}(z) = -i\omega \eta_{1,1} \frac{\sinh k(H+z)}{\sinh kH} \tag{4.54}$$

$$\mathbf{q}^{st}(z, T, \mathbf{X}) = \frac{a^2 \omega}{2 \sinh^2 kH} \cosh 2k(H+z) \mathbf{k} \tag{4.55}$$

where $|\eta_{1,1}| = a/2$. Equation (4.55) is the Stokes drift velocity obtained in MRL04. It is also used in ROMS/SWAN coupled models (Uchiyama *et al.*, 2010; Kumar *et al.*, 2011; Kumar *et al.*, 2012).

4.4 Vortex Force for Strong Depth Uniform Current

The horizontal vortex force (4.50) is only related to slow variations of $O(\epsilon)$ waves and the leading order current. Consider the simple case of depth uniform current, terms

related to $\boldsymbol{\xi}_{0,0}$ vanish from horizontal vortex force (4.50) with only the last term left. The vortex force now is the cross product of Stokes drift velocity and current vertical vorticity.

$$\mathbf{J} = -\mathbf{i}_z \times \mathbf{q}^{st} \chi_{1,0} \quad (4.56)$$

$$K = 0 \quad (4.57)$$

4.5 Vortex Force for Weak Current: Comparison with MRL04

The weak current assumption is used in wave-current interaction modeling as discussed in MRL04. Here we provide the wave-averaged forces for the weak current case and compare with their results. In MRL04, two horizontal space scales and three time scales are considered. The fast scales $(\mathbf{x}, z, t) \sim \epsilon^0$ are used to describe wave oscillatory motion and vertical variations. The slow scales $(\mathbf{X}, \tau) \sim \epsilon^{-2}$ are used to describe slowly varying features of both long waves and currents. The slowest time scale $T \sim \epsilon^{-4}$ is introduced as tidal current scale. The current velocities are assumed to be weaker than wave orbital velocity, $|\mathbf{q}^c/\mathbf{q}^w| \sim O(\epsilon)$ and therefore $|\mathbf{q}^c/\mathbf{c}_0| \sim O(\epsilon^2)$.

In our problem, we consider two horizontal space scales and two time scales. The slow time scale $T \sim O(\epsilon)$ in our paper is responsible for time variations of both long waves and current. The weak current assumption with our scaling method is $|\mathbf{q}^c/\mathbf{c}_0| \sim O(\epsilon^2)$. The wave forces are largely simplified as current related terms go at least one order $O(\epsilon)$ higher. With the weak current assumption, the leading current horizontal vorticity (4.41) is time independent up to $O(\epsilon^2)$, see (4.58) below. Thus, the time derivatives of $\boldsymbol{\xi}_{0,0}$ related terms are neglected in vortex force.

$$\frac{\partial \boldsymbol{\xi}_{0,0}}{\partial T} = O(\epsilon^3) \quad (4.58)$$

We apply weak current assumption and rescale the wave-averaged forces obtained in previous section (see Equation (4.48), (4.50) and (4.51)). After manipulation, the

vortex force (\mathbf{J}, K) are simplified as

$$\mathbf{J} = \mathbf{i}_z \times \left\{ 2 \left[\frac{\mathbf{E}^*}{\sigma_w} \cdot \nabla_H \boldsymbol{\xi}_{0,0} + \frac{\mathbf{E}^*}{\sigma_w} \frac{\partial \chi_{1,0}}{\partial z} - \frac{\boldsymbol{\xi}_{0,0}}{\sigma_w} \cdot \nabla_H \mathbf{E}^* \right] - \chi_{1,0} \mathbf{q}^{st} \right\} \quad (4.59)$$

$$K = -\frac{1}{k^2} \frac{\partial}{\partial z} \left(\frac{w_{1,1} w_{1,-1}}{\sigma_w} \right) \mathbf{k} \times \frac{\partial \boldsymbol{\xi}_{0,0}}{\partial z} \quad (4.60)$$

We take the current-free linear wave solutions into Equation (4.59) and (4.60) and reproduce equation (8.3) - (8.9) in MRL04 as shown below. Detailed derivation can be found in Appendix C.

$$\mathbf{J} = -\mathbf{i}_z \times \mathbf{q}^{st} \chi_{1,0} - w^{st} \frac{\partial \mathbf{q}_{0,0}}{\partial z} - \nabla_H \left[\int_{-H}^z \mathbf{q}^{st}(\zeta) d\zeta \cdot \frac{\partial \mathbf{q}_{0,0}}{\partial z} \right] \quad (4.61)$$

$$K = -\int_{-H}^z \mathbf{q}^{st}(\zeta) d\zeta \cdot \frac{\partial^2 \mathbf{q}_{0,0}}{\partial z^2} \quad (4.62)$$

$$\mathbf{E}^* = \sigma_w a^2 \frac{\sinh 2k(H+z)}{4 \sinh^2 kH} \frac{\mathbf{k}}{k} \quad (4.63)$$

$$\mathbf{q}^{st} = \sigma_w a^2 \frac{\cosh 2k(H+z)}{2 \sinh^2 kH} \mathbf{k} \quad (4.64)$$

$$w^{st} = -\nabla_{H^*} \left[\int_{-H}^z \mathbf{q}^{st}(\zeta) d\zeta \right] = -\nabla_{H^*} \left[\frac{\sigma_w a^2 \mathbf{k}}{4k \sinh^2 kH} \sinh 2k(H+z) \right] \quad (4.65)$$

where $w^{st}(z)$ is pseudo vertical Stokes drift velocity. Thus, the Stokes drift velocity (\mathbf{q}^{st}, w^{st}) satisfies the continuity equation.

$$\nabla_H \cdot \mathbf{q}^{st} + \frac{\partial w^{st}}{\partial z} = 0 \quad (4.66)$$

Additional manipulations of Equation (4.61) and (4.62) are needed to obtain the final form of wave vortex force as widely used in ROMS/SWAN coupled model (Uchiyama *et al.*, 2010; Kumar *et al.*, 2012). We rewrite the vertical vortex force K as

$$K = \mathbf{q}^{st} \cdot \frac{\partial \mathbf{q}_{0,0}}{\partial z} - \frac{\partial}{\partial z} \left[\int_{-H}^z \mathbf{q}^{st}(\zeta) d\zeta \cdot \frac{\partial \mathbf{q}_{0,0}}{\partial z} \right] \quad (4.67)$$

Following MRL04, the third term in horizontal vortex force (4.61) and the second term in vertical vortex force (4.67) can be treated as pressure gradient and therefore moved to the Bernoulli head term. The form of vortex force used in ROMS/SWAN coupled model by Uchiyama *et al.* (2010) and Kumar *et al.* (2012) is given as

$$\mathbf{J} = -\mathbf{i}_z \times \mathbf{q}^{st} \chi_{1,0} - w^{st} \frac{\partial \mathbf{q}_{0,0}}{\partial z} \quad (4.68)$$

$$K = \mathbf{q}^{st} \cdot \frac{\partial \mathbf{q}_{0,0}}{\partial z} \quad (4.69)$$

The vortex force with weak current assumption will be implemented in NHWAVE/SWAN ($NH\overline{WAVE}$ thereafter) model to compare with the strongly sheared current formulation. The comparison results are provide in Chapter 5.

4.6 Vortex Force for Constantly Sheared Current

In Chapter 3, we discussed the wave vorticity based on analytical solutions for constant shear current. Here we also use the constant shear current case to compare the present wave-averaged forces (DK16 thereafter) with MRL04 results. To simplify the comparison, we assume that waves travel exactly on either opposing current or following current over a flat bed. The constant shear flow is assumed to be in x -direction.

$$q_{0,0}^x = q_{0,0}^s(1 + \alpha \frac{z}{h}) \quad (4.70)$$

$$q_{0,0}^y = 0 \quad (4.71)$$

$$\alpha = \frac{\Omega^s h}{q_{0,0}^s} \quad (4.72)$$

where α is the normalized form of the constant vorticity Ω^s . The current vorticity is given as

$$\xi_{0,0}^x = 0 \quad (4.73)$$

$$\xi_{0,0}^y = \Omega^s \quad (4.74)$$

$$\chi_{0,0} = -(\frac{\partial q_{0,0}^s}{\partial Y} + \frac{\partial \Omega^s}{\partial Y} z) \quad (4.75)$$

$$\frac{\partial \chi_{0,0}}{\partial z} = -\frac{\partial \Omega^s}{\partial Y} \quad (4.76)$$

$$\mathbf{k} \cdot \boldsymbol{\xi}_{0,0} = 0 \quad (4.77)$$

The intrinsic frequency σ , surface intrinsic frequency σ_s and dispersion relation are given as

$$\sigma = \omega - kq_{0,0}^s(1 + \alpha \frac{z}{h}) \quad (4.78)$$

$$\sigma_s = \omega - kq_{0,0}^s \quad (4.79)$$

$$\frac{\partial \sigma}{\partial z} = -k\Omega^s \quad (4.80)$$

$$\sigma_s^2 = (gk - \sigma_s \Omega^s) \tanh kH \quad (4.81)$$

The wave-averaged forces are largely reduced. The vertical component of vortex force is zero for this case.

$$\begin{aligned} \mathbf{J} &= \mathbf{i}_z \times \left\{ 2 \left[\left(-\frac{2w_{1,1}w_{1,-1}}{\sigma_w^2} \frac{\partial \mathbf{q}_{0,0}}{\partial z} + \frac{\mathbf{E}^*}{\sigma_w} \right) \cdot \nabla_H \boldsymbol{\xi}_{0,0} + \frac{\mathbf{E}^*}{\sigma_w} \frac{\partial \chi_{1,0}}{\partial z} \right. \right. \\ &+ \left. \boldsymbol{\xi}_{0,0} \cdot \nabla_H \left(\frac{w_{1,1}w_{1,-1}}{\sigma_w^2} \frac{\partial \mathbf{q}_{0,0}}{\partial z} \right) + \frac{w_{1,1}w_{1,-1}}{\sigma_w^2} \boldsymbol{\xi}_{0,0} \cdot \nabla_H \left(\frac{\partial \mathbf{q}_{0,0}}{\partial z} \right) - \frac{\boldsymbol{\xi}_{0,0}}{\sigma_w} \cdot \nabla_H \mathbf{E}^* \right] \\ &- \left. \chi_{1,0} \mathbf{q}^{st}(z) \right\} \end{aligned} \quad (4.82)$$

$$K = 0 \quad (4.83)$$

$$\mathbf{q}^{st} = \frac{\partial}{\partial z} \left(\frac{\mathbf{k}}{k^2 \sigma_w} \frac{\partial w_{1,1} w_{1,-1}}{\partial z} \right) \quad (4.84)$$

Since waves and currents are co-directional, waves are still irrotational for this case (Constantin, 2011). The $O(\epsilon)$ wave solution for constant shear current are then given as

$$w_{1,1} = -i\sigma_s \eta_{1,1} F_{ss} \quad (4.85)$$

The vortex force involves the slow variation of current and waves. Hence we need to specify the current and wave scales for comparison. Consider waves with amplitude 2 m propagate on a constant shear flow with surface velocity $q_{0,0}^s = 3.5$ m/s and shear $|\alpha| = 1$. The water depth is set as 25 m. We vary the wave lengths so that the non-dimensional wave number kh ranges from shallow water ($kh = 0.2$) to deep water ($kh = 3$). The wave solutions for depth uniform current are applied to MRL04 vortex force (Uchiyama *et al.*, 2010). The analytical wave solutions are applied to DK16 vortex force. To calculate the spacial gradient of variables, the slow spacial scale is assumed to be 5 km. The y -direction gradient of current shear is assumed to be positive $\partial \Omega^s / \partial Y > 0$. Both opposing current and following current are considered in the comparison. The results are given for three cases: deep water ($kh = 3$) as shown in Figure 4.1 and 4.2, intermediate water ($kh = 1$) as shown in Figure 4.3 - 4.4 and shallow water ($kh = 0.2$) as shown in 4.5 - 4.6. The conclusions are given as below

1). The Stokes drift velocity is slightly modified by the current shear effect as shown in upper right panel. DK16 Stokes drift velocity is slightly smaller than MRL04 near the water surface and larger near the bottom for the opposing current. This effect

reverses for the following current. The Stokes drift velocity magnitude is smaller for long waves. The velocity profile tends to be depth uniform for shallow water.

2). The DK16 x -component vortex force magnitude is slightly larger than MRL04 result for the opposing current and smaller for the following current. The magnitude also decreases from deep water to shallow water. The vertical profile tends to be linear for shallow water. The direction of x -component vortex force is determined by the y -direction gradient of current shear $\partial\Omega^s/\partial Y$.

3). The DK16 y -component vortex force deviates from MRL04 result from deep water to shallow water. It decreases and changes sign as the shear effects become larger for longer waves. After changing the sign, the DK16 y -component vortex force magnitude increases. The MRL04 result is nearly zero for shallow water.

The effects of surface current velocity $q_{0,0}^s$ and current shear Ω^s are also evaluated in Figure 4.7 and 4.8. The figures indicate that DK16 Stokes drift velocity and vortex force converges to MRL04 results for smaller surface current velocity or smaller current shear.

4.7 Wave-averaged Forces with Full Perturbation Solutions

So far, we have obtained the general form of Bernoulli head and vortex force for strong current with strong shear. We need to seek wave solutions to evaluate the wave-averaged forces. There are two methods considered here to introduce the current effects on wave solutions. One is following MRL04 and formulates the problem by assuming weak current. This method leads to the current-free linear wave solutions at the leading order and includes the current effects in order $O(\epsilon^2)$ wave equations. The other method is to following our strong current and strong shear assumption and get the Rayleigh equation. However, to avoid directly solving the Rayleigh equation, we obtain wave solutions from the KC89 perturbation method. The current effects will then appear in $O(\epsilon)$ perturbation solutions for the leading order wave equation. In this chapter, we focus on the reduction of our wave-averaged forces based on perturbation solutions. The comparison between numerical solutions and perturbation solutions in

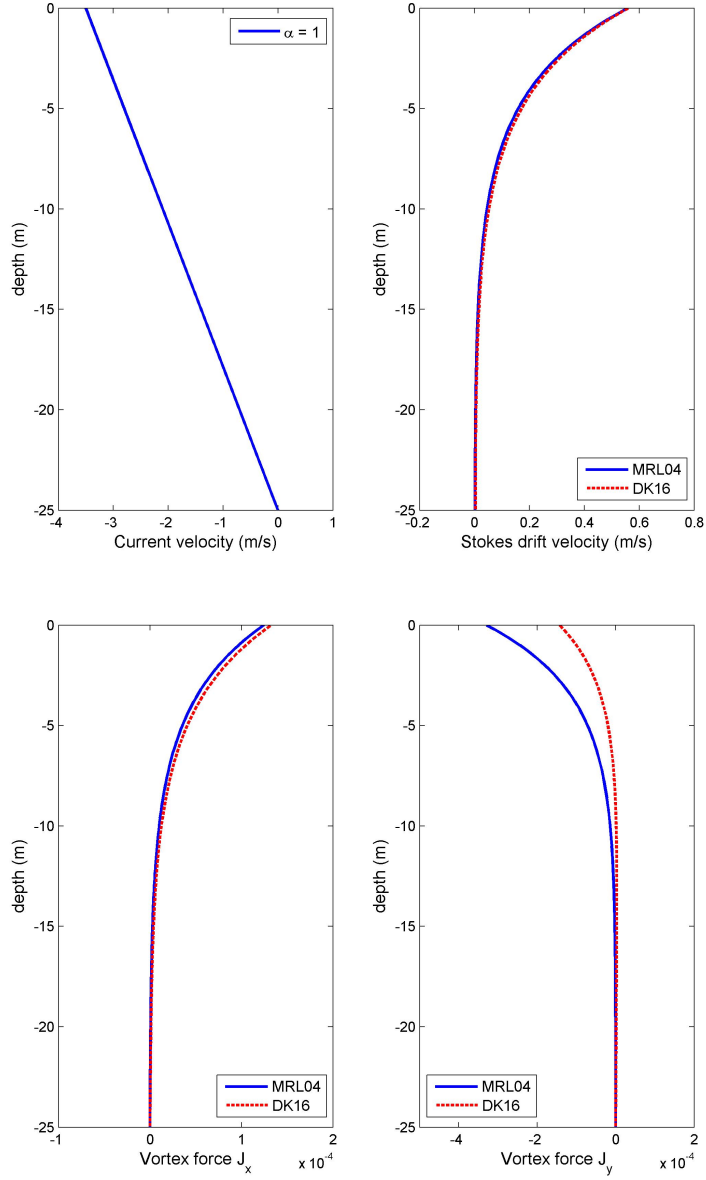


Figure 4.1: Opposing constant shear current and deep water ($\alpha = -1$, $kh = 3$). Blue Solid indicates MRL04 results; Red Dash indicates DK16 results. Upper Left: the surface current velocity is -3.5 m/s and bottom current velocity is zero. Upper Right: DK16 Stokes drift velocity is slightly larger than MRL04 for the opposing current. Lower Left: DK16 x -component vortex force magnitude is slightly larger than MRL04. Lower Right: DK16 y -component vortex force magnitude is smaller than MRL04.

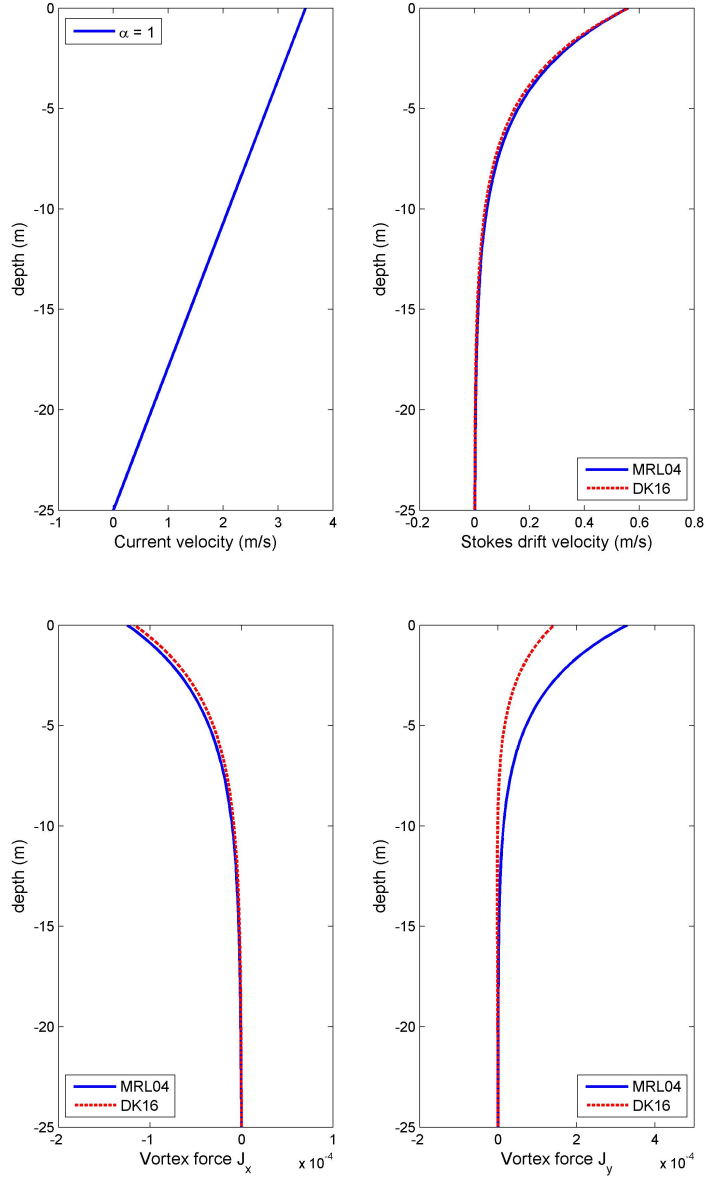


Figure 4.2: Following constant shear current in deep water ($\alpha = 1$, $kh = 3$). Blue Solid indicates MRL04 results; Red Dash indicates DK16 results. Upper Left: the surface current velocity is 3.5 m/s and bottom current velocity is zero. Upper Right: DK16 Stokes drift velocity is slightly smaller than MRL04 for the opposing current. Lower Left: DK16 x -component vortex force magnitude is slightly smaller than MRL04. Lower Right: DK16 y -component vortex force magnitude is smaller than MRL04.

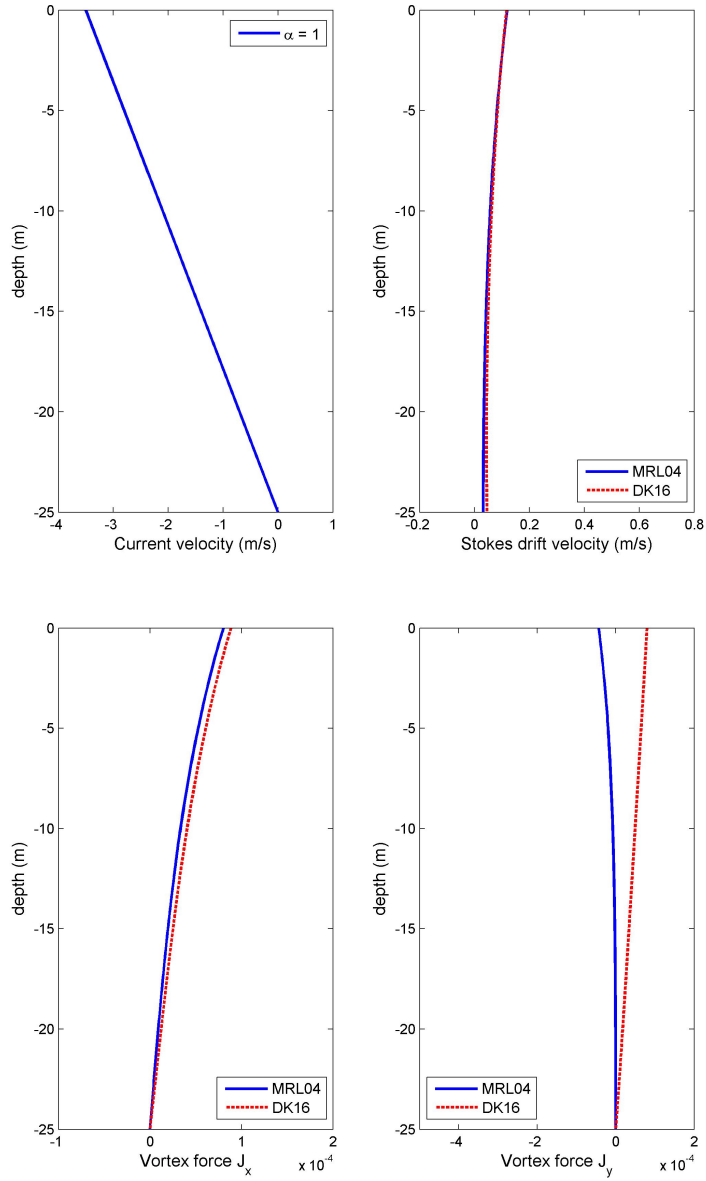


Figure 4.3: Opposing constant shear current in intermediate water ($\alpha = -1, kh = 1$). Blue Solid indicates MRL04 results; Red Dash indicates DK16 results. Upper Left: the surface current velocity is -3.5 m/s and bottom current velocity is zero. Upper Right: DK16 Stokes drift velocity is slightly smaller than MRL04 near the water surface and larger near the bottom. The velocity profile tends to be depth uniform. Lower Left: DK16 x -component vortex force magnitude is slightly larger than MRL04. Lower Right: DK16 y -component vortex force changes sign compared to MRL04 due to the current shear effect.

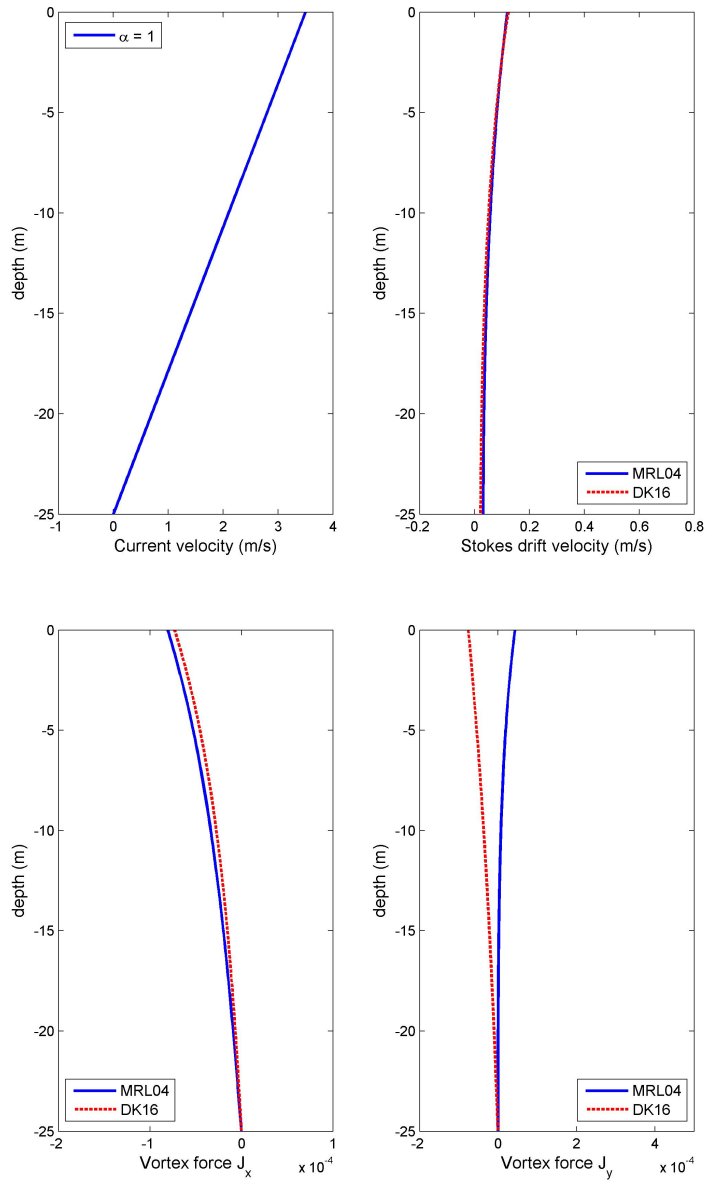


Figure 4.4: Following constant shear current and deep water ($\alpha = 1$, $kh = 1$). Blue Solid indicates MRL04 results; Red Dash indicates DK16 results. Upper Left: the surface current velocity is 3.5 m/s and bottom current velocity is zero. Upper Right: DK16 Stokes drift velocity is slightly larger than MRL04 near the water surface and smaller near the water bottom. The velocity profile tends to be depth uniform. Lower Left: DK16 x -component vortex force magnitude is slightly smaller than MRL04. Lower Right: DK16 y -component vortex force changes sign compared to MRL04 due to the current shear effect.

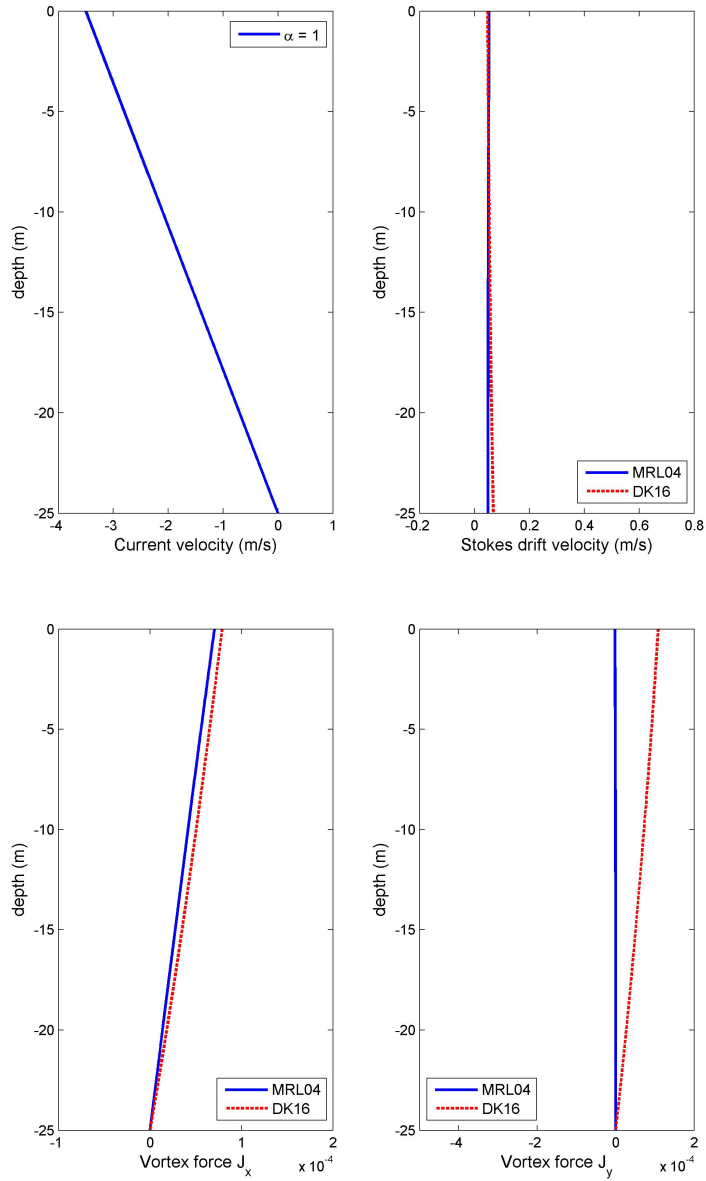


Figure 4.5: Opposing constant shear current in shallow water ($\alpha = -1$, $kh = 0.2$). Blue Solid indicates MRL04 results; Red Dash indicates DK16 results. Upper Left: the surface current velocity is -3.5 m/s and bottom current velocity is zero. Upper Right: DK16 Stokes drift velocity is slightly smaller than MRL04 near the water surface and larger near the bottom. The velocity profile tends to be depth uniform. Lower Left: DK16 x -component vortex force magnitude is slightly larger than MRL04. Lower Right: DK16 y -component vortex force changes sign compared to MRL04 due to the current shear effect. The MRL04 result is nearly zero.

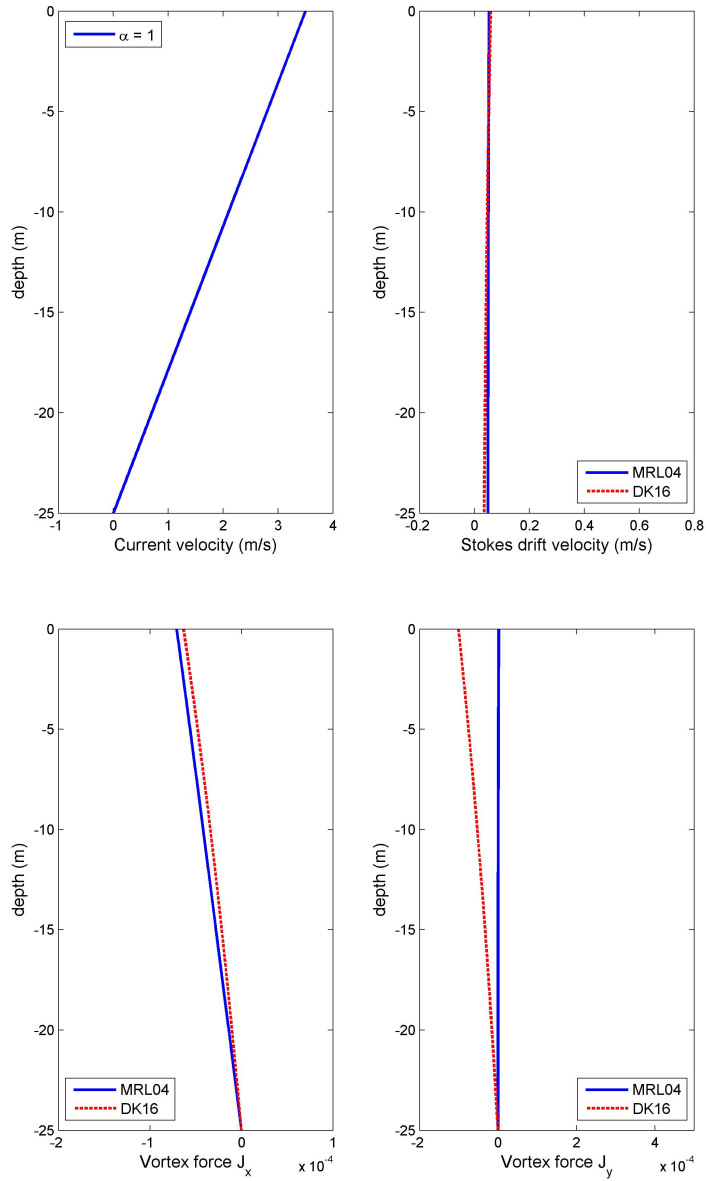


Figure 4.6: Following constant shear current and deep water ($\alpha = 1$, $kh = 0.2$). Blue Solid indicates MRL04 results; Red Dash indicates DK16 results. Upper Left: the surface current velocity is 3.5 m/s and bottom current velocity is zero. Upper Right: DK16 Stokes drift velocity is slightly larger than MRL04 near the water surface and smaller near the bottom. The velocity profile tends to be depth uniform. Lower Left: DK16 x -component vortex force magnitude is slightly smaller than MRL04. Lower Right: DK16 y -component vortex force changes sign compared to MRL04 due to the current shear effect. The MRL04 result is nearly zero.

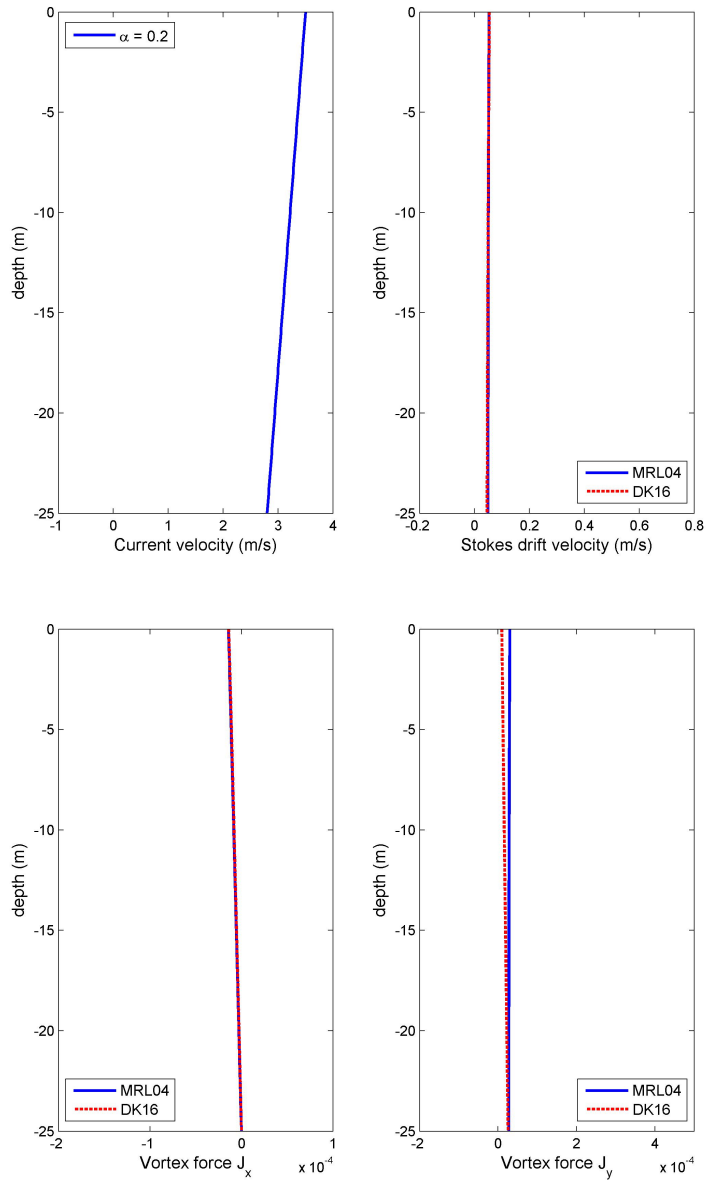


Figure 4.7: Following constant shear current in shallow water ($\alpha = 0.2$, $kh = 0.2$). Blue Solid indicates MRL04 results; Red Dash indicates DK16 results. Upper Left: the surface current velocity is -3.5 m/s. Upper Right: DK16 Stokes drift velocity converges to MRL04 for smaller current shear. Lower Left: DK16 x -component vortex force converges to MRL04 result. Lower Right: DK16 y -component vortex force converges to MRL04 result for smaller current shear. The MRL04 result is non-zero and proportional to Stokes drift velocity.

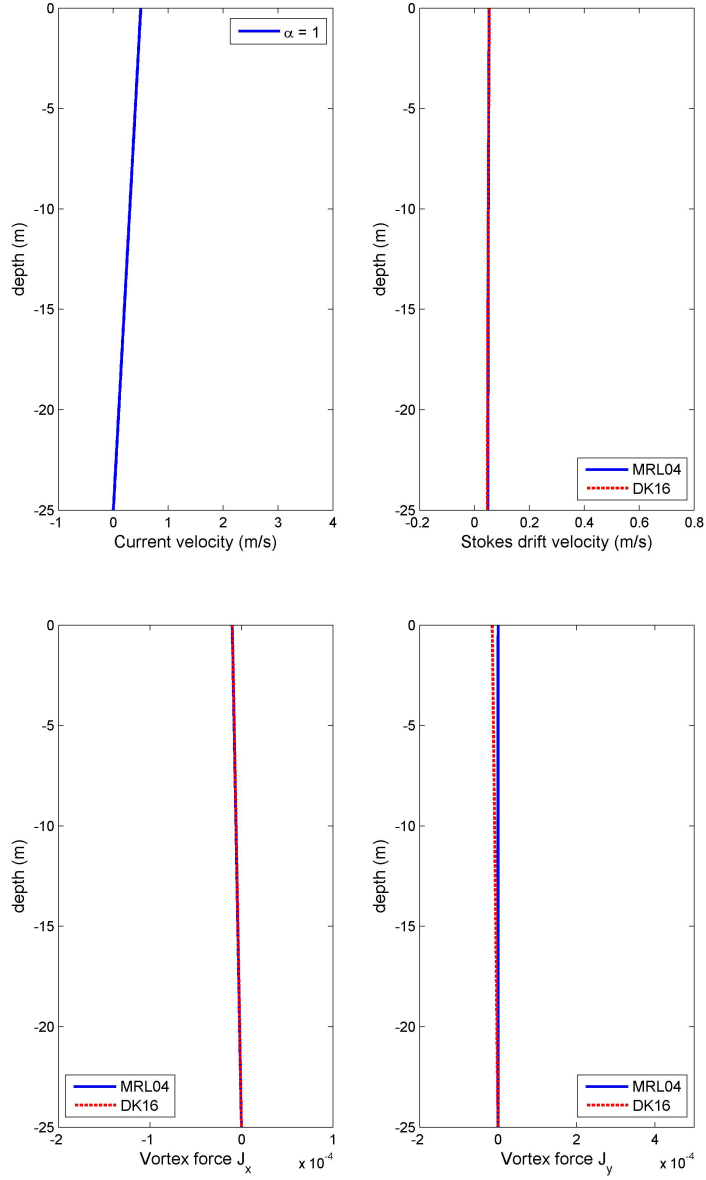


Figure 4.8: Following constant shear current in shallow water ($\alpha = 1$, $kh = 0.2$). Blue Solid indicates MRL04 results; Red Dash indicates DK16 results. Upper Left: the surface current velocity is -0.5 m/s. Upper Right: DK16 Stokes drift velocity converges to MRL04 for smaller surface current velocity. Lower Left: DK16 x -component vortex force converges to MRL04 result. Lower Right: DK16 y -component vortex force converges to MRL04 result for smaller surface current velocity. The MRL04 result is non-zero.

Chapter 3 suggests that the KC89 $O(\epsilon)$ perturbation solution is a good approximation. Hence, we follow the work done by KC89 to take $O(\epsilon)$ perturbation solutions to the wave-averaged forces (see Equation (4.48), (4.50) and (4.51)). It is noteworthy that slow scale variations ($\partial/\partial T, \nabla_H$) are not involved in $O(\epsilon)$ wave solutions. We may represent wave variables as the function of vertical coordinate z only. The Bernoulli head and vortex force can be rewritten as follow

$$\kappa = \epsilon^2 \kappa_2^{(0)} + \epsilon^3 (\kappa_2^{(1)} + \kappa_3^{(0)}) + O(\epsilon^4) \quad (4.86)$$

$$\kappa_2^{(0)} = \frac{1}{k^2} \frac{\partial w_{1,1}^{(0)}}{\partial z} \frac{\partial w_{1,-1}^{(0)}}{\partial z} + w_{1,1}^{(0)} w_{1,-1}^{(0)} + \frac{w_{1,1}^{(0)} w_{1,-1}^{(0)}}{\sigma_w^2} \frac{\partial \mathbf{q}_{0,0}}{\partial z} \cdot \frac{\partial \mathbf{q}_{0,0}}{\partial z} - \frac{w_{1,1}^{(0)} w_{1,-1}^{(0)}}{\sigma_w^2 k^2} \left(\frac{\partial \sigma_w}{\partial z} \right)^2 \quad (4.87)$$

$$\begin{aligned} \kappa_2^{(1)} &= \frac{1}{k^2} \left(\frac{\partial w_{1,1}^{(1)}}{\partial z} \frac{\partial w_{1,-1}^{(0)}}{\partial z} + \frac{\partial w_{1,1}^{(0)}}{\partial z} \frac{\partial w_{1,-1}^{(1)}}{\partial z} \right) + (w_{1,1}^{(1)} w_{1,-1}^{(0)} + w_{1,1}^{(0)} w_{1,-1}^{(1)}) \\ &+ \frac{w_{1,1}^{(1)} w_{1,-1}^{(0)} + w_{1,1}^{(0)} w_{1,-1}^{(1)}}{\sigma_w^2} \frac{\partial \mathbf{q}_{0,0}}{\partial z} \cdot \frac{\partial \mathbf{q}_{0,0}}{\partial z} - \frac{w_{1,1}^{(1)} w_{1,-1}^{(0)} + w_{1,1}^{(0)} w_{1,-1}^{(1)}}{\sigma_w^2 k^2} \left(\frac{\partial \sigma_w}{\partial z} \right)^2 \end{aligned} \quad (4.88)$$

$$\begin{aligned} \kappa_3^{(0)} &= \frac{1}{k^2} \left(\frac{\partial w_{1,1}^{(0)}}{\partial z} \frac{\partial w_{2,-1}^{(0)}}{\partial z} + \frac{\partial w_{1,-1}^{(0)}}{\partial z} \frac{\partial w_{2,1}^{(0)}}{\partial z} \right) + (w_{1,1}^{(0)} w_{2,-1}^{(0)} + w_{1,-1}^{(0)} w_{2,1}^{(0)}) \\ &+ \frac{w_{1,1}^{(0)} w_{2,-1}^{(0)} + w_{1,-1}^{(0)} w_{2,1}^{(0)}}{\sigma_w^2} \frac{\partial \mathbf{q}_{0,0}}{\partial z} \cdot \frac{\partial \mathbf{q}_{0,0}}{\partial z} - \frac{w_{1,1}^{(0)} w_{2,-1}^{(0)} + w_{1,-1}^{(0)} w_{2,1}^{(0)}}{\sigma_w^2 k^2} \left(\frac{\partial \sigma_w}{\partial z} \right)^2 \\ &+ \mathbf{Q}_{1,1}^{*(0)} \cdot \mathbf{q}_{1,-1}^{(0)} + \mathbf{Q}_{1,-1}^{*(0)} \cdot \mathbf{q}_{1,1}^{(0)} \end{aligned} \quad (4.89)$$

$$\begin{aligned} \mathbf{J} &= \mathbf{i}_z \times \left\{ -\frac{D}{DT} \left(\frac{\boldsymbol{\xi}_{0,0} \cdot \mathbf{k}}{\sigma_w^2} \mathbf{E}^{*(0)} + \frac{\partial \boldsymbol{\xi}_{0,0}}{\partial z} \frac{w_{1,1}^{(0)} w_{1,-1}^{(0)}}{\sigma_w^2} \right) - \frac{\mathbf{E}^{*(0)}}{\sigma_w^2} \frac{D}{DT} (\boldsymbol{\xi}_{0,0} \cdot \mathbf{k}) \right. \\ &- \frac{w_{1,1}^{(0)} w_{1,-1}^{(0)}}{\sigma_w^2} \frac{D}{DT} \left(\frac{\partial \boldsymbol{\xi}_{0,0}}{\partial z} \right) + \left(-\frac{2w_{1,1}^{(0)} w_{1,-1}^{(0)}}{\sigma_w^2} \frac{\partial \mathbf{q}_{0,0}}{\partial z} + \frac{\mathbf{E}^{*(0)}}{\sigma_w} \right) \cdot \nabla_H \boldsymbol{\xi}_{0,0} + \frac{\mathbf{E}^{*(0)}}{\sigma_w} \frac{\partial \chi_{1,0}}{\partial z} \\ &+ \left(\frac{2w_{1,1}^{(0)} w_{1,-1}^{(0)}}{\sigma_w^2} \frac{\partial \boldsymbol{\xi}_{0,0}}{\partial z} + \frac{\boldsymbol{\xi}_{0,0} \cdot \mathbf{k}}{\sigma_w^2} \mathbf{E}^{*(0)} \right) \cdot \nabla_H \mathbf{q}_{0,0} - \frac{\boldsymbol{\xi}_{0,0} \cdot \mathbf{k}}{\sigma_w^2} \mathbf{E}^{*(0)} \nabla_H \cdot \mathbf{q}_{0,0} \\ &+ \boldsymbol{\xi}_{0,0} \cdot \nabla_H \left(\frac{w_{1,1}^{(0)} w_{1,-1}^{(0)}}{\sigma_w^2} \frac{\partial \mathbf{q}_{0,0}}{\partial z} \right) + \frac{w_{1,1}^{(0)} w_{1,-1}^{(0)}}{\sigma_w^2} \boldsymbol{\xi}_{0,0} \cdot \nabla_H \left(\frac{\partial \mathbf{q}_{0,0}}{\partial z} \right) - \frac{\boldsymbol{\xi}_{0,0}}{\sigma_w} \cdot \nabla_H \mathbf{E}^{*(0)} \\ &\left. - \chi_{1,0} \mathbf{q}^{st(0)}(z) \right\} + O(\epsilon^4) \end{aligned} \quad (4.90)$$

$$K = \epsilon^2 K_2^{(0)} + \epsilon^3 (K_2^{(1)} + K_3^{(0)}) + O(\epsilon^4) \quad (4.91)$$

$$K_2^{(0)} = \frac{2w_{1,1}^{(0)}w_{1,-1}^{(0)}}{\sigma_w^2} \frac{\partial \mathbf{q}_{0,0}}{\partial z} \times \frac{\partial \boldsymbol{\xi}_{0,0}}{\partial z} - \frac{\sigma_w}{k^2} \frac{\partial}{\partial z} \left(\frac{w_{1,1}^{(0)}w_{1,-1}^{(0)}}{\sigma_w^2} \right) \mathbf{k} \times \left(\frac{\partial \mathbf{q}_{0,0}}{\partial z} \frac{\boldsymbol{\xi}_{0,0} \cdot \mathbf{k}}{\sigma_w} + \frac{\partial \boldsymbol{\xi}_{0,0}}{\partial z} \right) \quad (4.92)$$

$$K_2^{(1)} = \frac{2(w_{1,1}^{(1)}w_{1,-1}^{(0)} + w_{1,1}^{(0)}w_{1,-1}^{(1)})}{\sigma_w^2} \frac{\partial \mathbf{q}_{0,0}}{\partial z} \times \frac{\partial \boldsymbol{\xi}_{0,0}}{\partial z} - \frac{\sigma_w}{k^2} \frac{\partial}{\partial z} \left(\frac{w_{1,1}^{(1)}w_{1,-1}^{(0)} + w_{1,1}^{(0)}w_{1,-1}^{(1)}}{\sigma_w^2} \right) \mathbf{k} \times \left(\frac{\partial \mathbf{q}_{0,0}}{\partial z} \frac{\boldsymbol{\xi}_{0,0} \cdot \mathbf{k}}{\sigma_w} + \frac{\partial \boldsymbol{\xi}_{0,0}}{\partial z} \right) \quad (4.93)$$

$$\begin{aligned} K_3^{(0)} &= i\mathbf{q}_{1,1}^{(0)} \times \left[\frac{\mathbf{O}_{2,-1}^{(0)}}{\sigma_w} - i \frac{\partial \mathbf{q}_{0,0}}{\partial z} \frac{P_{2,-1}^{(0)}}{\sigma_w^2} + \frac{\partial \mathbf{q}_{0,0}}{\partial z} \frac{w_{2,-1}^{(0)}(\boldsymbol{\xi}_{0,0} \cdot \mathbf{k})}{\sigma_w^2} + \frac{\partial \boldsymbol{\xi}_{0,0}}{\partial z} \frac{w_{2,-1}^{(0)}}{\sigma_w} \right] \\ &- i\mathbf{q}_{1,-1}^{(0)} \times \left[\frac{\mathbf{O}_{2,1}^{(0)}}{\sigma_w} + i \frac{\partial \mathbf{q}_{0,0}}{\partial z} \frac{P_{2,1}^{(0)}}{\sigma_w^2} + \frac{\partial \mathbf{q}_{0,0}}{\partial z} \frac{w_{2,1}^{(0)}(\boldsymbol{\xi}_{0,0} \cdot \mathbf{k})}{\sigma_w^2} + \frac{\partial \boldsymbol{\xi}_{0,0}}{\partial z} \frac{w_{2,1}^{(0)}}{\sigma_w} \right] \\ &+ \left\{ \frac{1}{\sigma_w} \left[w_{2,-1}^{(0)} \frac{\partial \mathbf{q}_{0,0}}{\partial z} - \frac{\mathbf{k}}{k^2} \left(\sigma_w \frac{\partial w_{2,-1}^{(0)}}{\partial z} - w_{2,-1}^{(0)} \frac{\partial \sigma_w}{\partial z} \right) \right] + \mathbf{Q}_{1,-1}^{*(0)} \right\} \\ &\times \left[\frac{\partial \mathbf{q}_{0,0}}{\partial z} \frac{(\boldsymbol{\xi}_{0,0} \cdot \mathbf{k})w_{1,1}^{(0)}}{\sigma_w^2} + \frac{\partial \boldsymbol{\xi}_{0,0}}{\partial z} \frac{w_{1,1}^{(0)}}{\sigma_w} \right] \\ &+ \left\{ \frac{1}{\sigma_w} \left[w_{2,1}^{(0)} \frac{\partial \mathbf{q}_{0,0}}{\partial z} - \frac{\mathbf{k}}{k^2} \left(\sigma_w \frac{\partial w_{2,1}^{(0)}}{\partial z} - w_{2,1}^{(0)} \frac{\partial \sigma_w}{\partial z} \right) \right] + \mathbf{Q}_{1,1}^{*(0)} \right\} \\ &\times \left[\frac{\partial \mathbf{q}_{0,0}}{\partial z} \frac{(\boldsymbol{\xi}_{0,0} \cdot \mathbf{k})w_{1,-1}^{(0)}}{\sigma_w^2} + \frac{\partial \boldsymbol{\xi}_{0,0}}{\partial z} \frac{w_{1,-1}^{(0)}}{\sigma_w} \right] \end{aligned} \quad (4.94)$$

$$\begin{aligned} \mathbf{Q}_{1,1}^{*(0)} &= \frac{i}{\sigma_w} \left[\frac{\mathbf{k}}{k^2} \mathbf{k} \cdot \left(\frac{D\mathbf{q}_{1,1}^{(0)}}{DT} + \frac{1}{\rho} \nabla_{HP} p_{1,1}^{(0)} + \mathbf{q}_{1,1}^{(0)} \cdot \nabla_H \mathbf{q}_{0,0} \right) \right. \\ &- \left. \left(\frac{D\mathbf{q}_{1,1}^{(0)}}{DT} + \frac{1}{\rho} \nabla_{HP} p_{1,1}^{(0)} + \mathbf{q}_{1,1}^{(0)} \cdot \nabla_H \mathbf{q}_{0,0} \right) + \frac{\mathbf{k}}{k^2} \sigma_w \nabla_H \cdot \mathbf{q}_{1,1}^{(0)} \right] \end{aligned} \quad (4.95)$$

$$\mathbf{E}^{*(0)} = \frac{\mathbf{k}}{k^2} \left(\frac{\partial w_{1,1}^{(0)}w_{1,-1}^{(0)}}{\partial z} - \frac{2w_{1,-1}^{(0)}w_{1,1}^{(0)}}{\sigma_w} \frac{\partial \sigma_w}{\partial z} \right) + O(\epsilon^3) \quad (4.96)$$

$$\begin{aligned} \mathbf{q}^{st(0)} &= \frac{\partial}{\partial z} \left[\frac{\mathbf{k}}{k^2 \sigma_w} \frac{\partial w_{1,1}^{(0)}w_{1,-1}^{(0)}}{\partial z} - \frac{w_{1,1}^{(0)}w_{1,-1}^{(0)}}{\sigma_w^2} \left(\frac{\mathbf{k}}{k^2} \frac{\partial \sigma_w}{\partial z} + \frac{\partial \mathbf{q}_{0,0}}{\partial z} \right) \right] \\ &- \frac{w_{1,1}^{(0)}w_{1,-1}^{(0)}}{\sigma_w^2} \left(\frac{\mathbf{k}}{k^2} \frac{\partial^2 \sigma_w}{\partial z^2} + \frac{\partial^2 \mathbf{q}_{0,0}}{\partial z^2} \right) + O(\epsilon^3) \end{aligned} \quad (4.97)$$

where $w_{1,1}^{(0)}$ and $w_{1,1}^{(1)}$ are the $O(\epsilon^0)$ and $O(\epsilon)$ perturbation solutions, respectively. The wave-averaged forces in terms of perturbation solutions will also be implemented in our $NH\overline{WAVE}$ model as formulation for the strongly sheared current.

4.8 Depth-integrated Equations for Wave-averaged Flow

In this section, we integrate the horizontal momentum equation for mean flow with wave-averaged forces over depth. The resulting equations are the barotropic mode governing equations for a 3D ocean circulation model. We have left out density variations at this point. We combine all the orders of mean flow equations ($n = 0, 1, 2, 3$) in this section and use ϕ^c as the mean flow variables and ϕ^w as wave variables.

$$\phi^c = \sum_{n=0}^{\infty} \epsilon^n \phi_{n,0} = \phi_{0,0}(\mathbf{X}, z, T) + \epsilon \phi_{1,0}(\mathbf{X}, z, T) + \epsilon^2 \phi_{2,0}(\mathbf{X}, z, T) + \dots \quad (4.98)$$

$$\begin{aligned} \phi^w &= \sum_n \sum_{m \neq 0} \epsilon^n \phi_{n,m} E^m \\ &= \epsilon [\phi_{1,1}(\mathbf{X}, z, T)E + c.c.] + \epsilon^2 [\phi_{2,1}(\mathbf{X}, z, T)E + \phi_{2,2}(\mathbf{X}, z, T)E^2 + c.c.] + \dots \end{aligned} \quad (4.99)$$

We integrate the horizontal momentum equation over depth. The results give the depth-integrated equations for wave-averaged flow. First we look at the surface boundary conditions.

The surface kinematic boundary condition is given by

$$\begin{aligned} w^c - \frac{\partial \eta^{pc}}{\partial T} - \mathbf{q}^c \cdot \nabla_H \eta^{pc} &= \epsilon^2 \left[\frac{\partial \eta^{st}}{\partial T} + \mathbf{q}^c \cdot \nabla_H \eta^{st} + \nabla_H \cdot \mathbf{Q}^{St} \right. \\ &\left. + \left(\langle \eta^w \frac{\partial \mathbf{q}^w}{\partial z} \rangle + \frac{1}{2} \frac{\partial^2 \mathbf{q}^c}{\partial z^2} \langle \eta^{w2} \rangle \right) \cdot \nabla_H \eta^c \right]; \quad z = \eta^c \end{aligned} \quad (4.100)$$

Here we treat the instantaneous surface elevation $\eta = \eta^c + \epsilon \eta^w$, where η^c is mean water surface level including wave setup/down. Therefore we can further divide $\eta^c = \eta^{pc} + \epsilon^2 \eta^{st}$, where η^{pc} stands for pure current and long wave contribution to mean water surface level and η^{st} accounts for wave setup/down. Then we expand kinematic surface

boundary condition at $z = \eta^c$ to be consistent with multiple scale expansion. We also consider the definition of Stokes drift in Eulerian framework.

$$\mathbf{Q}^{St} = \epsilon^2 \left(\frac{1}{2} \frac{\partial \mathbf{q}^c}{\partial z} \langle \eta^{w2} \rangle + \langle \mathbf{q}^w \eta^w \rangle \right) \Big|_{z=\eta^c} \quad (4.101)$$

The expression is equivalent to Equation 4.34 up to $O(\epsilon^2)$. Term $\nabla_H \cdot \mathbf{Q}^{St}$ is the mass transfer at the surface as mentioned in Hasselmann (1971) and Newberger and Allen (2007a). The last term on the right hand side in (4.100) is usually neglected as mean surface elevation is assumed to be much smaller than the water depth $\eta^c/h \sim O(\epsilon)$. However, this term can't be neglected in the surf zone. We keep it here in case that long wave amplitude is comparable to still water depth in shallow water region.

The surface dynamic boundary condition is given by

$$p^c = - \langle \eta^w \frac{\partial p^w}{\partial z} \rangle; \quad z = \eta^c \quad (4.102)$$

The wave pressure term in (4.102) corresponds to *MRL04* (9.11) in *Section 9.3*.

The vertical momentum equation gives the wave-averaged pressure $p^c(z)$. Here we only consider the wave-induced dynamic pressure.

$$\begin{aligned} p^c(z) &= p^c(\eta^c) + \rho g(\eta^c - z) + \rho [\epsilon^3 \int_z^{\eta^c} \nabla_H \cdot \langle \mathbf{q}^w w^w \rangle dz \\ &+ \epsilon^2 (\langle w^{w2}(\eta^c) \rangle - \langle w^{w2}(z) \rangle)]; \quad -h \leq z \leq \eta^c \end{aligned} \quad (4.103)$$

The term $\int_z^{\eta^c} \nabla_H \cdot \langle \mathbf{q}^w w^w \rangle dz$ is always zero because \mathbf{q}^w and w^w are out of phase. The $O(\epsilon)$ wave equations satisfy $\eta^w \partial p^w / \partial z \Big|_{z=\eta^c} = \rho \langle w^{w2}(\eta^c) \rangle$ at the free surface (see Equation (3.2) and (3.5)). Thus the wave-averaged pressure $p^c(z)$ can be reduced to

$$p^c(z) = \rho g(\eta^c - z) - \rho \langle w^{w2}(z) \rangle; \quad -h \leq z \leq \eta^c \quad (4.104)$$

The bottom condition is given by

$$w^c = -\mathbf{q}^c \cdot \nabla_H h; \quad z = -h \quad (4.105)$$

The depth-integrated continuity equation is given by

$$\begin{aligned} \frac{\partial \eta^{pc}}{\partial T} + \nabla_H \cdot \left(\int_{-h}^{\eta^c} \mathbf{q}^c dz \right) &= \epsilon^2 \left[-\frac{\partial \eta^{st}}{\partial T} \right. \\ &\left. - \nabla_H \cdot \mathbf{Q}^{St} - \left(\langle \eta^w \frac{\partial \mathbf{q}^w}{\partial z} \rangle + \frac{1}{2} \frac{\partial^2 \mathbf{q}^c}{\partial z^2} \langle \eta^{w2} \rangle \right) \cdot \nabla_H \eta^c \right]_{z=\eta^c} \end{aligned} \quad (4.106)$$

The depth-integrated horizontal momentum equation is given by

$$\begin{aligned} \frac{\partial}{\partial T} \left(\int_{-h}^{\eta^c} \mathbf{q}^c dz \right) + \nabla_H \cdot \left(\int_{-h}^{\eta^c} \mathbf{q}^c \mathbf{q}^c dz \right) + \int_{-h}^{\eta^c} \frac{1}{\rho} \nabla_H p^c dz &= \epsilon^2 \left\{ - \int_{-h}^{\eta^c} \nabla_H \kappa dz + \int_{-h}^{\eta^c} \mathbf{J} dz \right. \\ &\left. - \mathbf{q}^c|_{z=\eta^c} \left[\nabla_H \cdot \mathbf{Q}^{St} + \left(\langle \eta^w \frac{\partial \mathbf{q}^w}{\partial z} \rangle + \frac{1}{2} \frac{\partial^2 \mathbf{q}^c}{\partial z^2} \langle \eta^{w2} \rangle \right) \cdot \nabla_H \eta^c \right]_{z=\eta^c} \right\} \end{aligned} \quad (4.107)$$

To compare with Smith's (2006) mean flow equation (2.28 and 2.29), we adopt the leading order wave solutions for depth-uniform current and assume $\eta^c/h \sim O(\epsilon)$. Terms related to $\nabla_H \eta^c$ in surface boundary condition and depth-integrated continuity equation are neglected. The mean pressure (4.103) is kept up to $O(\epsilon^2)$. The first term on the RHS of (4.108) is the combined term of Bernoulli head and wave-induced dynamic pressure, which causes wave setup/down (4.109). The second term is the depth-integrated vortex force based on \mathbf{J} in (4.56) and \mathbf{q}^{st} in (4.65). The third term is the momentum change due to wave-induced mass source/sink at the surface. If we consider wave dissipation during propagation, we can add a dissipation term \mathbf{D}^w as a driving force on the RHS, which is identical to Smith's (2006) results.

$$\begin{aligned} \frac{\partial}{\partial T} \left(\int_{-h}^{\eta^c} \mathbf{q}^c dz \right) + \nabla_H \cdot \left(\int_{-h}^{\eta^c} \mathbf{q}^c \mathbf{q}^c dz \right) + gH \nabla_H \eta^c &= \epsilon^2 \{ gH \nabla_H \eta^{st} \\ &+ \mathbf{Q}^{St} \times (\nabla_H \times \mathbf{q}^c|_{z=\eta^c}) - \mathbf{q}^c|_{z=\eta^c} [\nabla_H \cdot \mathbf{Q}^{St}] \} + \mathbf{D}^w \end{aligned} \quad (4.108)$$

$$\eta^{st} = -\frac{1}{2g} \langle \mathbf{q}^{w2} - w^{w2} \rangle; \quad z = \eta^c \quad (4.109)$$

$$\mathbf{Q}^{St} = \int_{-h}^{\eta^c} \mathbf{q}^{st} dz \quad (4.110)$$

$$\frac{\partial \eta^{pc}}{\partial T} + \nabla_H \cdot \left(\int_{-h}^{\eta^c} \mathbf{q}^c dz \right) = \epsilon^2 \left[-\frac{\partial \eta^{st}}{\partial T} - \nabla_H \cdot \mathbf{Q}^{St} \right]_{z=\eta^c} \quad (4.111)$$

$$w^c - \frac{\partial \eta^{pc}}{\partial T} - \mathbf{q}^c \cdot \nabla_H \eta^{pc} = \epsilon^2 \left[\frac{\partial \eta^{st}}{\partial T} + \mathbf{q}^c \cdot \nabla_H \eta^{st} + \nabla_H \cdot \mathbf{Q}^{St} \right]; \quad z = \eta^c \quad (4.112)$$

$$p^c = - \langle \eta^w \frac{\partial p^w(\eta^c)}{\partial z} \rangle = -\rho \langle w^{w2}(\eta^c) \rangle; \quad z = \eta^c \quad (4.113)$$

$$p^c(z) = \rho g(\eta^c - z) - \rho \langle w^{w2}(z) \rangle; \quad -h \leq z \leq \eta^c \quad (4.114)$$

Chapter 5

THE COUPLED NHWAVE/SWAN MODEL ($NH\overline{WAVE}$)

The wave-current interaction theory and application for waves propagating on a strongly sheared current have been presented in the last few chapters. The wave-averaged forces in the mean flow momentum equation are given in terms of the Craik-Leibovich vortex force formalism. The wave action conservation equation including the effect of vertical current shear is derived. Solutions to wave Rayleigh instability equation are required to obtain the wave-averaged forces. The comparison with numerical solutions and perturbation solutions of the wave Rayleigh equation based on the measured current velocity profile is discussed. Results suggest that the perturbation solution up to $O(\epsilon)$ is a fairly good approximation to wave solutions for the real current velocity profile. Furthermore, the numerical study of the wave action conservation equation recommends that the depth-weighted current be used as the equivalent uniform current in the wave action flux. In addition, the dependence of the depth-weighted current on wave number should also be considered in the wave action advection velocity for the spectral wave model. Finally, the wave-averaged forces are computed using the perturbation solution instead of the numerical solution to avoid extra computation time. The formulation is an extension of the McWilliams *et al.* (2004) vortex force formalism to include strong current vertical shear effects. The ultimate goal of the study is to apply the wave-current interaction theory to the coupled ocean circulation/wave model system.

Efforts have been made in the numerical modeling of wave-current interaction during the past decade. Warner *et al.* (2008) developed a three-dimensional wave-current interaction model based on the USGS/ROMS and SWAN wave model. The

wave-averaged forces in the coupled model are based on Mellor’s (2003, 2005) depth-dependent radiation stress formulation. The model coupling of ROMS and SWAN relies on the Model-Coupling Toolkit (MCT), which provides protocols for the decomposition and allocation of model grids among different processors and efficient data transfer between models. SWAN sends wave heights, wavelength, averaged wave periods at surface and bottom, wave direction, near-bottom orbital velocity and wave energy dissipation to ROMS. ROMS sends water depth, mean surface elevation and depth-averaged current velocity to SWAN. In the COAWST model, the depth-weighted current derived by Kirby and Chen (1989) is implemented by Kumar *et al.* (2011). The time interval of data exchange between wave model and flow model can be adjusted for different cases.

The formulation obtained by Dingemans *et al.* (1987) is adopted in the coupled Delft3D-FLOW and SWAN model. The radiation stress is separated into three components in terms of wave energy dissipation, the gradient of a volume force and some extra rotational terms. In the 3D implementation, the wave dissipation due to depth-induced breaking and whitecapping is applied to the top layer and the wave dissipation due to bottom friction is applied to the bed layer. The remaining terms are added to the momentum equation and spread over the water column. The depth-weighted current of KC89 also included as an option passing to SWAN in the coupled Delft3D-FLOW and SWAN model (Lesser, 2009; Elias *et al.*, 2012).

The wave-averaged forces that consist of a surface stress caused by wave dissipation, a body force which is related to the vortex force and a gradient part of the radiation stress are derived by Newberger and Allen (2007a). The formulation is applied to the extended Princeton Ocean Model (POM) and validated with DUCK94 data (Newberger and Allen, 2007b). Shi *et al.* (2006) formulate a Craik-Leibovich wave vortex force for a quasi-3D circulation model. In the model, numerical consistency in using two different types of wave forces (radiation stress and vortex force) are discussed. The model is validated in rip currents simulations. Results suggest that both formulations generate identical results when the wave and circulation models are closely coupled.

The Craik-Leibovich vortex force formulation gives a closer result than the radiation stress formulation, when the models are not closely coupled at each time step. The paper also indicates that a tight model coupling plays a key role in the wave-current interaction. Uchiyama *et al.* (2010) present a wave-current interaction model with the vortex force formulation based on UCLA/ROMS and SWAN (McWilliams *et al.*, 2004; Uchiyama *et al.*, 2010). The wave dissipation driving force is divided vertically by using a depth-dependent function that represents the vertical penetration of momentum induced by breaking waves and rollers from the surface. Several alternative shapes of the vertical function are provided including the first one as proposed by Warner *et al.* (2008). The function is designed to vertically distribute the stress terms related to wave rollers and exponentially decays with depth. The model is validated using DUCK94 experiment (Newberger and Allen, 2007b). Kumar *et al.* (2011, 2012) apply both revised version of radiation stress by Mellor (2008) and vortex force formulation by McWilliams *et al.* (2004) in USGS/ROMS and SWAN. Several simulations such as longshore current, rip current and DUCK94 are presented and the cross-shore and vertical distribution of wave forces are illustrated.

In this paper, the coupling of a wave-averaged version of the NHWAVE (Ma *et al.*, 2012) non-hydrostatic circulation model with the SWAN wave model is developed. The McWilliams *et al.* (2004) vortex force formalism is first utilized and tested in this coupled model. An extension to the strong current shear discussed in Chapter 4 is then added and compared with McWilliams *et al.* (2004) vortex force formalism.

5.1 Introduction to NHWAVE Model

A non-hydrostatic model (NHWAVE) for simulating dispersive free-surface hydrodynamics has been developed by Ma *et al.* (2012). The model solves the incompressible Reynolds-Averaged Navier-Stokes equations in surface and terrain-following form using a σ -coordinate transformation. A hybrid finite-volume and finite-difference scheme is adopted to discretize the equations. A staggered grid framework is provided, in which the velocity is at the cell center and the pressure is at the cell vertical

face. Thus the pressure boundary condition at the free surface can be precisely imposed. A Shock-capturing Godunov-type scheme is used to solve the momentum equations. Bottom movement is considered in order to simulate the underwater landslide-generated tsunamis. The hydrostatic equations are solved by a well-balanced finite volume method. The fluxes at cell faces are estimated by HLL Riemann approximation. To obtain the second-order temporal accuracy, the nonlinear Strong Stability-Preserving (SSP) Runge-Kutta scheme is adopted for adaptive time stepping (Gottlieb *et al.*, 2001). The model is parallelized using the Message Passing Interface (MPI). The high performance pre-conditioner HYPRE software library is used to solve the Poisson equation (<http://acts.nersc.gov/hypre/>).

5.1.1 Governing equations

Following Ma *et al.* (2012), the incompressible Navier-Stokes equations in Cartesian coordinates (x^*, y^*, z^*, t^*) are transformed into σ -coordinates (x, y, σ, t) , where $\sigma = (z^* + h)/H$. $h(x, y, t)$ is still water depth, $\eta(x, y, t)$ water surface elevation, and $H(x, y, t) = h + \eta$ is the total local water depth. The final form of momentum equations are given below. g is gravitational acceleration. $u(x, y, \sigma, t)$, $v(x, y, \sigma, t)$, $w(x, y, \sigma, t)$ are the flow velocity. $\omega(x, y, \sigma, t)$ is the vertical velocity in σ -coordinates, which is defined as the velocity normal to a constant σ level. ρ is water density. $p(x, y, \sigma, t)$ is pressure. $p_d(x, y, \sigma, t)$ is dynamic pressure. p and p_d are related by $p = p_d + \rho g(\eta - z^*)$. τ_{ij} , $(i, j) = x, y, z$ is the turbulence stress. The resulting equations are given by

$$\frac{\partial H}{\partial t} + \frac{\partial Hu}{\partial x} + \frac{\partial Hv}{\partial y} + \frac{\partial \omega}{\partial \sigma} = 0 \quad (5.1)$$

$$\frac{\partial \mathbf{U}}{\partial t} + \frac{\partial \mathbf{F}}{\partial x} + \frac{\partial \mathbf{G}}{\partial y} + \frac{\partial \mathbf{H}}{\partial \sigma} = \mathbf{S}_h + \mathbf{S}_p + \mathbf{S}_\tau \quad (5.2)$$

$$\mathbf{U} = (Hu, Hv, Hw)^T \quad (5.3)$$

$$\mathbf{F} = (Huu + \frac{1}{2}gH^2, Huv, Hwv)^T \quad (5.4)$$

$$\mathbf{G} = (Huv, Hvv + \frac{1}{2}gH^2, Hvw)^T \quad (5.5)$$

$$\mathbf{H} = (u\omega, v\omega, w\omega)^T \quad (5.6)$$

$$\mathbf{S}_h = (gH \frac{\partial h}{\partial x}, gH \frac{\partial h}{\partial y}, 0)^T \quad (5.7)$$

$$\mathbf{S}_p = (-\frac{H}{\rho}(\frac{\partial p_d}{\partial x} + \frac{\partial p_d}{\partial \sigma} \frac{\partial \sigma}{\partial x^*}), -\frac{H}{\rho}(\frac{\partial p_d}{\partial y} + \frac{\partial p_d}{\partial \sigma} \frac{\partial \sigma}{\partial y^*}), -\frac{1}{\rho} \frac{\partial p_d}{\partial \sigma})^T \quad (5.8)$$

$$\mathbf{S}_\tau = (HS_{\tau x}, HS_{\tau y}, HS_{\tau z})^T \quad (5.9)$$

$$S_{\tau x} = \frac{\partial \tau_{xx}}{\partial x} + \frac{\partial \tau_{xx}}{\partial \sigma} \frac{\partial \sigma}{\partial x^*} + \frac{\partial \tau_{xy}}{\partial y} + \frac{\partial \tau_{xy}}{\partial \sigma} \frac{\partial \sigma}{\partial y^*} + \frac{\partial \tau_{xz}}{\partial \sigma} \frac{\partial \sigma}{\partial z^*} \quad (5.10)$$

$$S_{\tau y} = \frac{\partial \tau_{yx}}{\partial x} + \frac{\partial \tau_{yx}}{\partial \sigma} \frac{\partial \sigma}{\partial x^*} + \frac{\partial \tau_{yy}}{\partial y} + \frac{\partial \tau_{yy}}{\partial \sigma} \frac{\partial \sigma}{\partial y^*} + \frac{\partial \tau_{yz}}{\partial \sigma} \frac{\partial \sigma}{\partial z^*} \quad (5.11)$$

$$S_{\tau z} = \frac{\partial \tau_{zx}}{\partial x} + \frac{\partial \tau_{zx}}{\partial \sigma} \frac{\partial \sigma}{\partial x^*} + \frac{\partial \tau_{zy}}{\partial y} + \frac{\partial \tau_{zy}}{\partial \sigma} \frac{\partial \sigma}{\partial y^*} + \frac{\partial \tau_{zz}}{\partial \sigma} \frac{\partial \sigma}{\partial z^*} \quad (5.12)$$

where ω is defined as the vertical velocity in σ -coordinates. ω is zero at the surface and the bottom.

$$\omega = H \frac{d\sigma}{dt^*} = H(\frac{\partial \sigma}{\partial t^*} + u \frac{\partial \sigma}{\partial x^*} + v \frac{\partial \sigma}{\partial y^*} + w \frac{\partial \sigma}{\partial z^*}) \quad (5.13)$$

$$\omega(1) = 0 \quad (5.14)$$

$$\omega(0) = 0 \quad (5.15)$$

The turbulent stress is expressed using velocity strain rate and turbulent viscosity ν_t .

$$\tau_{xx} = 2\nu_t(\frac{\partial u}{\partial x} + \frac{\partial u}{\partial \sigma} \frac{\partial \sigma}{\partial x^*}) \quad (5.16)$$

$$\tau_{yy} = 2\nu_t(\frac{\partial v}{\partial y} + \frac{\partial v}{\partial \sigma} \frac{\partial \sigma}{\partial y^*}) \quad (5.17)$$

$$\tau_{zz} = 2\nu_t(\frac{\partial w}{\partial \sigma} \frac{\partial \sigma}{\partial z^*}) \quad (5.18)$$

$$\tau_{xy} = \tau_{yx} = \nu_t(\frac{\partial u}{\partial y} + \frac{\partial u}{\partial \sigma} \frac{\partial \sigma}{\partial y^*} + \frac{\partial v}{\partial x} + \frac{\partial v}{\partial \sigma} \frac{\partial \sigma}{\partial x^*}) \quad (5.19)$$

$$\tau_{xz} = \tau_{zx} = \nu_t(\frac{\partial u}{\partial \sigma} \frac{\partial \sigma}{\partial z^*} + \frac{\partial w}{\partial x} + \frac{\partial w}{\partial \sigma} \frac{\partial \sigma}{\partial x^*}) \quad (5.20)$$

$$\tau_{yz} = \tau_{zy} = \nu_t(\frac{\partial v}{\partial \sigma} \frac{\partial \sigma}{\partial z^*} + \frac{\partial w}{\partial y} + \frac{\partial w}{\partial \sigma} \frac{\partial \sigma}{\partial y^*}) \quad (5.21)$$

The relation between σ with x^* , y^* , z^* , t^* is

$$\frac{\partial \sigma}{\partial t^*} = \frac{1}{H} \frac{\partial h}{\partial t^*} - \frac{\sigma}{H} \frac{\partial H}{\partial t^*} = \frac{1}{H} \frac{\partial h}{\partial t} - \frac{\sigma}{H} \frac{\partial H}{\partial t} \quad (5.22)$$

$$\frac{\partial \sigma}{\partial x^*} = \frac{1}{H} \frac{\partial h}{\partial x^*} - \frac{\sigma}{H} \frac{\partial H}{\partial x^*} = \frac{1}{H} \frac{\partial h}{\partial x} - \frac{\sigma}{H} \frac{\partial H}{\partial x} \quad (5.23)$$

$$\frac{\partial \sigma}{\partial y^*} = \frac{1}{H} \frac{\partial h}{\partial y^*} - \frac{\sigma}{H} \frac{\partial H}{\partial y^*} = \frac{1}{H} \frac{\partial h}{\partial y} - \frac{\sigma}{H} \frac{\partial H}{\partial y} \quad (5.24)$$

$$\frac{\partial \sigma}{\partial z^*} = \frac{1}{H} \quad (5.25)$$

5.1.2 Boundary Conditions

In NHWAVE, boundary conditions are required to solve the governing equations. At the free surface, the continuity of normal and tangential stresses are enforced. Without wind stress, the tangential stress equals zero. If we assume that the mean water surface is never steep or wavy and neglect $\partial \sigma / \partial x^*$ and $\partial \sigma / \partial y^*$ terms in higher order derivatives (Derakhti *et al.*, 2016), the surface boundary condition can be written as

$$\left. \frac{\partial u}{\partial \sigma} \right|_{z=\eta} = \left. \frac{\partial v}{\partial \sigma} \right|_{z=\eta} = 0 \quad (5.26)$$

The kinematic boundary condition at the free surface is

$$w|_{z=\eta} = \frac{\partial \eta}{\partial t} + u \frac{\partial \eta}{\partial x} + v \frac{\partial \eta}{\partial y} \quad (5.27)$$

Without atmospheric pressure changes, tangential stress or normal stress, the zero pressure condition is enforced at the free surface when solving the Poisson equation.

$$p|_{z=\eta} = 0 \quad (5.28)$$

At the bottom, the tangential stress and normal velocity are prescribed. The normal velocity w includes the rate of change of bottom with time to generate landslide (Ma *et al.*, 2013).

$$w|_{z=-h} = -\frac{\partial h}{\partial t} - u \frac{\partial h}{\partial x} - v \frac{\partial h}{\partial y} \quad (5.29)$$

For the horizontal velocities, either free-slip boundary conditions

$$\frac{\partial u}{\partial \sigma}\bigg|_{z=-h} = \frac{\partial v}{\partial \sigma}\bigg|_{z=-h} = 0 \quad (5.30)$$

The Neumann boundary condition is used to get the dynamic pressure, which is directly obtained from the vertical momentum equation.

$$\frac{\partial p}{\partial \sigma}\bigg|_{z=-h} = -\rho H \frac{dw}{dt}\bigg|_{z=-h} \quad (5.31)$$

where w is given by the bottom boundary condition.

5.1.3 Turbulence Model

In this study, the nonlinear $k-\epsilon$ model (Lin and Liu, 1998) is applied to simulate the turbulence generated by sheared current. The equations are given by

$$\begin{aligned} \frac{\partial H k^{tur}}{\partial t} + \nabla \cdot (H \mathbf{u}_m k^{tur}) &= \nabla \cdot \left[H \left(\nu + \frac{\nu_t}{\sigma_k} \right) \nabla k^{tur} \right] + H (P_s + P_b - \epsilon^{tur}) \quad (5.32) \\ \frac{\partial H \epsilon^{tur}}{\partial t} + \nabla \cdot (H \mathbf{u}_m \epsilon^{tur}) &= \nabla \cdot \left[H \left(\nu + \frac{\nu_t}{\sigma_\epsilon} \right) \nabla \epsilon^{tur} \right] \\ &+ \frac{\epsilon^{tur}}{k^{tur}} H (C_{1\epsilon} P_s + C_{3\epsilon} P_b - C_{2\epsilon} \epsilon^{tur}) \quad (5.33) \end{aligned}$$

where \mathbf{u}_m is the mixture fluid phase velocity considering both liquid and bubble. k^{tur} is turbulent kinetic energy, ϵ^{tur} is turbulent dissipation rate, $\sigma_k = 1.0$, $\sigma_\epsilon = 1.3$, $C_{1\epsilon} = 1.44$, $C_{2\epsilon} = 1.92$, $C_{3\epsilon} = -1.4$ are empirical coefficients (Rodi, 1980). P_s is the shear production. P_b is the buoyancy production, which is described as

$$P_b = -\frac{1}{\rho_0} g \nu_t \frac{\partial \rho_m}{\partial z} \quad (5.34)$$

ρ_0 is the reference density of the incompressible liquid, and ρ_m is the mixture fluid phase density.

5.2 Introduction to SWAN Wave Model

The calculation of the wave-averaged driving forces in the momentum equations requires wave properties such as wave height, wave direction, wave length and wave energy dissipation. Wave period and bottom orbital velocity are needed for wave-averaged

bottom stress. In the coupled numerical model, these variables are obtained from the third-generation numerical wave model SWAN (Simulating Waves Nearshore) (Booij *et al.*, 1999). The model governing equation is the wave action conservation equation for each discrete spectral component, which accounts for wave refraction by bathymetry and ambient currents. The model is driven by local winds and boundary data. Physical processes such as wind generation, white-capping, bottom dissipation and quadruplet wave-wave interactions are explicitly represented. Depth-induced wave breaking and triad wave-wave interactions are also included. The numerical propagation scheme is implicit.

5.2.1 Wave Action Balance Equation

In SWAN, wave propagation is described using the two-dimensional wave action density spectrum $N(\sigma_w, \theta)$, where σ_w is wave intrinsic (relative) frequency and θ is wave direction. The reason to using the wave action as the computing property is because wave energy density is no longer conserved in the presence of the slowly varying ambient current (Bretherton and Garrett, 1968). Therefore the evolution of wave action spectrum is described in the Cartesian coordinates.

$$\frac{\partial N}{\partial t} + \frac{\partial}{\partial x}(c_x N) + \frac{\partial}{\partial y}(c_y N) + \frac{\partial}{\partial \sigma_w}(c_\sigma N) + \frac{\partial}{\partial \theta}(c_\theta N) = \frac{S}{\sigma_w} \quad (5.35)$$

The first term on the LHS is the local changing rate of wave action density with time. The second and the third term account for the wave action density propagation in horizontal space. The fourth term stands for the shifting of the intrinsic frequency due to the variations in bathymetry and ambient currents. The fifth term represents wave refraction induced by varying bathymetry and currents. Both the wave action density and the propagation speeds in SWAN are based on linear wave theory. The term S on the RHS contains all the source terms such as wind-generation, dissipation and nonlinear wave-wave interactions. The introduction to each source term included in SWAN is given by Booij *et al.* (1999).

In our coupled model, we provide the depth-weighted current by Kirby and Chen (1989) as an alternative. The effects of depth-averaged current and depth-weighted current on wave action have been compared in Chapter 3. In the strongly sheared current case, the current velocity (see Equation (3.97)) is applied.

5.3 Coupling Scheme of NHWAVE and SWAN

Following the coupling scheme of SHORECIRC-SWAN by Shi *et al.* (2013), we subdivide the NHWAVE code into multiple regions using a domain decomposition technique and assign each sub-domain to a separate processor core. The Message Passing Interface (MPI) with non-blocking communication is used to exchange data in the overlapping region between neighboring processors.

For the SWAN code, we keep the existing domain decomposition scheme which is slightly different from the NHWAVE code (see Figure 5.1). The version 40.51AB of SWAN uses a single-direction domain decomposition and takes into account the number of dry points in the grid splitting. Due to the different domain decompositions between NHWAVE and SWAN, it is difficult to directly pass variables between the decomposed domains. We now use a two-step mapping method which first gathers a passing variable into the global domain and then distributes it into each sub-domain.

The input parameters and variables are merged into one single input file. The computation time duration and interval are defined in SWAN input part. The NHWAVE and SWAN are coupled at each time step. During the coupled model run, SWAN passes to NHWAVE the significant wave height, peak direction, peak period, wave bottom velocity, dissipation by white-capping, dissipation by breaking, dissipation by friction, total dissipation rate and fraction of breaking waves. NHWAVE passes to SWAN the depth-averaged current and water surface elevation. To avoid directional spreading effect in lateral direction, the SWAN variables at the center line of computation domain are extracted and passed to NHWAVE.

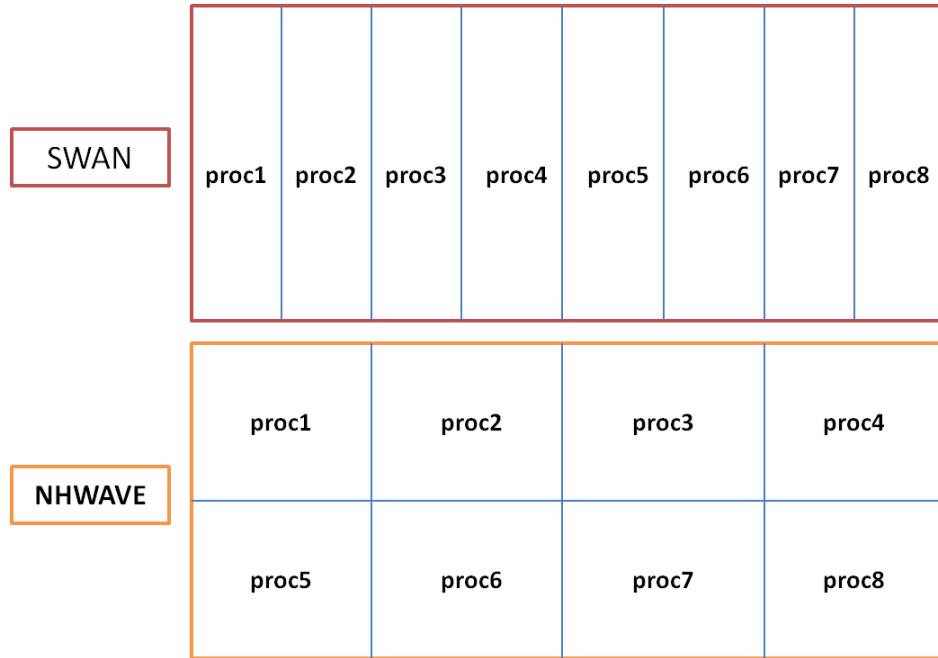


Figure 5.1: Domain decomposition of SWAN and NHWAVE. SWAN uses a single direction domain decomposition. The direction is chosen for dimension with more grid cells. NHWAVE uses a more flexible decomposition technique.

5.4 Numerical Application of Vortex Forces by Uchiyama *et al.* (2010)

5.4.1 Governing equations

The NHWAVE and SWAN are first coupled using vortex force formulation originally from McWilliams *et al.* (2004). The asymptotic theory has been rearranged and applied in numerical model ROMS/SWAN and validated with measurements (Uchiyama *et al.*, 2010). With the weak current assumption, our theory yields exactly the results obtained by McWilliams *et al.* (2004). It is easier to start with this version of forcing formulation since the arbitrary vortex force formulation is largely reduced. We extend it to include the present strong shear formulation in the next section. The governing equations with wave vortex force are first given in Cartesian coordinates for comparison

purpose.

$$\frac{\partial \mathbf{q}^c}{\partial t} + (\mathbf{q}^c \cdot \nabla_h) \mathbf{q}^c + w^c \frac{\partial \mathbf{q}^c}{\partial z} + \frac{1}{\rho} \nabla_h p^c = -\nabla_h \kappa + \mathbf{J} + \mathbf{F}^w \quad (5.36)$$

$$\frac{\partial w^c}{\partial t} + (\mathbf{q}^c \cdot \nabla_h) w^c + w^c \frac{\partial w^c}{\partial z} + \frac{1}{\rho} \frac{\partial p^c}{\partial z} + g = -\frac{\partial \kappa}{\partial z} + K \quad (5.37)$$

$$\nabla_h \cdot \mathbf{q}^c + \frac{\partial w^c}{\partial z} = 0 \quad (5.38)$$

$$w^c|_{-h} + \mathbf{q}^c|_{-h} \cdot \nabla_h h = 0 \quad (5.39)$$

$$w^c|_{\eta^c} - \frac{\partial \eta^c}{\partial t} - (\mathbf{q}^c \cdot \nabla_h) \eta^c = \nabla_h \cdot \mathbf{Q}^{st} \quad (5.40)$$

$$p^c|_{\eta^c} = P^w \quad (5.41)$$

In the momentum equations, the Coriolis force and turbulence Reynolds stress are firstly neglected, which can be easily added to the equation later. The wave-averaged forces consist of the gradient of Bernoulli head κ , vortex force (\mathbf{J}, K) as well as the non-conservative wave dissipation forces \mathbf{F}^w . (\mathbf{q}^c, w^c) represent the Eulerian mean flow velocity. The depth-dependent continuity equation indicates the mass conservation of the mean flow with the wave part removed after wave-averaged. The divergence of the depth-integrated Stokes drift $\nabla_h \cdot \mathbf{Q}^{st}$ appears on the RHS of the kinematic surface boundary condition as a wave-induced mass source/sink term (Hasselmann, 1970). The mean water surface elevation η^c includes wave setup/setdown. P^w is the wave-averaged forcing term at $z = \eta^c$. The Stokes drift velocity is given

$$\mathbf{q}^{st}(z) = \frac{A^2 \sigma_w \mathbf{k}}{2 \sinh^2 kH} \cosh 2k(z+h) \quad (5.42)$$

$$w^{st}(z) = -\nabla_h \cdot \int_{-h}^z \mathbf{q}^{st} dz' \quad (5.43)$$

where A is defined as wave amplitude. \mathbf{q}^{st} and w^{st} satisfies the mass conversation law.

$$\nabla_h \cdot \mathbf{q}^{st} + \frac{\partial w^{st}}{\partial z} = 0 \quad (5.44)$$

The Stokes transport is the depth integral of \mathbf{q}^{st} ,

$$\mathbf{Q}^{st} = \int_{-h}^{\eta^c} \mathbf{q}^{st} dz = \frac{A^2 \sigma_w \mathbf{k}}{4k \sinh^2 kH} \sinh 2kH = \frac{E}{\rho c} \frac{\mathbf{k}}{k} = \frac{N}{\rho} \mathbf{k} \quad (5.45)$$

where E is the total wave energy and N is wave action. In addition, the surface roller is usually introduced to better represents surf zone currents (Svendsen, 1984). Surface rollers are defined as onshore-traveling bores of broken primary waves. As waves propagate onshore, a fraction α_r of wave energy is converted to rollers before dissipating, while the remaining fraction $1 - \alpha_r$ causes local dissipation. The rollers store the dissipated wave energy and gradually transfer it to the mean flow causing a lag in the transfer of momentum. α_r varies between 0 and 1. $\alpha_r = 0$ means that no wave energy converts to roller energy, while $\alpha_r = 1$ means full wave energy converts to roller energy. The roller area (A_R) is obtained from Svendsen (1984).

$$A_R = 0.06H_wL_w \quad (5.46)$$

where H_w is the wave height and L_w is the wave length. The roller action density (N^r) is then defined as

$$I^r = \frac{\rho g H A_R Q_s}{2L_w \sigma_w} \quad (5.47)$$

where Q_s is the fraction of broken waves obtained from SWAN model ($0 \leq Q_s \leq 1$). σ_w is wave intrinsic frequency. A wave roller model is provided to describe the wave roller energy evolution by Reniers *et al.* (2004).

$$\frac{\partial N^r}{\partial t} + \nabla_h \cdot (N^r \mathbf{c}) = \frac{\alpha_r \epsilon^b - \epsilon^r}{\sigma_w} \quad (5.48)$$

where \mathbf{c} is the wave phase speed; ϵ^b is wave dissipation as a source passed from SWAN to NHWAVE; ϵ^r is the roller dissipation rate as a sink. According to Svendsen (1984), the roller transport is

$$\mathbf{Q}^r = \frac{N^r}{\rho} \mathbf{k} \quad (5.49)$$

The total wave-induced transport considering wave rollers is rewritten as

$$\mathbf{Q}^{st} = \frac{N + N^r}{\rho} \mathbf{k} \quad (5.50)$$

We assume that the wave-induced transport is vertically distributed similarly to Stokes velocity, then the horizontal Stokes velocity is rewritten as

$$\mathbf{q}^{st} = \frac{\sigma_w^2 \cosh 2k(z + H)}{g \sinh^2 kH} (N + N^r) \mathbf{k} \quad (5.51)$$

The vortex force is represented in terms of current shear and Stokes drift velocity.

$$\mathbf{J} = -\mathbf{i}_z \times \mathbf{q}^{st} \chi^c - w^{st} \frac{\partial \mathbf{q}^c}{\partial z} \quad (5.52)$$

$$K = \mathbf{q}^{st} \cdot \frac{\partial \mathbf{q}^c}{\partial z} \quad (5.53)$$

The Bernoulli head is given by

$$\kappa = -\frac{1}{4} \frac{\sigma_w A^2}{k \sinh^2 kH} \int_{-h}^z \frac{\partial^2 \sigma_w}{\partial z'^2} \sinh 2k(z - z') dz' \quad (5.54)$$

According to Uchiyama *et al.* (2010), the non-conservative wave forces \mathbf{F}^w contain the depth-induced breaking and roller accelerations \mathbf{B}^b , the wave-induced bottom streaming \mathbf{B}^{wd} and the wave-enhanced turbulent vertical mixing \mathbf{D}^w at the surface and bottom layers. We introduce each of the terms below. The expression for \mathbf{F}^w is given by

$$\mathbf{F}^w = \mathbf{B}^b + \mathbf{B}^{wd} + \mathbf{D}^w \quad (5.55)$$

The wave breaking acceleration \mathbf{B}^b is used as a body force in mean flow momentum equations, which is given by

$$\mathbf{B}^b(z) = \frac{\epsilon^b \mathbf{k}}{\rho \sigma_w} f^b(z) \quad (5.56)$$

We introduce a vertical distribution function $f^b(z)$ that represents vertical penetration of momentum associated with breaking waves and rollers. The shape function is normalized as

$$\int_{-h}^{\eta^c} f^b(z') dz' = 1 \quad (5.57)$$

Three alternative shapes for the vertical distribution are given by Uchiyama *et al.* (2010).

$$f_1^b(z) = 1 - \tanh^4 k_b(\eta^c - z) \quad (5.58)$$

$$f_2^b(z) = 1 - \tanh^2 k_b(\eta^c - z) \quad (5.59)$$

$$f_3^b(z) = \cosh k_b(z + h) \quad (5.60)$$

where the vertical length scale k_b^{-1} is determined either by the wave height or by the wave length. k_b^{-1} represents the penetration depth of each shape function. We usually

represent $k_b^{-1} = a_b H_w$ or $k_b = 2k$, where a_b is an $O(1)$ constant, $H_w = 2A$ is wave height and k is wave number. For long waves, $k_b = 2k$ may give a penetration depth larger than wave height. $k_b^{-1} = a_b H_w$ is then recommended.

In the presence of the bottom friction, the horizontal and vertical wave orbital velocities (\mathbf{q}^w, w^w) are slightly in phase, causing a net-Reynolds stress $\langle \mathbf{q}^w w^w \rangle$. This stress generates bottom streaming (Longuet-Higgins, 1953; Xu and Bowen, 1994). Wave-induced bottom streaming \mathbf{B}^{wd} is similarly represented as a body force

$$\mathbf{B}^{wd}(z) = \frac{\epsilon^{wd} \mathbf{k}}{\rho \sigma_w} f^{wd}(z) \quad (5.61)$$

Three types of vertical distribution function are given by

$$f_1^{wd}(z) = 1 - \tanh^4 k_{wd}(h + z) \quad (5.62)$$

$$f_2^{wd}(z) = 1 - \tanh^2 k_{wd}(h + z) \quad (5.63)$$

$$f_3^{wd}(z) = \cosh k_{wd}(\eta^c - z) \quad (5.64)$$

where the vertical length scale k_{wd}^{-1} is determined by the wave boundary layer thickness. k_{wd}^{-1} is typically a few centimeters. When k_{wd}^{-1} is too thin to be resolved by the model grid, the bottom streaming acceleration is applied only as a stress in the bottom grid cell.

In the presence of waves, the eddy viscosity ν_t is augmented by wave breaking at the surface and current drag at bottom.

$$\mathbf{D}^w = \frac{\partial}{\partial z} [(\nu_t^{brk} + \nu_t^{cd}) \frac{\partial \mathbf{q}^c}{\partial z}] \quad (5.65)$$

Following Uchiyama *et al.* (2010), the mixing induced by surface wave breaking ν_t^{brk} is vertically distributed with a shape function $f^\nu(z)$.

$$\nu_t^{brk} = c_b \left[\frac{(1 - \alpha_r) \epsilon^b + \epsilon^r}{\rho} \right]^{1/3} H_w H f^\nu(z) \quad (5.66)$$

where H_w is wave height, c_b is an $O(10^{-1})$ constant. The vertical distribution function $f^\nu(z)$ is very similar to $f^b(z)$. The vertical scale k_ν^{-1} in the shape function is usually determined by wave height with $k_\nu^{-1} = a_\nu H_w$, where a_ν is an $O(1)$ constant. Both wave

breaking and wave roller-enhanced mixing are considered in the model. In the bottom boundary layer, the wave motions enhance the bottom stress $\boldsymbol{\tau}_{bot}^{cd}$ (Soulsby, 1995). ν_t^{cd} is determined by $\boldsymbol{\tau}_{bot}^{cd}$.

$$\boldsymbol{\tau}_{bot}^{cd} = \boldsymbol{\tau}_c [1.0 + 1.2 \left(\frac{|\tau_w|}{|\tau_w| + |\tau_c|} \right)^{3.2}] \quad (5.67)$$

$$\boldsymbol{\tau}_c = \rho \left[\frac{\kappa}{\ln(z_m/z_0)} \right]^2 |\mathbf{q}^c| \mathbf{q}^c \quad (5.68)$$

$$|\tau_w| = \frac{1}{2} \rho f_w |\mathbf{q}_{orb}^w|^2 \quad (5.69)$$

where $\boldsymbol{\tau}_c$ and τ_w are bottom stresses due to current and waves, respectively. κ is the von Karman constant; z_0 is the bed roughness; z_m is a reference depth above the bed, nominally equivalent to a half bottom-most grid cell height; $f_w = 1.39(\sigma_w z_0/|\mathbf{q}_{orb}^w|)^{0.52}$ is the wave friction factor given by Soulsby (1997). $|\mathbf{q}_{orb}^w| = \sigma_w H_w / (2 \sinh kH)$ is the bottom wave orbital velocity.

Wave set-down is given by

$$\eta^{st} = -\frac{A^2 k}{2 \sinh 2kH} \quad (5.70)$$

Surface pressure term is integrated and manipulated as in McWilliams *et al.* (2004).

$$P^w = \frac{2gA^2k^2 \tanh kH}{\sigma_w \sinh 2kH} \int_{-h}^{\eta^c} (\mathbf{k} \cdot \mathbf{q}^c) \cosh 2k(h+z) dz = \frac{\tilde{U}(k) g A^2 k^2 \tanh kH}{\sigma_w} \quad (5.71)$$

where $\tilde{U}(k)$ is the depth-weighted current speed (Kirby and Chen, 1989).

5.4.2 Application in model

5.4.2.1 Stokes drift velocity

First, we give wave-induced Stokes drift velocity $(\mathbf{q}^{st}, w^{st})$ in σ coordinate. The expression is given below

$$\mathbf{q}^{st} = \frac{A^2 \sigma_w \mathbf{k}}{2 \sinh^2 kH} \cosh 2kH\sigma \quad (5.72)$$

$$w^{st} = -\nabla_h \cdot \left[\frac{A^2 \sigma_w \mathbf{k}}{4k \sinh^2 kH} \sinh 2kH\sigma \right] \quad (5.73)$$

The mean water surface level is

$$\eta^c = \eta^{pc} + \eta^{st} \quad (5.74)$$

$$H = h + \eta^c \quad (5.75)$$

$$\sigma = \frac{z + h}{H} \quad (5.76)$$

There is no change in the form of the Stokes transport.

$$\mathbf{Q}^{st} = \frac{A^2 \sigma_w \mathbf{k}}{4k \sinh^2 kH} \sinh 2kH \quad (5.77)$$

5.4.2.2 Vortex force

The wave vortex force (\mathbf{J} , K) and Bernoulli head κ are re-written in σ -coordinates.

$$J_x = v^{st} \chi^c - \frac{w^{st}}{H} \frac{\partial u}{\partial \sigma} \quad (5.78)$$

$$J_y = -u^{st} \chi^c - \frac{w^{st}}{H} \frac{\partial v}{\partial \sigma} \quad (5.79)$$

$$K = \frac{u^{st}}{H} \frac{\partial u}{\partial \sigma} + \frac{v^{st}}{H} \frac{\partial v}{\partial \sigma} \quad (5.80)$$

$$\begin{aligned} \kappa = & \frac{\sigma_w A^2}{4k \sinh^2 kH} \left[-\left(\frac{k_x}{H} \frac{\partial u}{\partial \sigma} \Big|_{-h} + \frac{k_y}{H} \frac{\partial v}{\partial \sigma} \Big|_{-h} \right) \sinh 2kH \sigma \right. \\ & \left. + 2k \int_0^\sigma \frac{\partial(\mathbf{k} \cdot \mathbf{q}^c)}{\partial \sigma'} \cosh 2kH(\sigma - \sigma') d\sigma' \right] \end{aligned} \quad (5.81)$$

5.4.2.3 Wave dissipation

The shape functions for wave breaking accelerations are rewritten in σ coordinates. f_3^b is used here.

$$f_1^b = 1 - \tanh^4 k_b H (1 - \sigma) \quad (5.82)$$

$$f_2^b = 1 - \tanh^2 k_b H (1 - \sigma) \quad (5.83)$$

$$f_3^b = \cosh k_b H \sigma \quad (5.84)$$

The shape functions for wave bottom streaming acceleration are rewritten in σ coordinates. f_3^{wd} is used here.

$$f_1^{wd} = 1 - \tanh^4 k_{wd} H \sigma \quad (5.85)$$

$$f_2^{wd} = 1 - \tanh^2 k_{wd} H \sigma \quad (5.86)$$

$$f_3^{wd} = \cosh k_{wd} H (1 - \sigma) \quad (5.87)$$

5.4.2.4 Continuity equation

In the presence of waves, the wave-averaged continuity equation may include Stokes drift velocity. However, the Stokes drift velocity has already been assumed to satisfy mass conservation as shown in (5.44). Stokes drift velocity is unnecessary in continuity equation. Thus, we write the σ -coordinates continuity equation in terms of Eulerian velocity (u^c, v^c, w^c).

$$\frac{\partial H}{\partial t} + \frac{\partial H u^c}{\partial x} + \frac{\partial H v^c}{\partial y} + \frac{\partial \omega^c}{\partial \sigma} = 0 \quad (5.88)$$

5.4.2.5 Boundary condition

The wave-averaged surface boundary condition is given by

$$w^c|_{\eta^c} = \frac{\partial \eta^c}{\partial t} + u^c|_{\eta^c} \frac{\partial \eta^c}{\partial x} + v^c|_{\eta^c} \frac{\partial \eta^c}{\partial y} + \nabla_h \cdot \mathbf{Q}^{st} \quad (5.89)$$

$$p^c|_{\eta^c} = \frac{2gA^2k^2 \tanh kH}{\sigma_w \sinh 2kH} \int_0^1 (\mathbf{k} \cdot \mathbf{q}^c) \cosh 2kH \sigma H d\sigma \quad (5.90)$$

The wave-induced mass source/sink term $\nabla_h \cdot \mathbf{Q}^{st}$ is represented by the depth-integration of continuity equation. In σ -coordinates, the surface boundary condition satisfies

$$\omega^c|_{\eta^c} = 0 \quad (5.91)$$

The bottom boundary condition is

$$w^c|_{-h} = -\left(\frac{\partial h}{\partial t} + u^c|_{-h} \frac{\partial h}{\partial x} + v^c|_{-h} \frac{\partial h}{\partial y}\right) \quad (5.92)$$

It is noteworthy that the boundary conditions are also valid for non-hydrostatic case.

5.4.2.6 Momentum equation

The momentum equation is given with wave-averaged forces in σ -coordinate.

$$\frac{\partial \mathbf{U}}{\partial t} + \frac{\partial \mathbf{F}}{\partial x} + \frac{\partial \mathbf{G}}{\partial y} + \frac{\partial \mathbf{H}}{\partial \sigma} = \mathbf{S}_h + \mathbf{S}_p + \mathbf{S}_w^{(1)} + \mathbf{S}_w^{(2)} + \mathbf{S}_w^{\text{NC}} + \mathbf{S}_\tau \quad (5.93)$$

$$\mathbf{U} = (Hu^c, Hv^c, Hw^c)^T \quad (5.94)$$

$$\mathbf{F} = (Hu^c u^c + \frac{1}{2}gH^2, Hu^c v^c, Hu^c w^c)^T \quad (5.95)$$

$$\mathbf{G} = (Hv^c u^c, Hv^c v^c + \frac{1}{2}gH^2, Hv^c w^c)^T \quad (5.96)$$

$$\mathbf{H} = (\omega^c u^c, \omega^c v^c, \omega^c w^c)^T \quad (5.97)$$

$$\mathbf{S}_h = (gH \frac{\partial h}{\partial x}, gH \frac{\partial h}{\partial y}, 0)^T \quad (5.98)$$

$$\mathbf{S}_p = (-\frac{H}{\rho} (\frac{\partial p_d^c}{\partial x} + \frac{\partial p_d^c}{\partial \sigma} \frac{\partial \sigma}{\partial x^*}), -\frac{H}{\rho} (\frac{\partial p_d^c}{\partial y} + \frac{\partial p_d^c}{\partial \sigma} \frac{\partial \sigma}{\partial y^*}), -\frac{1}{\rho} \frac{\partial p_d^c}{\partial \sigma})^T \quad (5.99)$$

$$\mathbf{S}_w^{(1)} = (-H (\frac{\partial \kappa}{\partial x} + \frac{\partial \kappa}{\partial \sigma} \frac{\partial \sigma}{\partial x^*}), -H (\frac{\partial \kappa}{\partial y} + \frac{\partial \kappa}{\partial \sigma} \frac{\partial \sigma}{\partial y^*}), -\frac{\partial \kappa}{\partial \sigma})^T \quad (5.100)$$

$$\mathbf{S}_w^{(2)} = (H(v^{st} \chi^c - \frac{w^{st}}{H} \frac{\partial u^c}{\partial \sigma}), H(-u^{st} \chi^c - \frac{w^{st}}{H} \frac{\partial v^c}{\partial \sigma}), u^{st} \frac{\partial u^c}{\partial \sigma} + v^{st} \frac{\partial v^c}{\partial \sigma})^T \quad (5.101)$$

$$\mathbf{S}_w^{\text{NC}} = H\mathbf{F}^w \quad (5.102)$$

$$\chi^c = (\frac{\partial v^c}{\partial x} + \frac{\partial v^c}{\partial \sigma} \frac{\partial \sigma}{\partial x^*}) - (\frac{\partial u^c}{\partial y} + \frac{\partial u^c}{\partial \sigma} \frac{\partial \sigma}{\partial y^*}) \quad (5.103)$$

$$\mathbf{S}_\tau = (HS_{\tau x}, HS_{\tau y}, HS_{\tau z})^T \quad (5.104)$$

$$S_{\tau x} = \frac{\partial \tau_{xx}}{\partial x} + \frac{\partial \tau_{xx}}{\partial \sigma} \frac{\partial \sigma}{\partial x^*} + \frac{\partial \tau_{xy}}{\partial y} + \frac{\partial \tau_{xy}}{\partial \sigma} \frac{\partial \sigma}{\partial y^*} + \frac{\partial \tau_{xz}}{\partial \sigma} \frac{\partial \sigma}{\partial z^*} \quad (5.105)$$

$$S_{\tau y} = \frac{\partial \tau_{yx}}{\partial x} + \frac{\partial \tau_{yx}}{\partial \sigma} \frac{\partial \sigma}{\partial x^*} + \frac{\partial \tau_{yy}}{\partial y} + \frac{\partial \tau_{yy}}{\partial \sigma} \frac{\partial \sigma}{\partial y^*} + \frac{\partial \tau_{yz}}{\partial \sigma} \frac{\partial \sigma}{\partial z^*} \quad (5.106)$$

$$S_{\tau z} = \frac{\partial \tau_{zx}}{\partial x} + \frac{\partial \tau_{zx}}{\partial \sigma} \frac{\partial \sigma}{\partial x^*} + \frac{\partial \tau_{zy}}{\partial y} + \frac{\partial \tau_{zy}}{\partial \sigma} \frac{\partial \sigma}{\partial y^*} + \frac{\partial \tau_{zz}}{\partial \sigma} \frac{\partial \sigma}{\partial z^*} \quad (5.107)$$

$\mathbf{S}_w^{(1)}$ is the wave-induced Bernoulli head gradient. $\mathbf{S}_w^{(2)}$ is the rearranged wave vortex force. The wave-induced dynamic pressure is included in $\mathbf{S}_w^{(1)}$ and $\mathbf{S}_w^{(2)}$. Thus \mathbf{S}_p accounts for mean flow and long wave dynamic pressure. The multiple scale expansion procedure preserves the non-hydrostatic behavior in the momentum equation. The non-hydrostatic motion can appear in pressure $p_{2,0}$ and vertical velocity $w_{1,0}$. In the hydrostatic mode, the contribution of $w_{1,0}$ to $p_{2,0}$ is neglected. Thus, $p_{2,0}$ only contains wave-induced pressure. \mathbf{S}_w^{NC} is non-conservative wave forcing including wave breaking and whitecapping dissipation \mathbf{B}^b , bottom streaming \mathbf{B}^{wd} and wave-induced mixing \mathbf{D}^w

(see Equation (5.55)). Wave mixing contains wave effect on eddy viscosity and bottom drag. \mathbf{S}_τ only accounts for mean flow turbulent stresses.

The vortex force formulations in Uchiyama *et al.* (2010) and Kumar *et al.* (2012) are very similar. Here we compare our governing equations with Kumar *et al.* (2012). First of all, our governing equations are based on Eulerian velocity while Kumar *et al.* (2012) are based on Lagrangian velocity. However, the Eulerian velocity and Stokes velocity are written separately in Kumar *et al.* (2012) momentum equations (Equation 11, 12). Specifically, $\partial\mathbf{U}/\partial t$ is the local acceleration (marked as ACC in Kumar *et al.*, 2012 and thereafter). The momentum flux part of $(\partial\mathbf{F}/\partial x + \partial\mathbf{G}/\partial y + \partial\mathbf{H}/\partial\sigma)$ gives the horizontal advection (HA) and vertical advection (VA). Compared to Kumar *et al.* (2012), Stokes velocity terms are not showing in our momentum equations because we use Eulerian continuity equation. The Coriolis forces induced by Eulerian and Stokes flow (COR and StCOR) are not considered in our problem and therefore neglected. The pressure part of $(\partial\mathbf{F}/\partial x + \partial\mathbf{G}/\partial y + \partial\mathbf{H}/\partial\sigma)$, $\mathbf{S}_{(h)}$ and $\mathbf{S}_w^{(1)}$ give the pressure gradient (PG). The horizontal component of $\mathbf{S}_w^{(2)}$ gives the horizontal vortex force (HVF). \mathbf{S}_w^{NC} is corresponding to the contribution of breaking (BA) and roller (RA) acceleration, bottom (BtSt) streaming terms and the wave-induced mixing terms (BF + HM + VM). In conclusion, the expressions in Uchiyama *et al.* (2010) and Kumar *et al.* (2012) are not exactly the same as our implementation.

5.5 Numerical Application of the Present Formulation

5.5.1 Governing equations

The wave vortex force formulation for strongly sheared current are similarly applied to $NH\overline{WAVE}$ model. With the strong current shear assumption, the expressions of Stokes velocity, vortex force and Bernoulli head are modified. All the other formula remain the same as in Uchiyama *et al.*'s (2010) vortex force formulation. The governing

equations keep the same form except the surface kinematic boundary condition.

$$\frac{\partial \mathbf{q}^c}{\partial t} + (\mathbf{q}^c \cdot \nabla_h) \mathbf{q}^c + w^c \frac{\partial \mathbf{q}^c}{\partial z} + \nabla_h p^c = -\nabla_h \kappa + \mathbf{J} + \mathbf{F}^w \quad (5.108)$$

$$\frac{\partial w^c}{\partial t} + (\mathbf{q}^c \cdot \nabla_h) w^c + w^c \frac{\partial w^c}{\partial z} + \frac{\partial p^c}{\partial z} + \frac{g\rho}{\rho_0} = -\frac{\partial \kappa}{\partial z} + K \quad (5.109)$$

$$\nabla_h \cdot \mathbf{q}^c + \frac{\partial w^c}{\partial z} = 0 \quad (5.110)$$

$$w^c|_{-h} + \mathbf{q}^c|_{-h} \cdot \nabla_h h = 0 \quad (5.111)$$

$$\begin{aligned} w^c|_{\eta^c} - \frac{\partial \eta^{pc}}{\partial t} - \mathbf{q}^c|_{\eta^c} \cdot \nabla_h \eta^{pc} &= \epsilon^2 \left[\frac{\partial \eta^{st}}{\partial t} + \mathbf{q}^c|_{\eta^c} \cdot \nabla_h \eta^{st} + \nabla_h \cdot \mathbf{Q}^{St} \right. \\ &\left. + (\langle \eta^w \frac{\partial \mathbf{q}^w}{\partial z} \rangle + \frac{1}{2} \frac{\partial^2 \mathbf{q}^c}{\partial z^2} \langle \eta^{w2} \rangle) \cdot \nabla_h \eta^c \right] \end{aligned} \quad (5.112)$$

$$p^c|_{\eta^c} = P^w; \quad z = \eta^c \quad (5.113)$$

The difference from the former surface boundary condition is that $(\langle \eta^w \partial \mathbf{q}^w / \partial z \rangle + \partial^2 \mathbf{q}^c / \partial z^2 \langle \eta^{w2} \rangle / 2) \cdot \nabla_h \eta^c$ is added. To include current shear effects, $O(\epsilon)$ wave perturbation solutions are adopted.

$$w_{1,1} = w_{1,1}^{(0)} + \epsilon w_{1,1}^{(1)} = -i\sigma_s \eta_{1,1} \frac{f(z)}{f(\eta^c)} \quad (5.114)$$

$$w_{1,1}^{(0)} = -i\sigma_s \eta_{1,1} \frac{f_0(z)}{f(\eta^c)} \quad (5.115)$$

$$w_{1,1}^{(1)} = -i\sigma_s \eta_{1,1} \frac{f_1(z)}{f(\eta^c)} \quad (5.116)$$

$$\sigma_w(z) = k(c_0 + \tilde{U}) - \mathbf{k} \cdot \mathbf{q}_{0,0}(z) \quad (5.117)$$

where

$$f(z) = f_0(z) + f_1(z) \quad (5.118)$$

$$f_0(z) = \sinh k(H + z) \quad (5.119)$$

$$c_0^2 = \frac{g}{k} \tanh kH \quad (5.120)$$

$$f_1(z) = -\left[\frac{\hat{\mathbf{k}} \cdot \mathbf{q}_{0,0}(z) + \hat{\mathbf{k}} \cdot \mathbf{q}_{0,0}(-h)}{c_0} + \frac{2kI_1(z)}{c_0} \right] f_0(z) + \frac{2I_2(z)}{c_0} \frac{\partial f_0}{\partial z} \quad (5.121)$$

$$I_1(z) = \int_{-H}^z \hat{\mathbf{k}} \cdot \mathbf{q}_{0,0}(\zeta) \sinh 2k(H + \zeta) d\zeta \quad (5.122)$$

$$I_2(z) = \int_{-H}^z \hat{\mathbf{k}} \cdot \mathbf{q}_{0,0}(\zeta) \cosh 2k(H + \zeta) d\zeta \quad (5.123)$$

$$\tilde{U}(k) = \frac{2k}{\sinh 2kH} \int_{-H}^{\eta^c} \hat{\mathbf{k}} \cdot \mathbf{q}_{0,0}(z) \cosh 2k(H + z) dz \quad (5.124)$$

The strong current shear vortex force formulation is given in Chapter 4. Components κ_3 in Bernoulli head and K_3 in vertical vortex force are expressed using $O(\epsilon^2)$ wave perturbation solutions, which make very little contribution compared to other components. Thus, the two components are neglected in the model. In addition, the time derivatives in horizontal vortex force are neglected since these terms are relatively small. Let $\hat{f}(z) = f(z)/f(\eta^c)$, the equations used for numerical application are rearranged in terms of wave amplitude A as below.

$$\kappa = \frac{\sigma_s^2 A^2}{4} \left[\frac{1}{k^2} \left(\frac{\partial \hat{f}}{\partial z} \right)^2 + \hat{f}^2 + \frac{\hat{f}^2}{\sigma_w^2} \frac{\partial \mathbf{q}_{0,0}}{\partial z} \cdot \frac{\partial \mathbf{q}_{0,0}}{\partial z} - \frac{\hat{f}^2}{\sigma_w^2 k^2} \left(\frac{\partial \sigma_w}{\partial z} \right)^2 \right] \quad (5.125)$$

$$\begin{aligned} \mathbf{J} = & \mathbf{i}_z \times \left\{ \left(-\frac{\sigma_s^2 A^2 \hat{f}^2}{2\sigma_w^2} \frac{\partial \mathbf{q}_{0,0}}{\partial z} + \frac{\mathbf{E}^*}{\sigma_w} \right) \cdot \nabla_h \boldsymbol{\xi}_{0,0} + \frac{\mathbf{E}^*}{\sigma_w} \frac{\partial \chi_{1,0}}{\partial z} \right. \\ & + \left(\frac{\sigma_s^2 A^2 \hat{f}^2}{2\sigma_w^2} \frac{\partial \boldsymbol{\xi}_{0,0}}{\partial z} + \mathbf{k} \cdot \frac{\boldsymbol{\xi}_{0,0}}{\sigma_w^2} \mathbf{E}^* \right) \cdot \nabla_h \mathbf{q}_{0,0} - \mathbf{k} \cdot \frac{\boldsymbol{\xi}_{0,0}}{\sigma_w^2} \mathbf{E}^* \nabla_h \cdot \mathbf{q}_{0,0} \\ & + \boldsymbol{\xi}_{0,0} \cdot \nabla_h \left(\frac{\sigma_s^2 A^2 \hat{f}^2}{4\sigma_w^2} \frac{\partial \mathbf{q}_{0,0}}{\partial z} \right) + \frac{\sigma_s^2 A^2 \hat{f}^2}{4\sigma_w^2} \boldsymbol{\xi}_{0,0} \cdot \nabla_h \left(\frac{\partial \mathbf{q}_{0,0}}{\partial z} \right) \\ & \left. - \frac{\boldsymbol{\xi}_{0,0}}{\sigma_w} \cdot \nabla_h \mathbf{E}^* - \chi_{1,0} \mathbf{q}^{st}(z) \right\} \end{aligned} \quad (5.126)$$

$$\begin{aligned} K = & \frac{\sigma_s^2 A^2 \hat{f}^2}{2\sigma_w^2} \frac{\partial \mathbf{q}_{0,0}}{\partial z} \times \frac{\partial \boldsymbol{\xi}_{0,0}}{\partial z} \\ & - \frac{\sigma_w \sigma_s^2 A^2}{4k^2} \frac{\partial}{\partial z} \left(\frac{\hat{f}^2}{\sigma_w^2} \right) \mathbf{k} \times \left(\frac{\partial \mathbf{q}_{0,0}}{\partial z} \mathbf{k} \cdot \frac{\boldsymbol{\xi}_{0,0}}{\sigma_w} + \frac{\partial \boldsymbol{\xi}_{0,0}}{\partial z} \right) \end{aligned} \quad (5.127)$$

$$\mathbf{E}^* = \frac{\sigma_s^2 A^2 \mathbf{k}}{4k^2} \left(\frac{\partial \hat{f}^2}{\partial z} - \frac{2\hat{f}^2}{\sigma_w} \frac{\partial \sigma_w}{\partial z} \right) \quad (5.128)$$

$$\begin{aligned} \mathbf{q}^{st} = & \frac{\sigma_s^2 A^2}{4} \frac{\partial}{\partial z} \left[\frac{\mathbf{k}}{k^2 \sigma_w} \frac{\partial \hat{f}^2}{\partial z} - \frac{\hat{f}^2}{\sigma_w^2} \left(\frac{\mathbf{k}}{k^2} \frac{\partial \sigma_w}{\partial z} + \frac{\partial \mathbf{q}_{0,0}}{\partial z} \right) \right] \\ & - \frac{\sigma_s^2 A^2 \hat{f}^2}{4\sigma_w^2} \left(\frac{\mathbf{k}}{k^2} \frac{\partial^2 \sigma_w}{\partial z^2} + \frac{\partial^2 \mathbf{q}_{0,0}}{\partial z^2} \right) \end{aligned} \quad (5.129)$$

$$\mathbf{Q}^{St} = \frac{A^2 \mathbf{k} \sigma_s}{2 k^2} \left(\frac{\partial \hat{f}}{\partial z} - \frac{1}{\sigma_s} \frac{\partial \sigma_w}{\partial z} \right) \Big|_{\eta^c} - \frac{A^2}{4} \frac{\partial \mathbf{q}_{0,0}(\eta^c)}{\partial z} \quad (5.130)$$

Equation (5.126) and (5.127) indicate that vertical Stokes drift velocity w^{st} is not needed for wave vortex force. The wave forces $(\partial\kappa/\partial z, K)$ in vertical momentum equation indicate that the wave-induced dynamic pressure is included in the Bernoulli head gradient and vortex force terms. The dynamic surface boundary condition (5.113) is consistent with Bernoulli head gradient and vortex force at surface.

$$p^c = - \left\langle \eta^w \frac{\partial p^w}{\partial z} \right\rangle; \quad z = \eta^c \quad (5.131)$$

The wave dissipation accelerations are assumed to be the same as the weak current assumption in last section. The wave set-down η^{st} is the combined effect of leading order Bernoulli head and wave-induced dynamic pressure and included in the momentum equation. \mathbf{S}_w^2 needs to be modified since the vortex force for strongly sheared current loses the concise form as in Uchiyama *et al.* (2010). The general form is given by

$$\mathbf{S}_w^{(2)} = (HJ_x, HJ_y, HK)^T \quad (5.132)$$

where J_x and J_y are the components of the horizontal vortex force.

5.6 Application to Longshore Current Simulation

5.6.1 Model setup

To test the wave vortex force formulations for both weak current assumption and strongly sheared current assumption, an ideal longshore current case is used. This problem was first presented by Haas and Warner (2009). The purpose was to compare a quasi-3D model (SHORECIRC) with a fully-3D model (ROMS) based on radiation stress formulation. It was also used by Uchiyama *et al.* (2010) and Kumar *et al.* (2011, 2012) for both vortex force formulation and radiation stress formulation. The test case simulates longshore current driven by obliquely incident waves on a planar beach with constant slope of 1/80. Following Uchiyama *et al.* (2010), the offshore waves are specified by the JONSWAP spectrum with 2 m significant wave height, 10 s peak period and an angle 10° off the shore-normal direction. The wave fields are obtained from an independent SWAN run and used here as input in the coupled model. The wave

parameters such as significant wave heights, peak wave period, peak wave direction and wave dissipation are provided as input files to NHWAVE without necessarily activating SWAN.

The longshore current case is only used to test the vortex force formulation. SWAN is not activated. The model results will be compared with the previous results (Haas and Warner, 2009; Uchiyama *et al.*, 2010; Kumar *et al.*, 2012). The incident waves are idealized in input files. The horizontal domain is 1260 m in cross-shore direction (x) and 140 m in longshore direction (y). The size of grid cell is constant $\Delta x = \Delta y = 20$ m. The water depth h starts at 12 m offshore and decreases to 0.01 m. The vertical direction (z) is discretized with 20 uniform vertical σ levels. The model imposes a solid wall boundary with minimum actual water depth $h_{min} = 0.01$ m (wave set up included) at the shoreward boundary. The longshore boundary condition is set as periodic to obtain the longshore uniform wave forcing and current velocity. The earth rotation is neglected since the space scale is relatively small. There is no lateral momentum diffusion or stratification. Wave roller and bottom streaming accelerations are also excluded (Uchiyama *et al.*, 2010). During the model run, the breaking acceleration \mathbf{B}^b uses a type (3) shape function (see Equation (5.84)) with $k_b = 2k$. The wave up is generated by the cross-shore wave dissipation. The $k - \epsilon$ turbulence model is used in the simulation. The bottom stress model is used as $\tau_{bot}^{cd} = \rho c_D |\bar{\mathbf{u}}| \mathbf{u}$, where the drag coefficient $c_D = 0.0015$. $|\bar{\mathbf{u}}|$ is depth-averaged horizontal current velocity. \mathbf{u} is the horizontal current velocity at the bottom-most grid cells. The time integration is continued until a steady solution occurs. The cross-shore distribution of wave height and wave dissipation is shown in Figure 5.2. The shoreward decrease in H_{sig} is caused by wave breaking. The shoreline is at $x = 1000$ m in cross-shore distance. The wave breaking occurs between $x = 500$ m to $x = 1000$ m with the wave dissipation peak near $x = 750$ m.

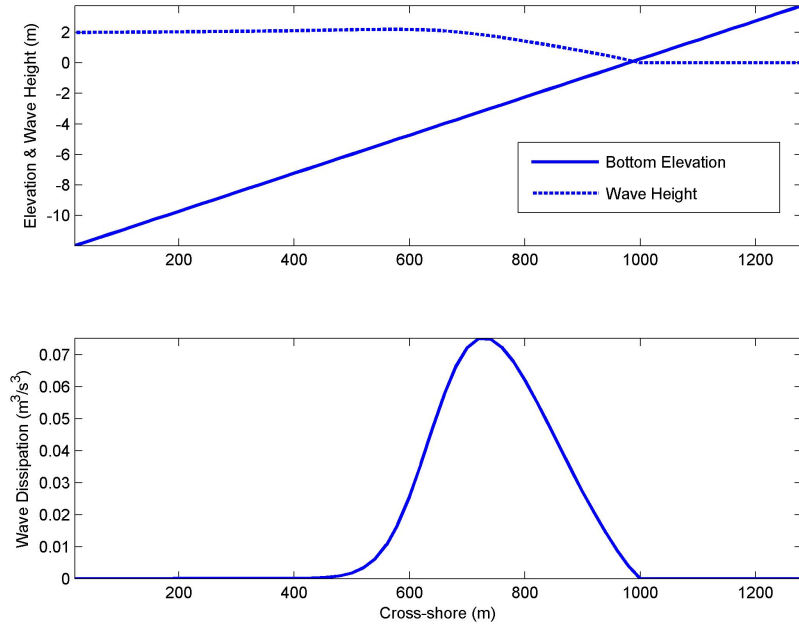


Figure 5.2: (Upper) Cross-shore distribution of water depth and incident significant wave height. Solid line: water depth; Dotted Line: significant wave height. The bathymetry is idealized as a planar beach with slope 1/80. The incident significant wave height is set as 2 m offshore. As waves approaching nearshore, the wave height increases due to shoaling effect and decreases to zero due to break at the surfzone. (Lower) Cross-shore distribution of wave dissipation (ϵ^b/ρ_0).

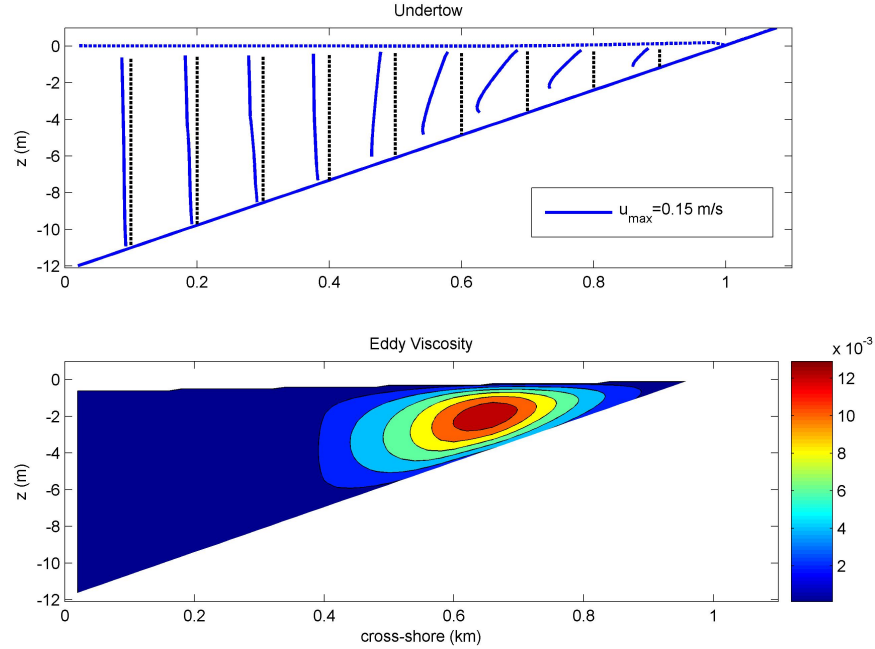


Figure 5.3: (Upper) Cross-shore and vertical distribution of undertow with maximum velocity 0.15 m/s . Black dotted line: zero-velocity at each cross-shore location; Blue solid line: x -direction velocity at each cross-shore location. (Lower) Color map of eddy viscosity in $x - z$ coordinate plane. Results are based on Uchiyama *et al.* (2010) vortex force formulation and $k - \epsilon$ turbulence model.

5.6.2 Results from Uchiyama *et al.* (2010) vortex force

The model results based on 3-hour run using Uchiyama *et al.* (2010) vortex force formula are given as below. The upper panel of Figure 5.3 illustrates the undertow distribution in the $x - z$ coordinate plane. The maximum horizontal velocity is about 0.15 m/s. The lower panel of Figure 5.3 gives the distribution of eddy viscosity in $x - z$ coordinate plane. The maximum eddy viscosity occurs between $x = 0.6$ km and $x = 0.7$ km in cross-shore direction, where the maximum current vertical shear happens.

In the cross-shore direction (see upper panel of Figure 5.4), the depth-integrated

(2D) Eulerian onshore transport $H\bar{u}^{st}$ induced by Stokes drift in the surfzone is balanced with the offshore undertow $H\bar{u}^c$ according to mass conservation.

$$\bar{u}^c = -\bar{u}^{st} \quad (5.133)$$

In the longshore direction (see middle panel of Figure 5.4), a strong current velocity is driven by wave breaking-induced dissipation. The analytical solution of the longshore current velocity \bar{v} is obtained from the depth-integrated (2D) momentum balance of wave breaking acceleration and bottom drag as shown in Equation (5.134), where Equation (5.133) implies separate sub-balances between vortex force J_y and along-shore advection $-\bar{u}^{st}\partial\bar{v}/\partial x = \bar{u}^c\partial\bar{v}/\partial x$. The model output longshore current velocity is compared with the analytical solution in the middle panel of Figure 5.4. Overall, \bar{v} corresponds to the analytical solution fairly well. The model output maximum longshore current velocity \bar{v}_{max} agrees with analytical solution. The model results give slightly larger \bar{v} landward of \bar{v}_{max} and smaller \bar{v} seaward of \bar{v}_{max} because of the 3D current in the bottom drag force and residual vortex force term $-w^{st}\partial v/\partial z$.

$$\rho_0 c_D |\bar{\mathbf{u}}| \bar{v} = \frac{\epsilon^b k_y}{\sigma_w} \quad (5.134)$$

The wave-induced set up/down in the cross-shore direction is shown in the lower panel of Figure 5.4. The cross-shore barotropic momentum balance is dominated by the wave-average pressure gradient and wave breaking-induced acceleration as shown below.

$$g \frac{\partial \eta^c}{\partial x} = \frac{\epsilon^b k_x}{\rho_0 D \sigma_w} + g \frac{\partial \eta^{st}}{\partial x} \quad (5.135)$$

where η^{st} is wave set-down. The analytical mean surface elevation η^c can be retrieved by integrating Equation (5.135) from the offshore boundary where $\eta^c = \eta^{st}$ (assuming $\epsilon^b = 0$ at offshore boundary). We compare the analytical mean surface with the model output in the lower panel of Figure 5.4. The model results agree well with analytical solution outside of surf zone (see lower panel of Figure 5.4). The model output wave setup is slightly smaller than the analytical solution in the surf zone, which is caused by the residual Bernoulli head effect.

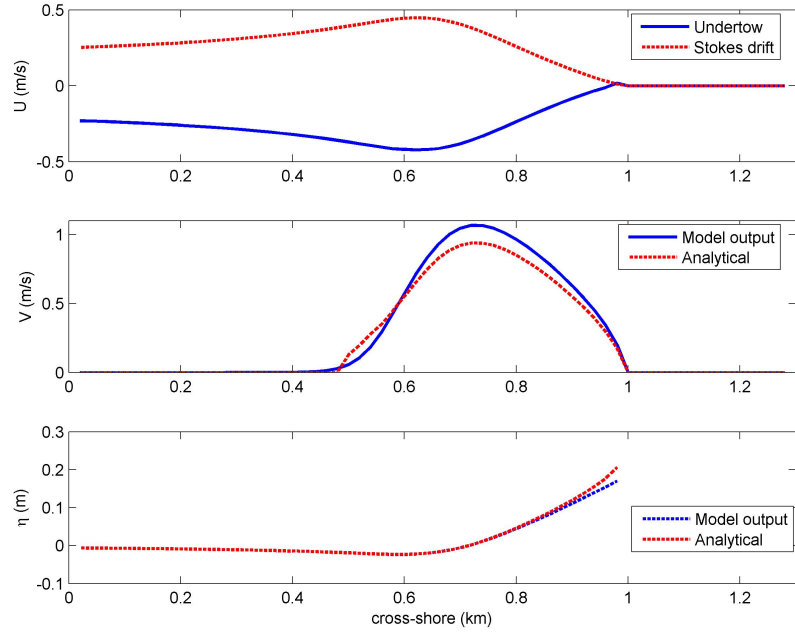


Figure 5.4: (Upper) Cross-shore distribution of depth-averaged x -component Stokes drift velocity u^{st} and undertow u^c . Solid line: undertow; Dotted line: Stokes drift velocity. (Middle) Cross-shore distribution of depth-averaged longshore current. Solid line: model output; Dotted line: analytical solution. (Lower) Cross-shore distribution of mean surface elevation. Solid line: model output; Dotted line: analytical solution. The analytical cross-shore profile of η^c is approximately retrieved by integrating Equation (5.135) from offshore boundary with $\eta^c = \eta^{st}$. Results are based on Uchiyama *et al.* (2010) vortex force formulation.

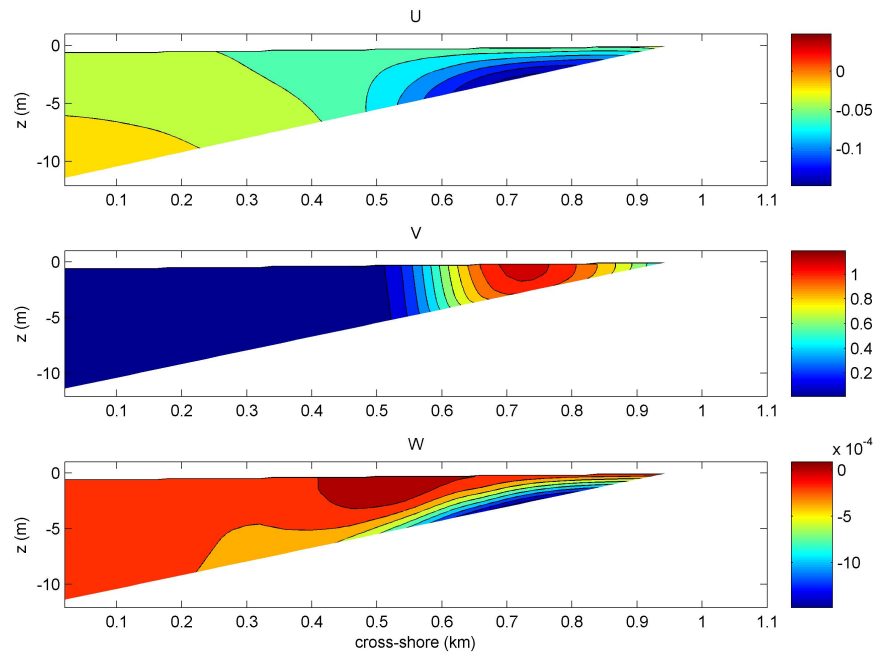


Figure 5.5: Color map of current velocity in cross-shore section ($x - z$ coordinate plane). (Upper) cross-shore (x -component) current velocity u^c . (Middle) longshore (y -component) current velocity v^c . (Lower) vertical (z -component) current velocity w^c . Results are based on Uchiyama *et al.* (2010) vortex force formulation.

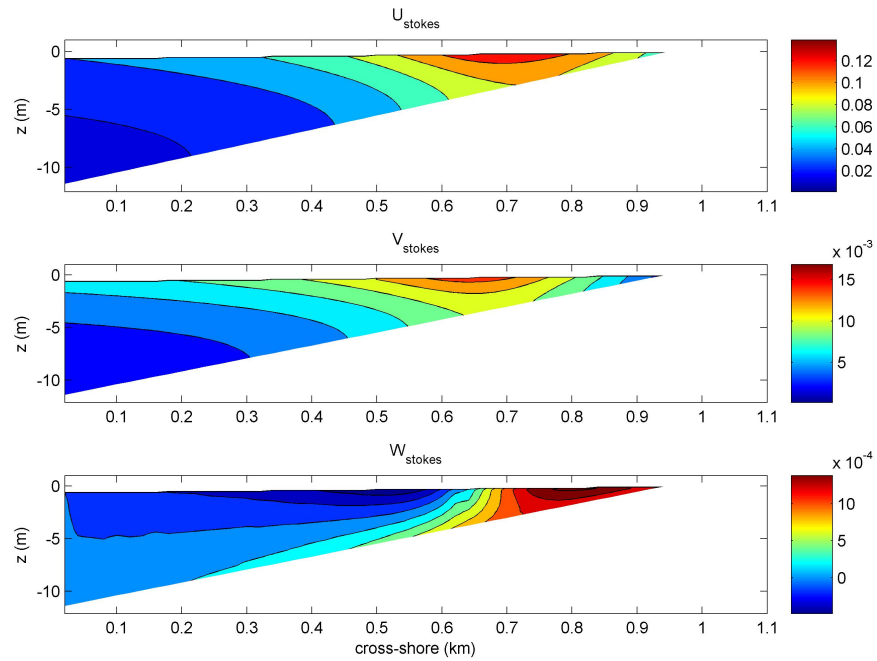


Figure 5.6: Color map of wave Stokes drift velocity in cross-shore section ($x - z$ coordinate plane). (Upper) cross-shore (x -component) Stokes velocity u^{st} . (Middle) longshore (y -component) Stokes velocity v^{st} . (Lower) vertical (z -component) Stokes velocity w^{st} . Results are based on Uchiyama *et al.* (2010) vortex force formulation.

The color map of current velocity and Stokes drift velocity are given in Figure 5.5 and Figure 5.6, respectively. Figure 5.5 gives the vertical distribution of undertow (x) in the upper panel, longshore current (y) in the middle panel and vertical velocity (z) in the lower panel. The onshore mass transport induced by Stokes drift creates a descending flow near the bottom in the surf zone. The vertical velocity is relatively small compared to undertow and longshore current. Figure 5.6 gives the vertical structure of wave-induced Stokes velocity u^{st} (upper), v^{st} (middle) and w^{st} (lower). The flow patterns of x -component mean velocity u and y -component velocity v are provided by Uchiyama *et al.* (2010) in Figure 18. The flow patterns of both mean velocity and Stokes drift velocity are also provided by Kumar *et al.* (2012) in Figure 2. The comparison among these results indicates that the flow patterns are very similar.

The vertical distribution of wave breaking dissipation is calculated using Type III shape function in (5.84) with $k_b = 2k$ (Figure 5.7). The vertical distribution of wave breaking acceleration can largely affect the flow patterns of both undertow and longshore current as indicated in Figure 2 of Uchiyama *et al.* (2010). The more surface-confined wave breaking force (Column a in Figure 2) generates stronger surface onshore transport and weaker longshore current compared to the more uniformly distributed wave breaking force (Column b in Figure 2).

The vortex forces and Bernoulli head gradient are shown in Figure 5.8 and Figure 5.9, respectively. The x and y components of vortex force in Figure 5.8 are very similar to Figure 3 in Kumar *et al.* (2012). However, the z -component vortex force is not given in either Uchiyama *et al.* (2010) or Kumar *et al.* (2012) results. As discussed in Chapter 4, the wave-averaged pressure consists of the hydrostatic pressure $\rho g(\eta^c - z)$ and the wave-induced dynamic pressure $-\rho \langle w^{w2}(z) \rangle$ in hydrostatic mode (4.104). In our model, the Bernoulli head includes the wave-induced dynamics pressure $-\rho \langle w^{w2}(z) \rangle$ and wave set-down η^{st} . The wave set-down is reflected in x -component Bernoulli head gradient as the upper panel of Figure 5.9. The x -direction gradient of wave set-down is depth-uniform. The wave-averaged force is the sum of vortex forces and Bernoulli head gradient, which is shown in Figure 5.10.

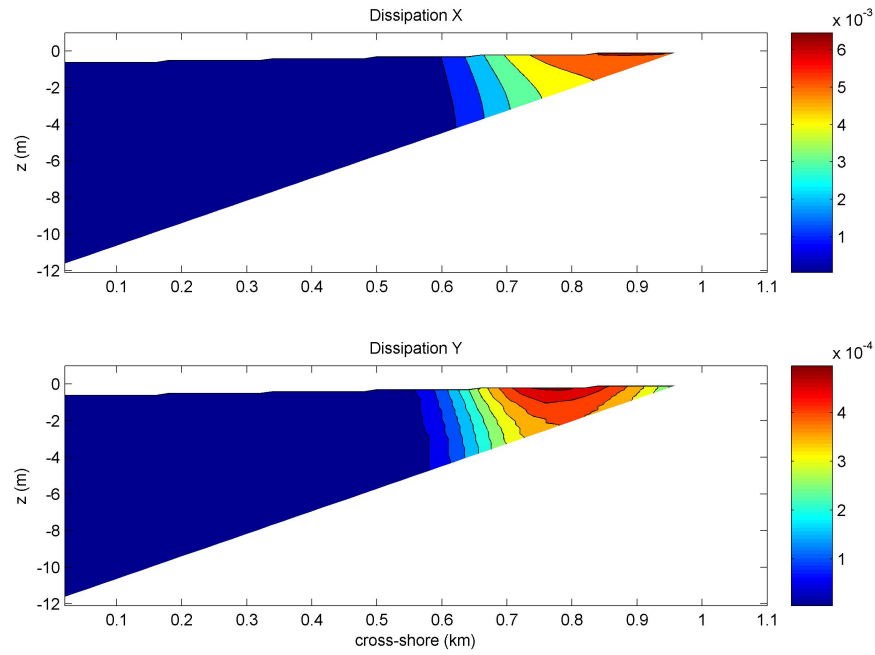


Figure 5.7: Color map of wave breaking dissipation force (\mathbf{B}^b) in cross-shore section ($x - z$ coordinate plane). The wave dissipation force is applied in wave direction and therefore has cross-shore and longshore component. (Upper) cross-shore (x -component) wave dissipation. (Lower) longshore (y -component) wave dissipation. Results are based on Uchiyama *et al.* (2010) vortex force formulation.

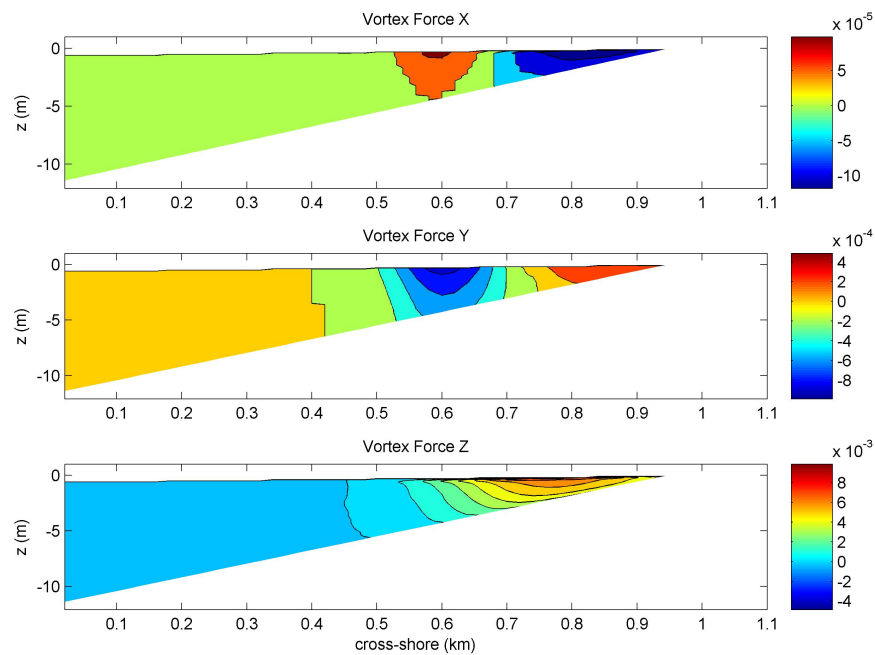


Figure 5.8: Color map of wave vortex force in $x - z$ coordinate plain. (Upper) x -component vortex force. (Middle) y -component vortex force. (Lower) z -component vortex force. Results are based on Uchiyama *et al.* (2010) vortex force formulation.

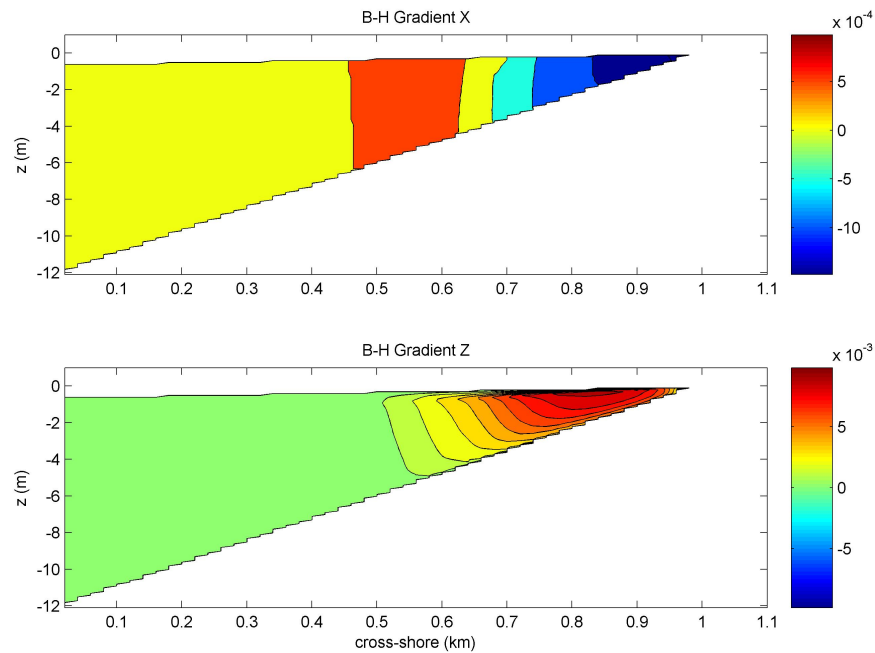


Figure 5.9: Color map of wave Bernoulli head gradient in $x - z$ coordinate plain. (Upper) x -component Bernoulli head gradient. (Middle) y -component Bernoulli head gradient. (Lower) z -component Bernoulli head gradient. Results are based on Uchiyama *et al.* (2010) vortex force formulation.

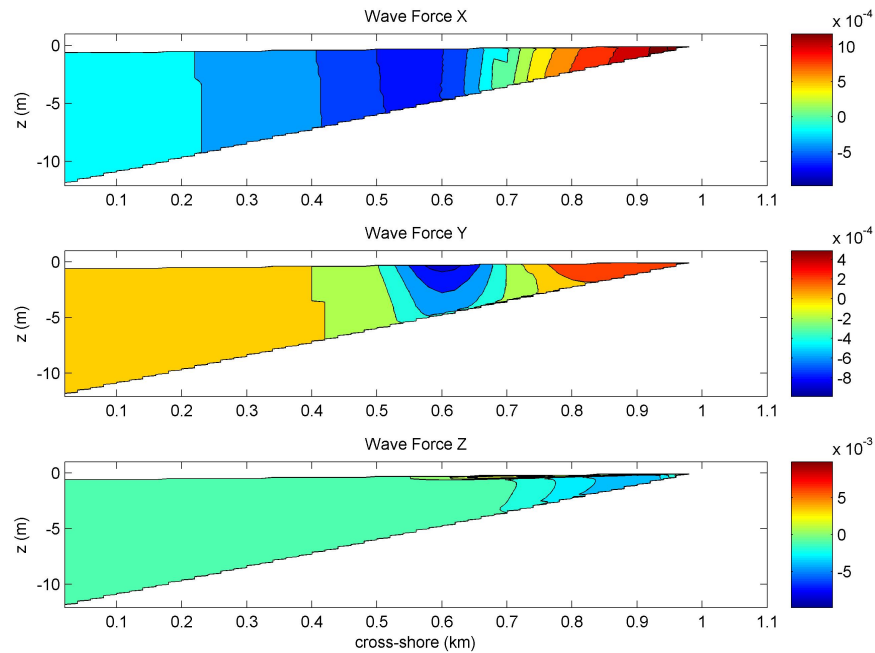


Figure 5.10: Color map of wave-averaged force (- Bernoulli head gradient + vortex force) in $x - z$ coordinate plain. (Upper) x -component wave-averaged force. (Middle) y -component wave-averaged force. (Lower) z -component wave-average force. Results are based on Uchiyama *et al.* (2010) vortex force formulation.

5.6.3 Results from the present vortex force

The model results based on the present theory described in Chapter 3-4 are shown in Figure 5.11 - 5.15. The present results are subtracted by Uchiyama *et al.* (2010) formulation results for comparison. In the MC vortex force formulation, the gradient part of vortex force is moved to the Bernoulli head. Thus, the difference comparison of wave-averaged force is based on the sum of vortex force and Bernoulli head gradient.

In the cross-shore direction, the comparison of undertow velocity profile between Uchiyama *et al.* (2010) formulation (thereafter MC) and Dong & Kirby (thereafter DK) formulation is given in the upper panel of Figure 5.11. The color map of DK eddy viscosity is shown in the lower panel of Figure 5.11. Overall, the undertow profiles and eddy viscosity are very similar. However, in the surf zone (between $x = 0.5$ km and $x = 0.7$ km), the DK undertow is slightly larger near the bottom and smaller near the surface. Outside of the surf zone ($x \leq 0.5$ km), the DK undertow is slightly smaller near the surface and larger near the bottom. The color map of mean current velocity difference (see the upper panel of Figure 5.13) gives a better view. In addition, the magnitude of DK depth-averaged Stokes drift and undertow is slightly larger than MC results (see the upper panel of Figure 5.12). It is because DK model gives a larger onshore Stokes transport than MC (see the upper panel of Figure 5.14). The mean surface elevations between MC and DK are also identical (see the lower panel of Figure 5.12). The DK wave-averaged force is larger than MC results landward of surf zone ($x \geq 0.7$ km) and smaller seaward of surf zone ($x \leq 0.7$ km) as shown in the upper panel of Figure 5.15.

In the longshore direction, the bottom drag is balanced with wave-breaking induced acceleration. There is no change in the wave dissipation driving force and therefore the DK and MC depth-averaged longshore current velocities are very similar (see the middle panel of Figure 5.12). However, the DK longshore current is slightly larger than MC longshore current near the surface and smaller near the bottom (see the middle panel of Figure 5.13). It is because DK wave-averaged force is smaller than

MC results near the bottom (see the middle panel of Figure 5.15). The magnitude of difference is less than 0.01 m/s. The longshore Stokes drift velocity comparison (see the middle panel of Figure 5.14) indicates that DK longshore Stokes drift velocity is smaller than MC results near the surface and larger near the bottom. It is because the current vertical shear is included in the DK longshore Stokes drift velocity.

The magnitudes of vertical mean velocity difference and vertical Stokes drift velocity difference are less than 0.001 m/s.

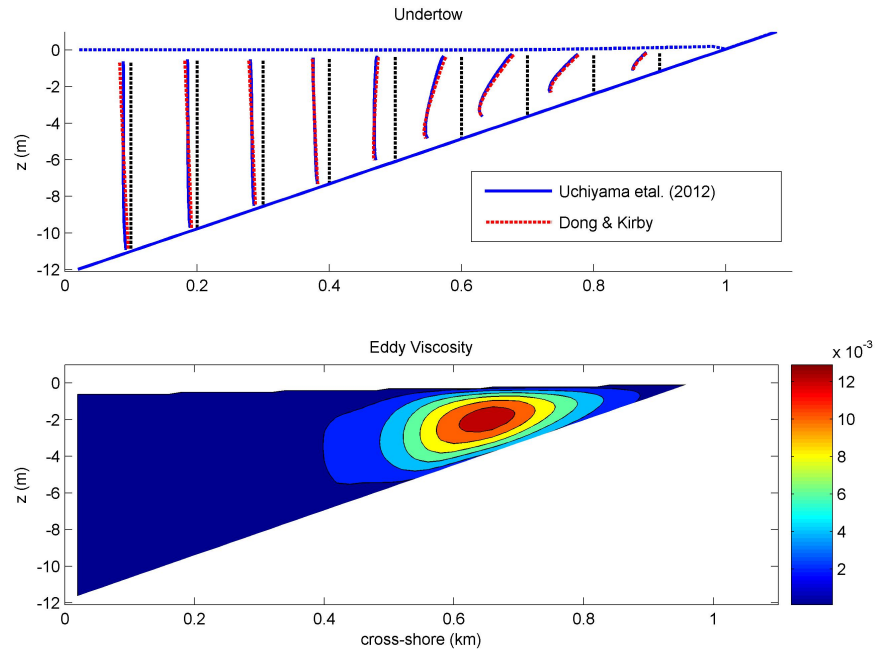


Figure 5.11: (Upper) Cross-shore and vertical distribution of DK undertow and MC undertow. Black dotted line: zero-velocity at each cross-shore location; Blue solid line: MC undertow at each cross-shore location. Red dotted line: DK undertow at each cross-shore location. (Lower) Color map of DK eddy viscosity in $x - z$ coordinate plane. Results are based on the present vortex force formulation.

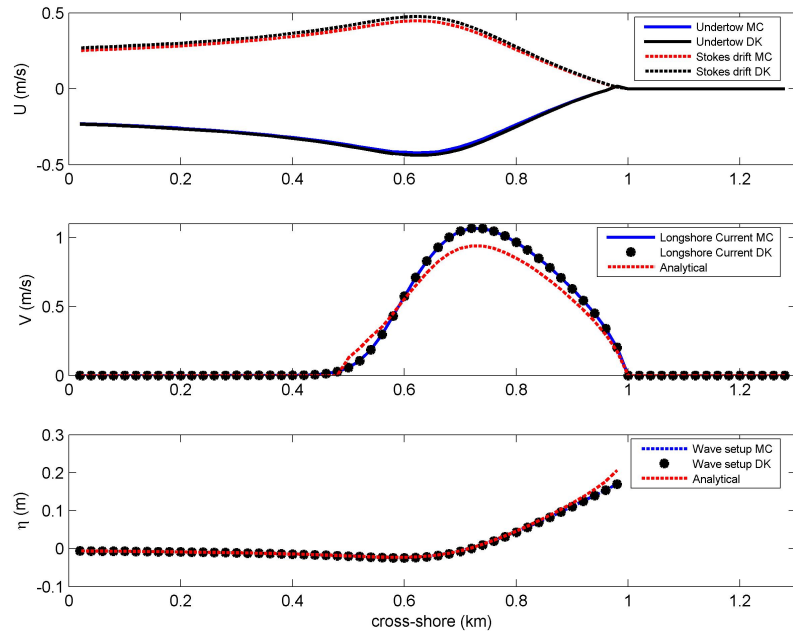


Figure 5.12: (Upper) Cross-shore distribution of depth-averaged x -component Stokes drift velocity u^{st} and undertow u^c . Blue solid line: MC undertow; Black solid line: DK undertow; Red dotted line: MC Stokes drift velocity. Black dotted line: DK Stokes drift velocity. (Middle) Cross-shore distribution of depth-averaged longshore current. Blue solid line: MC longshore current; Black starred line: DK longshore current; Red dotted line: analytical solution. (Lower) Cross-shore distribution of mean surface elevation. Blue solid line: MC mean surface; Black starred line: DK mean surface; Red dotted line: analytical solution. Results are based on the present vortex force formulation.

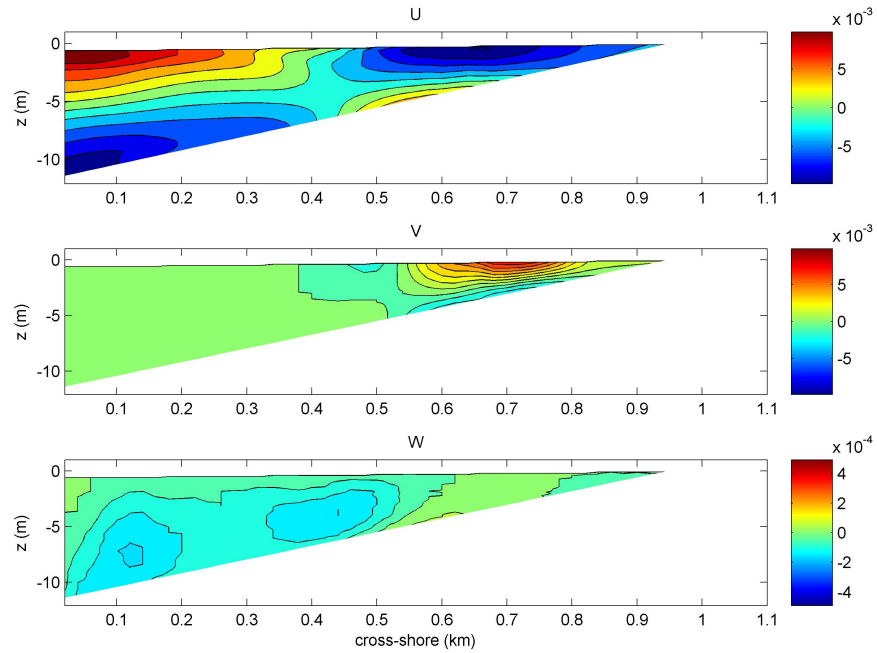


Figure 5.13: Color map of current velocity difference (DK - MC) in $x - z$ coordinate plain. (Upper) x -component current velocity u^c difference. (Middle) y -component current velocity v^c difference. (Lower) z -component current velocity w^c difference. Results are based on present vortex force formulation.

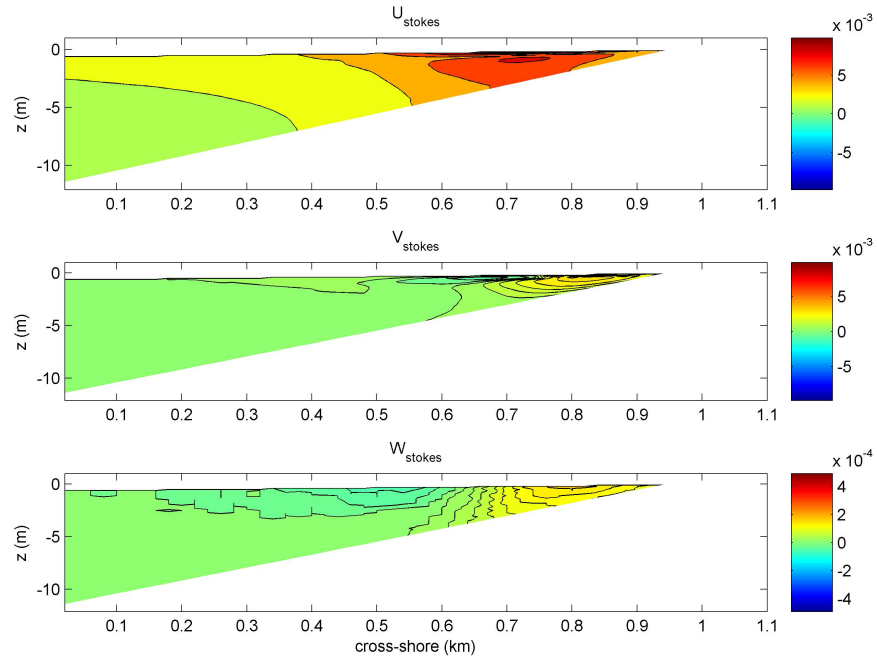


Figure 5.14: Color map of wave Stokes drift velocity difference (DK - MC) in $x - z$ coordinate plane. (Upper) x -component current velocity u^{st} difference. (Middle) y -component current velocity v^{st} difference. (Lower) z -component current velocity w^{st} difference. Results are based on the present vortex force formulation.

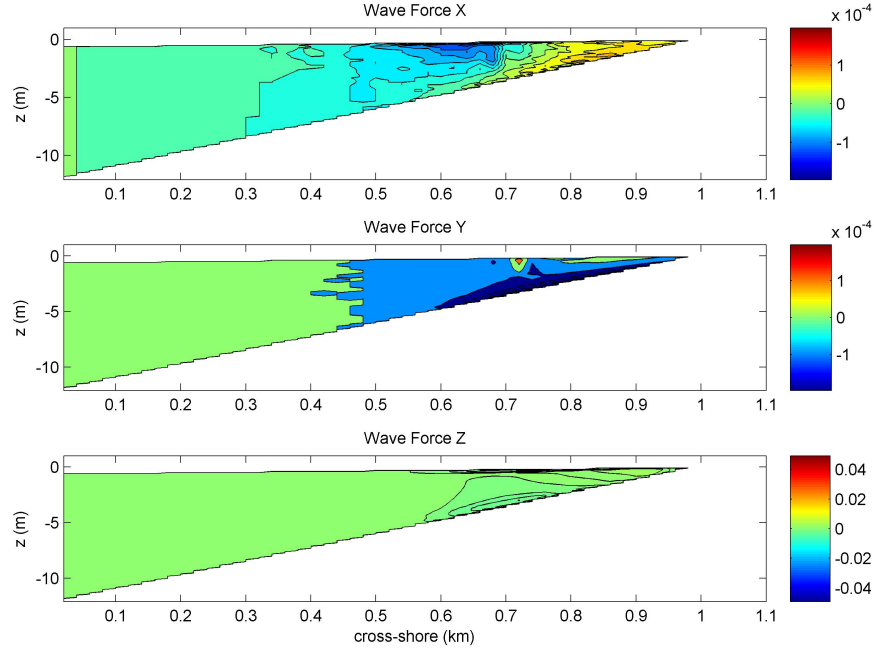


Figure 5.15: Color map of wave-averaged force difference (- Bernoulli head gradient + vortex force, DK - MC) in $x - z$ coordinate plain. (Upper) x -component wave-averaged force. (Middle) y -component wave-averaged force. (Lower) z -component wave-averaged force. Results are based on the present vortex force formulation.

5.7 Application to Columbia River

5.7.1 Model Setup

The Columbia River is the largest river in the Pacific Northwest region of North America. It accounts for 77 % of the drainage along the U.S. West coast north of San Francisco (Barnes *et al.*, 1972). The river originates from Rocky Mountains and flows westward into the Pacific Ocean between the states of Washington and Oregon. Due to the narrow outlet to the ocean, significant freshwater discharge and strong tidal currents, the westward surface current speed at the river mouth usually exceeds 3 m/s during ebb tide (Hickey *et al.*, 2010). Meanwhile, the stratification at the river mouth generates a strong vertical shear in the current velocity profile. Thus the Columbia River is an ideal case for the interaction of waves and strongly sheared current.

In this section, we setup a model to simulate wave-current interaction at the mouth of Columbia River. To simplify the simulation, we consider a longshore uniform case. In the cross-shore direction, we use the profile of real bathymetry along the green solid line in Figure 5.16. The bathymetry data is extracted from a Digital Elevation Model (DEM) of Astoria V3, Oregon developed by the National Geophysical Data Center (NGDC) in 2016 (<http://www.ngdc.noaa.gov/dem/squareCellGrid/download/5490>). The DEM has 1/3 arc-second horizontal resolution and is referenced to mean high water (MHW). To better represent the wave climate, we analyze the wave hindcast data at USACE Wave Information Studies (WIS) station 83014 and 83015, which are the closest to the study area (See yellow points in Figure 5.16). The wave roses at WIS station 83014 and 83015 indicate that the dominant offshore wave direction is from west to east and the dominant significant wave height is between 1 m and 3 m (see Figure 5.17, 5.18).

We use 128 grid cells in cross-shore (x) direction, 4 grid cells in along-shore (y) direction, and 20 vertical levels. The cross-shore distance is 14.3 km as drawn in Figure 5.16. The cell size $\Delta x = 112$ m and $\Delta y = 112$ m. Therefore the total computation domain size is 14336 m * 448 m. The water depth along the cut profile starts with 26.4 m at the river mouth and ends with 91.3 m offshore. The water depth at the sand bar is about 16.5 m as shown in Figure 5.19.

The SWAN model is not suitable for the periodic boundary condition as in NHWAVE. Thus we take SWAN output at the center line of computational grid in cross-shore direction and populates in alongshore direction to get the longshore uniform wave field. Meanwhile, we extract mean water level and depth-averaged current velocity at the center line in NHWAVE grid and pass them to SWAN. In NHWAVE, the x -direction boundary condition is set as influx at east with salinity = 0 PSU and outflux at west with salinity = 30 PSU. The y -direction boundary condition is set as periodic and free-slip. The bottom boundary condition is set as bottom friction with roughness $z_{ob} = 0.001$ m. We impose the volume flux to force the river flow from east to west. The volume flux at both sides is set to zero at $t = 0$ s and gradually decreases to -20



Figure 5.16: Aerial view of the mouth of Columbia River. Green solid line: profile of bathymetry used in the model setup. The distance is about 14.3 km Yellow point: USACE Wave Information Studies (WIS) station locations (83014, 83015)

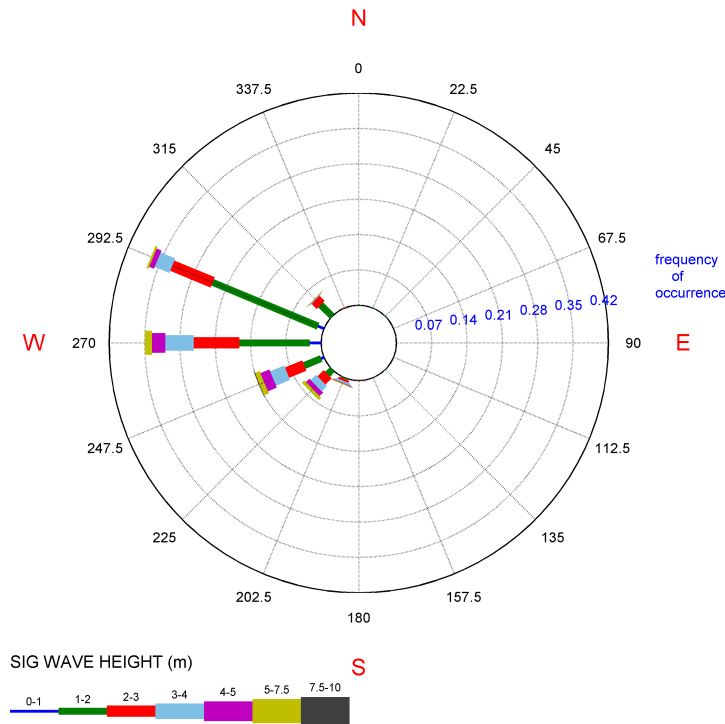
m^2/s (westward) to minimize mean surface variation. To simulate the stratification, we set the initial salinity at 30 PSU in the computational domain.

Three scenarios are included in the test: NHWAVE only, SWAN only and \overline{NHWAVE} (NHWAVE-SWAN coupled). In this way, we can analyze the wave effects on current and current effects on waves. The first run uses the NHWAVE module alone. The model is run for 5 hours to simulate the ebb tide. The current velocity profiles at $t = 3$ hour are shown in Figure 5.19. The current profiles are plotted every 1120 m across shore. The maximum current speed is about 1.46 m/s, which appears above the sand bar. A reverse flow appears near the plume front between $x = 10$ km and $x = 14$ km. This reverse flow is driven by the pressure gradient from salt water to freshwater. The contour map of the current velocity (u, w) is given in Figure 5.20.



Pacific WIS Station 83014
01-Jan-1980 thru 31-Dec-2011
Long: -124.25° Lat: 46.33° Depth:77 m
Total Obs : 280511

WAVE ROSE



US Army Engineer Research & Development Center ST83014_v01

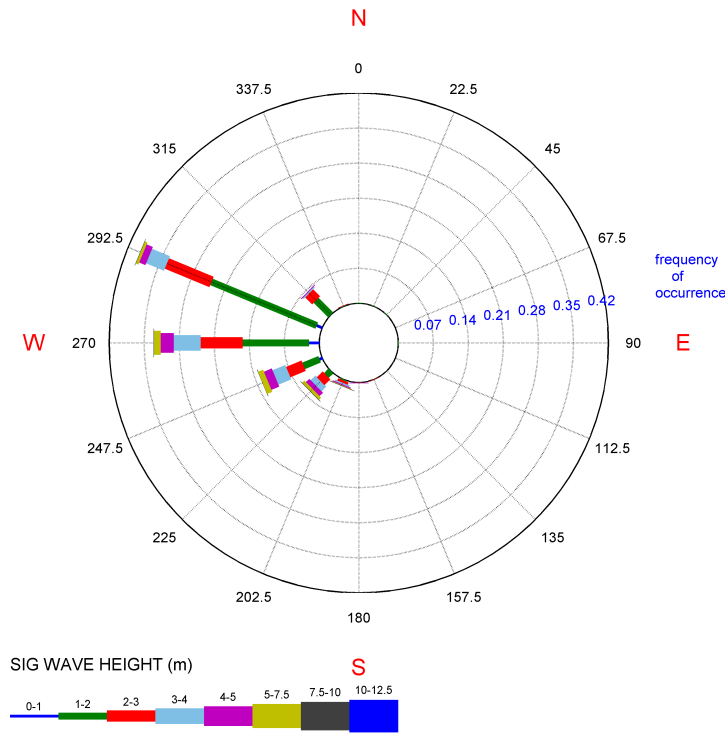
Figure 5.17: Wave Rose at WIS station 83014. Plots are based on wave hindcast model data from 1980 to 2011. The wave rose suggests that the dominant wave direction is from west to east. The dominant significant wave height is between 1 m 3 m. Figure provided by USACE WIS website ([http : //wis.usace.army.mil/data/pac/wvrs/ST83014.WAVE_allyrs.png](http://wis.usace.army.mil/data/pac/wvrs/ST83014.WAVE_allyrs.png))

The simulation is actually 2D vertical. Thus, the y -direction component is neglected. Equal volume fluxes are applied at both sides of the cross-shore domain. Due to mass conservation, the u component reaches its maximum over the sand bar. There is a downwelling velocity beneath the plume front due to the spreading of plume. The w component of velocity is also negative landward of the sand bar, which is generated by



Pacific WIS Station 83015
01-Jan-1980 thru 31-Dec-2011
Long: -124.25° Lat: 46.17° Depth:87 m
Total Obs : 280511

WAVE ROSE



US Army Engineer Research & Development Center ST83015_v01

Figure 5.18: Wave Rose at WIS station 83015. Plots are based on wave hindcast model data from 1980 to 2011. The wave rose suggests that the dominant wave direction is from west to east. The dominant significant wave height is between 1 m and 3 m. Figure provided by USACE WIS website ([http : //wis.usace.army.mil/data/pac/wvrs/ST83015_WAVE_allyrs.png](http://wis.usace.army.mil/data/pac/wvrs/ST83015_WAVE_allyrs.png))

the reverse flow. Its magnitude is much less than the u component.

After running NHWAVE only, we run the SWAN model alone to analyze the wave climate. The JONSWAP waves are applied at the western boundary (offshore). The significant wave height is set at 3 m and peak period at 20 s. The waves propagate toward the river mouth from offshore. The SWAN model is also run for 5 hours to

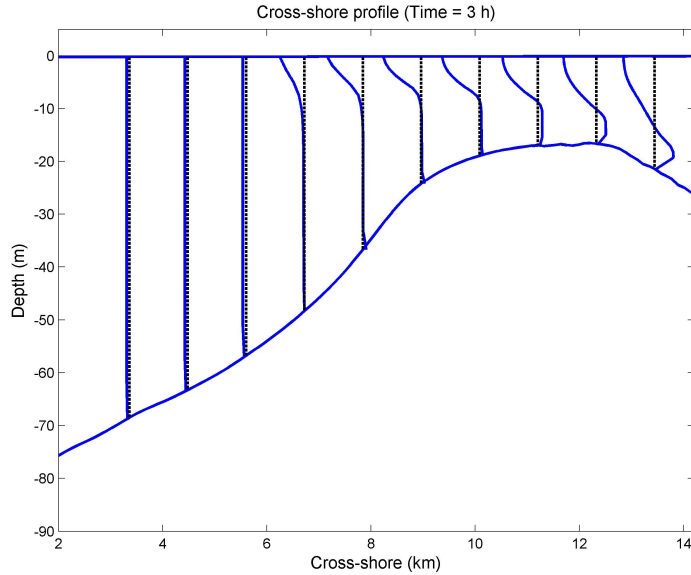


Figure 5.19: NHWAVE only result. Cross-shore bathymetry, water surface level and current profiles at mouth of Columbia River (MCR). The water depth starts with 26.4 m at the river mouth and ends with 91.3 m offshore. The water depth at the sand bar is about 16.5 m. The mean water surface ranges from -0.27 m to -0.02 m. Current profiles are plotted every 1100 m across shore. The maximum current speed is about 1.46 m/s appearing above the sand bar. A reverse flow appears near the plume front between $x = 10$ km and $x = 14$ km due to pressure gradient from salt water to fresh water.

allow the dominant waves to arrive at the river mouth. SWAN time step is 20 s. The model results are given in Figure 5.22. The wave height gradually increases towards to the river mouth due to shoaling effect and then decreases after passing the sand bar (see upper panel of Figure 5.22). The wave direction at the offshore boundary is mostly from the west. The wave directional spreading effect is minimized by extracting the wave information at the center line of computational grid in x direction (see middle panel of Figure 5.22). The wave dissipation is mainly due to the bottom friction, and therefore is very small (see lower panel of Figure 5.22). The depth induced breaking and wave white-capping in the simulation are negligible in this case.

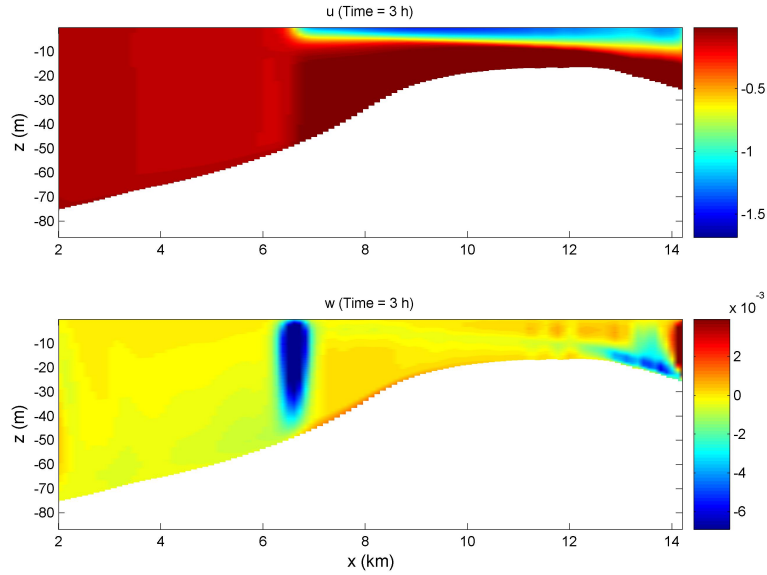


Figure 5.20: NHWAVE only result. Contour map of current velocity components. Upper: current velocity in x -direction (cross-shore). Equal fluxes are added at both sides of cross-shore domain. Due to the mass conservation, u component reaches its maximum over the sand bar. Lower: current velocity in z -direction (vertical). Its magnitude is much less than u component.

Next we run NHWAVE and SWAN coupled model using the present formulation. All the input parameters in NHWAVE and SWAN remain the same. The coupling time interval is 20 s. The flow outputs are shown in Figure 5.23 - 5.29. The comparison between NHWAVE only and $NH\overline{WAVE}$ coupled model results indicate that the opposing waves significantly affects the current velocity profiles. The plume front is thickened and extended offshore by the opposing waves.

The maximum cross-shore velocity is increased to 1.58 m/s near the sand bar as shown in Figure 5.23. Compared with NHWAVE only result (red dashed), there is an obvious offshore velocity near the bottom between $x = 6$ km and $x = 8$ km in $NH\overline{WAVE}$ result. Meanwhile, there is an onshore velocity in middle layer between $x = 7$ km and $x = 8$ km. The cross-shore velocity difference is obtained by subtracting

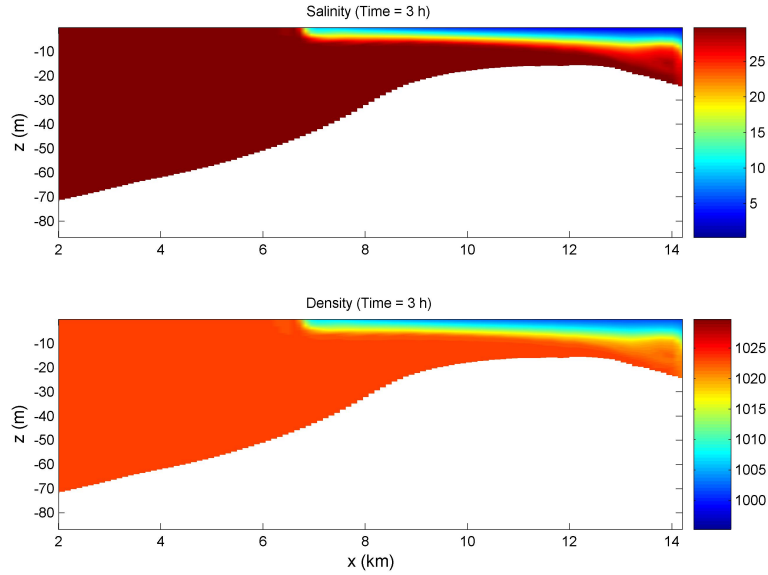


Figure 5.21: NHWAVE only result. Contour map of water salinity and density. The freshwater flows into the salt water domain from eastern boundary and forms a plume near the surface due to buoyancy.

NHWAVE only velocity from \overline{NHWAVE} velocity as shown in Figure 5.24. The velocity difference indicates that waves create vertical variations in current profile. At the water surface, a negative difference appears between $x = 5$ km and $x = 6$ km while a positive difference appears between $x = 6.5$ km and $x = 12$ km. The difference profile changes signs several times as it goes to the bottom. It is caused by the combination of vortex force and Bernoulli head gradient (see Figure 5.31, 5.32). The 27 PSU salinity contour comparison indicates that the plume front is extended and thickened by waves. Waves also creates oscillatory features at the plume base over the sand bar as seen in green dotted line of Figure 5.24. The current shear $\partial u/\partial z$ profile is given in Figure 5.25. Most of the current shear appears at the plume base. There is also shear near the bottom.

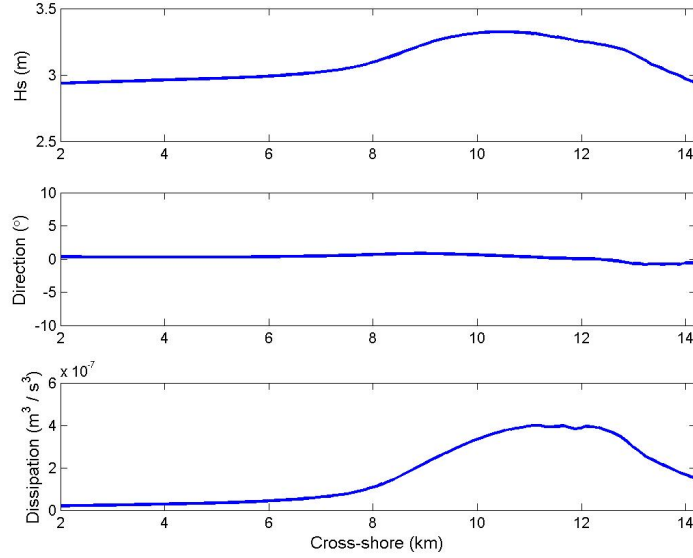


Figure 5.22: SWAN only result. Upper: Significant wave height; Middle: Peak wave direction; Lower: wave dissipation. The wave height at the western boundary is 3 m. Then wave height increases before the sand bar and decreases after the sand bar. The wave direction is mostly from the west. The wave dissipation is very small since waves are in deep water.

The contour map of $NH\overline{WAVE}$ current velocity is given in Figure 5.26. The u component has an offshore velocity near the bottom between $x = 6$ km and $x = 8$ km. The w component has an upwelling seaward of the plume front and a downwelling beneath the plume front. There are also pulses in w component between $x = 9$ km and $x = 13$ km. The salinity comparison between NHWAVE only and $NH\overline{WAVE}$ coupled model also indicate that the plume front is extended offshore and disturbed vertically by the opposing waves (see Figure 5.21 and 5.29).

The current velocity anomaly between $NH\overline{WAVE}$ and NHWAVE is given in Figure 5.27. The u velocity is accelerated by waves between $x = 8$ km and $x = 12$ km. The u velocity at the plume front is slowing down. An offshore velocity anomaly is generated near the bottom right beneath the plume front. In w velocity, there is an upward anomaly landward of the plume front and downward anomaly right beneath the plume front. The current velocity anomaly with Uchiyama's vortex force formulation

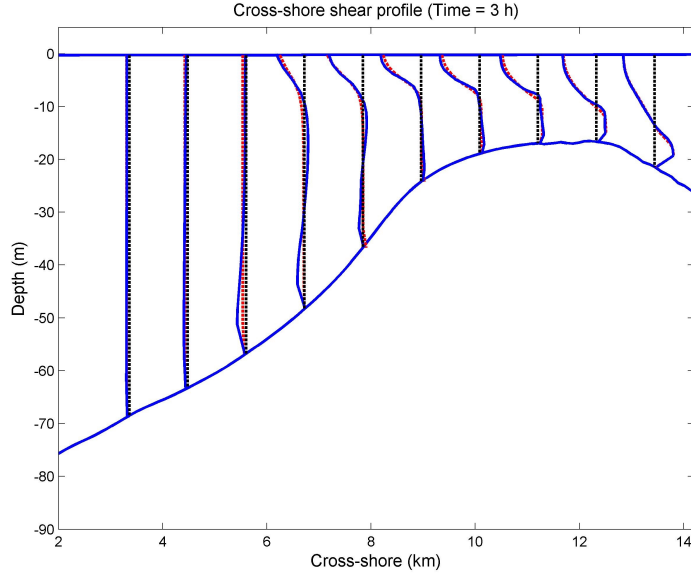


Figure 5.23: Cross-shore bathymetry, water surface level and comparison of current profiles at Columbia River mouth. Red Dash: NHWAVE only current profile as shown in Figure 5.19; Blue Solid: $NHWAVE$ coupled current profile. The mean water surface ranges from -0.37 m to -0.1 m. Current profiles are plotted every 1120 m across shore. The maximum current speed is about 1.58 m/s appearing above the sand bar. Compared with NHWAVE only result, there is an offshore velocity near the bottom between $x = 3$ km and $x = 9$ km in $NHWAVE$ coupled result. Meanwhile, there is an onshore velocity in middle layer between $x = 3$ km and $x = 9$ km.

is given in Figure 5.28. The patterns of current anomaly are very similar. However, the present formulation gives larger velocity anomaly at the plume base and front.

The wave-induced Stokes drift velocity is given in Figure 5.30. The x -direction Stokes drift velocity component reaches its maximum at the sand bar, which is about 0.04 m/s. In the present formulation, the Stokes drift velocity is also affected by the current shear as shown in the upper panel of the figure. The y -direction Stokes drift velocity component is negligible since waves mostly propagate in cross-shore direction. The vertical direction Stokes drift velocity component is generated by the bathymetry variation and mass conservation in Stokes drift velocity (Figure 5.44). Specifically, the

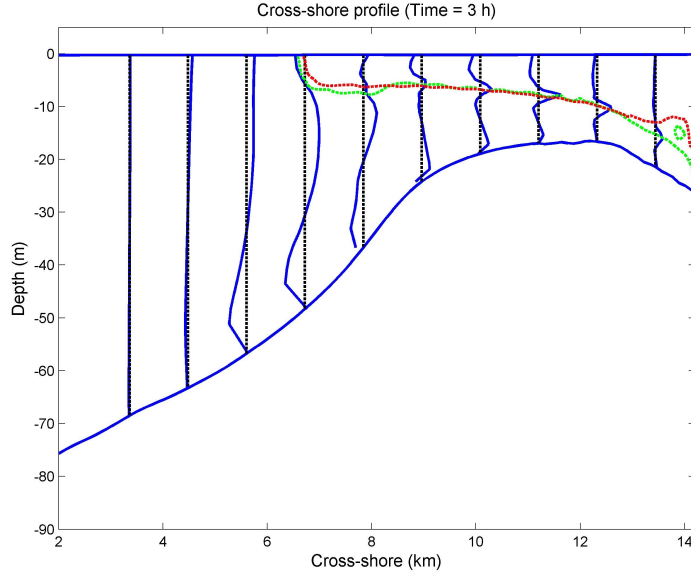


Figure 5.24: Cross-shore bathymetry, water surface level, salinity contour and current velocity difference profiles at Columbia River mouth. The green dotted line is 27 PSU salinity contour of $NHWAVE$ result. The red dotted line is 27 PSU salinity contour of NHWAVE result. The cross-shore velocity difference is obtained by subtracting NHWAVE only result from $NHWAVE$ coupled result. The mean water surface ranges from -0.37 m to -0.1 m. Current velocity difference is calculated by subtracting NHWAVE only output from $NHWAVE$ coupled output. The profiles are plotted every 1120 m across shore. The maximum current speed difference is about 0.31 m/s appearing near $x = 6$ km. The plots indicate that the opposing-waves create vertical variations in current cross-shore velocity.

vertical Stokes drift velocity is positive near the bottom because of decreasing depth between $x = 8$ km and $x = 10$ km. The mass conservation equation requires that it has to be negative near the surface. The vertical Stokes drift velocity then becomes negative near the bottom between $x = 12$ km and $x = 14$ km. It is positive near the surface.

The contour map of vortex force is given in Figure 5.31. The x component vortex force is positive at the plume front. Due to the longshore uniform assumption and onshore wave direction, the x -component vortex force is mostly determined current

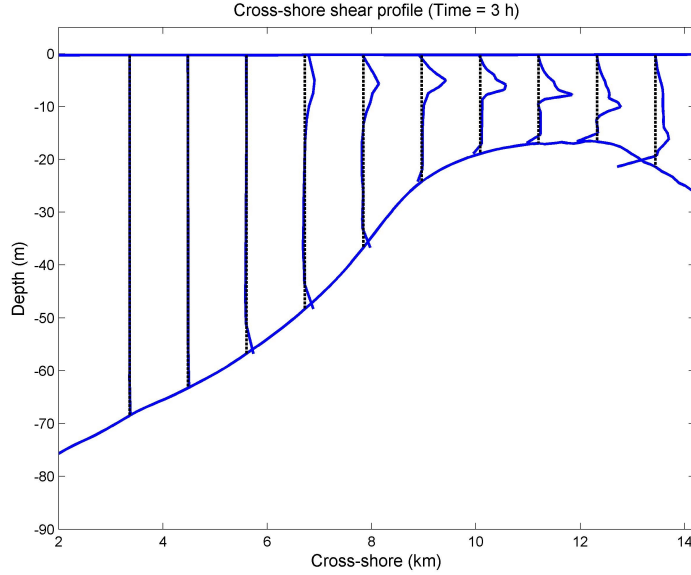


Figure 5.25: Cross-shore bathymetry, water surface level and current shear $\partial u/\partial z$ profiles at the mouth of Columbia River. The plot indicates that most of the current shear appears at the plume front. There is also shear near the bottom.

shear and vertical Stokes drift velocity according to term $-w^{st}\partial u/\partial z$. The current shear $\partial u/\partial z$ is negative along the density plume and changes to positive as approaching to the bottom. Meanwhile, the vertical Stokes drift velocity alter signs from surface to bottom, resulting in the negative vortex force above the plume and positive vortex force below the plume. The y -component vortex force is neglected. The z -component vortex force is determined by x -component Stokes drift velocity u^{st} and current shear according to term $u^{st}\partial u/\partial z$. The z -component of vortex force emerges near the plume front with negative values up and positive values down due to the current shear. There are also pulses in both x and z component of vortex force, which are caused by cross-shore variation of current shear.

The Bernoulli head gradient is given in Figure 5.32. The x -component of Bernoulli head gradient is positive (negative forcing) offshore of the sand bar and

negative (positive forcing) onshore of the sand bar. It is because the wave height increases at the sand bar and decreases after passing it as shown in Figure 5.22. The gradient is larger over shallow water area than deep area. The x -component gradient drives the current offshore seaward of the sand bar and extend the plume front. At the plume front, the vortex force applies a landward force, which slows down and thickens the plume. Both y and z components of Bernoulli head gradient are negligible.

The SWAN outputs are shown in Figure 5.33. The depth-weighted current is compared with the depth-averaged current. In the presence of the opposing current, the significant wave height at the sand bar is slightly larger than SWAN only case. The total wave dissipation at the sand bar is also larger than the SWAN only case due to increasing wave height. The current velocity is too small compared to wave phase speed to make significant impacts on wave. The results of depth-weighted current and depth-averaged current are very similar for this case.

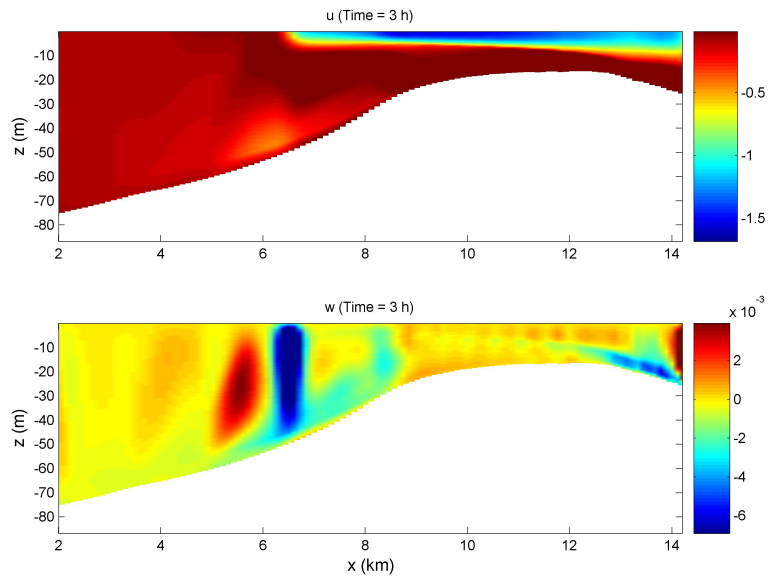


Figure 5.26: Contour map of current velocity components generated by $NHWAVE$ coupled model. Upper: current velocity in x -direction (cross-shore). Equal fluxes are added at both sides of cross-shore domain. Due to the mass conservation, u component reaches its maximum over the sand bar. The magnitude of u is confined near the surface due to stratification. Lower: current velocity in z -direction (vertical). There is an upwelling seaward of plume front and downwelling beneath the plume front. Its magnitude is much less than u component. There are pluses in w velocity near the plume base over the sand bar.

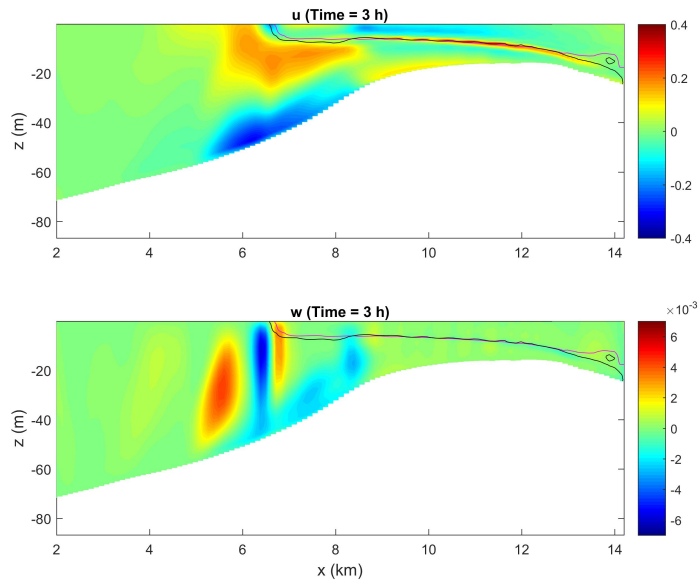


Figure 5.27: Contour map of current velocity anomaly generated by $NHWAVE$ - $NHWAVE$ results. Black Solid: 27 PSU salinity contour of $NHWAVE$ results. Pink Solid: 27 PSU salinity contour of $NHWAVE$ results. Upper: current velocity anomaly in x -direction (cross-shore). The u velocity is accelerated by waves between $x = 8$ km and $x = 12$ km. The u velocity at the plume front is slowing down. An offshore velocity is generated near the bottom beneath the plume front. Lower: current velocity anomaly in z -direction (vertical). There is an upward anomaly landward of the plume front and downward anomaly right beneath the plume front.

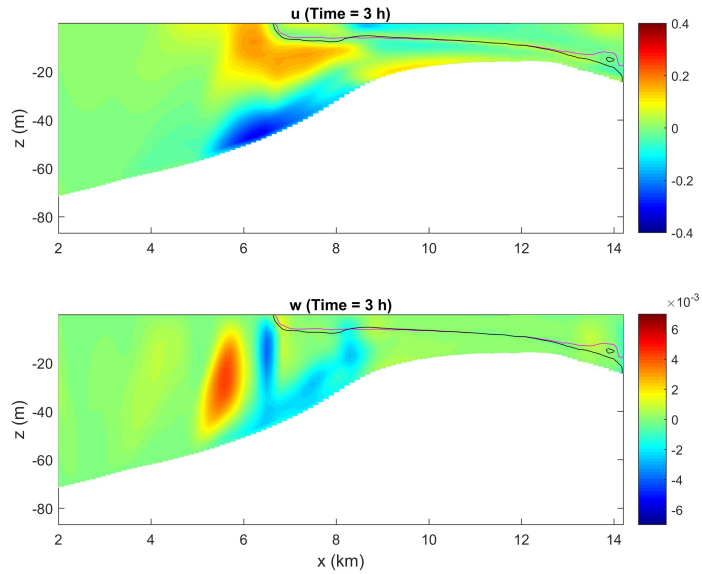


Figure 5.28: Contour map of current velocity anomaly generated by $NHWAVE$ - $NHWAVE$ results with Uchiyama's vortex force formulation. Black Solid: 27 PSU salinity contour of $NHWAVE$ results. Pink Solid: 27 PSU salinity contour of $NHWAVE$ results. Upper: current velocity anomaly in x -direction (cross-shore). The u velocity is accelerated by waves between $x = 8$ km and $x = 12$ km. The u velocity at the plume front is slowing down. A offshore velocity is generated near the bottom beneath the plume front. Lower: current velocity anomaly in z -direction (vertical). There is an upward anomaly landward of the plume front and downward anomaly right beneath the plume front.

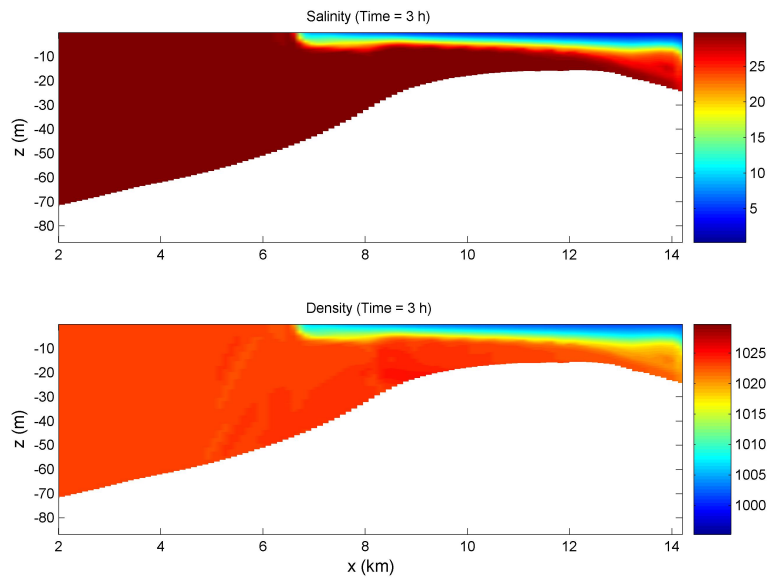


Figure 5.29: Contour map of water salinity. The water flows into the salt water domain with 0 PSU at eastern boundary. The flow is stratified and forms plume front at the upper layer. The comparison with NHWAVE only salinity (Figure 5.21) indicates that the plume front is thickened and extended offshore by waves.

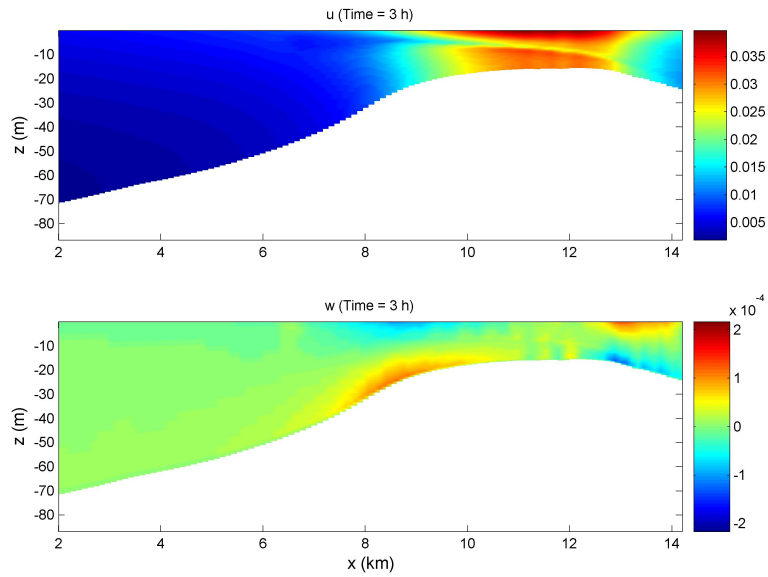


Figure 5.30: Contour map of wave-induced Stokes drift velocity. Upper: x -direction Stokes drift velocity component. u component reaches its maximum at the sand bar, which is about 0.04 m/s. Middle: y -direction Stokes drift velocity component. v component is negligible since waves mainly propagate in cross-shore direction. Lower: vertical direction Stokes drift velocity component. w component is generated by the bathymetry and mass conservation in Stokes drift velocity (Figure 5.44).

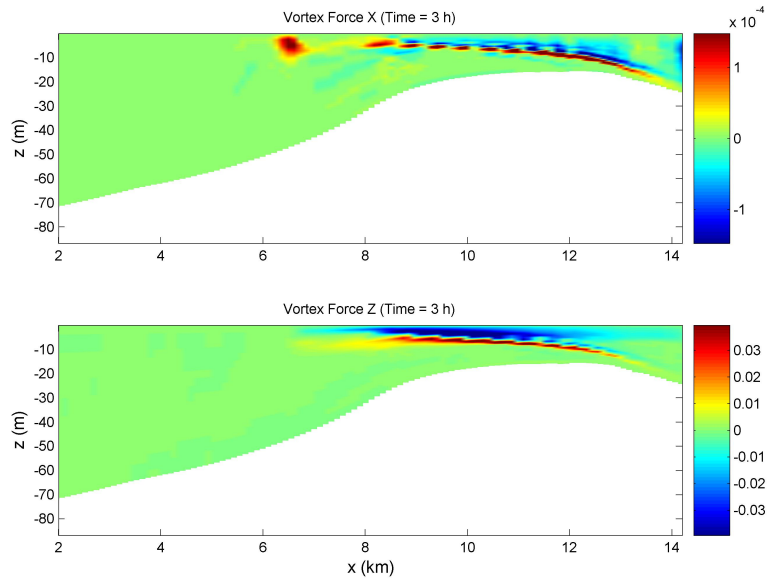


Figure 5.31: Contour map of vortex force. Upper: x -component. The x component of vortex force is about 10^{-4} m/s^2 . There is a positive vortex force at the plume front, where the fresh water is mixing with salt water. The x component vortex force appears along the plume base with negative value up and positive values down. Lower: vertical component of vortex force emerges at the sand bar. The vertical component of vortex force emerges near the plume front with negative values up and positive values down. There are pulses in both x and z component of vortex force, which is caused by the cross-shore variation of current shear.

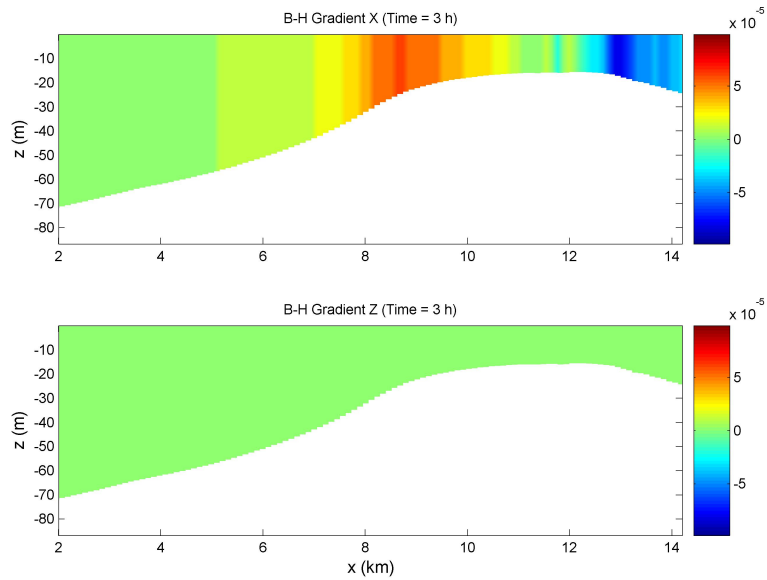


Figure 5.32: Contour map of Bernoulli head gradient. Upper: x component of Bernoulli head gradient is positive offshore of the sand bar and negative onshore of the sand bar. It is mainly because of the wave set down near the sand bar. The gradient is larger over shallow water area than deep area. The gradient drives the current offshore at the sand bar area. Both y and vertical components of Bernoulli head gradient are negligible.

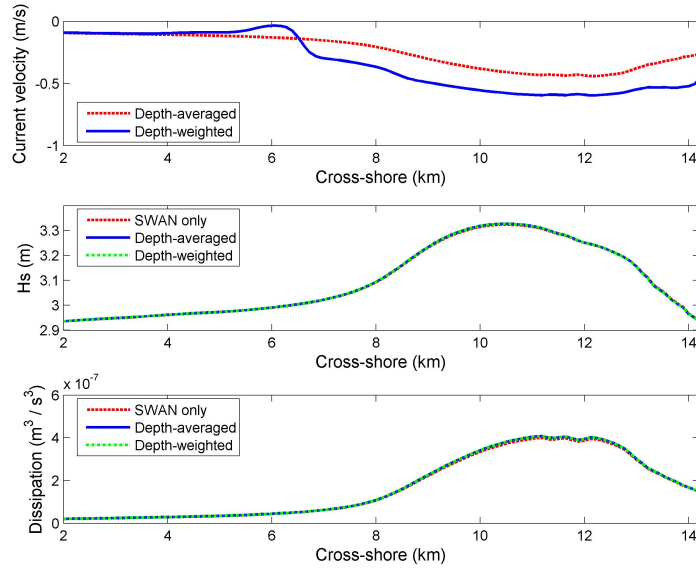


Figure 5.33: Comparison of significant wave height and total wave dissipation between SWAN only and $NH\overline{WAVE}$ coupled. Upper: significant wave height. Lower: total wave dissipation. Red Dash: results from SWAN model only; Blue Solid: results from $NH\overline{WAVE}$ coupled model depth-averaged current. Green Dash: results from $NH\overline{WAVE}$ coupled model depth-weighted current. The wave height at the western boundary is set as 3 m. The wave height gradually increases as approaching to the river mouth due to shoaling effect. In the presence of the opposing current, the significant wave height at the sand bar is slightly larger than SWAN only case (see Figure 5.22). The total wave dissipation at the sand bar is also larger than the SWAN only case due to the increasing wave height. The depth-weighted current generates very similar result as depth-averaged current.

Chapter 6

APPLICATION OF WAVE VORTEX FORCE TO LANGMUIR CIRCULATION USING $NH\overline{WAVE}$

Langmuir circulation was first discovered and characterized by Irving Langmuir, who observed the windrows of seaweed in the Sargasso Sea in 1927 (Langmuir, 1938). At the surface of lakes or oceans, bands of foam or other floating material are developed, which align with the downwind direction. Bands are produced by a flow convergence near the surface. A downward flow is formed below the bands while an upward flow is formed between the bands. The circulation can be represented as a set of vortices of alternating signs in horizontal direction (see Figure 6.1), known as Langmuir cells (LC). Among all the possible generating mechanisms of Langmuir cells, the interaction between the wind-driven shear current and the wave Stokes drift is widely accepted as the main driving force (Craik and Leibovich, 1976). Langmuir cells can extend from tens of meters to kilometers in downwind direction. The distance between the bands ranges from meters to kilometers. Thus Langmuir circulation is very important mixing process in the upper ocean (Thorpe, 2004).

Most observations of Langmuir cells are in the upper mixed layer over relatively deep water. However, recent field observations suggest that Langmuir cells can extend to the bottom boundary layer in shallow shelf coastal regions (Gargett and Wells, 2007). Langmuir cells in shallow water are believed to play a key role in sediment re-suspension and transport. Large-eddy simulation (LES) studies of Langmuir circulation in the wind-driven shear current in shallow water have been conducted (Tejada-Martinez and Grosch, 2007; Kukulka *et al.*, 2009). In the LES model, the Langmuir circulations are generated using the Craik-Leibovich vortex force formulation (Craik and Leibovich, 1976). According to the theory, a small spanwise perturbation in downwind Stokes

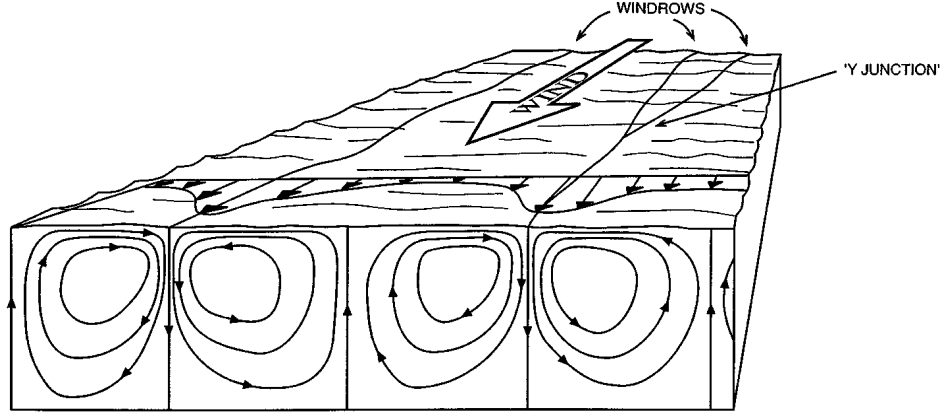


Figure 6.1: The Langmuir circulation flow pattern. The wind-generated mean flow is developed at the ocean surface with spanwise variations. Meanwhile, a downward flow is formed below the windrows while an upward flow is formed between the windrows. The cell is roughly in square form with size ranging from 2 m to 300 m. The circulation can be represented as a set of vortices of alternating signs in horizontal direction. Figure from Thorpe (2004).

drift and mean flow generates a vertical component of vorticity. The coupling of vertical vorticity with Stokes drift introduces a horizontal vortex force, which leads to a circulation with downwind vorticity.

In this chapter, the simplified wave vortex force is applied to $NH\overline{WAVE}$ with $k - \epsilon$ turbulence model to simulate Langmuir cells. We follow the model setup in Tejada-Martinez and Grosch (2007) in order to directly compare the results.

6.1 Model Setup

6.1.1 Governing Equations

In Chapter 4, we have obtained expressions for wave-averaged forces for the mean flow equations. We add viscous forces ($\nu\nabla^2\mathbf{q}, \nu\nabla^2w$) and turbulent stresses

$(\mathbf{F}_h^{turb}, F_z^{turb})$ to the equations.

$$\frac{\partial \mathbf{q}^c}{\partial t} + (\mathbf{q}^c \cdot \nabla_h) \mathbf{q}^c + w^c \frac{\partial \mathbf{q}^c}{\partial z} + \frac{1}{\rho} \nabla_h p^c = -\nabla_h \kappa + \mathbf{J} + \mathbf{F}^w + \nu \nabla^2 \mathbf{q} + \mathbf{F}_h^{turb} \quad (6.1)$$

$$\frac{\partial w^c}{\partial t} + (\mathbf{q}^c \cdot \nabla_h) w^c + w^c \frac{\partial w^c}{\partial z} + \frac{1}{\rho} \frac{\partial p^c}{\partial z} + g = -\frac{\partial \kappa}{\partial z} + K + \nu \nabla^2 w + F_z^{turb} \quad (6.2)$$

$$\nabla_h \cdot \mathbf{q}^c + \frac{\partial w^c}{\partial z} = 0 \quad (6.3)$$

ν is the kinematic viscosity. At the bottom and surface viscous boundary layers, the viscous forces can become very significant. The Langmuir number La_t and Reynolds number Re are defined as

$$La_t = \left(\frac{u_\tau}{u_*^{st}} \right)^{\frac{1}{2}} \quad (6.4)$$

$$Re = \frac{u_\tau \delta}{\nu} \quad (6.5)$$

$$u_\tau = \left(\frac{\tau_s}{\rho} \right)^{\frac{1}{2}} \quad (6.6)$$

$$u_*^{st} = a^2 \sigma_w k \quad (6.7)$$

where u_τ is the friction velocity defined by constant wind stress τ_s in x -direction applied over the surface, ρ is water density, $\delta = H/2$ is half of water depth, ν is the kinematic viscosity, a is wave amplitude, σ_w is wave frequency and k is wave number. u_*^{st} is defined as the characteristic Stokes drift velocity. The Langmuir number La_t indicates strength of wave effects. Smaller La_t represents stronger wave effects. The vortex force in the governing equation is the cross product of Stokes drift velocity and mean flow vorticity. The Reynolds number is determined by friction velocity, water depth and kinematic viscosity.

We also give a simple version of vortex force formulation in terms of Stokes velocity $\mathbf{u}^{st} = (u^{st}, 0, 0)$, current velocity \mathbf{u}^c and current vorticity $\boldsymbol{\Omega}^c$ as in Tejada-Martinez and Grosch (2007). The results of the present formulation and the simple version of formulation are compared.

$$(\mathbf{J}, K) = \frac{1}{La_t^2} \mathbf{u}^{st} \times \boldsymbol{\Omega}^c \quad (6.8)$$

$$\kappa = \frac{1}{2} (\mathbf{u}^{st} \cdot \mathbf{u}^{st} + \mathbf{u}^c \cdot \mathbf{u}^{st}) \quad (6.9)$$

6.1.2 Model Setup

The simulation is to test whether $NH\overline{WAVE}$ can generate Langmuir cells using $k - \epsilon$ turbulence model. Following Tejada-Martinez and Grosch (2007), two scenarios are considered in the simulation. Case (1) is wind-driven shear flow with C-L vortex force. Case (2) is wind-driven shear flow without C-L vortex force. During the simulation, all the other parameters are set to be the same for both cases. The water depth is $H = 15$ m. The wind stress is applied to the surface only in x -direction. Monochromatic waves are considered to propagate in the downwind direction. The wave length is set as $L = 2\pi H = 94.2$ m which is the same as in Tejada-Martinez and Grosch (2007). The domain size in x (streamwise) and y (spanwise) directions are set as $L_x = 2\pi H = 94.2$ m and $L_y = 4\pi/3H = 62.8$ m, respectively. The reason of choosing these lengths is that the observed crosswind scale of Langmuir cells is roughly 3-6 times their vertical scale ($3H - 6H$). The computational grids for both cases are 4 in x -direction (streamwise), 64 in y -direction (spanwise), 60 in z -direction (vertical) ($4*64*60$). In x -direction, the boundary conditions are set as periodic to allow the current to fully develop. All the variables are uniform during the simulation. Thus 4 cells are good enough for model. Langmuir cells develop in y (spanwise) and z (vertical) directions therefore we need more grid cells in y and z to resolve the structure. We also need more grid cells in z -direction to resolve bottom and surface boundary layers. The y -direction (spanwise) boundary condition is also set as periodic to avoid lateral wall boundaries.

We consider a set of realistic parameters here. The range of observed wind velocity 10 m above sea surface is around 7.8 – 11.0 m/s in most of cases (Gargett and Wells, 2007). Therefore we set wind velocity in x -direction equal to 10 m/s. The wave amplitude set is $a = 0.74$ m. Wave length is $2\pi H$, where $k = 2\pi/L = 1/H$ so that intermediate-depth waves are considered with $kH = 1$. The wave frequency is obtained based on dispersion relation $\sigma_w = \sqrt{gk \tanh kH}$. Langmuir number and Reynolds number can be determined based on these parameters, in this case $La_t = 0.7$ and $Re = 9450$ based on viscous kinematic viscosity or $Re = 94$ based on eddy kinematic

viscosity.

To generate the wind-driven shear flow, the model was first run for 50 hours without C-L vortex force to get a steady velocity profile (Figure 6.2). The shear flow velocity is about 0.48 m/s at the surface and 0.23 m/s near the bottom. The following cases adopted the steady velocity profile as the initial velocity condition. For convenience, the velocity components are labeled as U in x -direction, V in y -direction and W in z -direction. The horizontal velocity variations are necessary to form the Langmuir cells. To simulate Langmuir circulation, perturbations in horizontal velocity (ΔU) with magnitude up to 0.025 m/s were added to initial velocity of U . The initial condition is $U_0 = U(z) + \Delta U$, $V_0 = 0$, $W_0 = 0$. No perturbation is added to initial surface elevation η_0 . The model was run for 1 hour for cases with and without C-L vortex force. The model results for both cases are compared as below.

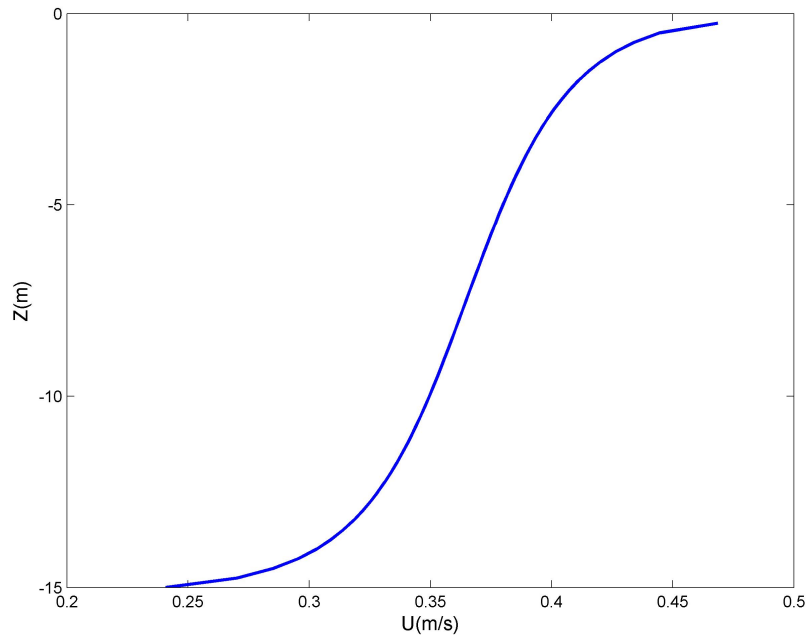


Figure 6.2: Wind-driven shear flow (x -direction) velocity profile after 50 hour run $U^c(z)$. Maximum velocity is 0.48 m/s at the surface and minimum velocity is 0.23 m/s near the bottom. Wind velocity (10 m above sea surface) is 10 m/s in x -direction only. Drag coefficient is set as 0.0013

6.2 Results

6.2.1 Comparison with Tejada-Martinez and Grosch (2007)

In Tejada-Martinez and Grosch (2007), Langmuir cells generated with C-L vortex force were shown in Figure 6.3. On the other hand, no Langmuir cells were generated in flow without C-L vortex force in Figure 6.4. The partial-averaging in the paper (Equation 3.1 in Tejada-Martinez and Grosch, 2007) is defined as the average over time and horizontal (x, y) directions. The fluctuating velocity is the difference between the instantaneous velocity and the partially averaged velocity.

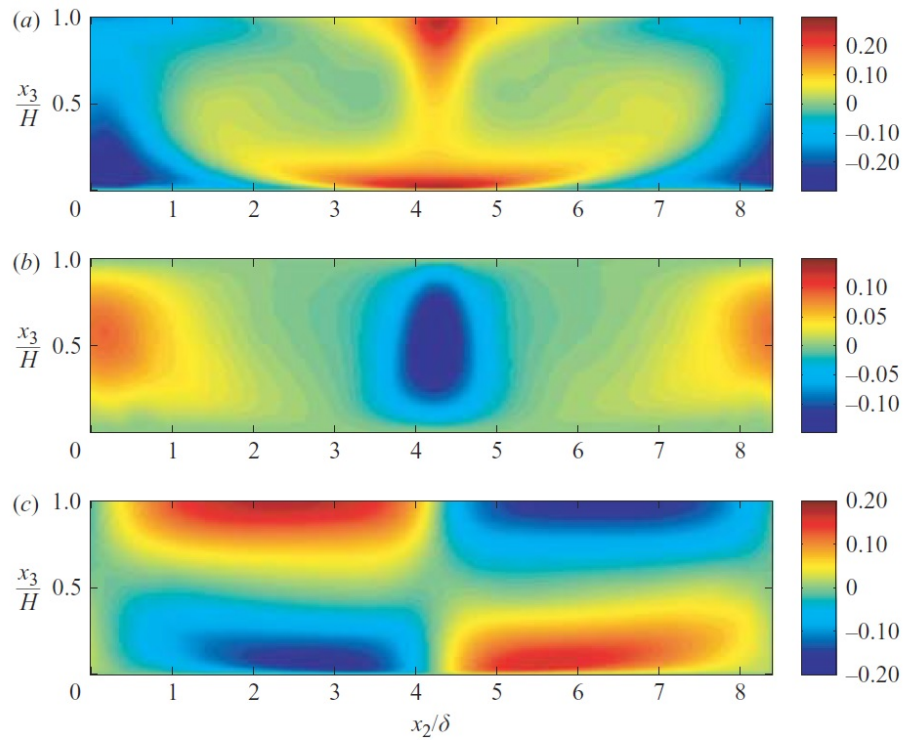


Figure 6.3: Color maps of partially (time, x and y direction) averaged fluctuating velocity components on the $y - z$ plane for flow with LC at $Re=395$ ($La_t=0.7$, $L=6H$). Velocity normalized by mean center line velocity in x -direction. (a) Normalized x -direction fluctuating velocity U . (b) Normalized z -direction fluctuating velocity W . (c) Normalized y -direction fluctuating velocity V . Cited from Figure 3 in Tejada-Martinez and Grosch (2007).

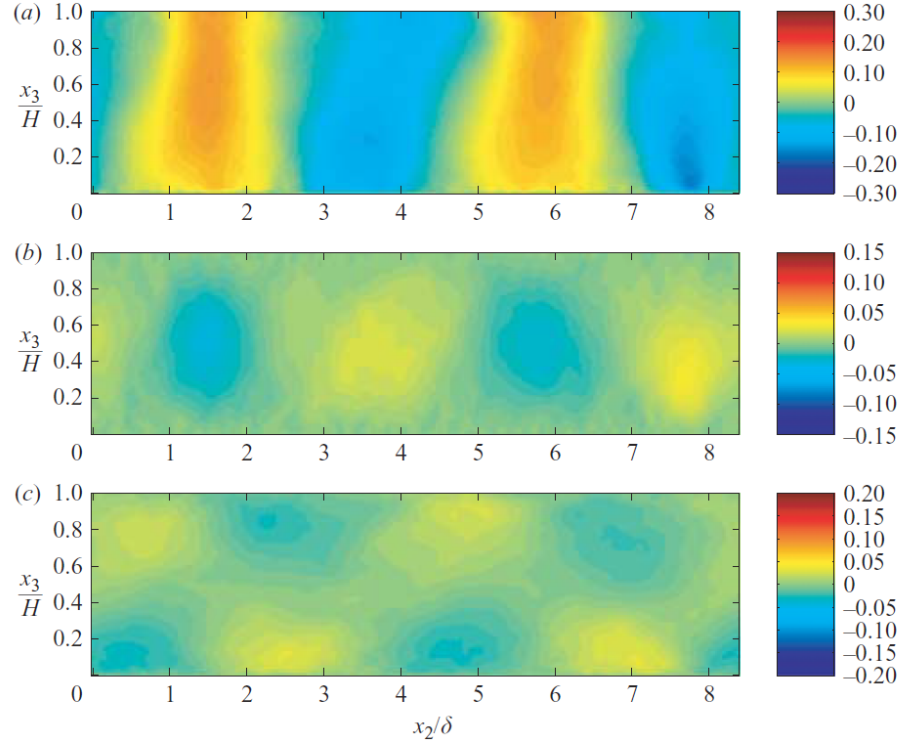


Figure 6.4: Color maps of partially (time, x and y direction) averaged fluctuating velocity components on the $y - z$ plane for flow without LC at $Re=395$ ($La_t = \infty$, $L=6H$). Velocity normalized by mean center line velocity in x -direction. (a) Normalized x -direction fluctuating velocity U . (b) Normalized z -direction fluctuating velocity V . (c) Normalized y -direction fluctuating velocity W . Cited from Figure 4 in Tejada-Martinez and Grosch (2007).

The $NH\overline{WAVE}$ model results illustrate the same pattern for flow with C-L vortex force in Figure 6.5 except some detailed features near the surface and bottom. Color map of x -direction velocity components U in both Figure 6.3 and Figure 6.5 indicate larger positive velocity anomalies appear near the surface and bottom and negative velocity anomalies appear in the lower water column on both sides. Velocity component V both have vortices with alternating signs in both y and z directions. Regions of positive W are referred to as upwelling limbs and regions of negative W are referred to as downwelling limbs. Figure 6.5 also indicates that the downwelling limbs have greater intensity than the upwelling limbs (Tejada-Martinez and Grosch,

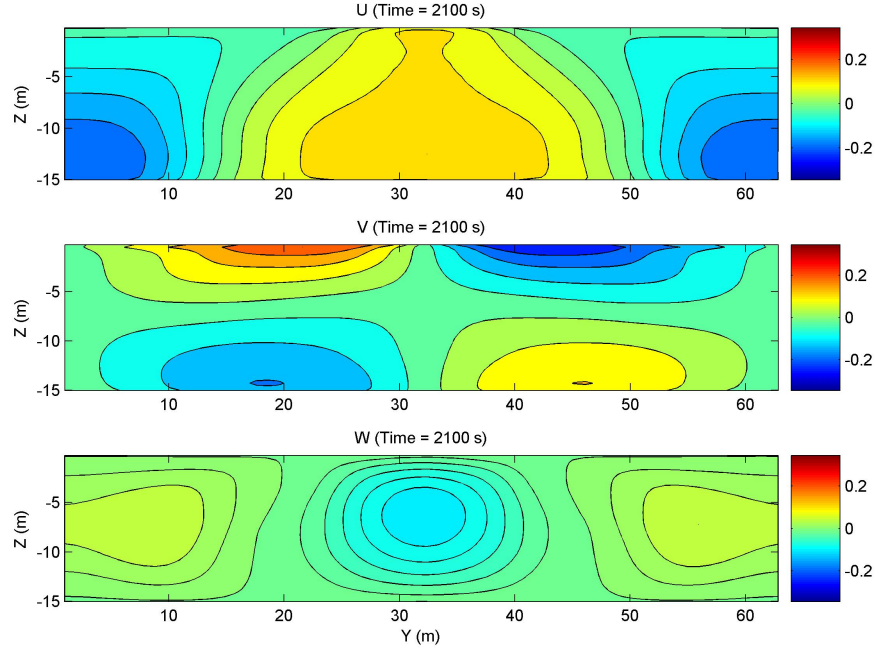


Figure 6.5: Color maps of fluctuating velocity components on the $y - z$ plane for flow with LC ($La_t = 0.7$, $L=2\pi H$). Results are based on the present formulation. Velocity normalized by the total mean velocity in x -direction. (Top) Normalized x -direction fluctuating velocity U . (Middle) Normalized y -direction fluctuating velocity V . (Bottom) Normalized z -direction fluctuating velocity W . Perturbations with magnitude up to 0.025 m/s are added to only U in initial condition.

2007). No Langmuir cells are generated without C-L vortex force. Results based on the simpler version of vortex force formulation (Equation (6.8) and (6.9)) are given in Figure 6.6. The flow pattern is very similar to the $NH\overline{WAVE}$ results. The Langmuir cells are unsteady and constantly evolving during the simulation. It is because the vortex force is determined by the velocity anomalies and forces the velocity anomalies in return.

The vortex force for the present formulation and the simple version of formulation are given in Figure 6.7 and 6.8, respectively. Overall, the vortex forces of the present formulation are confined near the upper layer, while the simple version vortex forces extend deeper in vertical direction. The x component vortex force in the present

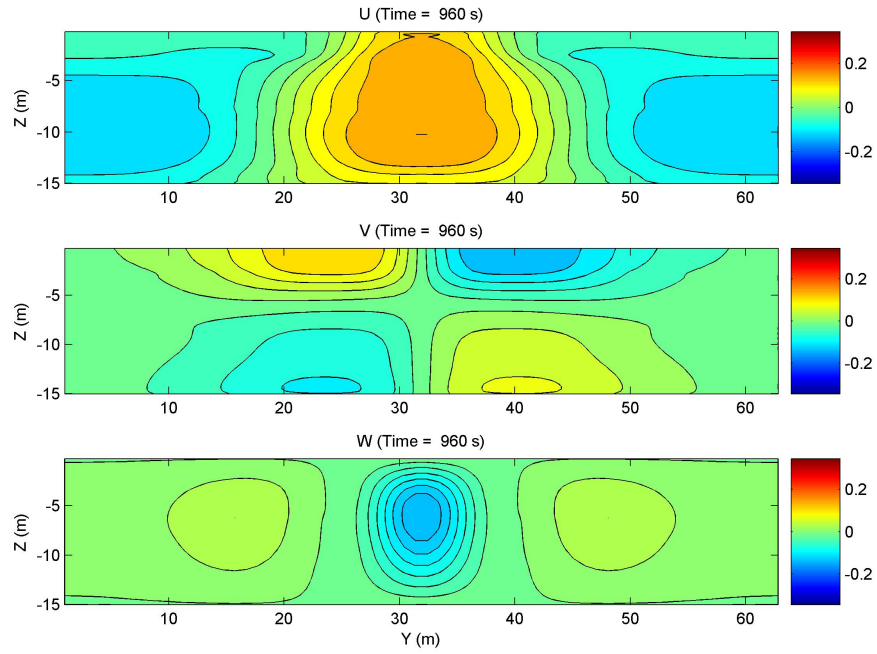


Figure 6.6: Color maps of fluctuating velocity components on the $y - z$ plane for flow with LC ($La_t = 0.7$, $L=2\pi H$). Results are based on the simple version formulation. Velocity normalized by the total mean velocity in x -direction. (Top) Normalized x -direction fluctuating velocity U . (Middle) Normalized y -direction fluctuating velocity V . (Bottom) Normalized z -direction fluctuating velocity W . Perturbations with magnitude up to 0.025 m/s are added to only U in initial condition.

formulation is generated by term $-w^{st}\partial u/\partial z$ (see upper in Figure 6.7). The x component in the simple version of formulation is zero since w^{st} is equal to zero (see upper in Figure 6.8). The y component vortex force in the present formulation is confined near the surface with alternating signs in spanwise direction (see middle in Figure 6.7). The y component vortex force in the simple version of formulation is larger in magnitude than the present formulation. In addition, the vortex force is symmetric with positive value at the left half and negative value at the right half (see middle in Figure 6.8). It is because the present vortex force includes the y derivative of term $\int_{-H}^z \mathbf{q}^{st}(\zeta)d\zeta \cdot (\partial \mathbf{q}^c/\partial z)$ as shown in Equation (4.61). The simple version vortex force doesn't include this term. The z component vortex force in the present formulation is negative in the upper layer, while the simple version give positive value. It is also because the present vortex force includes the vertical derivative of term $\int_{-H}^z \mathbf{q}^{st}(\zeta)d\zeta \cdot (\partial \mathbf{q}^c/\partial z)$ (see Equation (4.67)), which is not in the simple version. This term is moved to Bernoulli head in Uchiyama *et al.*'s (2010) vortex force formulation.

6.2.2 Flow structure

The crosswind distributions of velocity for both cases at different vertical levels are shown in Figure 6.9 and Figure 6.10, respectively. The three vertical levels are chosen as near surface ($z = -1.25$ m), middle depth ($z = -7.5$ m) and near bottom ($z = -13.75$ m). For the flow without LC, the crosswind variations of velocity are very small (see Figure 6.10). In the presence of LC, the vertical mixing is significant (see Figure 6.9). Through the water column, velocity component U is strengthened in the middle and diminished at both sides. The spanwise variations become smaller as vertical level gets closer to the bottom. The sign of velocity component V near the surface is opposite to the one near the bottom. At the middle depth, the flow is slightly affected by the lower cells. The magnitude of downwelling velocity is larger than upwelling velocity as shown in velocity component W . On the other hand, the regions of downwelling limbs are narrower than the regions of upwelling limbs.

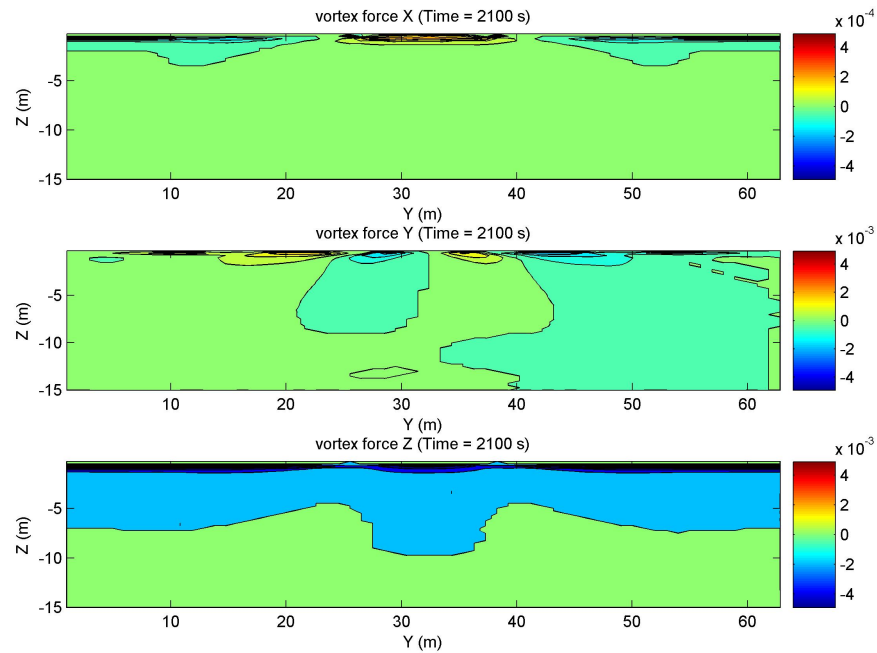


Figure 6.7: Color maps of vortex force on the $y - z$ plane for flow with LC ($La_t = 0.7$, $L=2\pi H$). Results are based on the present formulation. (Upper) x component of vortex force. The x component is nonzero. (Middle) y component of vortex force. The y component has alternating signs in spanwise direction. (Lower) z component of vortex force.

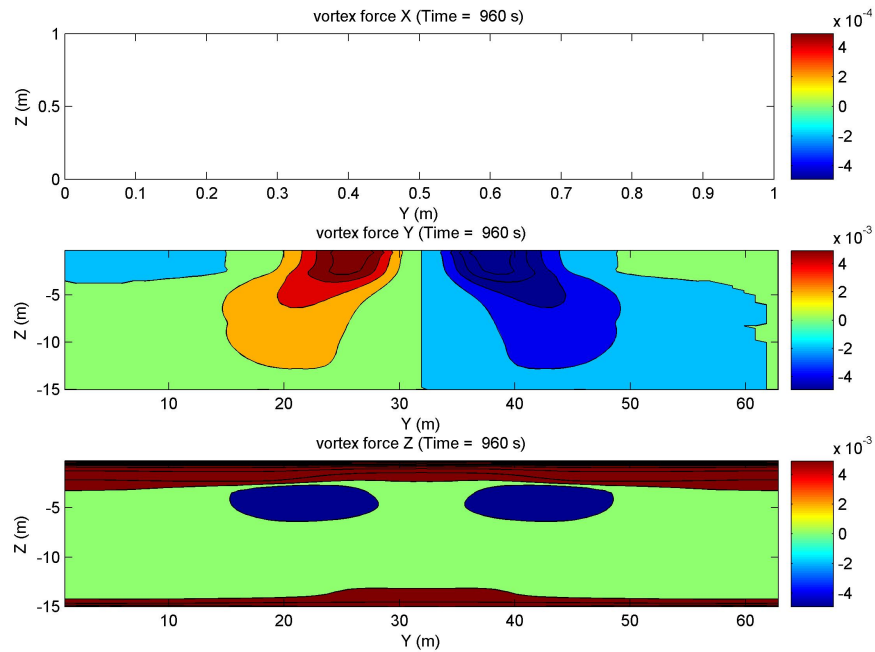


Figure 6.8: Color maps of vortex force on the $y-z$ plane for flow with LC ($La_t = 0.7$, $L=2\pi H$). Results are based on the simple version formulation. Results are based on the present formulation. (Upper) x component of vortex force. The x component is all zero. (Middle) y component of vortex force. The y component is symmetric in spanwise direction. (Lower) z component of vortex force.

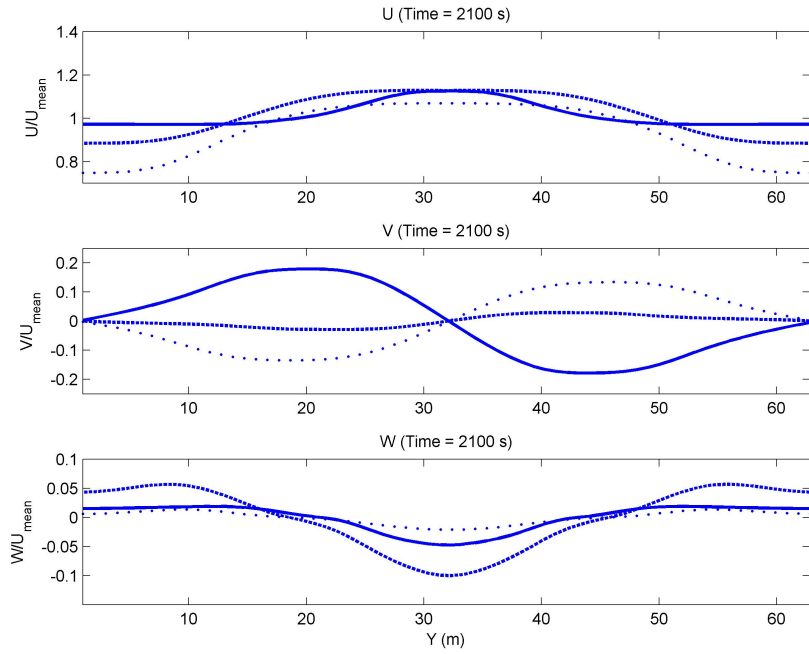


Figure 6.9: Crosswind distribution of mean velocity components on the $y - z$ plane for flow with LC ($La_t = 0.7$, $L = 2\pi H$). Velocity normalized by the total mean velocity in x -direction. (Top) Normalized x -direction fluctuating velocity. (Middle) Normalized y -direction fluctuating velocity. (Bottom) Normalized z -direction fluctuating velocity. Perturbations with magnitude up to 0.025 m/s are added to U and V in initial condition. Solid line: flow near surface ($z = -1.25$ m); Dash-dot line: flow at middle depth ($z = -7.5$ m); Dotted line: flow near bottom ($z = -13.75$ m).

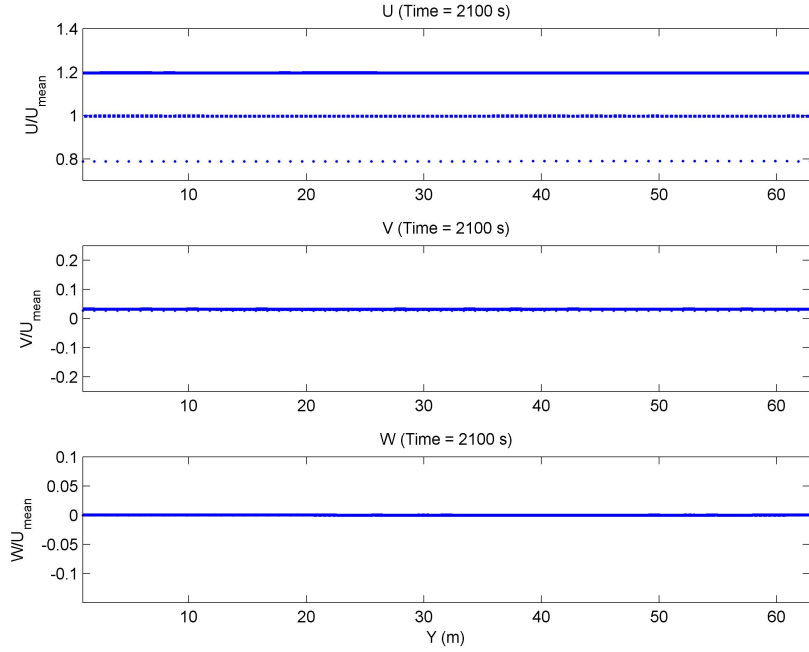


Figure 6.10: Color maps of partially averaged fluctuating velocity components on the $y - z$ plane for flow with LC ($La_t = \infty$, $L=6H$). Velocity normalized by the total mean velocity in x -direction. (Top) Normalized x -direction fluctuating velocity. (Middle) Normalized y -direction fluctuating velocity. (Bottom) Normalized z -direction fluctuating velocity. Perturbations with magnitude up to 0.025 m/s are added to U and V in initial condition. Solid line: flow near surface ($z = -1.25$ m); Dash-dot line: flow at middle depth ($z = -7.5$ m); Dotted line: flow near bottom ($z = -13.75$ m).

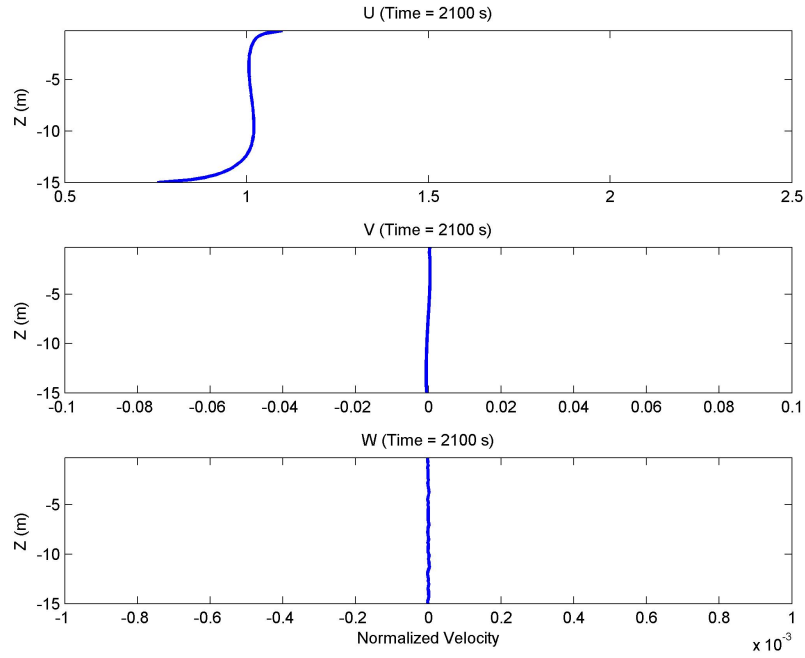


Figure 6.11: Profile of the averaged velocity over horizontal directions (x and y) with LC ($La_t = 0.7$, $L = 2\pi H$). Velocity normalized by the total mean velocity in x -direction. (Top) Normalized x -direction mean velocity U . (Middle) Normalized y -direction mean velocity V . (Bottom) Normalized z -direction mean velocity W . Perturbations with magnitude up to 0.025 m/s are added to U in initial condition. The vertical and crosswind transport is nearly zero.

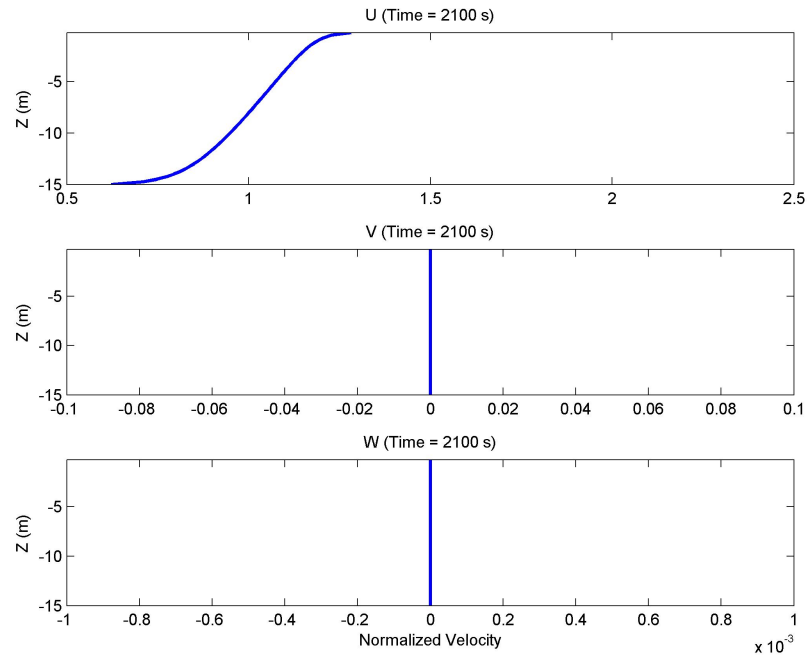


Figure 6.12: Profile of the averaged velocity over horizontal directions (x and y) with LC ($La_t = \infty$, $L = 2\pi H$). Velocity normalized by the total mean velocity in x -direction. (Top) Normalized x -direction mean velocity U . (Middle) Normalized y -direction mean velocity V . (Bottom) Normalized z -direction mean velocity W . Perturbations with magnitude up to 0.025 m/s are added to U in initial condition.

The velocity profiles with and without LC are given in Figure 6.11 and 6.12, respectively. All the velocity components are normalized by the horizontal mean velocity in the x -direction. The crosswind and vertical mean velocities are nearly zero for both cases. However, the x -direction velocity profile (with LC) is affected by the waves.

In the results above, Langmuir cells are generated by waves propagating in wind and shear flow direction. We simulated another case with waves propagating against wind and shear flow. The results suggest that no Langmuir cells are generated in this case.

Figure 6.13 illustrates the effect of Langmuir number La_t and wave length L_w on shear flow velocity profile. The La_t denotes the relative magnitude of C-L vortex force. The smaller Langmuir number indicates stronger C-L vortex force. In the figure, three velocity profiles are considered: $La_t = 0.7, L = 2\pi H$, $La_t = 0.4, L = 2\pi H$ and $La_t = 0.7, L = 4/3H$. C-L vortex force strengthens the vertical mixing and homogenize the shear flow in vertical direction.

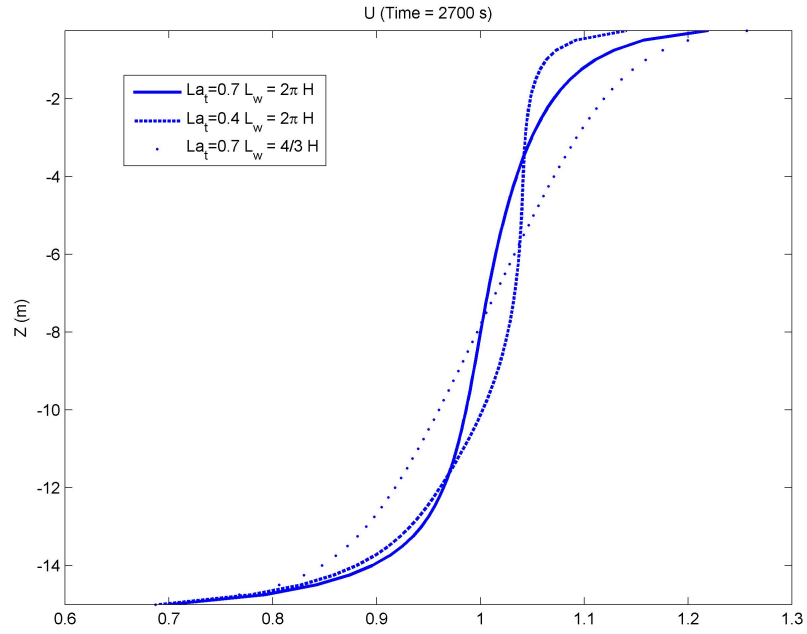


Figure 6.13: Profile of the averaged velocity component U over horizontal directions (x and y) with LC. Velocity normalized by the total mean velocity in x -direction. Solid line: $La_t = 0.7$, $L = 2\pi H$; Dash-dot line: $La_t = 0.4$, $L = 2\pi H$; Dotted line: $La_t = 0.7$, $L = 4/3 H$. Figure indicates smaller Langmuir number La_t and longer wave length L_w tend to homogenize shear flow in vertical direction.

Chapter 7

CONCLUSIONS

The interactions between surface gravity waves and vertically sheared current have been discussed in the thesis. The study consists of two parts: wave-current interaction theory and the numerical application.

7.1 Theory

In the theory part, a new framework is presented to describe the wave-current interaction for arbitrarily sheared current. The flow motions are considered to be the superposition of waves and currents. The wave equations are then separated from the mean flow equations by applying multiple scale expansion and wave-averaging. Both perturbation and numerical solutions to the resulting wave Raleigh equation have been discussed. The solvability condition of the second order wave Raleigh equation leads to the wave action equation for arbitrary current profile. The wave-averaged forces in terms of vortex force formulation are obtained from the mean flow equations. Conclusions are summarized as below:

(1) The discussion of wave vorticity for constant shear current indicates that the magnitude of wave vorticity depends on the current vertical shear Ω^s and the oblique angle θ between waves and flow direction. Specifically, for a fixed oblique angle, wave vorticity increases as current vertical shear becomes larger and decreases as current shear becomes smaller. When the waves and current are co-directional ($\theta = 0$ or $\theta = \pm\pi$), the wave vorticity is always zero and waves are irrotational. Otherwise, the magnitude of wave vorticity increases with the oblique angle and reaches to the maximum when waves are perpendicular to the current. With all the other variables set the same, waves with longer period have smaller wave vorticity.

(2) The comparison between numerical solution and perturbation solution to wave Raleigh equation indicates that $O(\epsilon)$ perturbation solution is a fairly good approximation. It is recommended in the numerical application as a substitute of numerical solution for computational efficiency. In addition, the vertical gradient of wave horizontal orbital velocity is increased by the opposing current and decreased by the following current.

(3) The resulting wave action equation for strongly sheared current reproduces the work done by Voronovich (1976). The reduction of wave action equation for depth-uniform current and constantly sheared current agrees with previous study. The numerical study of wave action equation suggests that the absolute group velocity obtained from the wave action equation converges to the group velocity obtained from the dispersion relation $\partial\omega/\partial k$. The current shear effects on the wave action are relatively small compared to effects on the group velocity. The combination of depth-weighted current $\tilde{U}(k)$ and its wave number derivative $k\partial\tilde{U}/\partial k$ is a good approximation to current advection velocity in wave action equation.

(4) The wave-averaged forces for strongly sheared current are written as vortex force and Bernoulli head gradient. The reduction of the present vortex force formula for weak current assumption agrees with MRL04 results. The numerical study of wave vortex force for constantly sheared current indicates that the magnitude of vortex force decreases from deep water ($kh \gg 1$) to shallow water ($kh \ll 1$). The present x -component vortex force magnitude is slightly larger than MRL04 result for the opposing current and smaller for the following current. The present y -component vortex force also deviates from MRL04 result in both deep water and shallow water. It can change sign as the shear effects become larger, while MRL04 does not. It is because the present vortex formulation includes additional shear-related terms.

(5) The Stokes drift velocity for strongly sheared current is also extracted from the vortex force. The reduction of Stokes drift velocity for weak shear agrees with the MRL04 results. The numerical study indicates that the Stokes drift velocity magnitude is smaller for long waves. The velocity profile tends to be depth uniform for shallow

water.

7.2 Numerical Application

In the numerical application part, both the present and Uchiyama *et al.* (2010) vortex force formulations are implemented in the $NH\overline{WAVE}$ coupled model. Three cases have been tested:

- 1) Obliquely incident waves on a planar beach.
- 2) Wave propagation on highly stratified, vertically sheared current at Columbia River mouth.
- 3) Formation of Langmuir circulation in the presence of wind-driven current and waves.

Test case (1) is used to compare the present vortex force formulation with Uchiyama *et al.* (2010) formulation. The SWAN module is not activated in this simulation. Instead, the waves are provided using an input file. Test case (2) is designed for the analysis of wave effects on currents and current effects on waves. Both NHWAVE and SWAN are activated and coupled in this simulation. Test case (3) is the application of the present formulation to Langmuir circulation. Conclusions are summarized as below:

(1) For the test case of obliquely incident waves on a planar beach, both the present and MRL04 vortex force formulations are implemented in the $NH\overline{WAVE}$ coupled model for comparison. In general, the two formulations generate very similar wave set up/down, undertow profiles and longshore currents. The flow patterns are corresponding well to the previous studies by Uchiyama *et al.* (2010) and Kumar *et al.* (2012).

(2) The wave-current interaction test case at the mouth of Columbia River (MCR) suggests that waves have significant impacts on current velocity profiles. The plume front is thickened and extended offshore by the opposing waves. The Bernoulli head gradient applies an offshore forcing that strengthens the surface current velocity. The x and z component vortex force emerge along the plume base where most of the

current shear exists. The Bernoulli head gradient is responsible for extending the plume offshore. The combined effects of vortex force and Bernoulli head gradient thicken the plume front.

(3) The formation of Langmuir cells in an ideal computational domain indicates the present vortex force formulation successfully generates Langmuir cells. The x component velocity U indicates the larger positive velocity anomalies appear near the surface and bottom and negative velocity anomalies appear in the lower water column on both sides. The y component velocity V have vortices with alternating signs in both y and z directions. Regions of positive W are referred to as upwelling limbs and regions of negative W are referred to as downwelling limbs. The Langmuir cells are unsteady and constantly evolve during the simulation, since the vortex force is determined by the velocity anomalies and forces the velocity anomalies in return.

REFERENCES

- [1] Andrews, D.G. and M.E. McIntyre, “An exact theory of nonlinear waves on a Lagrangian-mean flow.” *J. Fluid Mech.*, 89:609-646, 1978a.
- [2] Andrews, D.G. and M.E. McIntyre, “On wave action and its relatives.” *J. Fluid Mech.*, 89:647-664, 1978b.
- [3] Ardhuin, F., A.D. Jenkins and K.A. Belibassakis, “Comments on ‘The three-dimensional current and surface wave equations’.” *J. Phys. Oceanogr.*, 38:1340-1350, 2008a.
- [4] Ardhuin, F., N. Raschle and K.A. Belibassakis, “Explicit wave-averaged primitive equations using a Generalized Lagrangian Mean.” *Ocean Modelling*, 20:35-60, 2008b.
- [5] Banihashemi, S., J.T. Kirby and Z. Dong, 2016, “Approximation of wave action flux velocity in strongly sheared mean flows.”, submitted to Coastal Engineering Journal, under revision.
- [6] Barnes, C.A., A.C. Duxbury and B.A. Morse, “Circulation and selected properties of the Columbia River effluent at sea, in The Columbia River Estuary and Adjacent Ocean Waters, edited by A. T. Pruter and D. L. Alverson”, pp. 4180, *Univ. of Wash. Press*, Seattle, Washington, 1972.
- [7] Battjes, J.A., “Radiation stress in short-crested waves.” *J. Mar. Res.*, 30:56-64, 1972.
- [8] Booij, N., R.C. Ris and L.H. Holthuijsen, “A third-generation wave model for coastal regions, Part I, Model description and validation.” *J. of Geophys. Res.* 104 (C4):7649-7666, 1999.
- [9] Bowen, A.J., D. L. Inman and V. P. Simmons, “Wave ‘set-down’ and set-up.” *J. Geophys. Res.*, 73:2569-2577, 1968.
- [10] Bowen, A.J., “The generation of longshore currents on a plane beach.” *J. Mar. Res.*, 27:206-215, 1969.
- [11] Bretherton, F.P. and C.J.R. Garrett, “Wavetrains in inhomogeneous moving media.” *Proc. Roy. Soc. Lond. A*, 302:529-554, 1968.

- [12] Craik, A.D.D., “Wave-induced longitudinal-vortex instability in shear flows.” *J. Fluid Mech.*, 125:37-52, 1982.
- [13] Craik, A.D.D. and S. Leibovich, “A rational model for Langmuir circulations.” *J. Fluid Mech.*, 73:401-426, 1976.
- [14] Derakhti, M., J.T. Kirby, F. Shi and G. Ma, ”NHWAVE: Governing equations, exact boundary conditions and turbulence modeling”, submitted to *Ocean Modelling*, January 2016.
- [15] Dingemans, M.W., A.C. Radder and H.J. DeVriend, “Computation of the driving forces of wave induced currents.” *Coast. Eng.*, 11:539-563, 1987.
- [16] Dong, Z. and J.T. Kirby, “Theoretical and numerical stud of wave-current interaction in strongly-sheared flows.”, *Proc. 33rd Con. Coast. Eng.*, Santander, Spain, 2012.
- [17] Dong, Z. and J.T. Kirby, “Wave-current interaction in strongly sheared mean flows: Theory.” *J. Fluid Mech.*, in preparation.
- [18] Elias, E.P.L., G. Gelfenbaum and A.J. Van der Westhuysen, “Validation of a coupled wave-flow model in a high-energy setting: The mouth of the Columbia River.” *J. Geophys. Res* 117, C09011, doi:10.1029/2012JC008105, 2012.
- [19] Feddersen, F., “Effect of wave directional spread on the radiation stress: comparing theory and observations.” *Coast. Eng.*, 51:473-481, 2004.
- [20] Fenton, J.D., “Some results for surface gravity waves on shear flows.” *J. Inst. Math. Applic.*, 12:1-20, 1973.
- [21] Gargett, A.E. and J.R. Wells, “Langmuir turbulence in shallow water: Part I. Observations.” *J. Fluid. Mech.*, 576: 27-61, 2007.
- [22] Gottlieb, S., C.-W. Shu, E. Tadmor, “Strong stability-preserving high-order time discretization methods.” *SIAM Rev.*, 43: 891-923, 2001.
- [23] Groeneweg, J. and G. Klopman, “Changes of the mean velocity profiles in the combined wave-current motion described in a GLM formulation”, *J. Fluid. Mech.*, 370:271-296, 1998.
- [24] Haas, K.A. and J.C. Warner, “Comparing a quasi-3D to a full 3D nearshore circulation model: SHORECIRC and ROMS.” *Ocean Modeling*, 26:91-103, 2009.
- [25] Hasselmann, K., “On the mass and momentum transfer between short gravity waves and larger-scale motions.” *J. Fluid Mech.*, 50:189-205, 1971.

- [26] He, X.S., “On the evolution and instability of gravity waves with arbitrary velocity shear.” in M. Rahman (ed) , *Ocean Wave Mechanics, CFD and Math Modelling*, CMP, 271-277, 1990.
- [27] Hickey, B.M., etal., “River Influences on Shelf Ecosystems: Introduction and synthesis.”, *J. Geophys. Res.*, 115:C00B17, doi:10.1029/2009JC005452, 2010.
- [28] Jonsson, I.G., O. Brink-Kjaer and G.P. Thomas, “Wave action and set-down for waves on a shear current.” *J. Fluid Mech.*, 87:401-416, 1978.
- [29] Kemp, P.H. and R.R. Simons, “The interaction of waves and a turbulent current; waves propagating in the current.”, *J. Fluid Mech.*, 116:227-250, 1982.
- [30] Kemp, P.H. and R.R. Simons, “The interaction of waves and a turbulent current; waves propagating against the current.”, *J. Fluid Mech.*, 130:73-89, 1983.
- [31] Kilcher, L.F. and J.D. Nash, “Structure and dynamics of the Columbia river tidal plume front.” *J. Geophys. Res.*, 115:C05S90, doi:10.1029/2009JC006066, 2010.
- [32] Kirby, J.T., “A note on linear surface wave-current interaction over slowly varying topography.” *J. Geophys. Res.*, 89:745-747, 1984.
- [33] Kirby, J.T. and T-M. Chen, “Surface waves on vertically sheared flows: approximate dispersion relations.” *J. Geophys. Res.*, 94:1013-1027, 1989.
- [34] Klopman, G., “Vertical structure of the flow due to waves and currents.” *Progress Rep. Delft Hydraulics*, H 840.32, Part 1, 1992.
- [35] Klopman, G., “Vertical structure of the flow due to waves and currents.” *Progress Rep. Delft Hydraulics*, H 840.32, Part 1, 1994.
- [36] Kukulka, T., A.J. Plueddemann, J.H. Trowbridge and P.P. Sullivan, “Significance of Langmuir circulations in upper ocean mixing: A comparison between observations and large eddy simulations.”, *Geophys. Res. Lett.*, 36, L10603, doi:10.1029/2009GL03762, 2009.
- [37] Kumar N., G. Voulgaris and J.C. Warner, “Implementation and modification of a three-dimensional radiation stress formulation for surf zone and rip-current applications.” *Coast. Eng.*, 8:1097-1117, 2011.
- [38] Kumar N., G. Voulgaris, J.C. Warner, M. Olabarrieta, “Implementation of the vortex force formalism in the coupled ocean-atmosphere-wave-sediment transport (COAWST) modeling system for inner shelf and surf zone applications.”, *Ocean Modeling*, 47:65-95, 2012.
- [39] Lane, E.M., J.M. Restrepo, J.C. McWilliams, “Wavecurrent interaction: a comparison of radiation-stress and vortex-force representations.” *J. Phys. Oceanogr.*, 37:11221141, 2007.

- [40] Langmuir, I., "Surface motion of water induced by wind." *Science*, 87:119-23, 1938.
- [41] Lesser, G.R., "An approach to medium-term coastal morphological modelling." *UNESCO-IHE*, Institute for Water Education, 2009.
- [42] Lin, P. and P.L.-F. Liu, "A numerical study of breaking waves in the surf zone." *J. Fluid Mech.*, 359:239-264, 1998.
- [43] Longuet-Higgins, M.S., "Mass transport in water waves." *Philos. Trans. R. Soc. Lond., Ser. A* 245, 535-581, 1953.
- [44] Longuet-Higgins, M.S. and R.W. Stewart, "Changes in the form of short gravity waves on long waves and tidal currents." *J. Fluid Mech.*, 8:565-583, 1960.
- [45] Longuet-Higgins, M.S. and R.W. Stewart, "The changes in amplitude of short gravity waves on steady non-uniform currents." *J. Fluid Mech.*, 10:529-549, 1961.
- [46] Longuet-Higgins, M.S. and R.W. Stewart, "Radiation stress and mass transport in gravity waves, with applications to 'surf-beats'." *J. Fluid Mech.*, 13:481-504, 1962.
- [47] Longuet-Higgins, M.S. and R.W. Stewart, "Radiation stress in water waves: a physical discussion, with applications." *Deep-Sea Res. Oceanogr. Abstr.*, 11:529-562, 1964.
- [48] Longuet-Higgins, M.S., "Longshore currents generated by obliquely incident sea waves, 1.", *J. Geophys. Res.*, 75:6778-6789, 1970.
- [49] Longuet-Higgins, M.S., "Longshore currents generated by obliquely incident sea waves, 2.", *J. Geophys. Res.*, 75:6790-6801, 1970.
- [50] Ma, G., F. Shi and J.T. Kirby, "Shock-capturing non-hydrostatic model for fully dispersive surface wave processes." *Ocean Modell.*, 43-44:22-35, 2012.
- [51] Ma, G., J.T. Kirby and F. Shi, "Numerical simulation of tsunami waves generated by deformable submarine landslides", *Ocean Modell.*, 69, 146-165, 2013.
- [52] McWilliams, J.C., J.M. Restrepo and E.M. Lane, "An asymptotic theory for the interaction of waves and currents in coastal waters." *J. Fluid Mech.*, 511:135-178, 2004.
- [53] Mei, C.C., M. Stiassnie and D.K.-P. Yue, "Theory and application of ocean surface waves." *World Scientific*, 1136pp, 2005.
- [54] Mellor, G., "The three-dimensional current and surface wave equations." *J. Phys. Oceanogr.*, 33:1978-1989, 2003.

- [55] Mellor, G., "Some consequences of the three-dimensional current and surface wave equations." *J. Phys. Oceanogr.*, 35:2291-2298, 2005.
- [56] Mellor G., "The depth dependent current and wave interaction equations: a revision." *J. Phys. Oceanogr.*, 38:2587-2596, 2008.
- [57] Mellor G., "A Combined Derivation of the Integrated and Vertically Resolved, Coupled WaveCurrent Equations." *J. Phys. Oceanogr.*, 45:1453-1463, 2015.
- [58] Mellor G., "On theories dealing with the interaction of surface waves and ocean circulation." *J. Geophys. Res.*, 121:4474-4486, 2016.
- [59] Newberger, P.A. and J.S. Allen, "Forcing a three-dimensional, hydrostatic, primitive-equation model for application in the surf zone: 1. Formulation.", *J. Geophys. Res.*, 112, C08018, doi:10.1029/2006JC003472, 2007.
- [60] Newberger, P.A. and J.S. Allen, "Forcing a three-dimensional, hydrostatic, primitive-equation model for application in the surf zone: 2. Application to DUCK94.", *J. Geophys. Res.*, 112, C08019,10.1029/2006JC003474, 2007.
- [61] Peregrine, D.H., "Interaction of water waves and currents." *Adv. Appl. Mech.*, 16:9-117, 1976.
- [62] Peregrine, D.H. and I.G. Jonsson, "Interaction of waves and currents." *Misc. Rep. MR83-6*, Coastal Eng. Res. Center, U.S. Army Corps of Eng., Fort Belvoir, Virginia, 1983.
- [63] Phillips, W.R.C. and Z. Wu, "On the instability of wave-catalysed longitudinal vortices in strong shear." *J. Fluid Mech.*, 272:235-254, 1994.
- [64] Phillips, W.R.C., A. Dai and K.K. Tjan, "On Lagrangian drift in shallow water waves on moderate shear." *J. Fluid Mech.* 2010.
- [65] Phillips, O.M., "The dynamics of the upper ocean." *Cambridge*, 261pp, 1966.
- [66] Reniers, A.J.H.M., J.A. Roelvink, E.B. Thornton, "Morphodynamic modeling of an embayed beach under wave group forcing." *J. Geophys. Res.* 109, C01030. doi:10.1029/2002JC001586, 2004.
- [67] Rodi, W., "Turbulence models and their application in hydraulics - a state of the art review." In: IAHR, Delft, The Netherlands, 1980.
- [68] Shi, F., J.T. Kirby and K. Haas, "Quasi-3D nearshore circulation equations: a CL-vortex force formulation." *Coastal Eng.* p. 1029, 2006.
- [69] Shi, F., J.T. Kirby, T.-J. Hsu, J.-L. Chen and R. Mieras, "NearCoM-TVD: a hybrid TVD solver for the nearshore community model documentation and user's manual." Research Report NO. CACR-13-06, October 18, 2013.

- [70] Shrira, V.I., "Surface waves on shear currents: solution of the boundary value problem." *J. Fluid Mech.*, 252:565-584, 1993.
- [71] Skop, R.A., "An approximate dispersion relation for wave-current interactions." *J. Waterw., Port Coastal and Ocean Eng.*, 113:187-195, 1987.
- [72] Smith, J.A., "Wave-current interactions in finite depth." *J. Phys. Oceanogr.*, 36:1403-1419, 2006.
- [73] Soulsby, R.L., "Bed shear-stresses due to combined waves and currents." *Advances in Coastal Morphodynamics*. Delft Hydraulics, Delft, The Netherlands, pp. 420423, 1995.
- [74] Soulsby, R.L., "Dynamics of Marine Sands: A Manual for Practical Applications." *Thomas Telford*, London, 1997.
- [75] Stewart, R.H. and J.W. Joy, "HF radio measurements of surface currents." *Deep Sea Res.*, 21:1039-1049, 1974.
- [76] Svendsen, I.A., "Mass flux and undertow in a surf zone." *Coastal Eng.* 8, 347365, 1984.
- [77] Tejada-Martinez, A.E. and C.E. Grosch, "Langmuir turbulence in shallow water: Part II. Large-eddy simulations", *J. Fluid Mech.*, 576:63-108, 2007.
- [78] Thompson, P.D., "The propagation of small surface disturbances through rotational flow.", *Ann. N.Y. Acad. Sci.*, 51:463-474, 1949.
- [79] Thorpe, S.A., "Langmuir circulation." *Annu. Rev. Fluid Mech.*, 36:55-79, 2004.
- [80] Uchiyama, Y., J.C. McWilliams and A.F. Shchepetkin, "Wave-current interaction in an oceanic circulation model with a vortex-force formalism: application to the surf zone." *Ocean Modeling*, 34:16-35, 2010.
- [81] Van der Westhuysen, A., G. Lesser, "Evaluation and development of wave-current interaction in SWAN: activity 6.4 of SBW project 367", *Waddenzee. Tech. Rep.*, Deltares (WL), 2007.
- [82] Voronovich, A.G., "Propagation of internal and surface gravity waves in the approximation of geometrical optics", *Bull.(Izv.), Acad. Sci. USSR, Atmospheric and Oceanic Physics*, 12, No.8:850-857, 1976.
- [83] Warner, J.C., C.R. Sherwood, R.P. Signell, C.K. Harris and H.G. Arango, "Development of a three-dimensional, regional, coupled wave, current, and sediment-transport model." *Computers and Geosciences*, 34:1284-1306, 2008.
- [84] Whitham, G.B., "Mass, Momentum and energy flux in water waves." *J. Fluid Mech.*, 12:135-147, 1962.

- [85] Whitham, G.B., "Linear and nonlinear waves." *Wiley Interscience*, 636pp. 1974,
- [86] Xu, Z., A.J. Bowen, "Wave- and wind-driven flow in water of finite depth." *J. Phys. Oceanogr.* 24, 18501866, 1994.

Appendix A

WAVE SOLUTIONS FOR SPECIAL CURRENT PROFILES

A.1 Waves in a stationary domain with slowly varying depth

$O(\epsilon)$ wave solution:

$$w_{1,1}(z) = -i\omega\eta_{1,1}F_{ss} \quad (\text{A.1})$$

$$\mathbf{q}_{1,1}(z) = \omega\eta_{1,1}F_{cs}\frac{\mathbf{k}}{k} \quad (\text{A.2})$$

$$p_{1,1}(z) = \frac{\rho\omega^2\eta_{1,1}}{k}F_{cs} \quad (\text{A.3})$$

$$\omega^2 = gk \tanh kH \quad (\text{A.4})$$

$$F_{ss} = \frac{\sinh k(H+z)}{\sinh kH} \quad (\text{A.5})$$

$$F_{cs} = \frac{\cosh k(H+z)}{\sinh kH} \quad (\text{A.6})$$

$O(\epsilon^2)$ wave solution:

$$\begin{aligned} w_{2,1}(z) = & -\frac{g\eta_{1,1}}{kc_0 \cosh kH}(\mathbf{k}\cdot\nabla_H H) \cosh k(H+z) \\ & -\frac{g\eta_{1,1}}{kc_0 \cosh kH}(\mathbf{k}\cdot\nabla_H H)[k(H+z)] \sinh k(H+z) \\ & -g\left[\frac{\eta_{1,1}}{2k^2c_0 \cosh kH}(\nabla_H\cdot\mathbf{k}) + \frac{\mathbf{k}}{k}\cdot\nabla_H\left(\frac{\eta_{1,1}}{kc_0 \cosh kH}\right)\right] \\ & +\frac{\eta_{1,1}}{2k^3c_0 \cosh kH}(\mathbf{k}\cdot\nabla_H k)[k(H+z)] \cosh k(H+z) \\ & -\frac{g\eta_{1,1}}{2k^3c_0 \cosh kH}(\mathbf{k}\cdot\nabla_H k)[k(H+z)]^2 \sinh k(H+z) \end{aligned} \quad (\text{A.7})$$

$$\begin{aligned}
\mathbf{q}_{2,1}(z) &= -\frac{ig\mathbf{k}}{k} \left\{ \frac{\eta_{1,1}}{kc_0 \cosh kH} (\mathbf{k} \cdot \nabla_H H) \sinh k(H+z) \right. \\
&+ \left[-\frac{\eta_{1,1}}{2k^2 c_0 \cosh kH} \nabla_H \cdot \mathbf{k} + \frac{\eta_{1,1}}{2k^3 c_0 \cosh kH} (\mathbf{k} \cdot \nabla_H k) \right] \cosh k(H+z) \\
&+ \left[\frac{\eta_{1,1}}{2k^2 c_0 \cosh kH} \nabla_H \cdot \mathbf{k} + \frac{\mathbf{k}}{k} \cdot \nabla_H \left(\frac{\eta_{1,1}}{kc_0 \cosh kH} \right) \right. \\
&+ \left. \frac{\eta_{1,1}}{2k^3 c_0 \cosh kH} (\mathbf{k} \cdot \nabla_H k) \right] [k(H+z)] \sinh k(H+z) \\
&+ \frac{\eta_{1,1}}{kc_0 \cosh kH} (\mathbf{k} \cdot \nabla_H H) [k(H+z)] \cosh k(H+z) \\
&+ \left. \frac{\eta_{1,1}}{2k^3 c_0 \cosh kH} (\mathbf{k} \cdot \nabla_H k) [k(H+z)]^2 \cosh k(H+z) \right\}
\end{aligned} \tag{A.8}$$

$$\begin{aligned}
p_{2,1}(z) &= i\rho g \left\{ \left[\left(\frac{\eta_{1,1}}{kc_0 \cosh kH} \right)_T + \frac{c_0 \mathbf{k}}{k} \cdot \nabla_H \left(\frac{\eta_{1,1}}{kc_0 \cosh kH} \right) \right. \right. \\
&+ \frac{\eta_{1,1}}{2k^2 \cosh kH} (\nabla_H \cdot \mathbf{k}) - \frac{\eta_{1,1}}{2k^3 \cosh kH} (\mathbf{k} \cdot \nabla_H k) \left. \right] \cosh k(H+z) \\
&- \frac{\eta_{1,1}}{k \cosh kH} (\mathbf{k} \cdot \nabla_H H) [k(H+z)] \cosh k(H+z) \\
&+ \left[\frac{\eta_{1,1}}{2k^3 \cosh kH} (\mathbf{k} \cdot \nabla_H k) - \frac{\eta_{1,1}}{2k^2 \cosh kH} (\nabla_H \cdot \mathbf{k}) \right. \\
&- \left. \frac{\mathbf{k}}{k^2} \cdot \nabla_H \left(\frac{\eta_{1,1}}{\cosh kH} \right) \right] [k(H+z)] \sinh k(H+z) \\
&- \left. \frac{\eta_{1,1}}{2k^3 \cosh kH} (\mathbf{k} \cdot \nabla_H k) [k(H+z)]^2 \cosh k(H+z) \right\}
\end{aligned} \tag{A.9}$$

$$\begin{aligned}
\eta_{2,1} &= -\frac{i}{kc_0} \left\{ \eta_{11T} + \frac{g\eta_{1,1}}{kc_0 \cosh kH} (\mathbf{k} \cdot \nabla_H H) \cosh kH \right. \\
&+ \frac{g\eta_{1,1}}{kc_0 \cosh kH} (\mathbf{k} \cdot \nabla_H H) (kH) \sinh kH \\
&+ \left[\frac{g\eta_{1,1}}{2k^2 c_0 \cosh kH} (\nabla_H \cdot \mathbf{k}) + \frac{g\mathbf{k}}{k} \cdot \nabla_H \left(\frac{\eta_{1,1}}{kc_0 \cosh kH} \right) \right. \\
&+ \left. \frac{g\eta_{1,1}}{2k^3 c_0 \cosh kH} (\mathbf{k} \cdot \nabla_H k) \right] (kH) \cosh kH \\
&+ \left. \frac{g\eta_{1,1}}{2k^3 c_0 \cosh kH} (\mathbf{k} \cdot \nabla_H k) (kH)^2 \sinh kH \right\}
\end{aligned} \tag{A.10}$$

Only the $O(\epsilon^2)$ pure wave solutions are used in perturbation approximation. Current related terms are in higher order. We will not provide $O(\epsilon^2)$ or higher order wave solutions for the other special current profiles since they are out of our interests in this problem.

A.2 Depth uniform current

In our problem, only $O(\epsilon)$ wave solutions for depth uniform current are needed. Thus, the $O(\epsilon^2)$ solutions are not provided here.

$$w_{1,1}(z) = -i\sigma\eta_{1,1}F_{ss} \quad (\text{A.11})$$

$$\mathbf{q}_{1,1}(z) = \sigma\eta_{1,1}F_{cs}\frac{\mathbf{k}}{k} \quad (\text{A.12})$$

$$p_{1,1}(z) = \frac{\rho\sigma^2\eta_{1,1}}{k}F_{cs} \quad (\text{A.13})$$

$$\sigma^2 = gk \tanh kH \quad (\text{A.14})$$

$$\sigma = \omega - \mathbf{k}\cdot\mathbf{q}_{0,0} \quad (\text{A.15})$$

A.3 Constant shear current

Assume current profile has a constant shear as below.

$$\mathbf{q}_{0,0}(z) = \mathbf{q}_{0,0}^s + \mathbf{\Omega}^s z \quad (\text{A.16})$$

where $\mathbf{\Omega}^s$ stands for current vertical shear. $\mathbf{\Omega}^s$ does not have to be collinear with either $\mathbf{q}_{0,0}^s$ or \mathbf{k} . Now Rayleigh equation is reduced to the Laplace equation. (The possibility of σ taking on a value of zero at a critical level is not typically of interest in surface wave dynamics.)

$$\sigma(w_{1,1zz} - k^2w_{1,1}) = 0; \quad (\text{A.17})$$

$$w_{1,1}(-H) = 0; \quad (\text{A.18})$$

$$\sigma_s^2 w_{1,1z} = (gk^2 - \sigma_s \mathbf{\Omega}^s \cdot \mathbf{k})w_{1,1}; \quad z = 0 \quad (\text{A.19})$$

The solutions are given by

$$w_{1,1}(z) = -i\sigma_s\eta_{1,1}F_{ss} \quad (\text{A.20})$$

$$\mathbf{q}_{1,1}(z) = -\frac{\sigma_s\eta_{1,1}\boldsymbol{\Omega}^s}{\sigma}F_{ss} + \frac{\sigma_s\eta_{1,1}\mathbf{k}}{k^2}(kF_{cs} + \frac{\boldsymbol{\Omega}^s \cdot \mathbf{k}}{\sigma}F_{ss}) \quad (\text{A.21})$$

$$p_{1,1}(z) = \frac{\rho\sigma_s\eta_{1,1}}{k^2}(\boldsymbol{\Omega}^s \cdot \mathbf{k})F_{ss} + \frac{\rho\sigma_s\eta_{1,1}}{k}\sigma F_{cs} \quad (\text{A.22})$$

$$\sigma_s^2 = (g - \frac{\sigma_s\boldsymbol{\Omega}^s \cdot \mathbf{k}}{k^2})k \tanh kH \quad (\text{A.23})$$

Apparently, constant current shear affects the vertical structure of wave orbital velocity and wave pressure by modifying the dispersion relation and twisting wave horizontal velocity in the current shear direction. Now we may take a look at wave phase speed c and group speed c_g . c_a is absolute phase speed. c_r is relative phase speed at the surface.

$$c_a = \frac{\omega}{k} = c_r + \hat{k}q_{0,0}^s \quad (\text{A.24})$$

$$c_r = \frac{\sigma_s}{k} \quad (\text{A.25})$$

$$c_{gr} = \frac{\partial\sigma_s}{\partial k} = \frac{g(1+G) - (\boldsymbol{\Omega}^s \cdot \hat{\mathbf{k}})Gc_r}{2g - (\boldsymbol{\Omega}^s \cdot \hat{\mathbf{k}})c_r}c_r \quad (\text{A.26})$$

$$G = \frac{2kH}{\sinh 2kH} \quad (\text{A.27})$$

where $\hat{\mathbf{k}} = \frac{\mathbf{k}}{k}$ is non-dimensional wave number vector.

Appendix B

DERIVATION OF GENERAL FORM OF WAVE-AVERAGED FORCES

B.1 Bernoulli head: κ

The original definition of Bernoulli head is given in Chapter 4. Now we use the relation between $\mathbf{q}_{1,1}$ and $w_{1,1}$ in Chapter 3. The $O(\epsilon^2)$ Bernoulli head κ_2 is evaluated in terms of $w_{1,1}$ and its complex conjugate.

$$\kappa_2 = \frac{1}{k^2} \frac{\partial w_{1,1}}{\partial z} \frac{\partial w_{1,-1}}{\partial z} + w_{1,1} w_{1,-1} + \frac{w_{1,1} w_{1,-1}}{\sigma^2} \mathbf{q}_{0,0z} \cdot \mathbf{q}_{0,0z} - \frac{w_{1,1} w_{1,-1}}{\sigma^2 k^2} (\sigma_z)^2 \quad (\text{B.1})$$

We use the relation between $\mathbf{q}_{2,1}$ and $w_{2,1}$ in Chapter 3. The $O(\epsilon^3)$ Bernoulli head κ_3 is evaluated in terms of $w_{1,1}$, $\mathbf{q}_{1,1}$, $w_{2,1}$ and their complex conjugates.

$$\begin{aligned} \kappa_3 &= \frac{1}{k^2} (w_{1,1z} w_{2,-1z} + w_{1,-1z} w_{2,1z}) + (w_{1,1} w_{2,-1} + w_{1,-1} w_{2,1}) \\ &+ \frac{w_{1,1} w_{2,-1} + w_{1,-1} w_{2,1}}{\sigma^2} \mathbf{q}_{0,0z} \cdot \mathbf{q}_{0,0z} - \frac{w_{1,1} w_{2,-1} + w_{1,-1} w_{2,1}}{\sigma^2 k^2} (\sigma_z)^2 \\ &+ \mathbf{Q}_{1,1}^* \cdot \mathbf{q}_{1,-1} + \mathbf{Q}_{1,-1}^* \cdot \mathbf{q}_{1,1} \end{aligned} \quad (\text{B.2})$$

where $\mathbf{Q}_{1,1}^*$ is a variable with the dimension of velocity.

$$\begin{aligned} \mathbf{Q}_{1,1}^* &= \frac{i}{\sigma} \left[\frac{\mathbf{k}}{k^2} \mathbf{k} \cdot \left(\frac{D\mathbf{q}_{1,1}}{DT} + \frac{1}{\rho} \nabla_{HP1,1} + \mathbf{q}_{1,1} \cdot \nabla_H \mathbf{q}_{0,0} \right) \right. \\ &\quad \left. - \left(\frac{D\mathbf{q}_{1,1}}{DT} + \frac{1}{\rho} \nabla_{HP1,1} + \mathbf{q}_{1,1} \cdot \nabla_H \mathbf{q}_{0,0} \right) + \frac{\mathbf{k}}{k^2} \sigma \nabla_H \cdot \mathbf{q}_{1,1} \right] \end{aligned} \quad (\text{B.3})$$

Where

$$\frac{D}{DT} = \frac{\partial}{\partial T} + \mathbf{q}_{0,0} \cdot \nabla_H + w_{1,0} \frac{\partial}{\partial z} \quad (\text{B.4})$$

Apparently, $\mathbf{Q}_{1,1}^*$ can be evaluated only using $w_{1,1}$.

B.2 Horizontal vortex force \mathbf{J}

We use expressions for $O(\epsilon^2)$ wave vorticity, consider complex conjugate relations and rearrange horizontal vortex force. The manipulation of the vertical component vortex force is not clear and therefore we keep the original expression. To identify Stokes drift in the vortex force, we introduce variable $\mathbf{q}_{1,1}^*$, which is analogous to Lagrangian disturbance velocity in Andrews & McIntyre (1978a).

$$\mathbf{q}_{1,1}^*(z) = \mathbf{q}_{1,1} + \frac{iw_{1,1}}{\sigma} \mathbf{q}_{0,0z} \quad (\text{B.5})$$

The vortex force can be reduced to the form

$$\begin{aligned} \mathbf{J} &= \mathbf{i}_z \times \epsilon^3 \frac{i}{\sigma} \left[(w_{1,1} \frac{D\boldsymbol{\xi}_{1,-1}}{DT} - \mathbf{q}_{1,1}^* \frac{D\chi_{1,-1}}{DT}) + (w_{1,1} \mathbf{q}_{1,-1} \cdot \nabla_H \boldsymbol{\xi}_{0,0} - \mathbf{q}_{1,1}^* w_{1,-1} \chi_{1,0z}) \right. \\ &- (w_{1,1} \boldsymbol{\xi}_{1,-1} \cdot \nabla_H \mathbf{q}_{0,0} - \chi_{1,-1} \mathbf{q}_{1,1}^* w_{1,0z}) - (w_{1,1} \boldsymbol{\xi}_{0,0} \cdot \nabla_H \mathbf{q}_{1,-1} - \mathbf{q}_{1,1}^* \boldsymbol{\xi}_{0,0} \cdot \nabla_H w_{1,-1}) \\ &\left. - \chi_{1,0} (w_{1,1} \mathbf{q}_{1,-1z} - \mathbf{q}_{1,1}^* w_{1,-1z}) \right] + c.c. + O(\epsilon^4) \end{aligned} \quad (\text{B.6})$$

In our case, the depth dependent Stokes drift velocity can be expressed as

$$\mathbf{q}^{st} = w_{1,1} \mathbf{q}_{1,-1z} - \mathbf{q}_{1,1}^* w_{1,-1z} + c.c. \quad (\text{B.7})$$

B.3 Vertical vortex force K

We use the relation between $\mathbf{q}_{1,1}$, $\boldsymbol{\xi}_{1,1}$ and $w_{1,1}$ in Chapter 3. The $O(\epsilon^2)$ vertical vortex force K_2 is written as

$$K_2 = \frac{2w_{1,1}w_{1,-1}}{\sigma^2} \mathbf{q}_{0,0z} \times \boldsymbol{\xi}_{0,0z} - \frac{\sigma}{k^2} \left(\frac{w_{1,1}w_{1,-1}}{\sigma^2} \right)_z \mathbf{k} \times \left(\mathbf{q}_{0,0z} \frac{\boldsymbol{\xi}_{0,0} \cdot \mathbf{k}}{\sigma} + \boldsymbol{\xi}_{0,0z} \right) \quad (\text{B.8})$$

The $O(\epsilon^3)$ vertical vortex force K_3 is given by

$$\begin{aligned} K_3 &= i\mathbf{q}_{1,1} \times \left[\frac{\mathbf{O}_{2,-1}}{\sigma} - i\mathbf{q}_{0,0z} \frac{P_{2,-1}}{\sigma^2} + \mathbf{q}_{0,0z} \frac{w_{2,-1}(\boldsymbol{\xi}_{0,0} \cdot \mathbf{k})}{\sigma^2} + \boldsymbol{\xi}_{0,0z} \frac{w_{2,-1}}{\sigma} \right] \\ &- i\mathbf{q}_{1,-1} \times \left[\frac{\mathbf{O}_{2,1}}{\sigma} + i\mathbf{q}_{0,0z} \frac{P_{2,1}}{\sigma^2} + \mathbf{q}_{0,0z} \frac{w_{2,1}(\boldsymbol{\xi}_{0,0} \cdot \mathbf{k})}{\sigma^2} + \boldsymbol{\xi}_{0,0z} \frac{w_{2,1}}{\sigma} \right] \\ &+ \left\{ \frac{1}{\sigma} [w_{2,-1} \mathbf{q}_{0,0z} - \frac{\mathbf{k}}{k^2} (\sigma w_{2,-1z} - w_{2,-1} \sigma_z)] + \mathbf{Q}_{1,-1}^* \right\} \times \left[\mathbf{q}_{0,0z} \frac{(\boldsymbol{\xi}_{0,0} \cdot \mathbf{k}) w_{1,1}}{\sigma^2} + \boldsymbol{\xi}_{0,0z} \frac{w_{1,1}}{\sigma} \right] \\ &+ \left\{ \frac{1}{\sigma} [w_{2,1} \mathbf{q}_{0,0z} - \frac{\mathbf{k}}{k^2} (\sigma w_{2,1z} - w_{2,1} \sigma_z)] + \mathbf{Q}_{1,1}^* \right\} \times \left[\mathbf{q}_{0,0z} \frac{(\boldsymbol{\xi}_{0,0} \cdot \mathbf{k}) w_{1,-1}}{\sigma^2} + \boldsymbol{\xi}_{0,0z} \frac{w_{1,-1}}{\sigma} \right] \end{aligned} \quad (\text{B.9})$$

Appendix C

DERIVATION OF WAVE-AVERAGED FORCES FOR WEAK CURRENT

For weak current assumption, the forms of $O(\epsilon)$ wave perturbation solution $w_{1,1}, \chi_{1,1}$ remain the same, but $\mathbf{q}_{1,1}, p_{1,1}, \boldsymbol{\xi}_{1,1}$ are slightly changed.

$$\mathbf{q}_{1,1}^{(0)} = \frac{i}{\sigma} \frac{\mathbf{k}}{k^2} \sigma w_{1,1z}^{(0)} \quad (\text{C.1})$$

$$\mathbf{q}_{1,1}^{(1)} = -\frac{i}{\sigma} [w_{1,1}^{(0)} \mathbf{q}_{0,0z} - \frac{\mathbf{k}}{k^2} (\sigma w_{1,1z}^{(1)} - w_{1,1}^{(0)} \sigma_z)] \quad (\text{C.2})$$

$$p_{1,1}^{(0)} = \frac{i\rho}{k^2} \sigma w_{1,1z}^{(0)} \quad (\text{C.3})$$

$$p_{1,1}^{(1)} = \frac{i\rho}{k^2} (\sigma w_{1,1z}^{(1)} - w_{1,1}^{(0)} \sigma_z) \quad (\text{C.4})$$

$$\boldsymbol{\xi}_{1,1}^{(0)} = -i \boldsymbol{\xi}_{0,0z} \frac{w_{1,1}^{(0)}}{\sigma} - \frac{(\boldsymbol{\xi}_{0,0} \cdot \mathbf{k}) \mathbf{q}_{1,1}^{(0)}}{\sigma} \quad (\text{C.5})$$

$$\boldsymbol{\xi}_{1,1}^{(1)} = -i [\mathbf{q}_{0,0z} \frac{(\boldsymbol{\xi}_{0,0} \cdot \mathbf{k}) w_{1,1}^{(0)}}{\sigma^2} + \boldsymbol{\xi}_{0,0z} \frac{w_{1,1}^{(1)}}{\sigma}] - \frac{(\boldsymbol{\xi}_{0,0} \cdot \mathbf{k}) \mathbf{q}_{1,1}^{(1)}}{\sigma} \quad (\text{C.6})$$

$$(\text{C.7})$$

Derivation of Bernoulli head uses equations for $w_{1,1}^{(0)}, \mathbf{q}_{1,1}^{(0)}, w_{1,1}^{(1)}, \mathbf{q}_{1,1}^{(1)}, w_{2,1}^{(0)}, \mathbf{q}_{2,1}^{(0)}$.

$$\kappa = \epsilon^2 \kappa_2^{(0)} + \epsilon^3 \kappa_2^{(1)} + O(\epsilon^4) \quad (\text{C.8})$$

$$\kappa_2^{(0)} = \frac{1}{k^2} w_{1,1z}^{(0)} w_{1,-1z}^{(0)} + w_{1,1}^{(0)} w_{1,-1}^{(0)} \quad (\text{C.9})$$

$$\kappa_2^{(1)} = \frac{1}{k^2} w_{1,1z}^{(1)} w_{1,-1z}^{(0)} + \frac{1}{k^2} w_{1,1z}^{(0)} w_{1,-1z}^{(1)} + w_{1,1}^{(1)} w_{1,-1}^{(0)} + w_{1,1}^{(0)} w_{1,-1}^{(1)} \quad (\text{C.10})$$

Terms only related to $O(\epsilon)$ wave solutions yield Bernoulli head for weak current case.

Terms related to $O(\epsilon^2)$ wave solutions vanish after manipulation.

For vortex force \mathbf{J}, K , we have

$$\begin{aligned}
\mathbf{J} &= \mathbf{i}_z \times \left\{ -\left(\frac{\boldsymbol{\xi}_{0,0} \cdot \mathbf{k}}{\sigma^2} \mathbf{E}^{*(0)} + \boldsymbol{\xi}_{0,0z} \frac{w_{1,1}^{(0)} w_{1,-1}^{(0)}}{\sigma^2}\right)_T - \frac{\mathbf{E}^{*(0)}}{\sigma^2} (\boldsymbol{\xi}_{0,0} \cdot \mathbf{k})_T \right. \\
&+ \frac{\mathbf{E}^{*(0)}}{\sigma} \cdot \nabla_H \boldsymbol{\xi}_{0,0} + \frac{\mathbf{E}^{*(0)}}{\sigma} \chi_{1,0z} - \frac{\boldsymbol{\xi}_{0,0}}{\sigma} \cdot \nabla_H \mathbf{E}^{*(0)} - \chi_{1,0} \mathbf{q}^{st(0)}(z) \left. \right\} \\
&+ O(\epsilon^5)
\end{aligned} \tag{C.11}$$

$$K = -\frac{\sigma}{k^2} \left(\frac{w_{1,1}^{(0)} w_{1,-1}^{(0)}}{\sigma^2}\right)_z \mathbf{k} \times \boldsymbol{\xi}_{0,0z} + O(\epsilon^4) \tag{C.12}$$